University of Antwerp

Faculty of Science

Optoelectronic and transport properties of three-dimensional Dirac semimetals

Thesis submitted for the degree of
Doctor of Science: Physics
at the University of Antwerp to be defended by

Qinan Li

Supervisors
prof. dr. Wen Xu
prof. dr. Milorad V. Milošević

University of Antwerp, 2024

Jury

Chair
prof. dr. Shuncai Zhao, Kunming University of Science and Technology, China

Supervisors
prof. dr. Wen Xu, Yunnan University, China
prof. dr. Milorad V. Milošević, University of Antwerp, Belgium

Members
prof. dr. Hai Yang, Kunming University, China
prof. dr. Cuihong Yang, Nanjing University of Information Science and Technology, China
prof. dr. Cong Ren, Yunnan University, China
prof. dr. Lan Ding, Yunnan University, China

Contact

Qinan Li

Department of Physics, School of Physics and Astronomy, Yunnan University (China)
Department of Physics, Faculty of Science, University of Antwerp (Belgium)

Chenggong Campus of Yunnan University, 650500, Kunming (China)
M: liqinan@mail.ynu.edu.cn

Dutch title:

Opto-elektronische en transporteigenschappen van driedimensionale Dirac-semimetalen

Abstract

Topological materials have contributed significantly to technological advancements in the past few decades, and the discovery of three-dimensional (3D) Dirac semimetals (DSMs) has further expanded the field of topological semimetals. Based on whether they obey Lorentz invariance, 3D DSMs can be classified into type-I and type-II. Na_3Bi and Cd_3As_2 have been confirmed as type-I, while $PtTe_2$ is a representative material of type-II. These representative materials possess stable samples, mature preparation methods, and their theoretically predicted band structures have been experimentally verified, making them excellent platforms for extensive research. In this dissertation, we conduct theoretical research on their optoelectronic and transport properties using the random phase approximation (RPA) dielectric function and the energy-balance and momentum-balance equations derived from the Boltzmann equation. The main research work and results are as follows.

Based on Na_3Bi, we analyze the band structure of type-I 3D DSMs and calculate the optical conductivity (OC) of bulk Na_3Bi under linearly polarized light using the energy-balance equation. The results show that type-I 3D DSMs exhibit anisotropic energy dispersion, and the band inversion structure, along with Berry curvature, leads to a nontrivial density of states for low-electron-density samples. This study revealed that the anisotropic OC of bulk Na_3Bi originates from its band structure. At higher and lower photon energies, the OCs are contributed by interband and intraband transitions, respectively, leading to the optical absorption windows. The energy relaxation time, temperature, and electron density of the sample significantly affect its OC, further demonstrating the tunability of the OC in type-I 3D DSMs. Unique changes in OC along the z direction occur with variations in electron density, reflecting the influence of Berry curvature. This work explains existing experiments and explores the relationship between OC and topological properties in type-I 3D DSMs.

Using the RPA dielectric function, we calculate the plasmon dispersion of type-I 3D DSMs in different directions and at various electron densities. This study first reveals the anisotropic plasmon of type-I 3D DSMs, which can be tuned by electron density. The results derived from Na_3Bi and Cd_3As_2 demonstrate differences in plasmons due to variations in the band parameters. By reducing the electron density, one can observe that the plasmon wave vector in the k_z direction experiences a peculiar reduction influenced by the Berry curvature, exhibiting the topological properties in collective excitations. Consequently, plasmons in the k_z direction of type-I 3D DSMs are tunable.

Using the energy-balance equation, we calculate the optical conductivity (OC) of a type-II 3D DSM $PtTe_2$ under linearly polarized light. Unlike Na_3Bi, we found that the anisotropic OC of the bulk $PtTe_2$ originates from its tilted Dirac cone. The OCs of $PtTe_2$ are also induced by intra- and interband transitions, as well as the phenomenon of absorption windows, which stems from the gapless nature of Dirac fermions. The tilted Dirac cone causes significant differences in the interband transition at higher photon energies, reflecting the distinction between type-I and type-II 3D DSMs. The energy relaxation time, temperature, and electron density also affect the OC of

ii

PtTe$_2$, demonstrating its tunability. This work is the first to reveal the physical mechanisms and phenomena behind the OC of bulk PtTe$_2$, providing theoretical support for further experiments and exploring the potential of such materials in optoelectronic devices.

With the momentum-balance equation, we calculate the transport and quantum lifetimes of the bulk PtTe$_2$. The results obtained by introducing the impurity density as a fitting parameter are consistent with experiments, indicating that our theoretical model can provide an effective way to study background impurities. By analyzing the theoretical data and experimental results, we found that the anisotropic effective mass of the bulk PtTe$_2$ leads to anisotropic mobility, mainly due to its tilted Dirac cone. This research explains the existing transport results and predicts how the transport lifetime and mobility of PtTe$_2$ change with electron density, providing a theoretical foundation for future studies on the transport properties of type-II 3D DSMs.

In summary, this thesis studies the nontrivial band of type-I 3D DSMs and the effects of topological properties on their optical conductivites and plasmons. Meanwhile, optical conductivites and lifetimes primarily governed by tilted Dirac cones of type-II 3D DSMs are also investigated. These investigations provide theoretical foundations for understanding the optoelectronic and transport properties of emerging topological materials and exploring their potential applications.

Samenvatting

Topologische materialen hebben de afgelopen decennia aanzienlijk bijgedragen aan de technologische vooruitgang, en de ontdekking van driedimensionale (3D) Dirac-semimetalen (DSM's) heeft het veld van topologische semimetalen verder uitgebreid. Afhankelijk van of ze de Lorentz-invariantie respecteren, kunnen 3D DSM's worden ingedeeld in type-I en type-II. Na_3Bi en Cd_3As_2 zijn bevestigd als type-I, terwijl $PtTe_2$ een representatief materiaal is voor type-II. Deze representatieve materialen beschikken over stabiele stalen, goed ontwikkelde bereidingsmethoden, en hun theoretisch voorspelde bandstructuren zijn experimenteel bevestigd, waardoor ze als uitstekend platform kunnen dienen voor uitgebreid onderzoek. In deze dissertatie voeren we theoretisch onderzoek uit naar hun opto-elektronische en transporteigenschappen met behulp van de random phase approximation (RPA) diëlektrische functie en de energie- en momentumbalansvergelijkingen die zijn afgeleid van de Boltzmann-vergelijking. Het belangrijkste onderzoekswerk en de resultaten zijn als volgt.

Gebaseerd op Na_3Bi analyseren we de bandstructuur van type-I 3D DSM's en berekenen we de optische conductiviteit (OC) van bulk Na_3Bi onder lineair gepolariseerd licht met behulp van de energie-balansvergelijking. De resultaten tonen aan dat type-I 3D DSM's anisotrope energie-dispersie vertonen, en de bandinversiestructuur, samen met Berry-kromming, leidt tot een niet-triviale dichtheid van toestanden voor stalen met lage elektrondichtheid. Deze studie onthulde dat de anisotrope OC van bulk Na_3Bi voortkomt uit zijn bandstructuur. Bij hogere en lagere fotonenergieën worden de OC's respectievelijk bijgedragen door interband- en intrabandovergangen, wat leidt tot de optische absorptievensters. De energie-relaxatietijd, temperatuur en elektrondichtheid van het monster beïnvloeden de OC aanzienlijk, wat de afstelbaarheid van de OC in type-I 3D DSM's verder aantoont. Unieke veranderingen in OC in de z-richting treden op bij variaties in elektrondichtheid, wat de invloed van Berry-kromming weerspiegelt. Dit werk verklaart bestaande experimenten en verkent de relatie tussen OC en topologische eigenschappen in type-I 3D DSM's.

Met behulp van de RPA diëlektrische functie berekenen we de plasmon-dispersie van type-I 3D DSM's in verschillende richtingen en bij verschillende elektrondichtheden. Deze studie onthult voor het eerst de anisotrope plasmon van type-I 3D DSM's, die kan worden afgesteld door elektrondichtheid. De resultaten afgeleid van Na_3Bi en Cd_3As_2 demonstreren verschillen in plasmons door variaties in de bandparameters. Door de elektrondichtheid te verlagen, kan men observeren dat de plasmon-golfvector in de k_z-richting een merkwaardige afname ondergaat, beïnvloed door de Berry-kromming, wat de topologische eigenschappen in collectieve excitaties aantoont. Bijgevolg zijn plasmons in de k_z-richting van type-I 3D DSM's afstelbaar.

Met de energie-balansvergelijking berekenen we de optische conductiviteit (OC) van een type-II 3D DSM, $PtTe_2$, onder lineair gepolariseerd licht. In tegenstelling tot Na_3Bi vonden we dat de anisotrope OC van bulk $PtTe_2$ voortkomt uit zijn hellende Dirac-kegel. De OC's van $PtTe_2$ worden ook geïnduceerd door intra- en interbandovergangen, evenals het fenomeen van absorptievensters, dat voortkomt uit de bandkloofloze natuur van Dirac-fermionen. De hellende Dirac-kegel veroorzaakt aanzienlijke verschillen in de interbandovergang bij hogere fotonenergieën, wat

iii

iv

het onderscheid tussen type-I en type-II 3D DSM's weerspiegelt. De energie-relaxatietijd, temperatuur en elektrondichtheid beïnvloeden ook de OC van $PtTe_2$, wat de afstelbaarheid aantoont. Dit werk is de eerste die de fysieke mechanismen en fenomenen achter de OC van bulk $PtTe_2$ onthult, en biedt theoretische ondersteuning voor verdere experimenten en verkent het potentieel van dergelijke materialen in opto-elektronische apparaten.

Met de momentum-balansvergelijking berekenen we de transport- en kwantumlevensduur van de bulk $PtTe_2$. De resultaten verkregen door de onzuiverheidsdichtheid als een fittingparameter in te voeren, komen overeen met experimenten, wat aangeeft dat ons theoretische model een effectieve manier kan bieden om achtergrondonzuiverheden te bestuderen. Door de theoretische gegevens en experimentele resultaten te analyseren, vonden we dat de anisotrope effectieve massa van bulk $PtTe_2$ leidt tot anisotrope mobiliteit, voornamelijk als gevolg van zijn hellende Dirac-kegel. Dit onderzoek verklaart de bestaande transportresultaten en voorspelt hoe de transportlevensduur en mobiliteit van $PtTe_2$ veranderen met elektrondichtheid, wat een theoretische basis biedt voor toekomstige studies over de transporteigenschappen van type-II 3D DSM's.

Samengevat bestudeert deze thesis de niet-triviale band van type-I 3D DSM's en de effecten van topologische eigenschappen op hun optische conductiviteit en plasmons. Tegelijkertijd worden optische conductiviteiten en levensduren die voornamelijk worden bepaald door hellende Dirac-kegels van type-II 3D DSM's ook onderzocht. Deze onderzoeken bieden theoretische onderbouwing voor het begrijpen van de opto-elektronische en transporteigenschappen van opkomende topologische materialen en het verkennen van hun potentiële toepassingen.

Contents

Chapter 1

Introduction

In 1928, physicist P. A. M. Dirac proposed the famous Dirac equation, which for the first time reconciled special relativity with quantum mechanics [1]. The form of the Dirac equation stems from the constraints of relativity, where derivatives of time and space must appear at the same order in the equation describing the motion of electrons, and the probabilistic interpretation of the wave function ensures that the Dirac equation depends only on the first-order time derivative. Dirac's derivation used 4×4 complex matrices that in their modern form are referred to as gamma (γ) matrices and a four component wave function. The four components describe both positive and negative charge solutions, as well as spin-up and spin-down states. This epochal moment in theoretical physics, originating in these simple considerations, led to a new understanding of the concept of spin, predicted the existence of antimatter, and was the invention of quantum field theory itself. A number of variations of the Dirac equation quickly followed. In 1929, mathematician Hermann Weyl proposed a simplified Dirac equation, known as the Weyl equation, used to describe massless fermions with definite chirality or handedness [2]. In 1937, Ettore Majorana found a modification using real numbers, which described a neutral particle that was its own antiparticle [3]. These developments have found great application in modern particle physics. The Dirac equation is now the fundamental equation that describes relativistic electrons, and the Majorana equations are a candidate to describe neutrinos. The Dirac equation is also a key concept leading to topological phenomena such as zero modes and chiral anomalies in quantum field theories. Unfortunately, in the nearly 90 intervening years, no candidate Weyl fermions have been observed as fundamental particles in high-energy particle physics experiments.

In condensed matter physics, where one is interested in energy scales much smaller than the rest mass of the electron, it would appear that a nonrelativistic description, perhaps with minor corrections, would suffice and that Dirac equation would not play an important role. However, the propagation of even slow electrons through the periodic potential of a crystal leads to a dressing of the electronic states. In certain instances, this results in an effective low-energy description that once again resembles the Dirac equation. The most famous example is the two-dimensional (2D) Dirac electronic system in graphene. Monolayer graphene obtained by mechanical exfoliation of highly oriented pyrolytic graphite has a linear and gapless energy dispersion that is captured by the 2D massless Dirac equation [4, 5]. Angle-resolved photoemission spectroscopy (ARPES) experiments confirmed the band structure of monolayer graphene [6], as shown in Fig. 1.1. The following research quickly revealed that graphene has many unique properties, such as high carrier mobility [7–9], the quantum Hall effect (QHE) and Berry phase [10]. In recent years, it has been discovered that in some three-dimensional (3D) crystals, the low-energy dispersion of fermions can also be described by the massless Weyl or Dirac equation. These newly
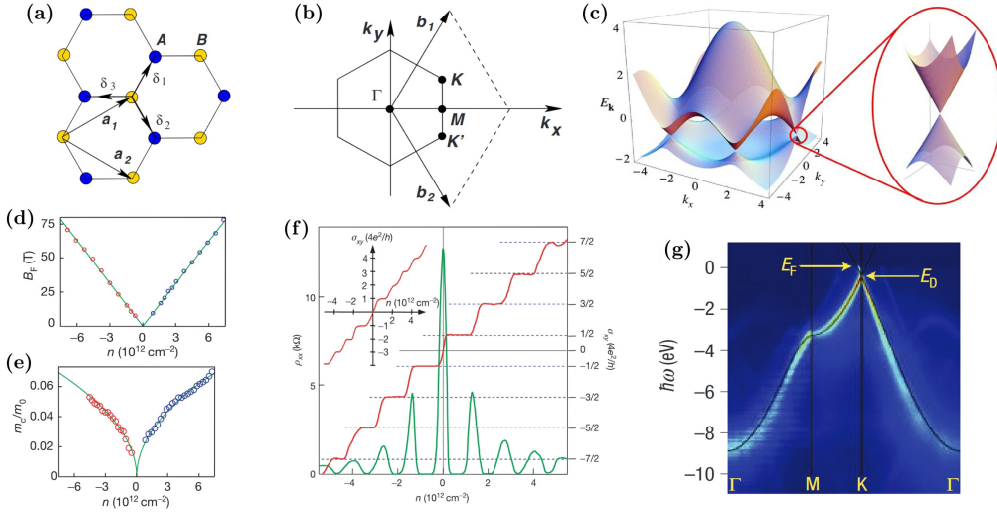
Figure 1.1: Properties of the two-dimensional Dirac electronic system in monolayer graphene. (a) Honeycomb lattice structure of monolayer graphene. (b) Brillouin zone corresponding to the lattice structure, with the K and K' points indicating the positions of the Dirac cones. (c) Energy band of graphene and the Dirac cone structure. (d) Relationship between the frequency of the Shubnikov-de Haas oscillations $B_F = (h/4e)n$ and the carrier concentration n, where $n > 0$ represents electrons and $n < 0$ represents holes. This result shows that the electron energy E is proportional to the wave vector k, thus confirming the linear band of graphene. (e) The cyclotron mass m_c of graphene is proportional to the square root of the carrier concentration $\sqrt{n}$. (f) Hall conductivity σ_{xy} and longitudinal resistivity ρ_{xx} of graphene at a temperature $T = 4$ K and magnetic field strength $B = 14$ T as functions of carrier concentration, where σ_{xy} increases in integer multiples of $4e^2/h$, demonstrating the quantum Hall effect in graphene. (f) ARPES experimental results clearly show the linear band structure at the Dirac point in monolayer graphene. The above results are adapted from Refs. [5] and [6].

discovered 3D crystals are classified as Weyl semimetals (WSMs) and Dirac semimetals (DSMs). These semimetals exhibit rich topological and physical properties, making them a new platform for studying the characteristics of topological electronic states in materials. This thesis primarily studies 3D DSMs, so the following sections will further introduce the development of the Dirac equation in condensed matter physics and related research on DSMs.

1.1   From Dirac equation to 3D Dirac semimetals (DSMs)

In 1929, shortly after Dirac wrote the Dirac equation containing 4×4 complex matrices, Weyl proposed a simplified Dirac equation using only the 2×2 Pauli matrices [2]. This simplification required the fermions to be massless. Weyl fermions are related to chirality or handedness, and a pair of Weyl fermions with opposite chiralities can combine to form a Dirac fermion. In another seemingly unrelated derivation in 1937, Conyers Herring studied the conditions for band degeneracy in crystals, where accidental twofold degeneracies of energy bands can occur in 3D crystalline materials even without any symmetry [11]. Near these "accidental degeneracies" or the touching points of bands, the energy dispersion of the electrons is typically linear and follows

the Weyl equation, linking these touching points to massless Weyl fermions.

It is noteworthy that certain properties of relativistic Weyl fermions, such as the chiral anomaly, also exist in nonrelativistic condensed matter physics. The chiral anomaly discussed by S. L. Adler, J. S. Bell, and R. Jackiw in 1969 is an example of a quantum anomaly, which, in its simplest form, proves that coupling a single Weyl fermion to an electromagnetic field leads to the nonconservation of electric charge [12, 13]. Therefore, in condensed matter physics, to avoid such nonphysical consequences, the net chirality of a pair of Weyl fermions must vanish within a specific lattice realization, which is an example of the fermion doubling theorem[1]. Moreover, it became clear that the chiral anomaly can significantly affect the properties of the crystals, further cementing the link between band touchings and chiral fermions in 3D crystals [14].

In 2011, a groundbreaking article that introduced topological semimetals and Fermi arc surface states referred to those touching points as "Weyl points" (or "Weyl nodes") [15]. The topological consequences of Weyl points began to be explored with the realization that the Berry curvature plays a key role in determining the Hall effect [16, 17], and the Weyl points are related to "diabolic points" discussed by Michael V. Berry as sources of Berry flux [18].

1.1.1 Topological electronic states and topological insulators

In daily life, the vortex is a common example of topological phenomena, and in condensed matter physics, topological structures similar to vortices are concealed behind the wave functions of electronic states. During 1972 and 1973, David J. Thouless from Princeton University and J. Michael Kosterlitz from Brown University theoretically derived a model for vortex motion in 2D superfluid/superconducting systems and predicted a unique phase transition of these systems with temperature changes [19, 20]. From a topological perspective, the phase configuration with a single vortex excitation cannot be continuously transformed into a nonvortex configuration, which means that they belong to different types of topology. Therefore, vortex excitations are referred to as topological excitations, and the phase transition induced by vortex excitation is known as the Kosterlitz-Thouless transition (KT transition). The Soviet scientist Berezinskii also made significant independent contributions to this concept, leading to the alternative name Berezinskii-Kosterlitz-Thouless transition (BKT transition) [21]. Subsequent studies by Thouless and Kosterlitz extended the concept of topology to the electronic states of condensed matter physics [14], leading to the well-known TKNN invariant (named after the authors Thouless, Kohmoto, Nightingale, and den Nijs), i.e., a topological invariant in momentum space. This groundbreaking work on the topological structure of electronic wave functions built the foundation for an important research field and was one of the achievements of the 2016 Nobel Prize in Physics[2].

The problem addressed by the TKNN invariant is the topological classification of electronic wave functions, which is a very vast field. However, TKNN focused on a specific and relatively simple class: (i) the wave functions are noninteracting, which means that they can be described by a Slater determinant; (ii) the wave functions describe an insulating band structure. Since the system is noninteracting, the many-electron wave function can be constructed by filling up

---

[1] The fermion doubling theorem, or the Nielsen-Ninomiya theorem, states that if a Weyl node with non-zero topological charge exists in the 3D Brillouin zone, it must be accompanied by at least one other Weyl node to neutralize the total topological charge in the entire Brillouin zone, so Weyl fermions always appear in pairs.

[2] The 2016 Nobel Prize in Physics was awarded to three theoretical physicists, David J. Thouless from the University of Washington, J. Michael Kosterlitz from Brown University, and F. Duncan M. Haldane from Princeton University, for their theoretical work on topological phase transitions and topological phases in condensed matter systems.
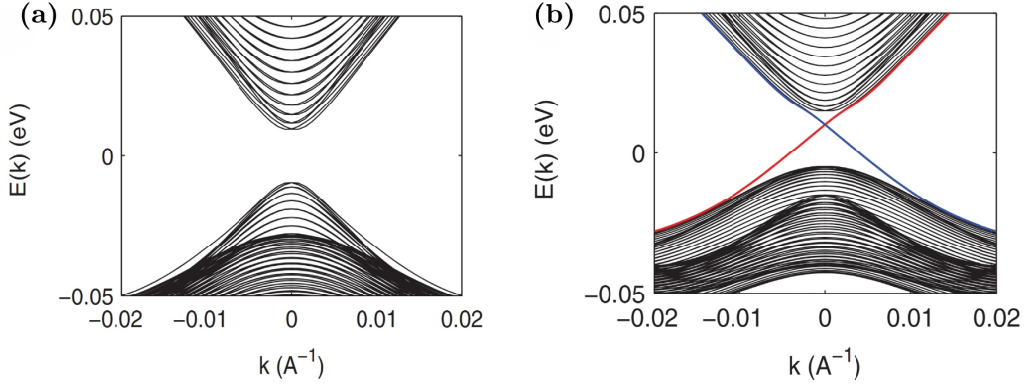
Figure 1.2: In a CdTe-HgTe-CdTe quantum well, the 2D TI's band structure is closely tied to the thickness of the HgTe layer, with a critical value around 6.5 nm. (a) When the thickness of the HgTe is less than 6.5 nm, the material exhibits a topologically trivial insulator phase. The low-energy band structure features a bandgap, which characterizes its insulating properties. (b) When the thickness of the HgTe layer exceeds 6.5 nm, the quantum well enters a nontrivial topological insulator phase. The band still maintains an insulating gap, but the surface states exhibit a gapless and linear dispersion, similar to that of graphene. This phase transition is crucial for the study of TIs, where the surface states remain conductive even though the system remains insulating. The above results are adapted from Ref. [22]. Similar topologically nontrivial surface states are also observed in 3D TIs like Bi_2Se_3 and Bi_2Te_3, as discussed in Ref. [23].

the occupied single-electron states to form a Fock state. Furthermore, because the system is an insulator, all occupied single-electron states fill the entire Brillouin zone. Thus, the classification of the many-electron state can be simplified to the question of whether the single-electron wave function has a topological structure throughout the Brillouin zone. The developments based on the TKNN invariant have led to significant advances in condensed matter physics, including the study of topological insulators (TIs), topological semimetals, quantum spin Hall effect, quantum anomalous Hall effect, and so on [21].

In recent years, both theoretical predictions and experimental discoveries of 2D and 3D TIs have led to significant exploration of the topological properties of electronic states in condensed matter physics [22–34]. TIs represent a novel quantum state of matter, characterized by being insulating in the bulk but conductive on their surface or edge. These surface or edge states exhibit topological robustness against local defects and disorder. In 2005, C. L. Kane and E. J. Mele proposed that time-reversal symmetry can result in a topological invariant, Z_2, which identifies the topological phase of an insulator [25]. This work expanded upon the foundational ideas introduced by the TKNN theory to new levels. As shown in Fig. 1.2, a Z_2 topologically nontrivial insulator exhibits a topologically nontrivial phase. Although its bulk state has a large bandgap similar to that of ordinary insulators, its surface state has a linear and gapless dispersion. The surface state remains topologically stable with the spin-momentum locking of the electrons as long as the time-reversal symmetry is preserved.

The topological classification based on symmetry, as seen in topological insulators, can be extended beyond time-reversal symmetry to encompass more crystal symmetries and can be applied to metallic systems as well. An ideal topological metal features a degeneracy point formed by the conduction and valence bands near the Fermi level, resulting in zero density of state at zero Fermi

energy. Such materials are named as topological semimetals [35], with Weyl semimetals (WSMs) and Dirac semimetals (DSMs) being the most representative and widely researched systems.

1.1.2 Weyl points, Berry phase, and Berry curvature in 3D Weyl semimetals

In 2011, a team from Nanjing University reported that Weyl points lead to the appearance of exotic surface states in the form of Fermi arcs in the electronic states of materials [15]. This result intuitively showed the topological properties of Weyl fermions in condensed matter and is widely regarded as the first instance where topologically nontrivial electronic states were extended from insulators to semimetals. For such semimetals with Weyl points, their electrons near the Fermi level exhibit Dirac cone dispersion formed by the crossing of nondegenerate conduction and valence bands, and their low-energy excitation can be described by the Weyl equation [2], thus they are called Weyl semimetals (WSMs) [15]. Further research has shown that in WSMs, Weyl points must appear in pairs with opposite chirality [14], while the spatial inversion symmetry ($\mathscr{P}$) or the time-reversal symmetry ($\mathscr{T}$) must be broken [36]. As a result, WSMs can be classified into two types: magnetic WSMs, where $\mathscr{T}$ is broken, and nonmagnetic WSMs, where $\mathscr{P}$ is broken. Nonmagnetic WSMs with broken centrosymmetry, such as the TaAs family, have been theoretically predicted [37] and experimentally verified [38, 39]. Magnetic WSMs were the first to be theoretically proposed [40–42], but the specific materials were identified very recently [43–45].

The exploration of Weyl points starting from the Weyl equation offers a better understanding of WSMs. Near a specific Weyl point, after resetting the spatial coordinates, the low-energy effective Hamiltonian is exactly the Weyl equation. One critical characteristic of the Weyl equation is that its solutions possess a specific chirality [2], meaning that the spin of the particle is always strictly aligned with the direction of its translational motion around the center of mass. This allows for the classification of particles into two categories: left-handed and right-handed, with the corresponding spins pointing anti-parallel and parallel to the momentum direction, respectively. This is the origin of the chirality of the Weyl points. However, it is important to note that in condensed matter physics, the spin at Weyl points is not the real spin of electrons but rather the so-called "pseudospin". In relativistic particle physics, the excitations near Weyl points are regarded as massless fermions, while in condensed matter physics, they can be understood in terms of a magnetic field in momentum space.

Band theory describes the electronic states in a crystal using the single-particle wave function $|u_n(\mathbf{k})\rangle$, which is defined within a unit cell, where $\mathbf{k}$ and n represent the electron momentum and the band index, respectively. The Berry connection corresponding to band n is defined as $A_n(\mathbf{k}) = i\langle u_n(\mathbf{k})|\nabla_{\mathbf{k}}|u_n(\mathbf{k})\rangle$, which reflects the relationship between the occupied states near the $\mathbf{k}$ point and formally can be viewed as a "vector potential" in momentum space. The Berry phase of the wavefunction can be obtained by integrating the Berry connection along a path, $\gamma_n = \oint_C d\mathbf{k} \cdot A_n(\mathbf{k})$, which is also equivalent to the surface integral of the Berry curvature. The Berry curvature corresponding to band n is defined as $\Omega_n(\mathbf{k}) = \nabla_{\mathbf{k}} \times A_n(\mathbf{k})$ [18, 46] and can be interpreted as a "pseudo-magnetic field" in momentum space. If we consider the Berry connection as a gauge field, then the Berry curvature corresponds to the field strength [21]. From the perspective of condensed matter physics, Weyl points are singularities in Berry curvature, appearing as monopoles of the "pseudo-magnetic field" in momentum space [47, 48]. Furthermore, starting from the Berry curvature, the TKNN index is the surface integral of it over the 2D Brillouin zone,

or the "magnetic flux" through the entire 2D Brillouin zone. Using the Berry curvature, one can also elegantly prove the Nielsen-Ninomiya theorem in topological semimetals [21].

From the above introduction to WSMs, one can see that the study of topological properties in topological semimetals is closely related to concepts like the Berry curvature and Berry connection. This relation is present in WSMs, but extends beyond that. The Weyl equation is a simplified form of the Dirac equation, and if the electronic states in a 3D material can be described by the Dirac equation, then similar topological properties and concepts such as Berry curvature will also appear, just as they do in WSMs.

1.1.3   3D Dirac semimetals and fourfold degenerate Dirac points

As previously introduced, Weyl points in 3D materials can only appear when either $\mathscr{T}$ or $\mathscr{P}$ is broken. When $\mathscr{P}$ is preserved, a Weyl point with a wave vector (or momentum) of $\mathbf{k}$ in the energy band must be accompanied by another Weyl point with the same energy, opposite topological charge, and a wavevector of $-\mathbf{k}$ [15, 41]. Conversely, if $\mathscr{T}$ is preserved, this pair of Weyl points with opposite momenta must carry the same topological charge [49]. Since the net topological charge in a Brillouin zone must be zero, time-reversal symmetry further requires the presence of two additional Weyl points to compensate for the topological charge [49]. This indicates that if a crystalline material satisfies combined symmetry, that is, both time-reversal and spatial-inversion symmetries ($\mathscr{P} \cdot \mathscr{T}$) are present, the Weyl points in the energy band can no longer be twofold degenerate.

Interestingly, when $\mathscr{P} \cdot \mathscr{T}$ symmetry is preserved, degenerate Weyl points with opposite charges can stably exist at the same momentum. According to Kramers' theorem, if the $\mathscr{P} \cdot \mathscr{T}$ symmetry is preserved, the energy bands will degenerate throughout the Brillouin zone [22]. As a result, a pair of Weyl points with opposite chiralities will overlap, forming a fourfold degenerate singularity in momentum space. This fourfold degenerate point is not topologically protected because its net Chern number is zero, and the remaining momentum terms in the Hamiltonian might mix the states, leading to the opening of a gap in the energy spectrum [36]. However, in some special cases, the space group symmetry of the 3D crystal can prevent the effect of these remaining terms, keeping the fourfold degenerate point intact. This type of degeneracy is known as symmetry-protected degeneracy [36]. The fourfold degenerate point is formed by the overlap of two Weyl points, and the low-energy excitations near it can be described by the Dirac equation. Therefore, it is referred to as a Dirac point. Consequently, 3D Dirac semimetals (DSMs) were theoretically proposed as a new class of topological material. Since a 3D Dirac point is formed by a pair of Weyl points, and combined symmetry requires the presence of two pairs of Weyl points in the system, a DSM will have two Dirac points located at $\pm\mathbf{k}$ in momentum space.

The newly discovered 3D DSMs were initially described as "3D graphene." However, this understanding is not appropriate. Both 3D and 2D Dirac systems have low-energy excitations that can be described by the Dirac equation, but the Dirac points in a 3D DSMs are protected by crystal symmetries. Therefore, even in the presence of spin-orbit interactions (probably strong), the 3D Dirac points remain stable and degenerate. In contrast, spin-orbit coupling (SOC) removes the degeneracy of the 2D Dirac points in graphene and opens a gap in the energy spectrum. The band structure of this gapped graphene is the prototype quantum spin Hall insulator [25, 26].

The features of 3D WSMs and DSMs can be intuitively explored using a simple model. Consider a 3D electronic system with two orbitals plus spin, We can expand a 4×4 Hamiltonian
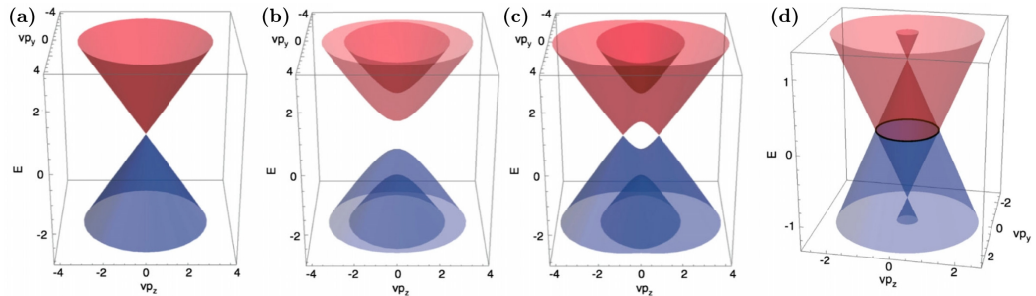
Figure 1.3: The energy dispersion $\varepsilon_{s\mu}(0, k_y, k_z)$ corresponding to Eqs. (1.1) and (1.2) under different conditions of m, b, and b'. (a) $m = b = b' = 0$ corresponds to a DSM. There is a fourfold degenerate Dirac point. (b) $m = 1$, $b = 0.5$, and $b' = 0$ correspond to a magnetic semiconductor. (c) $m = 0.5$, $b = 1$, and $b' = 0$ correspond to a WSM. At the Weyl points, there is only a twofold degeneracy. The band inversion between the Weyl points illustrates the influence of the Berry curvature on the band. (d) $m = b = 0$ and $b' \neq 0$ correspond to a nodal line semimetal.

matrix at the center of the Brillouin zone (the Γ point) [36, 50, 51]:

$$
\begin{aligned}
H(\mathbf{k}) &= v\tau_x(\boldsymbol{\sigma} \cdot \mathbf{k}) + m\tau_z + b\sigma_z + b'\tau_z\sigma_z \\
&= \begin{pmatrix} mI + b\sigma_z + b'\sigma_x & v\boldsymbol{\sigma} \cdot \mathbf{k} \\ v\boldsymbol{\sigma} \cdot \mathbf{k} & -mI + b\sigma_z - b'\sigma_x \end{pmatrix},
\end{aligned}
\tag{1.1}
$$

where $\hbar = 1$ is used for simplify, $\mathbf{k} = (k_x, k_y, k_z)$ is the momentum of electrons, $\boldsymbol{\sigma} = (\sigma_x, \sigma_y, \sigma_z)$ are the Pauli matrices for spin degrees of freedom; (τ_x, τ_y, τ_z) are the Pauli matrices for pseudospin degrees of freedom, which relates to orbitals of atoms or sublattices, and I is a 2×2 identity matrix. This Hamiltonian also includes the velocity parameter v and the mass parameter m. Additionally, b and b' correspond to the intrinsic Zeeman fields in the x and z directions, which can exist in magnetic materials that break time-reversal symmetry. Many interesting properties of Eq. (1.1) will be related to m, b, and b'. When $b' = 0$, the energy eigenvalues corresponding to Eq. (1.1) are given by

$$
\varepsilon_{s\mu}(\mathbf{k}) = s\sqrt{m^2 + b^2 + v^2 k^2 + 2\mu b \sqrt{v^2 k_z^2 + m^2}},
\tag{1.2}
$$

where $k = |\mathbf{k}|$, $\mu = \pm 1$ represents the spin degree of freedom, and $s = \pm 1$ denotes the conduction and valence bands. The results of the energy spectrum $\varepsilon_{s\mu}(0, k_y, k_z)$ are shown in Fig. 1.3: (a) Taking $m = b = 0$, the energy spectrum corresponds to a single Dirac cone of a DSM, where the fourfold degenerate Dirac point is located at $\mathbf{k} = 0$. It is important to note that the results shown are from a simple model; in actual 3D DMSs, the Dirac points appear in pairs. (b) The case of $|m| > |b|$ describes the states of a gapped magnetic semiconductor with the energy gap being $|E| < |m| - |b|$. (c) $|b| > |m|$ represents the WSM state, which differs from the DSM state in that its conduction and valence bands are not degenerate; the intermediate conduction and valence bands touch at two separate Weyl points at $\mathbf{k} = (0, 0, \pm\sqrt{b^2 - m^2}/v)$. The band inversion between the two Weyl points reflects the influence of the Berry curvature discussed in Sec. 1.1.2, with a van Hove singularity occurring at $k_z = 0$ in the inverted band. Furthermore, in the case where $b' \neq 0$ and $m = b = 0$, the eigenvalue is given by $\varepsilon_{s\mu}(\mathbf{k}) = s\sqrt{v^2 k_x^2 + [v\sqrt{k_y^2 + k_z^2} + \mu b']^2}$, representing a nodal line semimetal, as shown in Fig. 1.3(d). Fig. 1.4 further illustrates the relationship between
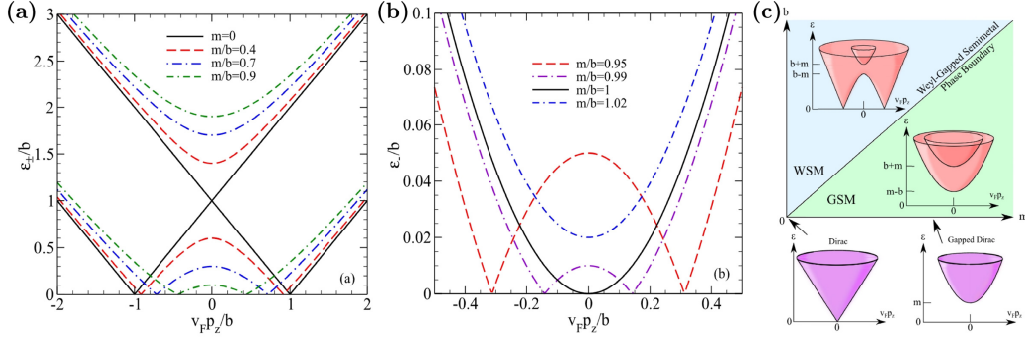
Figure 1.4: The energy band and phase diagram based on Eq. (1.2) as functions of m and b. (a) The WSM state varies with m/b when $s = +1$ and $\mu = \pm 1$. When $m \neq 0$, the $\mu = +1$ band has a band gap, while the $\mu = -1$ band still retains a pair of Weyl points. (b) The phase transition of the $\mu = -1$ band near $m/b = 1$ when $s = +1$. (c) Phase diagram based on Eq. (1.2), where the system is a WSM for $m/b < 1$ and a gapped semiconductor for $m/b > 1$. For $b = 0$, a degenerate DSM state can be observed, and at $m = b = 0$, there exists a massless Dirac fermion with a fourfold degeneracy. Adapted from Ref. [50].

the energy dispersion based on Eq. (1.2) and the ratio of m to b, as well as the evolution of electrons in the crystal momentum space with respect to m and b.

1.2   Research Progress on 3D Dirac Semimetals

In 2012, two papers almost simultaneously reported the existence of a 3D DSM state protected by crystal symmetries in bulk β-cristobalite BiO_2 and A_3Bi (A = Na, K, Rb) [52, 53]. In 2013, bulk Cd_3As_2 is also predicted to be a 3D DSM similar to that in Na_3Bi [54]. During 2014 and 2015, a large number of experimental results, including ARPES measurements, directly verified the existence of 3D DSM states in bulk Na_3Bi and Cd_3As_2 [55–63], making them representative platforms for studying the properties of 3D DSMs. Later, similar 3D DSM states have also been reported in many other materials [64–67].

In 2015, a significant work proposed a new type of WSM state in WTe_2 by breaking the Lorentz invariance [68]. This state features tilted energy bands near the Weyl points and is termed type-II WSMs. In 2016, a theoretical work predicted that a tilted energy band, akin to type-II WSMs, could also be achieved in transition metal dichalcogenides (TMDs) such as PtX_2 (X = S, Se, Te) and $PdTe_2$ through the breaking of Lorentz invariance. Moreover, this energy band retains a fourfold degeneracy at the Dirac points and aligns with the Dirac equation, leading to the naming of these new materials as type-II 3D DSMs [69]. In 2017, experiments confirmed the existence of type-II 3D DSM states in $PtTe_2$, $PtSe_2$, and $PdTe_2$ [70–73], greatly expanding topological semimetals. Following this, numerous studies on type-II 3D DSMs have been reported [74–78]. Meanwhile, the materials Na_3Bi and Cd_3As_2 mentioned above are classified as type-I 3D DSMs.

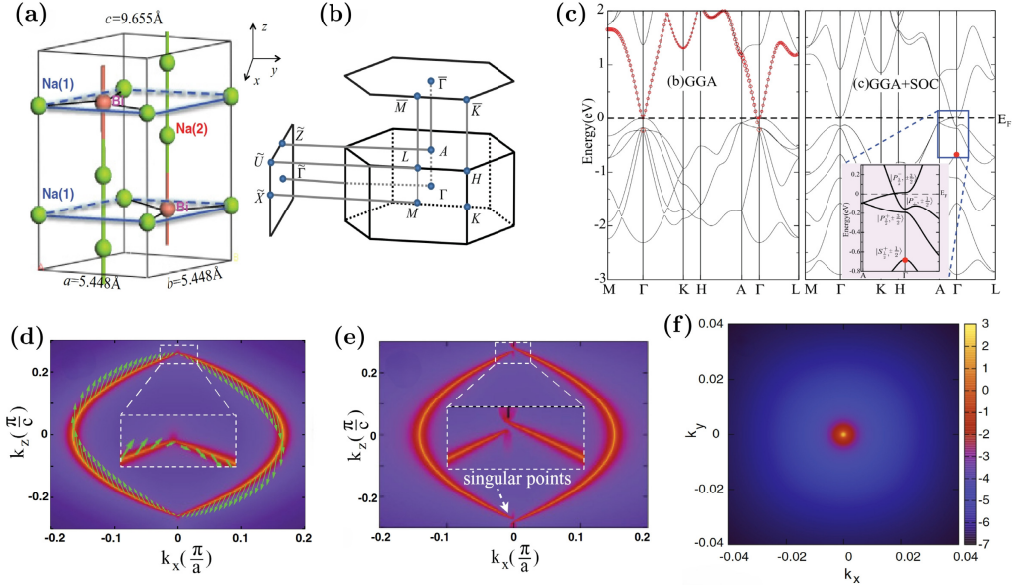Figure 1.5: The crystal structure, electronic structure, and Fermi surface of the bulk Na$_3$Bi. (a) Na$_3$Bi belongs to hexagonal, with $P6_3/mmc$ space group symmetry. (b) The Brillouin zone of Na$_3$Bi. (c) The electronic structure of Na$_3$Bi calculated by first-principles, with the results with and without SOC. (d) The Fermi surface of a type-I 3D DSM features a pair of Fermi arcs with opposite spin textures between the two Dirac points, and the spin is degenerate at the Dirac points. (e) When crystal symmetries are broken, the Fermi arcs open a gap at the Dirac points, at which point the pair of Fermi arcs exhibit opposite chirality, and the phase transition from a DSM state into a WSM state can be observed. (f) A type-I 3D DSM has a point-like Fermi surface at the Dirac points. Adapted from Refs. [53, 54].

1.2.1 Discovery of type-I 3D Dirac semimetals

Based on Na$_3$Bi, the lattice structure, the electronic structure, and the Fermi surface of type-I 3D DSMs are shown in Fig. 1.5. The lattice structure shown in Fig. 1.5(a) indicates that Na$_3$Bi is isotropic in the *x-y* plane but anisotropic in the *z* direction. Figs. 1.5(b) and 1.5(c) show that Na$_3$Bi has a pair of Dirac points symmetrically located on the central axis of the Brillouin zone. Moreover, the results considering spin-orbit coupling (SOC) in Fig. 1.5(c) indicate that the Dirac points of the a 3D DSM protected by crystal symmetries have robustness and can strongly suppress perturbations such as defects or impurities. Even in the presence of SOC, the fourfold degeneracy is maintained, distinguishing 3D DSMs from graphene [25, 26, 53]. In WSMs, a pair of Fermi arcs with opposite chirality connects two Weyl points [15]. However, as shown in Fig. 1.5(d), in DSMs the spins of a pair of Fermi arcs disappear at the Dirac points, representing a different electronic state compared to WSMs [53, 54]. If crystal symmetries are broken, such as compression 1% along the *y* axis of a bulk Na$_3$Bi, a gap (about 6 meV) will open at its Dirac points, leading to a topological phase transition from Dirac to Weyl semimetal states [53], as shown in Fig. 1.5(e). Furthermore, Fig. 1.5 (f) illustrates the point-like Fermi surface at the Dirac point in type-I 3D DSMs, which is an important characteristic that distinguishes them from type-II 3D DSMs [69, 70].

After the proposal of Na_3Bi, the instability of its samples in air made experimental research challenging. So, a new type-I 3D DSM, Cd_3As_2, was theoretically predicted [54]. As a well-known compound, Cd_3As_2 was previously considered a narrow-gap semiconductor due to early research limitations [79–81]. However, the new theories have shown that this material is similar to Na_3Bi as a type-I 3D DSM. Cd_3As_2 is very stable in air, making experiments relatively easier, and although its lattice structure differs from that of Na_3Bi, its DSM state also exhibits the Fermi surface and the surface states of Fermi arcs as shown in Figs. 1.5(d)-(f). Thus, Na_3Bi and Cd_3As_2 are still classified as the same type of DSMs [54].

Considering time-reversal, inversion, and space group symmetries, the effective $\mathbf{k} \cdot \mathbf{p}$ Hamiltonian of a 3D DSM is described by a 4×4 matrix [53, 54]:

$$H(\mathbf{K}) = \varepsilon_{\mathbf{K}} \times I + \begin{pmatrix} M_{\mathbf{K}} & Ak_+ & Dk_- & B_{\mathbf{K}}^* \\ Ak_- & -M_{\mathbf{K}} & B_{\mathbf{K}}^* & 0 \\ Dk_+ & B_{\mathbf{K}} & M_{\mathbf{K}} & -Ak_- \\ B_{\mathbf{K}} & 0 & -Ak_+ & -M_{\mathbf{K}} \end{pmatrix}, \tag{1.3}$$

where $\mathbf{K} = (\mathbf{k}, k_z) = (k_x, k_y, k_z)$ is the 3D wave vector of the electron, I is a 4×4 identity matrix, the z direction corresponds to the c axis in Fig. 1.5(a), $k_\pm = k_x \pm ik_y$, $\varepsilon_{\mathbf{K}} = C_0 + C_1 k_z^2 + C_2 k^2$, $M_{\mathbf{K}} = M_0 - M_1 k_z^2 - M_2 k^2$. Furthermore, C_0, C_1, C_2, M_0, M_1, M_2, and A are band parameters, which take different values in Na_3Bi and Cd_3As_2, but both yield fourfold degenerate Dirac points. This is due to the mechanism in which type-I 3D DSMs have stable Dirac points induced by band inversion in a large parameter space [36]. $B_{\mathbf{K}} = B_3 k_z k^2 + \sim K^3$ represents higher-order terms contributing to electron motion, arising from spin-orbit interactions, which only have significant effects at large momenta. The terms containing D describe the breaking of crystal symmetries, where $D = 0$ if crystal symmetries are preserved. The eigenenergy corresponding to Eq. (1.3) can be analytically obtained as $E_\pm(\mathbf{K}) = \varepsilon_{\mathbf{K}} \pm \sqrt{M_{\mathbf{K}}^2 + A^2 k^2 + |B_{\mathbf{K}}|^2}$, where $+$ and $-$ correspond to the conduction and valence bands, respectively. For k_z along the $\Gamma - A$ symmetry line in Fig. 1.5(b), the electronic state has a mass term: $M(k_z) = M_0 - M_1 k_z$, where $M_0 M_1 > 0$ describes the inverted band structure, revealing a pair of gapless points protected by c-axis rotational symmetry, located at $k_z = \pm k_z^c = \pm\sqrt{M_0/M_1}$. Hence, we can find that the coordinates of the pair of Dirac points are $\mathbf{K^c} = (0, 0, \pm k_z^c)$. The first-principles calculations in Fig. 1.5(c) show that for Na_3Bi, $M_0 \approx -0.087$ eV and $M_1 \approx -10.64$ eV, so the two Dirac points in Na_3Bi are located at $k_z = \pm 0.09$ Å^{-1} away from the center of the Brillouin zone [53]. Similar results appear in Cd_3As_2, where the two Dirac points are located at $k_z^c = \pm 0.03$ Å^{-1} [54].

The ARPES results for bulk Na_3Bi are shown in Fig. 1.6 [56]. From Figs. 1.6(a)-(c), one can observe the type-I 3D DSM state and the 3D Dirac points in Na_3Bi. The experimentally observed Dirac points are located at $k_z^c = \pm 0.08$ Å^{-1}, which is very close to the theoretical value of $k_z^c = \pm 0.09$ Å^{-1}, demonstrating the the theoretical predictions based on Eq. (1.3). Fig. 1.6(d) shows a pair of Fermi arcs of a type-I 3D DSM, consistent with the theoretical results. Figs. 1.6(e)-(f) further confirm that the $B_{\mathbf{K}}$ terms in Eq. (1.3) is approximately zero for small momentum and verify the fourfold degeneracy at the 3D Dirac point. This can simplify Eq. (1.3) by spin degeneracy, which is particularly useful for studying low-energy and small-momentum problems [53, 54]. In addition, other ARPES experiments [55], as well as scanning tunneling microscopy (STM) and transport measurements at low temperatures, further confirmed the massless linear dispersion around the Dirac points in Na_3Bi [62].

Similar experimental results were obtained for Cd_3As_2, which also show good agreement with theoretical predictions [54, 57–61]. Landau quantization and quasiparticle interference experiments also validated the linear band structure near the Dirac points in Cd_3As_2 [82]. However, a
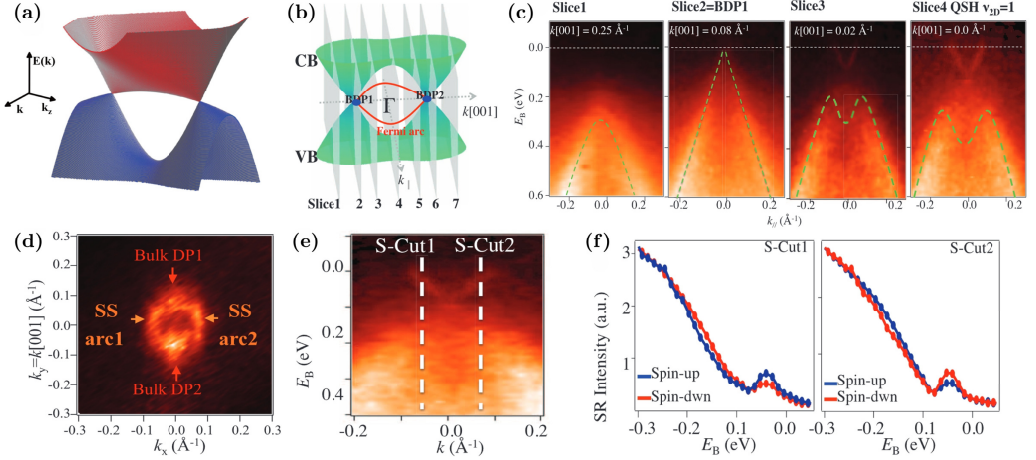
Figure 1.6: ARPES measurement results for Na_3Bi. (a) The 3D energy band of Na_3Bi corresponding to Eq. (1.3) with $B_{\mathbf{K}} \approx 0$, where k represents the isotropic energy dispersion in the k_x-k_y plane. (b) The ARPES experiment took seven 2D slices in the band of Na_3Bi. Due to band symmetry, slices 1 and 7, 2 and 6, 3 and 5 are equivalent. The 3D Dirac points are observed in slices 2 and 6, and a pair of Fermi arcs is located between them. (c) ARPES results corresponding to the slices in (b). The bulk Dirac point (BDP) appears in slice 2, and topological semimetal surface states are visible in slice 4. (d) A pair of Fermi arcs, observed between the two Dirac points, parallel to the $k[001]$ direction of (b). (e) Spin-resolved ARPES measurements were taken along two tangential lines in slice 4. (f) The results corresponding to (e) show that the 3D DSM exhibits spin degeneracy near the Dirac points. The above results are adapted from Ref. [56].

notable discrepancy between theory and experiment was observed: the Fermi velocity in Cd_3As_2 was significantly higher than the theoretical predictions, leading to further refinement of the band parameters [58, 82].

1.2.2 Investigations of type-I 3D Dirac semimetals

After the discovery of type-I 3D DSMs, their unique band structure leads to many novel physical properties [83]. Since Cd_3As_2 is highly stable in air while Na_3Bi is unstable [58, 62, 84], the experiments for studying Cd_3As_2 are relatively less demanding, leading to more research based on Cd_3As_2. Because of the strong robustness in type-I DSMs, backscattering of electrons is suppressed, resulting in ultrahigh carrier mobilities. Transport experiments have shown that Cd_3As_2 can achieve a carrier mobility of about 8.6×10^6 cm^{2}V^{-1}s^{-1} at a temperature of 5 K [85], while in Na_3Bi, the carrier mobility reaches approximately 9.1×10^4 cm^{2}V^{-1}s^{-1} at 2 K [86, 87]. For comparison, graphene has a reported carrier mobility of about 2×10^5 cm^{2}V^{-1}s^{-1} at 2 K [9], and the highest carrier mobility reported so far is 9×10^6 cm^{2}V^{-1}s^{-1} in high-purity bismuth.

As introduced in Sec. 1.1.2 and Sec. 1.2.1, the electronic states of DSMs remain stable as long as crystal symmetries are preserved. However, once the time-reversal symmetry is broken, the DSM state undergoes a phase transition to the WSM state [53, 54]. One of the key characteristics of the WSM state is the chiral anomaly [36], which causes many interesting physical phenomena. In type-I DSMs, many effects arising from the chiral anomaly have already been discovered, such
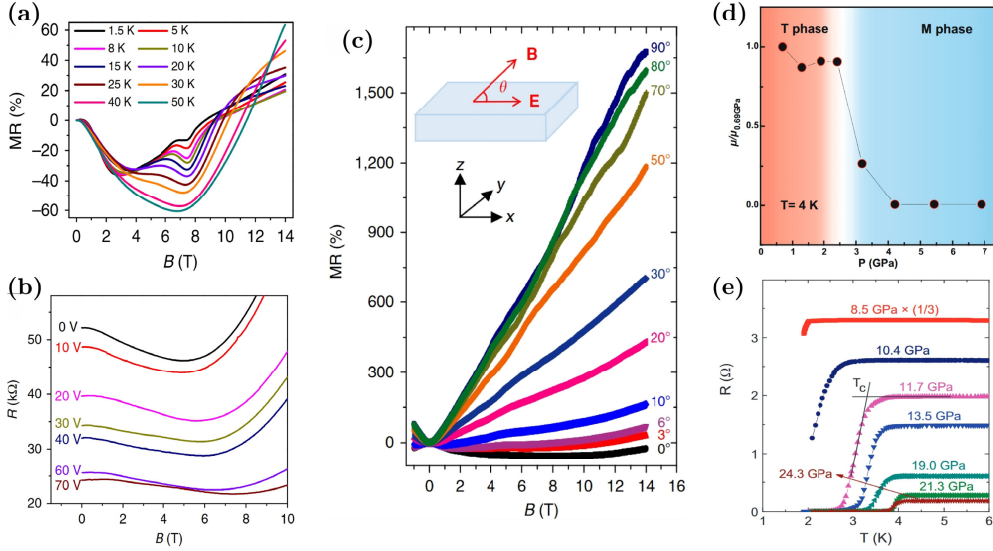
Figure 1.7: Topological phase transition in Cd_3As_2. (a) Negative magnetoresistance (MR) is observed in Cd_3As_2 nanowire samples (diameter ~ 200 nm) at different temperatures when an external electric field is parallel to the magnetic field ($B \parallel E$). (b) The negative MR in (a) can be modulated by a gate voltage. (c) The negative MR depends on the angle between the electric field and the magnetic field, where the linear MR can be observed at $B \perp E$. (d) External pressure can induce a phase transition in bulk Cd_3As_2, where the carrier mobility shows a sudden change when pressure increases to around 2.5 GPa. (e) External pressure might induce a topological superconducting phase in bulk Cd_3As_2. The above results are adapted from Refs. [90–93].

as the anomalous thermoelectric effect [88], nonlocal valley transport and the magneto-optical Kerr effect [89], and, most notably, the negative magnetoresistance (MR) effect [89–91]. The negative MR effect, caused by the chiral anomaly, is experimentally manifested when an electric field is applied parallel to a magnetic field ($B \parallel E$), resulting in an observable negative MR. In 2015, a team observed the negative MR in a Cd_3As_2 nanowire sample with a diameter of ~ 200 nm, as shown in Fig. 1.7(a). This phenomenon was even observed at room temperature [90], indicating that the topological phase transition in type-I DSMs can occur at high temperature. Fig. 1.7(b) further shows that this negative MR can be tuned by applying a gate voltage [90]. The angle-dependent negative MR shown in Fig. 1.7(c) further confirms that this phenomenon is caused by the chiral anomaly in Cd_3As_2 [91].

In addition to a magnetic field, external pressure can also induce a topological phase transition in type-I DSMs. As shown in Fig. 1.7(d), the carrier mobility of a bulk Cd_3As_2 exhibits a sudden change around 2.5 GPa, while mobility is nearly unaffected by pressure above or below this point. This suggests that a phase transition has occurred in bulk Cd_3As_2 [92]. Fig. 1.7(e) presents further research on the phase transition of Cd_3As_2, showing that type-I DSMs might have a topological superconducting state under high pressure [93]. In Sec. 1.1, we introduced the relationship between the Majorana equation and the Dirac equation [3]. In condensed matter physics, Majorana fermions, described by the Majorana equation, play a key role in topological superconducting states. Topological superconducting states represent a novel electronic state, characterized by the presence of Majorana fermions at the boundaries [94–96], and Majorana zero-energy modes is an important tool in the study of topological superconductors [97]. Many experiments in

Cd_3As_2, such as high-pressure superconductivity [93], point-contact-induced superconductivity [98, 99], Josephson supercurrent [100–103], and proximity-induced superconductivity [104], all demonstrate the great potential of type-I DSMs in the study of topological superconductivity and Majorana zero-energy modes. Furthermore, the phase transition in Cd_3As_2 induced by external pressure also affects its optoelectronic properties [105].

Transport experiments have also revealed other bulk-state properties of type-I DSMs. The Shubnikov-de Haas (SdH) oscillations, which originate from the Landau quantization of electron orbits in a strong magnetic field, are typically measured at very low temperatures. These oscillations can be described by the Lifshitz-Kosevich (LK) formula, $\cos[2\pi(F/B + \phi)]$, where B is the magnetic field strength, F is the oscillation frequency, and ϕ is the phase factor corresponding to the topology of the Fermi surface [106]. By combining SdH oscillations with the L-K formula, the Berry phase of topological materials can be experimentally determined. For 3D materials, the Berry phase is usually π, corresponding to $\phi = \pm 1/8$ (+ for holes, − for electrons) [46, 107]. Research on the Berry phase of Cd_3As_2 has revealed its unique topological structure, highlighting its differences from WSMs [60, 108–112]. Angle-dependent SdH oscillations or the de Haas-van Alphen (dHvA) effect can be used to map the Fermi surface geometry of type-I DSMs [110, 111], and the evolution of the Berry phase under certain conditions can also be determined by analyzing quantum oscillations [109, 112]. These findings further show that type-I 3D DSMs are excellent candidates for studying topological phase transitions. Linear MR sustained under strong magnetic fields and various temperatures [108, 113], Landau level splitting under strong magnetic fields [109], band splitting [114], and gate-tunable SdH oscillations [115], have also been reported in type-I DSMs.

In addition to the bulk-state properties, type-I DSMs exhibit intriguing surface-state phenomena. The Aharonov-Bohm (AB) effect observed in Cd_3As_2 nanostructures verifies the surface states [116–118]. The transition from π-AB effect to AB effect, observed in Cd_3As_2 nanowire, and the π-AB effect near the Dirac point confirm the helical spin structure of the topological surface states [117], which corresponds to the Fermi arc structure shown in Fig. 1.5 [53, 54], and is also shown in the ARPES observations in Fig. 1.6 [57–61]. Fano interference has been observed between the bulk and surface states in Cd_3As_2. When there is scattering in both a continuous and a discrete state, Fano proposed that interference between the scattering amplitudes of these two states would result in Fano resonance [119]. The Fano effect observed in Cd_3As_2 reveals the interaction between the bulk and surface states of type-I 3D DSMs [120], further shedding light on the mechanism of the topological phase transition to the Weyl orbital states [116, 121].

Quantum Hall Effect (QHE) is a significant focus in the topological materials, and as early as the theoretical predictions of type-I 3D DSMs, it was proposed that QHE could be observed in Na_3Bi and Cd_3As_2 [53, 54]. Taking Cd_3As_2 as an example, Eq. (1.3) represents the Hamiltonian of its bulk samples, where k_z is unconfined [54]. In Cd_3As_2 thin films with quantum well structures, k_z will be quantized with the reduced dimension, related to the thickness of the sample $L_z = c$ as $k_z \to \sin(k_z L_z)/L_z$ [54]. This makes the Cd_3As_2 thin films change into a topological insulator state. As the thickness further decreases, the band inversion is removed due to the finite size effect [122], leading to a thickness-dependent transition between trivial and nontrivial topological phases, as shown in Fig. 1.2 [54]. In this case, QHE can be observed with varying thickness. Interestingly, there is still a debate about the underlying mechanism that generates QHE in type-I DSMs [123]. Various studies have proposed different interpretations of QHE in type-I DSMs. Figure 1.8(a) illustrates QHE in samples with restricted thicknesses, where the Fermi arc structure of the subbands in confined bulk states of Cd_3As_2 allows electrons to undergo cyclotron motion [124, 125]. In 2017, a group theoretically predicted that the QHE can

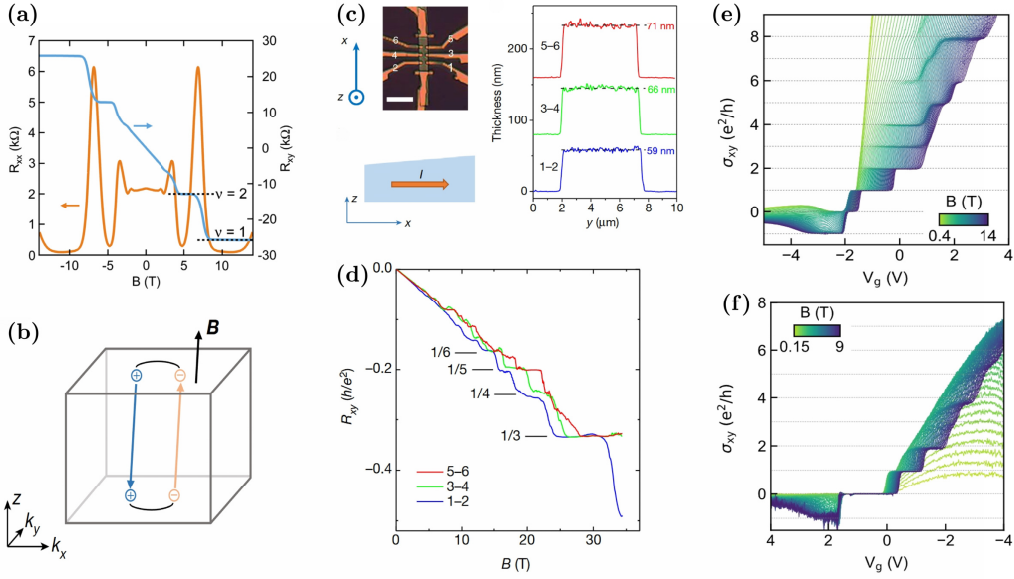Figure 1.8: Quantum Hall Effect (QHE) in Cd_3As_2. (a) QHE observed in a 20 nm thick Cd_3As_2 nanosheet, induced by the subbands from the quantum confinement of bulk states. (b) Weyl orbits present in a bulk Cd_3As_2 under an external magnetic field that breaks the time-reversal symmetry. (c) Three pairs of Hall electrodes on a Cd_3As_2 wedge-shaped bulk sample with a thickness gradient along the x direction, located at 59, 66, and 71 nm, respectively. (d) QHE induced by Weyl orbits corresponding to (b) and (c), with different colors representing different thicknesses shown in (c). (e) QHE induced by the nontrivial topological insulator state observed in a 20 nm thick Cd_3As_2 thin film, with the Fermi level tuned by the gate voltage. (f) QHE induced by the trivial topological insulator state observed in a sample with a reduced thickness of 14 nm, corresponding to (e). The above results are adapted from Refs. [125, 127, 129].

be induced by the Weyl orbits in Cd_3As_2 and Na_3Bi [126], and then another group observed a thickness-dependent QHE in a Cd_3As_2 sample with a thickness of 77 nm in 2019 [127], as shown in Figs. 1.8(b)-(d). They proposed that Weyl orbits arising in Cd_3As_2 under broken time-reversal symmetry allow electrons to execute cyclotron motion, thereby leading to QHE, with Weyl orbits being thickness-dependent [126, 127]. The QHE resulting from the topological insulator states of Cd_3As_2 was also investigated [128]. Furthermore, a recent study examined different QHE modes in Cd_3As_2 thin films with varying thicknesses under gate-tuned Fermi levels, as shown in Figs. 1.8(e) and 1.8(f) [129], confirming the transition of the topological insulator states between trivial and nontrivial phases [54]. These studies demonstrate the significant potential of type-I DSMs in exploring the QHE of topological materials.

Type-I DSMs exhibit a gapless linear dispersion and ultrahigh carrier mobility, suggesting excellent optoelectronic properties. In earlier studies, Cd_3As_2 was considered a narrow bandgap semiconductor [130–132]. However, the discovery of the DSM state in Cd_3As_2 has prompted a re-evaluation of its various optoelectronic properties. In 2016, it was first reported that the optical conductivity (OC) of bulk Cd_3As_2 is isotropic within the [001] plane and has an optical absorption window [133], as shown in Fig. 1.9(a). Around the same time, anisotropic OC corresponding to its band structure, along with massless Kane electrons, was also reported through magneto-optical experiments [134]. In 2017, theoretical predictions suggested that the Fermi arc
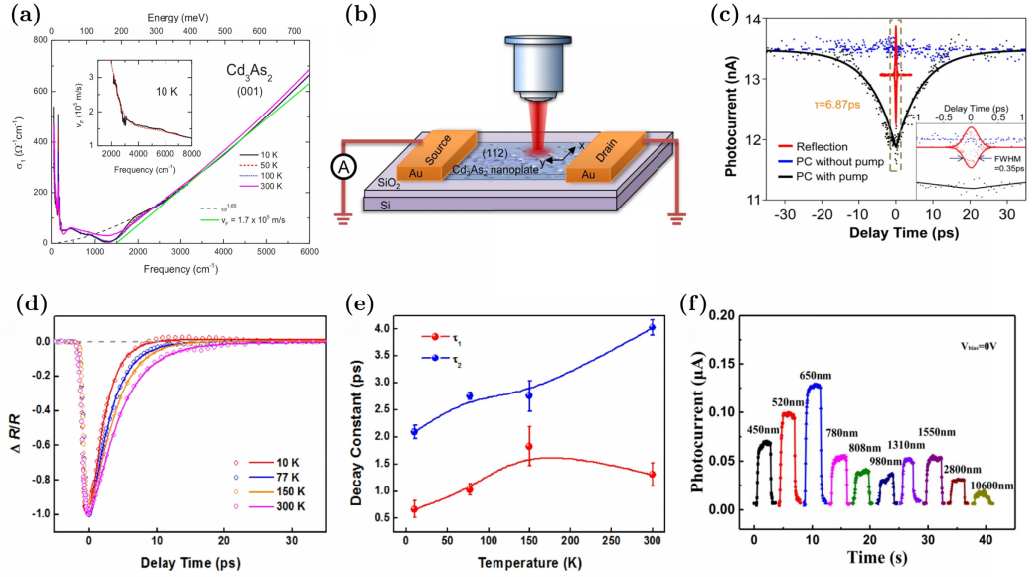
Figure 1.9: (a) The in-plane optical conductivity of a bulk Cd_3As_2 at different temperatures. (b) Spatial-resolved scanning photocurrent measurements of a Cd_3As_2 nanosheet. (c) Corresponding to (b), the relationship between the pump-on (black) and pump-off (blue) probe-induced photocurrent and the pump-probe pulse delay. (d) Normalized transient reflection spectra measured from bulk Cd_3As_2 at different temperatures using a 4 μm probe based on the negative peak signal. (e) Two relaxation times obtained by fitting (c) at different temperatures: the blue curve corresponds to the slower time, whereas the red curve corresponds to the faster time. (f) At room temperature, Cd_3As_2 heterojunctions exhibit excellent photoresponse over a very broad spectral range. The above results are adapted from Refs. [133, 136, 139].

could lead to a high OC [135]. Experiments demonstrated that Cd_3As_2 nanosheets exhibited an ultrafast transient time of approximately 6.87 ps [136], as shown in Figs. 1.9(b) and 1.9(c). This indicates that photodetectors based on Cd_3As_2 could support detections of around 145 GHz, with a strong light-matter interaction and a high responsivity of approximately 5.9 mA/W [136], outperforming graphene-based photodetectors [137, 138]. Furthermore, as shown in Figs. 1.9(d) and 1.9(e), ultrafast reflection experiments on bulk Cd_3As_2 revealed two distinct relaxation times associated with light interaction. Analysis using a two-temperature model revealed that these relaxation times correspond to electron-photon and electron-lattice (phonon) interactions, respectively [139]. Additionally, experiments found that Cd_3As_2 heterojunctions have excellent photoresponse over a wide spectral range at room temperature [140], as shown in Fig. 1.9(f). More studies further showed the exceptional optoelectronic properties of type-I DSMs [141–152]. Notably, some experiments pointed out that Cd_3As_2 exhibits strong tunability in both optoelectronic and thermoelectric applications [146]. Our research group also contributed to the identification of a phonon absorption peak around 1.7–1.8 THz in Cd_3As_2 through terahertz experiments [152].

In addition to the above overview, more detailed research on type-I DSMs can be found in the theoretical review by E. J. Mele on Weyl and Dirac semimetals [36] and the experimental review by the research team of Academicians Zhimin Liao and Dapeng Yu of Peking University [123]. The discovery of type-I 3D DSMs and their excellent transport and optoelectronic properties suggest a very high potential for applications. The new phenomena are closely related

to the topological properties, which makes type-I 3D DSMs essential for further theoretical and experimental studies.

1.2.3   Discovery of type-II 3D Dirac semimetals

In 2016, a research group theoretically proposed a new type of electronic state based on transition metal dichalcogenide (TMD) $PtSe_2$. This novel electronic state can be described by Eq. (1.3) as well, while maintaining crystal symmetries but breaking Lorentz invariance. In momentum space, there exists a pair of fourfold degenerate Dirac points along with linear energy dispersion. This new state is termed the type-II 3D DSM state [69]. The research group also predicted that $PtTe_2$, $PdTe_2$, and $PtBi_2$ are type-II 3D DSMs [69]. In 2017, experimental confirmations of $PtTe_2$ [70], $PtSe_2$ [71, 77], and $PdTe_2$ [72, 73, 77] as type-II 3D DSMs were reported. These discoveries significantly expanded the research field of Dirac semimetals and introduced many novel physical properties. Later, many other type-II DSMs were also proposed [74–76, 78].

In the discovered type-II DSMs, $PtTe_2$ is known for its stable properties and easy preparation [70, 153, 154], making it a representative material. As shown in Figs. 1.10(a) and 1.10(b), $PtTe_2$ crystallizes in a trigonal CdI_2-type lattice structure with the space group P$\bar{3}$m1 (No. 164). Bulk $PtTe_2$ is formed by the periodic stacking of fundamental atomic layers, with weak van der Waals interactions between the layers. In each layer, the Pt atoms are located between the Te atoms above and below, while two Te atoms have inversion symmetry [70]. Figs. 1.10(c) and 1.10(d) depict the 3D Brillouin zone and the electronic structure calculated from first principles, showing fourfold degenerate Dirac points located at $\pm D$. In contrast to type-I DSMs caused by band inversion, Dirac points in type-II DSMs are located at the contact points of electron and hole pockets in the energy bands [69, 70], as shown in Figs. 1.10(e) and 1.10(f). An important distinction between type-I and type-II DSMs is that the Fermi surface at the Dirac points in type-I DSMs is point-like [53, 54], as shown in Fig. 1.5(f). In contrast, the Fermi surface at the Dirac points in type-II DSMs outlines the contours of the electron and hole pockets [69, 70], as seen in Fig. 1.10(f). Figs. 1.10(g) and 1.10(h) present ARPES results that confirm the existence of the type-II DSM state [70]. Similar properties have been experimentally verified in $PtSe_2$ [71, 77] and $PdTe_2$ [72, 73, 77], indicating that these TMDs have very similar properties [77].

The effective Hamiltonian of type-II 3D DSMs is also described by Eq. (1.3). The corresponding eigenvalue is given by $E_{\pm}(\mathbf{K}) = \varepsilon_{\mathbf{K}} \pm \sqrt{M_{\mathbf{K}}^2 + A^2 k^2 + |B_{\mathbf{K}}|^2}$. The two Dirac points are located at $\mathbf{K^c} = (0, 0, \pm k_z^c)$, and this result is formally consistent with type-I DSMs. However, if we expand Eq. (1.3) around the Dirac point $\mathbf{K^c}$ and retain only the linear terms, one can obtain [69]:

$$H^c(\mathbf{K}) = \begin{pmatrix} h(\mathbf{K}) & 0 \\ 0 & h^*(\mathbf{K}) \end{pmatrix}, \tag{1.4}$$

where $h(\mathbf{K}) = A(k_x \sigma_x - k_y \sigma_y) - 2k_z k_z^c (C_1 I - M_1 \sigma_z)$, I is 2×2 identity matrix, $(\sigma_x, \sigma_y, \sigma_z)$ are Pauli matrices, C_1, M_1, and A are band parameters. The corresponding energy dispersion reads as

$$E_{\pm}(\mathbf{K}) = T(\mathbf{K}) \pm U(\mathbf{K}) = 2C_1 k_z^c k_z \pm \sqrt{A^2(k_x^2 + k_y^2) + (2M_1 k_z^c k_z)^2}, \tag{1.5}$$

where $T(\mathbf{K})$ is a linear kinetic term and $U(\mathbf{K})$ is the potential component. These two components can be used to distinguish between type-I and type-II DSMs. For the case of Na_3Bi and Cd_3As_2 where $U(\mathbf{K}) > T(\mathbf{K})$ follows the Lorentz invariance [53, 54], the Dirac cone is isotropic and a
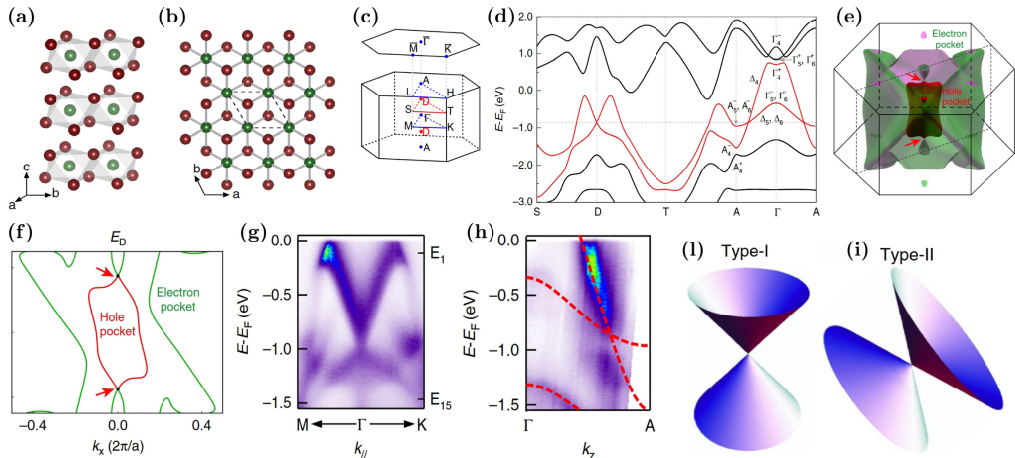
Figure 1.10: (a), (b) Lattice structure of PtTe$_2$ from side and top views, respectively. The green balls represent Pt atoms, and the red balls represent Te atoms. (c) 3D Brillouin zone of PtTe$_2$, where the two Dirac points are located on the high-symmetry axis on both sides of the Γ point at $\pm D$, shown in red points. (d) Electronic structure of PtTe$_2$ based on first-principle calculations, where two Dirac points are formed by the contact between the electron and hole pockets. (e) A 3D schematic of the electron and hole pockets. (f) The 2D contour of the electron and hole pockets when the electron energy is equal to the Dirac point energy E_D. (g), (h) Show the Dirac points of PtTe$_2$ observed in ARPES experiments, where the Dirac cone tilts along the k_z direction. (l), (i) Schematic diagrams of type-I and type-II 3D Dirac cones, respectively. The type-I Dirac cone is isotropic, whereas the type-II Dirac cone is anisotropic and tilted near the Dirac point. The results are adapted from Ref. [70].

point-like Fermi surface appears at the Dirac point, as shown in Fig. 1.5(f) and Fig. 1.10(l). On the other hand, when using the band parameters of PtSe$_2$ and PtTe$_2$ [69, 70], $U(\mathbf{K}) < T(\mathbf{K})$ can be found along the k_z direction accompanied by the breaking of the Lorentz invariance, and anisotropic and strongly tilted Dirac cones appear along the k_z direction near the Dirac point, as shown in Fig. 1.10(i). The unique tilted band in type-II DSMs will lead to novel properties, further expanding the research field of 3D DSMs.

1.2.4 Investigations of type-II 3D Dirac semimetals

After the type-II 3D DSMs were discovered, research on their transport properties brings many interesting results. First, SdH and dHvA experiments in type-II DSMs revealed their high carrier mobilities [155–159], which, although lower than that of Cd$_3$As$_2$ [85], can still reach approximately 10^4 cm^{2}V^{-1}s^{-1} [157]. Studies on Fermi surface structure have uncovered a nontrivial Berry phase, confirming the nontrivial topological properties of these materials [155, 157]. In contrast to type-I DSMs [86], type-II DSMs exhibit anisotropic transport properties [156, 157]. Additionally, they have ultrafast quantum lifetimes that are less than the picosecond scale [155–159]. Further experiments also found their ultrahigh transport conductivity [160–162]; as shown in Fig. 1.11(a), the conductivity of PtTe$_2$ can reach the order of 10^6 S/m at room temperature.

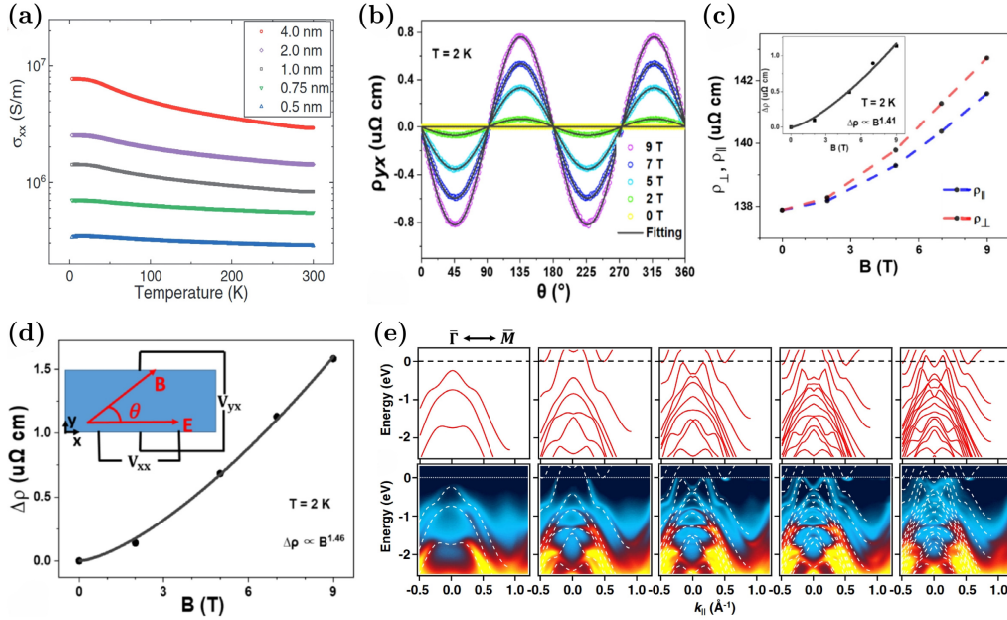As topological semimetals, type-II DSMs theoretically possess a phase transition from a DSM

Figure 1.11: (a) Ultrahigh transport conductivity of PtTe$_2$ thin films. (b) Hall resistivity of PdTe$_2$. (c) Anisotropic resistivity of PdTe$_2$ obtained from the fitting in (b). (d) Planar Hall effect (PHE) of PdTe$_2$, with the inset showing a schematic diagram of the measurement method. (e) In PtTe$_2$, a topological phase transition from a DSM state to a semiconductor state occurs with changes in thickness. The gradient of the different sample thicknesses is 1 trilayer (1-TL), with the thickness increasing from 1-TL to 5-TL from left to right. The upper part shows the results of the first-principles calculations, and the lower part compares the calculated results with the ARPES experiments. The results are adapted from Refs. [159, 162, 170].

state to a WSM state when the time-reversal symmetry is broken. However, the negative MR in these materials is difficult to observe because their chiral anomalies are often covered by a large orbital MR [163]. In recent years, a new phenomenon, called the planar Hall effect (PHE) has been discovered in the study of WSMs, which is directly related to the chiral anomaly [164, 165], offering a new method to study the topological properties [166]. Unlike the Hall effect, where the electric field, transverse voltage, and magnetic field are perpendicular to each other, in PHE studies the electric field, transverse voltage, and magnetic field are coplanar. In this case, the chiral anomaly in DSMs and WSMs can produce a noticeable transverse current in the plane, and its amplitude theoretically equals the chiral negative MR [164, 165]. In DSMs and WSMs, the transverse resistivity ρ_{yx} related to PHE and the longitudinal resistivity ρ_{xx} related to anisotropic magnetoresistance (AMR) are given by [164, 165]: $\rho_{yx} = -\Delta\rho \sin\theta \cos\theta$ and $\rho_{xx} = \rho_\perp - \Delta\rho \cos^2\theta$, where $\Delta\rho = \rho_\perp - \rho_\parallel$ is the anisotropic resistivity caused by the chiral anomaly. $\rho_\perp$ and $\rho_\parallel$ are the resistivities when the magnetic field B is perpendicular and parallel to the electric field E, respectively. In principle, when $B \parallel E$, there is no Lorentz force, so $\rho_\parallel$ and $\rho_\perp$ should equal the resistivity in the absence of an external field, thus making $\Delta\rho = 0$, leading to $\rho_{yx} = 0$ and ρ_{xx} being constant. However, in type-II DSMs, the chiral anomaly makes $\rho_\parallel$ to depend on B, resulting in $\Delta\rho \neq 0$, and both ρ_{yx} and ρ_{xx} exhibit periodic variations. Fig. 1.11(b) shows the periodic variation of ρ_{yx} observed in PdTe$_2$ [163], while further analysis in Figs. 1.11(c) and 1.11(d) finds the AMR and PHE in PdTe$_2$ caused by the chiral anomaly ($\Delta\rho \propto B^{1.46}$) [163].

Similar PHE and AMR have also been reported in type-I DSM Cd_3As_2 [167], type-II DSMs $PtTe_2$ [168] and VAl_3 [169], which confirms the existence of the WSM state in 3D DSMs.

Apart from the band structure, another important difference between type-II and type-I DSMs lies in their electronic states as the thickness is reduced. As shown in Fig. 1.8, type-I DSMs undergo a phase transition from a DSM state to a topological insulator state when the thickness decreases, allowing observation of the QHE in their thin films. In contrast, type-II DSMs have a phase transition from a DSM state to a semiconductor state [170]. In 2019, first-principles calculations investigated the electronic states of Pt sulfides as a function of thickness, suggesting that $PtTe_2$ has a phase transition from a DSM state to a semiconductor state when thickness decreases [170]. In 2020, this phase transition in $PtTe_2$ was experimentally confirmed. As shown in Fig. 1.11(e), ARPES measurements of $PtTe_2$ samples with different thicknesses indicate that the DSM state remains stable until two trilayers, at which point it transitions to a semiconductor state [171]. This result indicates that type-II DSMs do not meet the conditions for the QHE, as seen in type-I 3D DSMs. However, they still show a novel phase transition, which remains of great research value.

As Dirac materials with high mobility and gapless properties, type-II DSMs also have excellent optoelectronic properties. Fig. 1.12(a) shows the calculated anisotropic plasmon modes of the bulk $PtTe_2$, while Fig. 1.12(b) presents the experiment of high-resolution electron energy loss spectroscopy (HREELS) at different angles [172]. In Fig. 1.12(c), the green symbols correspond to the experimental results from Fig. 1.12(b), where a match between theory and experiment confirms the collective excitations of 3D Dirac fermions in bulk $PtTe_2$ [172]. Fig. 1.12(d) shows the optical absorption of $PtSe_2$ samples of varying thicknesses, where the results of the bilayer samples are clearly distinct from those of the multilayer samples [173]. Some theoretical and experimental studies have also reached similar conclusions [174–176], and thickness-tunable optoelectronic properties can also be observed in $PdTe_2$ [177]. Fig. 1.12(e) shows the unique negative terahertz photoconductivity (NTP) in $PtTe_2$ samples [178], which arises from its tilted Dirac cone, exhibiting distinct terahertz photoconductivity compared to type-I DSMs [see Fig. 1.9(d)]. Fig. 1.12(f) further demonstrates the thickness-tunability of NTP in $PtTe_2$ [178]. Further studies by this research group found that $PtTe_2$ has an ultrafast energy relaxation time for electron-photon interactions [179], the fastest being on the order of 10^2 fs. Type-II DSMs also have high potential for applications. As shown in Fig. 1.12(h), $PtTe_2$ has a wide photoresponse range [180, 181], with a response time of ~ 34 μs and a responsivity of about 0.04 mA/W. Van der Waals heterojunctions based on $PtTe_2$ also show excellent photoresponse performance at room temperature [182, 183]. Other studies on $PtTe_2$ and similar DSMs have also revealed the excellent optoelectronic properties of type-II DSMs [184–188]. Furthermore, high-frequency rectifiers based on type-II DSMs [189], highly efficient spintronic terahertz emitters based on $PtTe_2$ [190], and defect-induced and helicity-dependent terahertz emission [191] are also reported, demonstrating the high potential of type-II 3D DSMs in advanced electronic and optoelectronic device applications.

1.3 Research goals of the thesis

Extensive research on 3D DSMs has discovered numerous transport and optoelectronic phenomena. However, many of the experiments lack adequate theoretical explanations. Moreover, the models and methods used in existing theoretical studies tend to be simplistic, overlooking certain characteristics of the electronic states, which limits the theoretical findings. Thus, the purpose of this thesis is to provide theoretical explanations for some of the experiments, as well as to
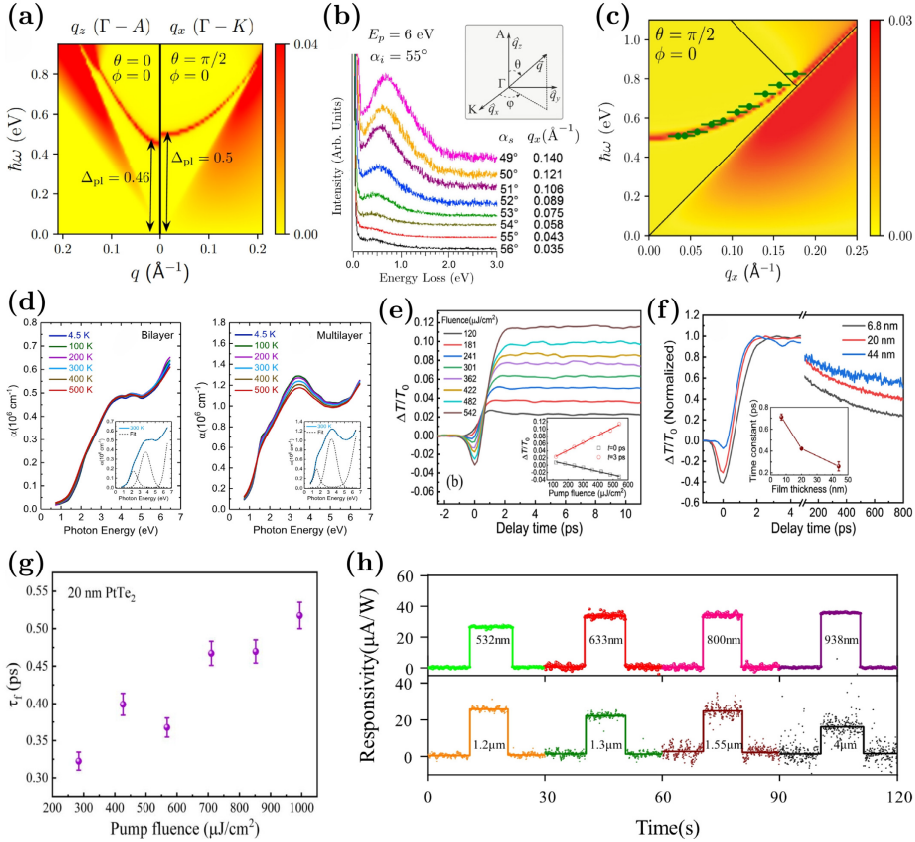
Figure 1.12: (a) Theoretical results of anisotropic plasmon modes in bulk PtTe$_2$. (b) Experimental results of angle-resolved high-resolution energy-loss spectroscopy for bulk PtTe$_2$. (c) Plasmon modes of type-II 3D Dirac fermion in bulk PtTe$_2$ obtained by combining the results of (a) and (b). (d) Optical absorption experiment for PtSe$_2$ samples of varying thicknesses. (e), (f) Negative terahertz photoconductivity observed in PtTe$_2$ samples and the result of its modulation by thickness, respectively. (g) Ultrafast energy relaxation times of electron-photon interactions observed in PtTe$_2$ thin films. (h) PtTe$_2$ exhibits good photoresponse properties across a wide spectral range. Adapted from Refs. [171, 172, 177–179].

further supplement and expand upon existing theoretical work. Meanwhile, this thesis will also explore the optoelectronic and transport properties of 3D DSMs from a theoretical perspective. The research goals of this thesis, based on the current research status, is as follows.

Experiments with type-I 3D DSMs have reported the isotropic in-plane optical conductivity (OC) and optical absorption windows of their bulk samples [133], while their anisotropic OC was also discovered [134]. However, the anisotropic OC cannot be explained using a simple energy dispersion such as a 3D Dirac cone; the OC caused by interband electronic transitions under higher photon energies shows nearly temperature-independent behavior, which remains unexplained; and the reason for the optical absorption windows in OC has not been addressed. The topological nature can affect the electronic excitations near the Dirac point in type-I DSMs. However, to date, no work has specifically analyzed the effect of topological properties on their OC. Therefore, the first goal of this thesis is to conduct a theoretical study of the OC of type-

I DSMs based on Na$_3$Bi. **The first work aims to provide reasonable explanations for the experiments and to explore the connections between the topological properties and the OC of such materials**.

The plasmon is the quantum of collective electron excitations and can be regarded as a quasi-particle of plasma oscillations. Phenomena related to plasmons can be traced back to 1902 [192], and it wasn't until 1941 that Fano conducted preliminary theoretical research on this phenomenon [193]. In 1957, the metal plasma was proposed [194] and was quickly validated experimentally [195]. Later, surface plasmon resonance [196] and surface plasmon excitation [197, 198] were discovered, thus establishing a relatively complete theory for the plasmon. With continuous advances in materials science and techniques in recent years, an increasing number of novel studies related to plasmons have contributed to a thriving and promising research field: Plasmonics [199]. Plasmonics holds significant application prospects in many fields, such as high-density data storage, super-resolution imaging, and negative refractive materials [200]. In recent years, plasmon studies of 2D Dirac systems, such as graphene, have made great progress, bringing many novel physical phenomena [201]. As a new topological material, type-I DSMs are expected for rich and interesting plasmon properties due to their topological nature and the unique 3D Dirac fermions. However, research on the plasmon of type-I DSMs is very limited, and existing studies often rely on the very simplistic model: $E_{\mathbf{K},s} = s\hbar v_F \mathbf{K}$ (where s is the band index and v_F is the Fermi velocity) [202–204]. This simplified band ignores the topological properties, leading to discrepancies between the theoretical and experimental results [36]. Therefore, existing research on the plasmons of type-I DSMs is insufficient. **Hence, the second goal of this thesis is to explore the plasmon properties of type-I DSMs based on a complete effective Hamiltonian and band structure and to further analyze the effect of topological nature on their collective excitations**.

In Sec. 1.2.4, we introduced the excellent optoelectronic properties of type-II 3D DSMs. However, the research on the optoelectronic properties of type-II DSMs is mainly based on their thin films, while studies focusing on bulk samples are very limited. As shown in Figs. 1.10 and 1.11, the thin films of type-II DSMs have a semiconductor state, while their bulk samples retain the anisotropic and tilted Dirac cones, indicating that their bulk and thin-film samples should have different optoelectronic properties. Currently, there are only a few theoretical studies on the optical conductivity (OC) of tilted 3D Dirac cones, and these works do not consider specific materials; they only study the effect of the tilt of the Dirac cone on OC [205, 206]. This suggests that the OC of bulk samples of type-II DSMs remains unclear. **Therefore, the third goal of this thesis is to conduct a theoretical study of the OC of the type-II DSM PtTe$_2$, to discover the phenomena, mechanisms, and the influence of the tilted Dirac cone on the OC, as well as how it changes with sample conditions such as temperature and electron density**.

As introduced in Sec. 1.2.4, many experiments have shown that type-II DSMs have high carrier mobility, anisotropic transport properties, and ultrafast lifetimes [155–159]. These experimental works suggest that these transport features arise from the Dirac fermion nature and the tilted Dirac cone of type-II DSMs. However, to date, there has been no systematic theoretical work that provides a reasonable explanation for these phenomena. At low temperatures, the transport properties, such as the momentum lifetime and carrier mobility, are primarily contributed by carrier-impurity scattering. Currently, there is very little research on background impurity scattering in type-II DSMs, indicating that the physical mechanisms for many experiments remain unclear. Among the type-II DSMs studied, PtTe$_2$ was the most extensively researched, and the corresponding transport experiments are quite comprehensive. **Therefore, the fourth goal of this thesis is to start from the effective Hamiltonian of bulk PtTe$_2$, calculate its transport**

and quantum lifetimes, and compare and analyze the theoretical results with existing experiments, which will further provide a detailed explanation for the transport properties of type-II 3D DSMs.

In summary, the research goals of this thesis are based on the many novel physical properties discovered in 3D DSMs and the experiments that still require explanation. The focus of this thesis is to conduct theoretical research on the OCs, plasmons, and momentum lifetimes of 3D DSMs, exploring the optoelectronic and transport properties of 3D DSMs.

1.4   Main content and structure of the thesis

This thesis focuses on the study of the optical and transport properties of 3D DSMs. The research employs the random phase approximation (RPA) dielectric function method to investigate the plasmon modes of type-I 3D DSMs. The anisotropic OCs of both type-I and type-II 3D DSMs are studied using the energy balance equation derived from the Boltzmann equation. The momentum lifetimes of type-II 3D DSMs are evaluated using the momentum balance equation derived from the Boltzmann equation. The main content and structure of the thesis are outlined as follows.

1.4.1   Main content of the thesis

The first work focuses on the anisotropic OC of the type-I 3D DSM Na_3Bi. By using the band structure with the spin-degeneracy [56], the 4×4 Hamiltonian matrix for Na_3Bi can be simplified into two time-reversal matrices. We first perform a detailed analysis of the band structure features of type-I DSMs, such as band inversion and Berry curvature in the momentum space, by calculating the energy dispersion, density of states, and Fermi level. Then, we consider the cases where linearly polarized light is incident parallel and perpendicular to the n-doped bulk Na_3Bi. Using the energy balance equation, we calculate the OC of Na_3Bi in different directions and provide explanations for the results based on the band features. Additionally, we further investigate how the OC of Na_3Bi is influenced by energy relaxation time, temperature, and electron density.

The second work in this thesis is a theoretical study for the plasmon modes of type-I 3D DSMs. Based on the effective Hamiltonian, we calculate the plasmon dispersion and energy loss spectra for Na_3Bi at both high and low electron densities using the RPA dielectric function. Meanwhile, we also calculate the plasmon modes for another type-I DSM, Cd_3As_2, at both higher and lower electron densities to explore some differences between these two similar materials. From the band features with the calculated plasmon results, we provide an explanation for the collective excitations in type-I DSMs and a comparative analysis with graphene and conventional 3D materials. Furthermore, we also analyze how the band inversion and Berry curvature of type-I DSMs affect their plasmons by examining the results for higher and lower electron densities.

The third work in this thesis focuses on the OC of bulk $PtTe_2$, a representative type-II DSM. Starting from its effective Hamiltonian, we consider the case where linearly polarized light incident either parallel or perpendicular to its n-doped bulk sample, and then we use the energy balance equation to investigate its OC in different directions. We identify and analyze the unique characteristics of its OC, while also discussing similarities with Na_3Bi and graphene. From the anisotropic and tilted Dirac cone of type-II DSMs, we explain the physical mechanism behind the

OC of $PtTe_2$ and analyze the effect of the tilted Dirac cone on its OC. Additionally, we further discuss how specific conditions, such as temperature, energy relaxation time, and electron density of the bulk sample affect its OC.

The fourth work of this thesis theoretically studies the momentum lifetimes of bulk $PtTe_2$, which are induced by electron-impurity scattering at low temperature. Using the RPA dielectric function, we first obtain the electron-electron screening length of the bulk $PtTe_2$ at low temperature. With the momentum balance equation, we calculated the in-plane momentum lifetimes for electron-impurity scattering, taking into account the effects of electron-electron screening. The calculations include the transport lifetime due to large-angle scattering and the quantum lifetime due to small-angle scattering. For the out-of-plane case, constrained by the lattice and band structure, we calculate only the out-of-plane quantum lifetime. By comparing the theoretical calculations with existing experiments, we first verify the validity of our theoretical results, and then further analyze and discuss the characteristics, mechanisms, and influence of the tilted Dirac cone on the momentum lifetimes in type-II 3D DSMs.

1.4.2 Structure of the thesis

The thesis is structured as follows:

In chapter 2 we provide a detailed introduction to the research methods used in this thesis. The random phase approximation (RPA) dielectric function theory and methods for studying plasmon modes are introduced. The Boltzmann equation, along with its derived methods, such as the energy balance equation and the momentum balance equation, is introduced.

In chapter 3 we first present calculations of the band structure, Fermi level, and electron density of states for bulk Na_3Bi. Then, the OC of the n-doped bulk Na_3Bi are calculated and discussed.

In chapter 4 we apply the RPA dielectric function to calculate the anisotropic plasmon modes and corresponding energy loss spectra in n-doped bulk Na_3Bi and Cd_3As_2. The plasmon modes of type-I DSMs are analyzed, the differences between the plasmon properties of Na_3Bi and Cd_3As_2 are discussed, and the effects of Berry curvature on the plasmons in these materials are further investigated.

In chapter 5 we begin with the band structure and Fermi level of the bulk $PtTe_2$, followed by calculations of the anisotropic OC of its n-doped bulk sample using the energy balance equation. The physical mechanisms behind the calculated OC are analyzed based on the band structure, and the effects of energy relaxation time, temperature, and electron density on its OC are explored.

In chapter 6 we utilize the RPA dielectric function and momentum balance equation methods to investigate the transport lifetime and quantum lifetime due to electron-impurity scattering in the n-doped bulk $PtTe_2$. By comparing the theoretical results with the experimental data, the transport properties of the bulk $PtTe_2$ are analyzed.

In chapter 7, the research work of this thesis is summarized and conclusions are offered. An outlook on future research is proposed as well.

Chapter 2

Theoretical approaches

In the study of plasmon modes in solid materials such as metals, the dielectric function in the framework of the random phase approximation (RPA) within the linear response theory is an efficient method to calculate the plasmon properties of intrinsic systems [207]. Meanwhile, when investigating the optoelectronic and transport properties of solid materials, three main approaches are commonly used: the Boltzmann equation, the quantum Boltzmann equation, and the Kubo formula for the current-current correlation function. In general, these three methods yield consistent results in terms of material properties [36, 208], but the Boltzmann equation has specific advantages in transport studies [208], which we will introduce later. Moreover, directly solving the Boltzmann equation for complex systems can be very challenging. However, the energy balance and momentum balance equation methods, derived from the Boltzmann equation, serve as powerful tools to study optical conductivity (OC) and momentum lifetimes in electronic systems and help avoid the difficulties when solving the Boltzmann equation directly [209].

Therefore, this thesis adopts the RPA dielectric function to study the plasmon properties of type-I DSMs, the energy balance equation to calculate the OCs of both type-I and type-II DSMs, and the momentum balance equation to calculate the momentum lifetimes in type-II DSMs. In this chapter, we will provide an introduction to the theoretical approaches used in the thesis.

2.1 Random phase approximation (RPA) dielectric function

The Lindhard response function, more commonly known as the random phase approximation (RPA) dielectric function, is a theoretical method used to investigate the static $\varepsilon(q)$ or dynamic $\varepsilon(\mathbf{q}, \omega)$ dielectric constant and related optoelectronic properties of materials. The RPA dielectric function can be derived through various approaches [208], such as the self-consistent field equation [210] and the Green's function Feynman diagram method [211].

In this thesis, the RPA dielectric function is introduced from the fluctuations of electronic states caused by interactions [207]. For the derivation of the response functions we begin with the Heisenberg equation and write the time evolution of the electron number density operator N as

$$i\hbar \frac{\partial}{\partial t} N = [H, N]. \tag{2.1}$$

Assuming that the effective Hamiltonian of a 3D electronic system is H_0, the corresponding Schrödinger equation is

$$H_0|\mathbf{k},l\rangle = E_{\mathbf{k},l}|\mathbf{k},l\rangle, \tag{2.2}$$

where $E_{\mathbf{k},l}$ is the eigenvalue, $|\mathbf{k},l\rangle$ is the electronic state, $\mathbf{k} = (k_x, k_y, k_z)$ is the 3D wave vector, and l is the band index. In solid materials, we use the Bloch wave function to describe the electronic state, which reads

$$|\mathbf{k},l\rangle = \Omega^{-1/2}u_{\mathbf{k},l}(\mathbf{r})e^{i\mathbf{k}\cdot\mathbf{r}}, \tag{2.3}$$

where Ω is the volume of the system, and $u_{\mathbf{k},l}(\mathbf{r}+\mathbf{R}) = u_{\mathbf{k},l}(\mathbf{r})$ with $\mathbf{R}$ a Bravais lattice vector. These states are eigenstates of both H_0 and N_0, with eigenvalues $E_{\mathbf{k},l}$, and obey the Fermi-Dirac distribution function:

$$f(E_{\mathbf{k},l}) = [e^{(E_{\mathbf{k},l}-E_F)/k_BT} + 1]^{-1},$$

with E_F being the Fermi energy and k_B being the Boltzmann constant. When a 3D electronic system interacts with an external field with energy $V(\mathbf{r},t)$, the total Hamiltonian becomes $H = H_0 + V$. The particle density in the system, $N(\mathbf{r},t)$, has two components: one is the unperturbed density N_0 corresponding to H_0, and the other is the density fluctuation $\delta N(\mathbf{r},t)$ induced by the interaction between the system and the external field. Thus, $N(\mathbf{r},t) = N_0 + \delta N(\mathbf{r},t)$, leading to

$$i\hbar\frac{\partial}{\partial t}\delta N = [H_0, \delta N] + [V, N_0], \tag{2.4}$$

where the second order terms in the perturbation (e.g. $V\delta N$) can be neglected.

In what follows, we first relate the induced charge density to the total potential energy $V(\mathbf{r},t)$ acting on our electron system. Taking the matrix elements of the Heisenberg equation between the initial state $|\mathbf{k},l\rangle$ and the final state $|\mathbf{k}+\mathbf{q},l'\rangle$ with $\mathbf{q} = (q_x, q_y, q_z)$ being the change in electron momentum caused by the total external potential, one can obtain

$$i\hbar\frac{\partial}{\partial t}\langle\mathbf{k}+\mathbf{q},l'|\delta N|\mathbf{k},l\rangle = \langle\mathbf{k}+\mathbf{q},l'|[H_0,\delta N]|\mathbf{k},l\rangle + \langle\mathbf{k}+\mathbf{q},l'|[V,N_0]|\mathbf{k},l\rangle. \tag{2.5}$$

Because these states are eigenstates of H_0, the first term on the right-hand side can be written as

$$\langle\mathbf{k}+\mathbf{q},l'|[H_0,\delta N]|\mathbf{k},l\rangle = (E_{\mathbf{k}+\mathbf{q},l'} - E_{\mathbf{k},l})\langle\mathbf{k}+\mathbf{q},l'|\delta N|\mathbf{k},l\rangle,$$

and the second term can be expressed as

$$\begin{aligned}\langle\mathbf{k}+\mathbf{q},l'|[V,N_0]|\mathbf{k},l\rangle = &[f(E_{\mathbf{k},l}) - f(E_{\mathbf{k}+\mathbf{q},l'})]\\&\times\langle\mathbf{k}+\mathbf{q},l'|\sum_{\mathbf{q}'}V(\mathbf{q}',t)e^{i\mathbf{q}'\cdot\mathbf{r}}|\mathbf{k},l\rangle,\end{aligned} \tag{2.6}$$

where the perturbing potential energy $V(\mathbf{r},t)$ has been expanded in its Fourier components. Note that $V(\mathbf{r},t)$ includes both the external and the induced potential. Now we substitute the explicit form of the Bloch states given above into the matrix element of Eq. (2.6), yielding

$$\langle\mathbf{k}+\mathbf{q},l'|\sum_{\mathbf{q}'}V(\mathbf{q}',t)e^{i\mathbf{q}'\cdot\mathbf{r}}|\mathbf{k},l\rangle = \Omega^{-1}\sum_{\mathbf{q}'}V(\mathbf{q}',t)\int_\Omega d\mathbf{r}u^*_{\mathbf{k}+\mathbf{q},l'}u_{\mathbf{k},l}e^{i(\mathbf{q}'-\mathbf{q})\cdot\mathbf{r}}, \tag{2.7}$$

where the volume integral involves the entire medium. As a consequence of the periodicity of $u_{\mathbf{k},l}$, it is possible to rewrite the above integral as an integral over the unit cell with an additional summation over all the unit cells. A change of variables $\mathbf{r} = \mathbf{R}_n + \mathbf{r}'$, where $\mathbf{R}_n$ is the position of the nth unit cell, and $\mathbf{r}'$ is the position within the unit cell, yields

$$\langle \mathbf{k}+\mathbf{q}, l' | \sum_{\mathbf{q}'} V(\mathbf{q}', t) e^{i\mathbf{q}'\cdot\mathbf{r}} | \mathbf{k}, l \rangle = \Omega^{-1} \sum_{\mathbf{q}'} \sum_n e^{i(\mathbf{q}'-\mathbf{q})\cdot\mathbf{R}_n} V(\mathbf{q}', t)$$
$$\times \int_\Delta d\mathbf{r}' u^*_{\mathbf{k}+\mathbf{q}, l'} u_{\mathbf{k}, l} e^{i(\mathbf{q}'-\mathbf{q})\cdot\mathbf{r}}, \tag{2.8}$$

where the integral extends over the volume of a single unit cell Δ, and the index n represents the summation over all unit cells. We note that $\sum_n e^{i(\mathbf{q}'-\mathbf{q}\cdot\mathbf{R}_n)}$ is negligible unless $\mathbf{q}' - \mathbf{q} = \mathbf{K}$, where $\mathbf{K} = 2\pi/\mathbf{R}$ is a reciprocal lattice vector. In the reduced zone scheme, we take $\mathbf{K} = 0$ and therefore

$$\sum_n e^{i(\mathbf{q}'-\mathbf{q})\cdot\mathbf{R}_n} = (\Omega/\Delta)\delta_{\mathbf{q}'\mathbf{q}},$$

with Ω/Δ being the total number of unit cells. Substituting this into Eq. (2.8) and using the δ-function to perform the summation over $\mathbf{q}'$ leads to

$$\langle \mathbf{k}+\mathbf{q}, l' | \sum_{\mathbf{q}'} V(\mathbf{q}', t) e^{i\mathbf{q}'\cdot\mathbf{r}} | \mathbf{k}, l \rangle = V(\mathbf{q}, t)\Delta^{-1} \int_\Delta u^*_{\mathbf{k}+\mathbf{q}, l'}(\mathbf{r}) u_{\mathbf{k}, l}(\mathbf{r}) d\mathbf{r}$$
$$= V(\mathbf{q}, t)\langle \mathbf{k}+\mathbf{q}, l' | e^{i\mathbf{q}\cdot\mathbf{r}} | \mathbf{k}, l \rangle_*, \tag{2.9}$$

where we have made use of $\langle \mathbf{k}+\mathbf{q}, l' | e^{i\mathbf{q}\cdot\mathbf{r}} | \mathbf{k}, l \rangle_*$ with the definition of $\langle \ \rangle_*$ denoting the integral over the volume of an unit cell. With these expressions, Eq. (2.5) is cast into the following form:

$$i\hbar \frac{\partial}{\partial t} \langle \mathbf{k}+\mathbf{q}, l' | \delta N | \mathbf{k}, l \rangle = (E_{\mathbf{k}+\mathbf{q}, l'} - E_{\mathbf{k}, l}) \langle \mathbf{k}+\mathbf{q}, l' | \delta N | \mathbf{k}, l \rangle$$
$$+ [f(E_{\mathbf{k}, l}) - f(E_{\mathbf{k}+\mathbf{q}, l'})] V(\mathbf{q}, t) \langle \mathbf{k}+\mathbf{q}, l' | e^{i\mathbf{q}\cdot\mathbf{r}} | \mathbf{k}, l \rangle_*. \tag{2.10}$$

This is a time-dependent equation for δN, the contribution to the density operator resulting from the induced particle density.

Next, we can use Eq. (2.10) to derive an expression for the complex dielectric function $\hat{\varepsilon}(\mathbf{q}, \omega)$. Starting from the total potential $\Phi(\mathbf{q}, t) = \Phi_{ext}(\mathbf{q}, t) + \Phi_{ind}(\mathbf{q}, t)$, where $\Phi_{ext}(\mathbf{q}, t)$ and $\Phi_{ind}(\mathbf{q}, t)$ are the external scalar potential and the induced potential, respectively, the dielectric constant $\hat{\varepsilon}(\mathbf{q}, t)$ is defined as

$$\Phi(\mathbf{q}, t) = \frac{\Phi_{ext}(\mathbf{q}, t)}{\hat{\varepsilon}(\mathbf{q}, \omega)} \tag{2.11}$$

The potential $\Phi(\mathbf{q}, t)$ leads to changes in the electronic density of states; these changes in turn can be obtained using the Heisenberg picture by treating $\Phi(\mathbf{q}, t)$ as a perturbation. Variations in the state density cause an induced potential $\Phi_{ind}(\mathbf{q}, t)$ through Poisson's equation, and, through the selfconsistent equations above, this finally yields the expression of the dielectric function in terms of the changes in the electronic states. Then, we use the so-called adiabatic approximation, where we assume that the perturbation is turned on gradually starting at $t \to -\infty$ with a time dependence $e^{\eta t}$, and we will take the limit $\eta \to 0$ after appropriate expressions for the response have been derived. Consequently, we assume that the time dependence of the external scalar potential has the form

$$\Phi_{ext}(\mathbf{r}, t) = \lim_{\eta \to 0} \Phi_{ext}(\mathbf{r}, 0) e^{-i\omega t + \eta t}, \tag{2.12}$$

Since the Fourier components are independent of each other, it is sufficient to consider only one component. We also assume that the induced screening potential energy, the total potential energy, and the density fluctuations all have the same time dependence $e^{-i\omega t + \eta t}$. With this we can rewrite Eq. (2.10) as

$$\lim_{\eta \to 0} (\hbar\omega - i\hbar\eta)\langle \mathbf{k} + \mathbf{q}, l' | \delta N | \mathbf{k}, l \rangle = (E_{\mathbf{k}+\mathbf{q}, l'} - E_{\mathbf{k}, l})\langle \mathbf{k} + \mathbf{q}, l' | \delta N | \mathbf{k}, l \rangle$$
$$+ [f(E_{\mathbf{k}, l}) - f(E_{\mathbf{k}+\mathbf{q}, l'})]V(\mathbf{q}, t)\langle \mathbf{k} + \mathbf{q}, l' | e^{i\mathbf{q}\cdot\mathbf{r}} | \mathbf{k}, l \rangle_*, \quad (2.13)$$

or, after some rearrangements,

$$\langle \mathbf{k} + \mathbf{q}, l' | \delta N | \mathbf{k}, l \rangle = V(\mathbf{q}, t)\langle \mathbf{k} + \mathbf{q}, l' | e^{i\mathbf{q}\cdot\mathbf{r}} | \mathbf{k}, l \rangle_* \lim_{\eta \to 0} \frac{f(E_{\mathbf{k}+\mathbf{q}, l'}) - f(E_{\mathbf{k}, l})}{E_{\mathbf{k}+\mathbf{q}, l'} - E_{\mathbf{k}, l} - \hbar\omega - i\hbar\eta}, \quad (2.14)$$

connecting δN, the induced density, to $V(\mathbf{q}, t)$, the total selfconsistent perturbing potential energy.

What we apply to the system is the external potential $\Phi_{ext}(\mathbf{r}, t)$; however, Eq. (2.14) is given in terms of $\Phi(\mathbf{r}, t)$, the total potential, which also includes the screening potential $\Phi_{ind}(\mathbf{r}, t)$. Rewriting Eq. (2.11) yields

$$\Phi(\mathbf{q}, t) = \frac{\Phi_{ind}(\mathbf{q}, t)}{1 - \hat{\varepsilon}(\mathbf{q}, t)}.$$

Our task now is to establish a relationship between the induced potential and the changes in the electronic density. The energy $V_{ind}(\mathbf{r}, t) = -e\Phi_{ind}(\mathbf{r}, t)$ of the induced screening potential is related by Poisson's equation:

$$\nabla^2 V_{ind}(\mathbf{r}, t) = -4\pi e^2 \langle \delta N(\mathbf{r}, t) \rangle.$$

The electronic charge density ρ can be written in terms of the particle density operator N as

$$\langle \rho \rangle = -e\langle N \rangle = -eTr\{N\delta(\mathbf{r} - \mathbf{r_0})\},$$

where Tr indicates the trace. Using the identity $\sum_{\mathbf{k},l} |\mathbf{k}, l\rangle\langle \mathbf{k}, l| = 1$ we obtain

$$\langle \delta N \rangle = Tr\{\delta N\delta\{\mathbf{r} = \mathbf{r_0}\}\}$$
$$= \sum_{\mathbf{k},\mathbf{q}} \sum_{l,l'} \langle \mathbf{k} + \mathbf{q}, l' | \delta N | \mathbf{k}, l \rangle\langle \mathbf{k}, l | \delta\{\mathbf{r} - \mathbf{r_0}\} | \mathbf{k} + \mathbf{q}, l' \rangle, \quad (2.15)$$

where $\mathbf{r}_0$ indicates the electron positions and l, l' are the band indices. Now we replace the states in the second matrix element with Bloch functions and use $\delta\{\mathbf{r} - \mathbf{r_0}\}$ to perform the integration over $\mathbf{r}$. Replacing $\mathbf{r}_0$ by $\mathbf{r}$, this yields

$$\langle \delta N \rangle = \Omega^{-1} \sum_{\mathbf{k},\mathbf{q}} \sum_{l,l'} u^*_{\mathbf{k},l} u_{\mathbf{k}+\mathbf{q}, l'} e^{i\mathbf{q}\cdot\mathbf{r}} \langle \mathbf{k} + \mathbf{q}, l' | \delta N | \mathbf{k}, l \rangle.$$

Putting this expression for the change in particle density into the Poisson equation gives the response to the change in the potential

$$\nabla^2 V_{ind}(\mathbf{r}, t) = -\frac{4\pi e^2}{\Omega} \sum_{\mathbf{k},\mathbf{q}} \sum_{l,l'} u^*_{\mathbf{k},l} u_{\mathbf{k}+\mathbf{q}, l'} e^{i\mathbf{q}\cdot\mathbf{r}} \langle \mathbf{k} + \mathbf{q}, l' | \delta N | \mathbf{k}, l \rangle;$$

and taking the Fourier transform of $\nabla^2 V_{ind}(\mathbf{r},t)$ leads to

$$-(q')^2 V(\mathbf{q}',t) = -\frac{4\pi e^2}{\Omega} \sum_{\mathbf{k},\mathbf{q}} \sum_{l,l'} \langle \mathbf{k}+\mathbf{q}, l' | \delta N | \mathbf{k}, l \rangle \int d\mathbf{r} u_{\mathbf{k},l}^* u_{\mathbf{k}+\mathbf{q},l'} e^{i(\mathbf{q}-\mathbf{q}'\cdot\mathbf{r})}. \tag{2.16}$$

We can utilize the periodicity of the function $u(\mathbf{r})$ in the same way as before, and hence convert the integral over the entire system to one over a single unit cell and a sum over the unit cells. Following the same procedure as we employed in deriving Eqs. (2.7)-(2.10), we arrive at the following expression for the induced potential energy:

$$V_{ind}(\mathbf{q},t) = \frac{4\pi e^2}{q^2 \Omega} \sum_{\mathbf{k}} \sum_{l,l'} \langle \mathbf{k}+\mathbf{q}, l' | \delta N | \mathbf{k}, l \rangle \langle \mathbf{k}, l | e^{-i\mathbf{q}\cdot\mathbf{r}} | \mathbf{k}+\mathbf{q}, l' \rangle_*, \tag{2.17}$$

where we have used the definition in Eq. (2.9). Substituting Eq. (2.14) into Eq. (2.17) gives a relationship between the induced energy and the total potential energy as

$$V_{ind}(\mathbf{q},t) = \lim_{\eta \to 0} \frac{4\pi e^2}{q^2 \Omega} \sum_{\mathbf{k}} \sum_{l,l'} V(\mathbf{q},t) \frac{f(E_{\mathbf{k}+\mathbf{q},l'}) - f(E_{\mathbf{k},l})}{E_{\mathbf{k}+\mathbf{q},l'} - E_{\mathbf{k},l} - \hbar\omega - i\hbar\eta} |\langle \mathbf{k}+\mathbf{q}, l' | e^{-i\mathbf{q}\cdot\mathbf{r}} | \mathbf{k}, l \rangle_*|^2. \tag{2.18}$$

Rearranging Eq. (2.11), we have

$$\hat{\varepsilon}(\mathbf{q},t) = 1 - \frac{\Phi_{ind}(\mathbf{q},t)}{\Phi(\mathbf{q},t)} = 1 - \frac{V_{ind}(\mathbf{q},t)}{V(\mathbf{q},t)};$$

and the previous two expressions allow us to write the Fourier component of the dielectric constant in terms of Bloch functions as follows:

$$\hat{\varepsilon}(\mathbf{q},\omega) = 1 - \lim_{\eta \to 0} \frac{4\pi e^2}{q^2 \Omega} \sum_{\mathbf{k}} \sum_{l,l'} \frac{f(E_{\mathbf{k}+\mathbf{q},l'}) - f(E_{\mathbf{k},l})}{E_{\mathbf{k}+\mathbf{q},l'} - E_{\mathbf{k},l} - \hbar\omega - i\hbar\eta} |\langle \mathbf{k}+\mathbf{q}, l' | e^{-i\mathbf{q}\cdot\mathbf{r}} | \mathbf{k}, l \rangle_*|^2, \tag{2.19}$$

an expression usually referred to as the Lindhard form for the RPA dielectric function; $\hat{\varepsilon}(\mathbf{q},\omega)$ refers to the longitudinal dielectric constant, the component related to the scalar potential. With the general relation (also called the Dirac identity):

$$\lim_{\eta \to 0} \frac{1}{x \pm i\eta} = P\left\{\frac{1}{x}\right\} \mp i\pi\delta(x),$$

we now can obtain the complex RPA dielectric function as $\hat{\varepsilon}(\mathbf{q},\omega) = \varepsilon_{Re}(\mathbf{q},\omega) + i\varepsilon_{Im}(\mathbf{q},\omega)$, where the real part has the form as

$$\varepsilon_{Re}(\mathbf{q},\omega) = 1 - \frac{4\pi e^2}{q^2 \Omega} \sum_{\mathbf{k}} \sum_{l,l'} \frac{f(E_{\mathbf{k}+\mathbf{q},l'}) - f(E_{\mathbf{k},l})}{E_{\mathbf{k}+\mathbf{q},l'} - E_{\mathbf{k},l} - \hbar\omega} |\langle \mathbf{k}+\mathbf{q}, l' | e^{-i\mathbf{q}\cdot\mathbf{r}} | \mathbf{k}, l \rangle_*|^2, \tag{2.20}$$

and the imaginary part has the form as

$$\varepsilon_{Im}(\mathbf{q},\omega) = \frac{4\pi e^2}{q^2 \Omega} \sum_{\mathbf{k}} \sum_{l,l'} [f(E_{\mathbf{k}+\mathbf{q},l'}) - f(E_{\mathbf{k},l})] |\langle \mathbf{k}+\mathbf{q}, l' | e^{-i\mathbf{q}\cdot\mathbf{r}} | \mathbf{k}, l \rangle_*|^2. \tag{2.21}$$

These expressions for the real and imaginary parts of the dielectric constant include both transitions between bands corresponding to different l and l' indices and also transitions between states within one band.

Next, substituting the eigenenergy and eigenfunction of a 3D electronic system, we can obtain the plasmon dispersion relation by solving the condition where the real part of the dielectric function equals zero, i.e., $\varepsilon_{Re}(\mathbf{q}, \omega) = 0$. Additionally, the energy loss spectrum of a 3D electronic system can be calculated using the definition of the energy loss function:

$$E_{loss} = -Im\left[\frac{1}{\hat{\varepsilon}(\mathbf{q}, \omega)}\right] = \frac{-\varepsilon_{Im}(\mathbf{q}, \omega)}{\varepsilon_{Re}(\mathbf{q}, \omega)^2 - \varepsilon_{Im}(\mathbf{q}, \omega)^2}. \tag{2.22}$$

2.2 The Boltzmann equation and balance equation theories

In condensed matter physics, the Boltzmann equation is an efficient method for studying scattering problems. In transport issues such as impurity scattering, the Boltzmann equation has the following advantages: first, the derivations that start from the Boltzmann equation easily yield accurate results; second, the first theoretical explanation of resistivity originates from the Boltzmann equation; third, the derivations from the Boltzmann equation provide formulas that are easy to understand and recognize; and finally, when scattering is strong, the results from the Boltzmann equation align better with experimental results [208]. Our research group has successfully studied the optoelectronic, magneto-optical, phonon scattering, and impurity scattering properties of 2D Dirac materials such as graphene using the Boltzmann equation theory and related balance equation methods [208, 209], as well as the optoelectronic and transport properties of 2D black phosphorus, 2D semi-Dirac systems, and type-I 3D DSM Na_3Bi [87, 212–214], demonstrating the powerful role of the Boltzmann equation in scattering research.

Consider a 3D electronic system, where the one-electron motion is described by the Hamiltonian $H_{\mathbf{K}}$, the eigenstate is $|\mathbf{K}, l\rangle$, and the eigenenergy is $E_{\mathbf{K}, l}$. Here, $\mathbf{K} = (k_x, k_y, k_z)$ represents the electron wave vector, and $l = +1$ and $l = -1$ correspond to the conduction and valence bands, respectively. In the following derivations, for clarity, we redefine the notations: $|\mathbf{K}, l\rangle \equiv |\zeta\rangle$ and $E_{\mathbf{K}, l} \equiv E_\zeta$. Then, based on the carrier-photon scattering due to the interaction between the system and linearly polarized light, as well as the carrier-impurity scattering at low temperatures due to internal impurities, we will introduce the relevant theories of the momentum balance equation and energy balance equation starting from the Boltzmann equation. Furthermore, methods for calculating the optical conductivity (OC) and lifetime of a 3D electronic system will be provided as well.

2.2.1 Carrier-photon scattering rate

Considering the interaction between the bulk sample of a 3D electronic system and a weak linearly polarized light, the carrier-photon (c-p) scattering process can be treated as a perturbation of the system. Linearly polarized light is a transverse plane electromagnetic wave, and assuming its frequency and electric field strength are ω and F_0, respectively, its vector potential can be expressed as $\mathbf{A}(t) = (F_0/\omega)\sin(\omega t)$. From the perturbation, the wave vector of the system can be modified as $\mathbf{K} \to \mathbf{K} - e\mathbf{A}(t)/\hbar$. Therefore, under the Coulomb gauge, the Hamiltonian of the system in the presence of an external light can be written as $H[\mathbf{K} - e\mathbf{A}(t)/\hbar]$. Thus, the carrier-photon interaction Hamiltonian is given by

$$H_{c-p}(t) \simeq H[\mathbf{K} - e\mathbf{A}(t)/\hbar] - H_{\mathbf{K}}. \tag{2.23}$$

For the case of the weak light, $H_{c-p}(t)$ can be written as $H_{c-p}(t) = H_{c-p}(e^{i\omega t} + e^{-i\omega t})$, where H_{c-p} is the time-independent coefficient of $H_{c-p}(t)$ after neglecting the higher-order terms of F_0. Assuming that the system has an anisotropic band structure, the Hamiltonian for the *c-p* interaction, when linearly polarized light acts perpendicular or parallel to the sample, will also be anisotropic. Hence, we express it as H_{c-p}^j, where $j = x, y,$ or z. Under the condition that the external light is periodic, with a sufficiently long irradiation time and different light polarization directions, the first-order steady-state transition rate for a carrier scttered from an initial state $|\zeta\rangle$ to a final state $|\zeta'\rangle$ through the *c-p* interaction can be obtained using Fermi's Golden Rule as

$$W_{\zeta\zeta'}^{j;c-p} = \frac{2\pi}{\hbar}|\langle\zeta'|H_{c-p}^j|\zeta\rangle|^2\delta(E_{\zeta'} - E_\zeta - \hbar\omega), \tag{2.24}$$

Here, energy conservation $\delta(E_{\zeta'} - E_\zeta - \hbar\omega)$ indicates the process in which the carrier transitions from an initial state to a final state by absorbing a photon with energy $\hbar\omega$. In the presence of an external light field, we can mainly focus on the photon absorption process.

2.2.2   Carrier-impurity scattering rate

Consider a uniform high-quality bulk sample of a 3D electronic system, where impurities are randomly distributed. The electron states are plane waves, and the electrons scatter with isolated impurities. If the impurities are sufficiently dilute, interference between successive scattering events can be neglected. The carrier-impurity (*c-i*) interaction involves carriers being affected by the weak 3D Coulomb potential of charged impurities. Thus, the *c-i* interaction Hamiltonian, which includes the screening length of electron-electron (*e-e*) interaction, is given by

$$H_{c-i} = \frac{e^2}{\kappa|\mathbf{R} - \mathbf{R}_i|}e^{-K_s R} \tag{2.25}$$

Here, $\mathbf{R} = (x, y, z)$ is the coordinates of a carrier, while the charged impurity is located at $\mathbf{R}_i = (x_i, y_i, z_i)$; κ is the static dielectric constant of the material; K_s is the inverse of the *e-e* interaction screening length, which can be obtained from the real part of the RPA dielectric function in Eq. (2.20): considering the low-temperature limit ($T \to 0$), the long-wavelength limit ($Q \to 0$), and the static case ($\omega = 0$), the relationship between the screening length $1/K_s$ and the real part of the dielectric function in 3D is given by $\varepsilon_{Re}(\mathbf{Q}, 0) = 1 + K_s^2(\mathbf{Q})/Q^2$. Then, assuming that the electron state $|\zeta\rangle$ and the impurity state $|I\rangle$ can be described separately, i.e., $|\zeta; I\rangle = |\zeta\rangle|I\rangle$, we can also apply Fermi's Golden Rule to obtain the first-order steady-state transition rate for the carrier scattered from the initial state $|\zeta; I\rangle$ to the final state $|\zeta'; I\rangle$ via *c-i* interaction, which reads as

$$\begin{aligned}W_{\zeta\zeta'}^{c-i} &= \frac{2\pi}{\hbar}|\langle I; \zeta'|H_{c-i}|\zeta; I\rangle|^2\delta(E_{\zeta'} - E_\zeta) \\ &= \frac{2\pi}{\hbar}N_i|\langle\zeta'|H_{c-i}|\zeta\rangle|^2\delta(E_{\zeta'} - E_\zeta), \end{aligned} \tag{2.26}$$

Here, $N_i = |\langle I|I\rangle|^2$ represents the impurity concentration, and the energy conservation $\delta(E_{\zeta'} - E_\zeta)$ indicates that the impurity scattering described above does not involve any energy transfer.

2.2.3   Boltzmann equation theory

After obtaining the scattering rates for the carrier-photon and carrier-impurity interactions in a 3D electronic system, we can study its physical properties such as optical conductivity and life-

time using the Boltzmann equation and the related theoretical approaches. Now, let us start with the Boltzmann equation. In Boltzmann theory, carriers can be described by the classical distribution function $f(\mathbf{R}, \mathbf{K}, t)$, and the time rate of change of this distribution function is governed by the Boltzmann equation [208]:

$$0 = \frac{df}{dt} = \frac{\partial f}{\partial t} + \mathbf{v} \cdot \nabla_{\mathbf{R}} f + \frac{\partial \mathbf{K}}{\partial t} \cdot \nabla_{\mathbf{K}} f + \left(\frac{\partial f}{\partial t} \right)_{coll}, \tag{2.27}$$

The last term is the time rate of change due to collisions with the photons or impurities. There is no $\mathbf{R}$ dependence in $f(\mathbf{R}, \mathbf{K}, t)$ since the material is assumed to be homogeneous. Also, for the dc conductivity, there is no time dependence. The system has a weak external electric field, and the current flows in a steady-state fashion. The distribution function is only a function of wave vector $f(\mathbf{K})$ and obeys the equation

$$0 = \frac{\partial \mathbf{K}}{\partial t} \cdot \nabla_{\mathbf{K}} f + \left(\frac{\partial f}{\partial t} \right)_{coll}. \tag{2.28}$$

In a solid, the factor $\partial \mathbf{K}/\partial t$ is equivalent to an acceleration equal to the external forces on the carrier [208, 209]: $\partial \mathbf{K}/\partial t = e\mathbf{F}/\hbar - e\mathbf{v} \times \mathbf{H_0}/c$. In the present problem, there is an electric field $\mathbf{F}$ and no magnetic field ($\mathbf{H_0} = 0$), so that we can express the steady-state Boltzmann equation for the 3D electronic system as

$$\left(\frac{\partial f}{\partial t} \right)_{coll} = -\frac{e\mathbf{F}}{\hbar} \cdot \nabla_{\mathbf{K}} f_\zeta = g \sum_{\zeta'} [f_{\zeta'}(1 - f_\zeta) W_{\zeta\zeta'} - f_\zeta(1 - f_{\zeta'}) W_{\zeta'\zeta}]. \tag{2.29}$$

In the above equation, g represents the degeneracy of the system, $f_\zeta = f_l(\mathbf{K})$ represents the momentum distribution function of carriers in the initial state $|\zeta\rangle$, and $W_{\zeta\zeta'}$ is the steady-state transition rate for carriers scattering from the initial state to the final state during the scattering process. Assuming that the 3D electronic system has an anisotropic band structure, Eq. (2.29) can be further expressed as

$$-\frac{eF_j}{\hbar} \frac{\partial f_\zeta}{\partial k_j} = g \sum_{\zeta'} [f_{\zeta'}(1 - f_\zeta) W_{\zeta\zeta'}^j - f_\zeta(1 - f_{\zeta'}) W_{\zeta'\zeta}^j], \tag{2.30}$$

with $j = x$, y, or z.

By substituting Eqs. (2.24) or (2.26) into Eq. (2.30) along with the eigenenergy and eigenstate, we can investigate the scattering processes of carriers with photons or impurities in a 3D electronic system. However, after incorporating the relevant expressions, it becomes challenging to obtain an analytical solution for Eq. (2.30) or to perform straightforward calculations. At this point, by using the balance equation theory derived from the Boltzmann equation, we can circumvent the difficulties of directly solving the Boltzmann equation while retaining the advantages of the effective response of carriers to different external fields present in the Boltzmann equation. Next, we will introduce the energy balance equation and momentum balance equation derived from the Boltzmann equation, as well as the methods for studying the optoelectronic properties and transport properties of electronic systems.

2.2.4 Energy balance equation and optical conductivity

The energy balance equation can be obtained by multiplying $g \sum_\zeta E_\zeta$ on both sides of Eq. (2.30). Since the perturbation Hamiltonian for the carrier-photon interaction is Hermitian, that is,

$\langle \zeta' | H_{c-p}^j | \zeta \rangle = \langle \zeta | H_{c-p}^j | \zeta' \rangle^*$ in Eq. (2.24), the c-p scattering rate has symmetry $W_{\zeta\zeta'}^{j,c-p} = W_{\zeta'\zeta}^{j,c-p}$. Thus, we can iterate Eq. (2.30) into

$$-\frac{eF_j}{\hbar} g \sum_{\zeta} E_\zeta \frac{\partial f_\zeta}{\partial k_j} = g^2 \sum_{\zeta,\zeta'} (E_{\zeta'} - E_\zeta) f_\zeta (1 - f_{\zeta'}) W_{\zeta\zeta'}^{j,c-p}. \tag{2.31}$$

On the left-hand side of the above equation, under the condition of carrier number conservation, we have

$$g \sum_{\zeta} E_\zeta \frac{\partial f_\zeta}{\partial k_j} = -\hbar N_0 v_j^*,$$

where v_j^* is the average drift velocity of the carriers caused by F_j, and N_0 is the total carrier density in the system. In Eq. (2.24), the energy conservation for the carrier-photon scattering indicates that $E_{\zeta'} - E_\zeta = \hbar\omega$. Thus, we can obtain the energy balance equation corresponding to different light polarization directions as

$$eF_j N_0 v_j^* = g^2 \hbar\omega \sum_{\zeta,\zeta'} f_\zeta (1 - f_{\zeta'}) W_{\zeta\zeta'}^{j,c-p}. \tag{2.32}$$

In steady state, the current density $\mathbf{J}$ induced by the external field $\mathbf{F}$ is defined as $\mathbf{J} = eN_0\mathbf{v}^*$ [209], and its relationship with the conductivity σ induced by the external field is given by $\mathbf{J} = \sigma\mathbf{F}$ [209]. If we only change the polarization direction of light, then we have $F_x = F_y = F_z = F_0$; further assuming that the momentum distribution of carriers in Eq. (2.32) can be described by a statistical energy distribution such as the Fermi-Dirac function, $f_\zeta = f_l(\mathbf{K}) = f_l(E_{\mathbf{K},l})$, where $f_+(E_{\mathbf{K},+}) = [e^{(E_{\mathbf{K},+} - E_F^e)/k_B T} + 1]^{-1}$ represents the electron distribution in the conduction band with the Fermi level of E_F^e, and $f_-(E_{\mathbf{K},-}) = [e^{(E_{\mathbf{K},-} - E_F^h)/k_B T} + 1]^{-1}$ represents the hole distribution in the valence band with the Fermi level of E_F^h; thus, we can obtain the longitudinal optical conductivity induced by different transition channels of carriers under different light polarization directions, which reads as

$$\sigma_{jj}^{ll'}(\omega) = g^2 \frac{\hbar\omega}{F_0^2} \sum_{\mathbf{K},\mathbf{K}'} f_l(E_{\mathbf{K},l})[1 - f_{l'}(E_{\mathbf{K}',l'})] W_{\zeta\zeta'}^{j,c-p}. \tag{2.33}$$

Because the optical conductivity of the system in an applied light field mainly comes from the case where its carriers absorb photon energy, the situation where electrons lose energy can be ignored, i.e., $\sigma_{jj}^{+-}(\omega) \approx 0$. Therefore, the total optical conductivity of the system can be written as

$$\sigma_{jj}(\omega) = \sum_{l,l'} \sigma_{jj}^{ll'}(\omega) = \sigma_{jj}^{++}(\omega) + \sigma_{jj}^{--}(\omega) + \sigma_{jj}^{-+}(\omega), \tag{2.34}$$

In this equation, $++$ and $--$ represent the optical conductivity caused by transitions within the conduction band and the valence band, respectively, while $-+$ represents the optical conductivity caused by the transition channel where electrons are excited from the valence band to the conduction band through photon absorption. Now, we can calculate the optical conductivity in different directions of a 3D electronic system using Eqs. (2.33) and (2.34).

2.2.5 Momentum balance equation and momentum lifetime

In Eq. (2.26), the Hamiltonian for the carrier-impurity interaction also has Hermitian $\langle \zeta' | H_{c-i} | \zeta \rangle = \langle \zeta | H_{c-i} | \zeta' \rangle^*$, and $W_{\zeta\zeta'}^{c-i}$ also exhibits symmetry $W_{\zeta\zeta'}^{c-i} = W_{\zeta'\zeta}^{c-i}$. Therefore, the equation corre-

sponding to impurity scattering, Eq. (2.30), can be simplified to

$$-\frac{eF_j}{\hbar}\frac{\partial f_\zeta}{\partial k_j} = g\sum_{\zeta'}(f_\zeta W^{c-i}_{\zeta\zeta'} - f'_\zeta W^{c-i}_{\zeta'\zeta}). \tag{2.35}$$

The momentum balance equation for carrier-impurity scattering can be obtained by multiplying $g\sum_\zeta k_j$ on both sides of the above equation, which reads as

$$-\frac{eF_j}{\hbar}g\sum_\zeta k_j\frac{\partial f_\zeta}{\partial k_j} = g^2\sum_{\zeta,\zeta'}(k'_j - k_j)f_\zeta W^{c-i}_{\zeta\zeta'}. \tag{2.36}$$

On the left-hand side there is

$$g\sum_\zeta f_\zeta = N_e + N_h = N_0,\ g\sum_\zeta k_j\frac{\partial f_\zeta}{\partial k_j} = -N_0,$$

where N_e, N_h, and N_0 represent the electron density, hole density, and total conducting carrier density of the system, respectively. Thus, Eq. (2.36) can be further expressed as

$$\frac{eF_j}{\hbar}N_0 = g^2\sum_{\zeta,\zeta'}(k'_j - k_j)f_\zeta W^{c-i}_{\zeta\zeta'}. \tag{2.37}$$

Then, we consider that the electric field F_j caused by the charged impurities induces a drift in the carrier momentum. Assuming that the momentum distribution of the carriers can be described by the Fermi-Dirac distribution function, we have $f_\zeta = f_l[E_l(\mathbf{K} - m^*\mathbf{v}^*/\hbar)]$, where $\mathbf{v}^*$ is the average drift velocity of the carriers. The average drift velocity of carriers in each direction, v^*_j, is induced by the electric field F_j of the charged impurities, while m^*_j is the effective mass of the electrons in the j direction. Condition $m^*_j v^*_j \ll k_j$ is satisfied since F_j is sufficiently weak, so that we can apply a first-order Taylor expansion and obtain

$$f_\zeta \simeq f_l(E_\zeta) - \frac{m^*_j v^*_j}{\hbar}\frac{\partial E_\zeta}{\partial k_j}\frac{\partial f_l(E_\zeta)}{\partial E_\zeta}. \tag{2.38}$$

Substituting the above expression into Eq. (2.37), $\sum_{\zeta,\zeta'}(k'_j - k_j)f_l(E_\zeta)W^{c-i}_{\zeta\zeta'} = 0$ can be found through the symmetry of $W_{\zeta\zeta'}$. Thus, Eq. (2.37) can be further simplified to

$$eF_j N_0 = -g^2\sum_{\zeta,\zeta'}(k'_j - k_j)W^{c-i}_{\zeta\zeta'}m^*_j v^*_j\frac{\partial E_\zeta}{\partial k_j}\frac{\partial f_l(E_\zeta)}{\partial E_\zeta}. \tag{2.39}$$

By using the definition of carrier mobility [209]: $\mu_j = -v^*_j/F_j = e\tau_j/m^*_j$, and combining it with Eq. (2.39), we can derive the expression for the momentum lifetime of carriers in a 3D electronic system, which reads

$$\frac{1}{\tau^l_j} = \frac{g^2}{N_0}\sum_{\zeta,\zeta'}(k'_j - k_j)W^{c-i}_{\zeta\zeta'}\frac{\partial E_\zeta}{\partial k_j}\frac{\partial f_l(E_\zeta)}{\partial E_\zeta}. \tag{2.40}$$

It is important to note that the carrier-impurity scattering is sufficiently weak. The energy conservation in $W^{c-i}_{\zeta\zeta'}$ indicates that impurity scattering is not strong enough to induce interband transitions; therefore, the momentum lifetime is primarily contributed by the intraband transitions of the carriers. Now, by using Eqs. (2.26) and (2.40), we can calculate the momentum lifetime for a 3D electronic system.

Energy band characteristics and optical conductivity of type-I 3D DSMs

Monolayer graphene is a typical 2D Dirac system, characterized by its gapless linear energy dispersion and masslessness at the Dirac point. Research on graphene has revealed many optoelectronic properties of 2D Dirac systems, such as the optical absorption window in the mid-infrared range and the universal optical conductance in the visible range [215, 216], the varying optical transmittance under different layers [217], tunable optical conductance and optical absorption windows [216, 218], among others.
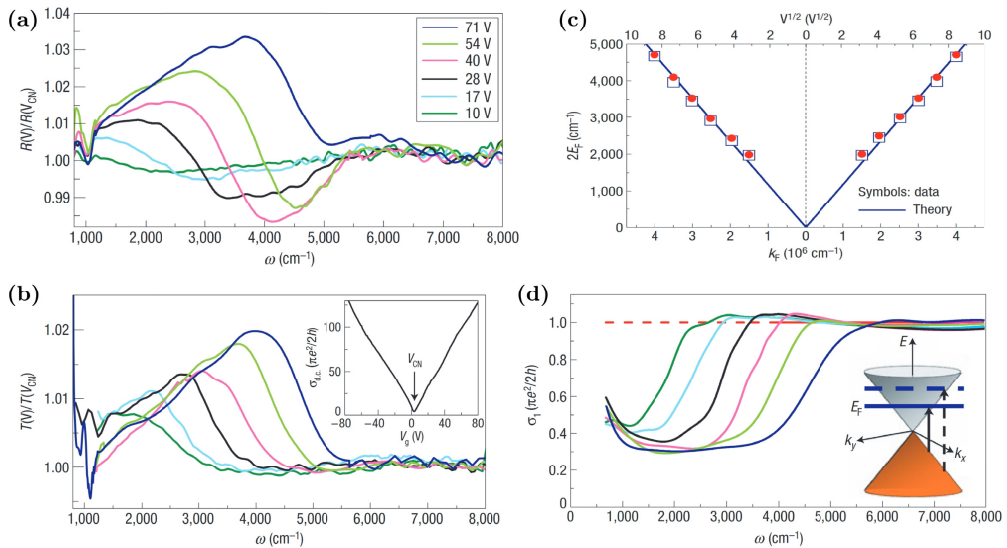
Figure 3.1: Gate-voltage tunable optoelectronic properties of monolayer graphene. (a) Transmission and (b) reflection are gate-tunable in monlayer graphene. (c) The Fermi energy E_F and the Fermi wave vector k_F change linearly with the square root of the gate voltage $\sqrt{V}$ ($E_F \propto k_F \propto \sqrt{V}$). (d) Gate-voltage can modulate the optical conductance of monolayer graphene. A universal conductance of $e^2/4\hbar$ in the high-frequency range can be observed, and a gate-tunable optical absorption window in the mid-infrared to terahertz spectrum can be found. Adapted from Ref. [220].

As shown in Figs. 3.1(a) and 3.1(b), the reflection and transmission that are tunable through gate-voltage were observed in monolayer graphene. Based on the linear energy dispersion, the relationships can be derived from the electron density N and the Fermi velocity v_F, which reads $E_F = \hbar v_F \sqrt{\pi N}$, $N = C_g V/e$ (where $C_g = 115$ aFμm^{-2} is the gate capacitance per unit area), $k_F = \sqrt{\pi N} = \sqrt{\pi C_g V/e}$ [215], as shown in Fig. 3.1(c). These relationships indicate that the applied gate-voltage can tune the electron density in graphene, thereby changing its Fermi level and tuning the relevant optoelectronic properties. From Fig. 3.1(d), we can see that its optical conductance, derived from Figs. 3.1(a) and 3.1(b), exhibits a universal conductance of $e^2/4\hbar$ in the high photon energy range ($\omega > 5000$ cm^{-1}), which is independent of N and the gate-voltage. In the mid-infrared to terahertz range, since optical absorption is proportional to optical conductance, an optical absorption window tuned by the gate-voltage can be observed [215]. Fig. 3.1(d) has an explanation that the optical absorption window in graphene arises from the differing energy requirements for intraband and interband electronic transitions within its gapless linear band structure. As the gate-voltage increases, the electron density is also higher, resulting in a higher Fermi level. Consequently, the photon energy required for the intraband and interband transitions increases, leading to a systematic blueshift in the optical conductance as the electron density increases [219, 220]. These results indicate that the optoelectronic properties of monolayer graphene at specific frequencies can be switched on and off by varying the electron density, showcasing the potential of 2D Dirac systems for optimization and development in optoelectronic devices such as optical modulators.

As analogs of graphene, type-I 3D DSMs also have massless, gapless, and linear energy dispersion near the Dirac point. As shown in Figs. 3.2(a) and 3.2(b), the optical conductivity (OC) of the bulk Cd$_3$As$_2$ has been found to be isotropic in the x-y plane and to feature an optical absorption window [133], similar to monolayer graphene. Additionally, its OC is nearly temperature independent at higher photon energies [133], which requires further explanation. In Fig. 3.2(c), the authors obtained the in-plane OC of Cd$_3$As$_2$ by fitting it with a simple 3D Dirac cone model, revealing that OC at higher photon energies is primarily contributed by interband transitions of electrons [133]. However, this theoretical result does not explain the physical mechanism of OC at lower photon energies, thus failing to account for the optical absorption window. Similar temperature-dependent reflection experiments have also been reported in Na$_3$Bi [202]. The subsequently discovered anisotropic OC in bulk Cd$_3$As$_2$ demonstrates the differences between type-I DSMs and graphene [134], but this result lacks explanations. Furthermore, as shown in
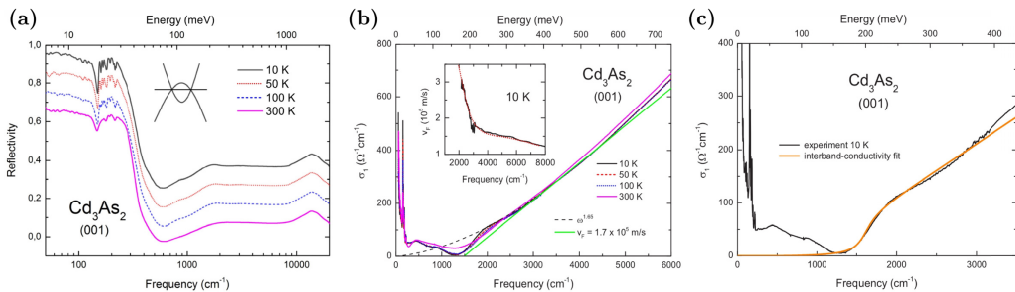
Figure 3.2: Experimental research on the optoelectronic properties of bulk Cd$_3$As$_2$. (a) The reflectivity of bulk Cd$_3$As$_2$ in the x-y plane varies with photon energy and is influenced by temperature. (b) The in-plane OC of bulk Cd$_3$As$_2$, derived from (a), changes with photon energy, showing the presence of an absorption window. (c) The yellow curve represents the theoretical result of the interband OC obtained by fitting with a simple 3D Dirac cone. Adapted from Ref. [133].

Fig. 1.7(b), it has been reported that the electron density in 3D DSMs can be tuned by an external gate-voltage [90]. Therefore, in these materials, the tunability of OC with gate-voltage, similar to that of graphene, is also worth further exploration. The many interesting physical phenomena discovered in the optical experiments of type-I DSMs, along with the unexplained aspects, prompt us to conduct in-depth theoretical research on the OC of type-I DSMs.

From the similarities between type-I 3D DSMs and graphene, we have reason to believe that their optoelectronic properties, such as the OC, have some common features, stemming from gapless Dirac fermions. However, type-I DSMs possess nontrivial topological features, indicating that their optoelectronic properties should have more differences that must be explained based on their nontrivial band structure. Along the k_z direction of type-I DSMs, band inversion can be found between a pair of Dirac points, which corresponds to the Berry curvature region that obviously affects the electron momentum. To theoretically study the optoelectronic properties of type-I DSMs, it is essential to have a clear understanding of the energy band characteristics of these materials. Therefore, in this chapter, we begin with a detailed analysis of the band structure of type-I DSMs. Theoretically, the anisotropy and Berry curvature in Na_3Bi are stronger than those in Cd_3As_2. Thus, we will then conduct investigations of OC in type-I DSMs based on Na_3Bi. An in-depth analysis of the OC of type-I 3D DSMs not only provides reasonable explanations for experimental results but also reveals how their OC is influenced by topological properties.

3.1 Spin degenerate energy band of type-I 3D DSMs

Under the $\mathbf{k} \cdot \mathbf{p}$ theory, the effective Hamiltonian for the low-energy excitations of 3D DSMs is given by Eq. (1.3) [53, 54]:

$$H(\mathbf{K}) = \varepsilon_{\mathbf{K}} \times I + \begin{pmatrix} M_{\mathbf{K}} & Ak_+ & Dk_- & B_{\mathbf{K}}^* \\ Ak_- & -M_{\mathbf{K}} & B_{\mathbf{K}}^* & 0 \\ Dk_+ & B_{\mathbf{K}} & M_{\mathbf{K}} & -Ak_- \\ B_{\mathbf{K}} & 0 & -Ak_+ & -M_{\mathbf{K}} \end{pmatrix},$$

where $\mathbf{K} = (k_x, k_y, k_z)$ is the 3D wave vector, and I is the 4×4 identity matrix; the lattices of Na_3Bi and Cd_3As_2 are periodic stacking structures of the basic atomic layers [53, 54], with the k_z direction corresponding to the stacking direction; $k_\pm = k_x \pm ik_y$, $\varepsilon_{\mathbf{K}} = C_0 + C_1 k_z^2 + C_2 k^2$, and $M_{\mathbf{K}} = M_0 - M_1 k_z^2 - M_2 k^2$; C_0, C_1, C_2, M_0, M_1, M_2, and A are the band parameters; $B_{\mathbf{K}} = B_3 k_z k_+^2 \sim K^3$ is a higher-order term contributing to electron motion, which only has a significant effect when the electron momentum is very large; the terms containing D describe the breaking of crystal symmetries, with $D = 0$ when maintaining crystal symmetries. The analytical solution for the energy dispersion is given by $E_\pm(\mathbf{K}) = \varepsilon_{\mathbf{K}} \pm \sqrt{M_{\mathbf{K}}^2 + A^2 k^2 + |B_{\mathbf{K}}|^2}$, where $+$ and $-$ correspond to the conduction band and the valence band, respectively, and the two Dirac points are located at $k = 0$ and $k_z = \pm k_z^c = \pm[M_0/M_1]^{1/2}$.

Angle-resolved photoemission spectroscopy (ARPES) and spin-resolved ARPES measurements indicate that the band structures of Na_3Bi and Cd_3As_2 maintain spin degeneracy over a range of lower energies and small momenta [55–58], and that band splitting can only be observed under very strong magnetic fields [82, 109, 114]. These results are consistent with theoretical findings, where the $B_{\mathbf{K}}$ term is approximately 0 under a lower energy and small momentum, and the band structure of type-I DSMs maintains spin degeneracy and has strong robustness near the Dirac

points [53, 54]. In this study, weak external fields only affect the carriers at lower energies and smaller momenta, thereby we can neglect the $B_\mathbf{K}$ term in the Hamiltonian; at the same time, weak external fields do not break the crystal symmetries, so there is $D = 0$. Thus, the effective Hamiltonian of type-I 3D DSMs can be simplified as

$$H(\mathbf{K}) = \begin{pmatrix} H_u(\mathbf{K}) & 0 \\ 0 & H_l(\mathbf{K}) \end{pmatrix},$$

where $H_u(\mathbf{K})$ and $H_l(\mathbf{K})$ are two 2×2 matrices. Crystal symmetries indicate that $H_l(\mathbf{K})$ is the time-reversal of $H_u(\mathbf{K})$, that is, $H_l(\mathbf{K}) = H_u^*(-\mathbf{K})$, which allows us to focus on $H_u(\mathbf{K})$ for further study.

After considering the crystal symmetries and spin degeneracy, we obtain the simplified Hamiltonian for type-I 3D DSMs as

$$H_u(\mathbf{K}) = \begin{pmatrix} \varepsilon_\mathbf{K} + M_\mathbf{K} & Ak_+ \\ Ak_- & \varepsilon_\mathbf{K} - M_\mathbf{K} \end{pmatrix}. \tag{3.1}$$

The corresponding eigenvalue and eigenfunction are, respectively,

$$E_{\mathbf{K},l} = \varepsilon_\mathbf{K} + l\big[M_\mathbf{K}^2 + A^2 k^2\big]^{1/2} = \varepsilon_\mathbf{K} + l\big[\xi_{\mathbf{K},l} + M_\mathbf{K}\big], \tag{3.2}$$

and

$$\psi_{\mathbf{K},l}(\mathbf{R}) = |\mathbf{K},l\rangle = a_{\mathbf{K},l} \begin{pmatrix} 1 \\ b_{\mathbf{K},l} \end{pmatrix} e^{i\mathbf{K}\cdot\mathbf{R}}. \tag{3.3}$$

Here, $l = +1$ ($l = -1$) denotes the conduction (valence) band, $\mathbf{R} = (x, y, z)$, $\xi_{\mathbf{K},l} = \big[M_\mathbf{K}^2 + A^2 k^2\big]^{1/2} - lM_\mathbf{K}$,

$$a_{\mathbf{K},l} = Ak(\xi_{\mathbf{K},l}^2 + A^2 k^2)^{-1/2}, \qquad b_{\mathbf{K},l} = l\xi_{\mathbf{K},l}/Ak_-. \tag{3.4}$$

Eqs. (3.1)-(3.4) with different band parameters are suitable for studying both Na_3Bi and Cd_3As_2.

In this study, we consider n-doped bulk Na_3Bi, where the valence band is fully occupied. The density of states (DOS) in the conduction band is given by the imaginary part of the Green's function, which reads as

$$D_+(E) = -\frac{g_s}{\pi} \sum_\mathbf{K} \delta(E - E_{\mathbf{K},+}), \tag{3.5}$$

where $g_s = 2$ represents spin degeneracy. By performing a Lorentzian expansion of the Dirac-δ function, i.e., $\delta(x) = (\Gamma/\pi)(x^2 + \Gamma^2)^{-1}$, and substituting the broadening $\Gamma = 1$ meV, we can obtain the DOS of type-I DSMs. The condition of carrier number conservation is defined as $N_l = g_s \sum_\mathbf{K} f_l[E_l(\mathbf{K})]$, where N_l represents the density of electrons or holes, and $f_l[E_l(\mathbf{K})]$ is the Fermi-Dirac function for electrons or holes. Using this condition, we can find the relationship between the electron density N_e and the Fermi energy E_F^e in the conduction band as

$$N_e = \frac{1}{\pi^2} \int_0^\infty dk_z \int_0^\infty dk \frac{k}{e^{(E_{\mathbf{K},+} - E_F^e)/k_B T} + 1}. \tag{3.6}$$

For an n-doped Dirac system under an external field, electrons in the valence band can easily transition to the conduction band after absorbing photons because of the gapless nature, leaving behind holes in the valence band. If N is the electron density without an external field, then the electron density in the presence of a field is given by $N_e = N + \Delta N_e$, where ΔN_e is the photon-excited electron density. Meanwhile, the carrier number conservation gives $\Delta N_e = N_h$, where

N_h is the hole density. Therefore, the corresponding hole Fermi energy E_F^h related to N_h can be expressed as

$$N_h = \frac{1}{\pi^2} \int_0^\infty dk_z \int_0^\infty dk k \left[1 - \frac{1}{e^{(E_{\mathbf{K},-} - E_F^h)/k_B T} + 1} \right]. \tag{3.7}$$

3.2 Optical conductivities of type-I 3D DSMs in different light polarization directions

Bulk Na$_3$Bi is isotropic in the x-y plane. Therefore, we consider the case where linearly polarized light is incident perpendicular to its x-y plane, with light polarization along the x direction. At the same time, we also consider the case where linearly polarized light is incident parallel to its x-y plane, with the light polarization along the z direction, to study its anisotropic OCs.

Introducing Eq. (3.1) into Eq. (2.23), we can obtain the perturbation Hamiltonian for the carrier-photon (c-p) interaction in a type-I DSM when the light polarization is along the x and z directions, respectively, as

$$H_{c-p}^x(t) = \frac{2eA(t)}{\hbar} \begin{pmatrix} (M_2 - C_2)k_x & -A/2 \\ -A/2 & -(M_2 + C_2)k_x \end{pmatrix}, \tag{3.8}$$

and

$$H_{c-p}^z(t) = \frac{2eA(t)k_z}{\hbar} \begin{pmatrix} (M_1 - C_1) & 0 \\ 0 & -(M_1 + C_1) \end{pmatrix}. \tag{3.9}$$

Here, $A(t) = (F_0/\omega)\sin(\omega t)$ is the vector potential of the light field, where F_0 is its electric field strength and ω its frequency. Since we only change the polarization direction of the light, we have $F_0 = F_x = F_z$. Considering the light field as a weak radiation field, we neglect the higher-order terms F_0^2 in the perturbation Hamiltonian that represent strong light fields.

Substituting the time-independent coefficients H_{c-p}^x and H_{c-p}^z of the perturbation Hamiltonian into Eq. (2.24), we can obtain the first-order transition rate for the carriers in Na$_3$Bi, scattering from the initial state $|\zeta\rangle \equiv |\mathbf{K}, l\rangle$ to the final state $|\zeta'\rangle \equiv |\mathbf{K}', l'\rangle$ under different light polarization directions as

$$W_{\zeta\zeta'}^{j,c-p} = \frac{2\pi}{\hbar} |\langle \zeta'|H_{c-p}^j|\zeta\rangle|^2 \delta(E_{\zeta'} - E_\zeta - \hbar\omega)$$
$$= \frac{2\pi}{\hbar} \left(\frac{eF_0}{\hbar\omega} \right)^2 |U_{\zeta\zeta'}^j|^2 \delta_{\mathbf{K},\mathbf{K}'} \delta(E_{\zeta'} - E_\zeta - \hbar\omega), \tag{3.10}$$

where $j = x$ or z, E_ζ and $E_{\zeta'}$ come from Eq. (3.2),

$$|U_{\zeta\zeta'}^j|^2 = \frac{|G_{\zeta\zeta'}^j|^2}{[\xi_\zeta^2 + A^2 k^2][\xi_{\zeta'}^2 + A^2 k'^2]}, \tag{3.11}$$

$\xi_\zeta = \xi_{\mathbf{K},l}$ comes from Eq. (3.3), $G_{\zeta\zeta'}^x = A^2(lk_+\xi_\zeta + l'k_-\xi_{\zeta'})/2 - k_x[A^2k^2(M_2 - C_2) - ll'(M_2 + C_2)\xi_\zeta\xi_{\zeta'}]$, $G_{\zeta\zeta'}^z = k_z[A^2k^2(M_1 - C_1) - ll'(M_1 + C_1)\xi_\zeta\xi_{\zeta'}]$, the momentum conservation $\delta_{\mathbf{K},\mathbf{K}'}$ and

energy conservation $\delta(E_{\zeta'} - E_{\zeta} - \hbar\omega)$ indicate that the c-p interaction has a photon absorption process without changing the electron momentum.

The longitudinal OC caused by the different transition channels in a 3D electronic system under different light polarization directions is given by Eq. (2.33):

$$\sigma_{jj}^{ll'}(\omega) = g^2 \frac{\hbar\omega}{F_0^2} \sum_{\mathbf{K},\mathbf{K'}} f_l(E_{\mathbf{K},l})[1 - f_{l'}(E_{\mathbf{K'},l'})]W_{\zeta\zeta'}^{j,c-p},$$

where $g = g_s = 2$ represents spin degeneracy. Substituting Eqs. (3.10) and (3.11) into this equation, momentum conservation $\delta_{\mathbf{K},\mathbf{K'}}$ implies that $\mathbf{K} = \mathbf{K'}$; considering the energy relaxation process, where the carrier has a broadened scattering state near the Fermi level, the energy relaxation time approximation can be applied, i.e., $\delta(x) \simeq (E_{\tau}/\pi)(x^2 + E_{\tau}^2)^{-1}$ (where $E_{\tau} = \hbar/\tau$, and τ is the energy relaxation time of the carriers), to handle $\delta(E_{\zeta'} - E_{\zeta} - \hbar\omega)$. Thus, for the case where the light polarization is along the x direction of the n-doped bluk Na_3Bi, we can obtain the in-plane OCs induced by intraband transitions as

$$\sigma_{xx}^{ll}(\omega) = \frac{\sigma_0}{(\pi\hbar\omega)^2} \frac{\omega\tau}{1+(\omega\tau)^2} \int_0^{\infty} dk_z \int_0^{\infty} dk k^3 G_{ll}^x(\mathbf{K}) f_l(E_{\mathbf{K},l})[1 - f_l(E_{\mathbf{K},l})], \tag{3.12}$$

where $l = +1$ denotes the conduction band, $f_+(E_{\mathbf{K},+}) = [e^{(E_{\mathbf{K},+} - E_F^e)/k_B T} + 1]^{-1}$, $l = -1$ denotes the valence band, $f_-(E_{\mathbf{K},-}) = [e^{(E_{\mathbf{K},-} - E_F^h)/k_B T} + 1]^{-1}$, $\sigma_0 = e^2/\hbar$ is the quantum conductance, and

$$G_{ll}^x(\mathbf{K}) = \left[\frac{A^2[k^2(M_2 - C_2) - l\xi_{\mathbf{K},l}] - (M_2 + C_2)\xi_{\mathbf{K},l}^2}{\xi_{\mathbf{K},l}^2 + A^2 k^2} \right]^2.$$

Since we only consider the photon absorption, there is $\sigma_{xx}^{+-}(\omega) \simeq 0$, and we can obtain the intra-band transition induced in-plane OC as

$$\sigma_{xx}^{-+}(\omega) = \frac{\sigma_0 A^2 \omega\tau}{(\pi\hbar\omega)^2} \int_0^{\infty} dk_z \int_0^{\infty} dk k G_{-+}^x(\mathbf{K}) \frac{f_-(E_{\mathbf{K},-})[1 - f_+(E_{\mathbf{K},+})]}{1 + \tau^2(\omega - 2\sqrt{M_{\mathbf{K}}^2 + A^2 k^2}/\hbar)^2}, \tag{3.13}$$

with

$$G_{-+}^x(\mathbf{K}) = 1 + \frac{(2M_2 k^2 + M_{\mathbf{K}})^2}{M_{\mathbf{K}}^2 + A^2 k^2}.$$

For the case where the light polarization is along the z direction, the out-of-plane OCs induced by intraband transitions read as

$$\sigma_{zz}^{ll}(\omega) = \frac{2\sigma_0}{(\pi\hbar\omega)^2} \frac{\omega\tau}{1+(\omega\tau)^2} \int_0^{\infty} dk_z \int_0^{\infty} dk k k_z^2 G_{ll}^z(\mathbf{K}) f_l(E_{\mathbf{K},l})[1 - f_l(E_{\mathbf{K},l})], \tag{3.14}$$

with

$$G_{ll}^z = \left[\frac{A^2 k^2(M_1 - C_1) - (M_1 + C_1)\xi_{\mathbf{K},l}}{\xi_{\mathbf{K},l}^2 + A^2 k^2} \right]^2.$$

For interband OC in the z direction, we also have $\sigma_{zz}^{+-}(\omega) \simeq 0$ and

$$\sigma_{zz}^{-+}(\omega) = \frac{2\sigma_0 \omega\tau}{(\pi\hbar\omega)^2} \int_0^{\infty} dk_z \int_0^{\infty} dk \frac{A^2 M_1^2 k^3 k_z^2}{M_{\mathbf{K}}^2 + A^2 k^2} \frac{f_-(E_{\mathbf{K},-})[1 - f_+(E_{\mathbf{K},+})]}{1 + \tau^2(\omega - 2\sqrt{M_{\mathbf{K}}^2 + A^2 k^2}/\hbar)^2}. \tag{3.15}$$

Using the above equations, we can calculate the OCs of the n-doped bulk Na$_3$Bi corresponding to different light polarization directions and different carrier transition channels. Additionally, the Hamiltonian for Na$_3$Bi and Cd$_3$As$_2$ is the same, differing only in band parameters. Therefore, by replacing the band parameters of Cd$_3$As$_2$ into the above equations, we can also calculate the OCs of Cd$_3$As$_2$.

3.3 Result and discussion

3.3.1 Energy band characteristics of type-I 3D DSMs

In the numerical calculations, the band parameters of Na$_3$Bi and Cd$_3$As$_2$ are listed in Tab. 3.1. The band parameters of Na$_3$Bi are obtained by fitting first-principles calculations using Eq. (1.3) [53]. ARPES experiments show that the theoretical results are in line with the experiments [55, 56], so we directly use the theoretical parameters in the following calculations. For Cd$_3$As$_2$, ARPES experiments [57–59] and transport experiments [60, 82] indicate that the experimental band structure is basically consistent with theoretical predictions [54], but there are some differences, the one being that the experimental Fermi velocity is much higher than the theoretical predictions [57, 58, 82]. Therefore, the band parameters for Cd$_3$As$_2$ used in this work are obtained by fitting the ARPES measurements [82].

To facilitate understanding of the topological properties of type-I 3D DSMs, we first introduce the Berry curvature described in Sec. 1.1.2. In WSMs, the Berry curvature can be treated as a "pseudo-magnetic field" in momentum space, and the Weyl points serve as its source or magnetic monopoles [47, 48]. In type-I DSMs, each Dirac point can be regarded as an overlap of a pair of Weyl points with opposite chirality [53, 54]. Therefore, a Berry curvature also exists between the two Dirac points (or magnetic monopoles). As shown in Fig. 3.3(a), the band inversion between the two Dirac points of a type-I DSM can be found. The Berry curvature in a topological material is determined by its band structure [221], and therefore, the determined Berry curvature shown in Fig. 3.3(b) demonstrates the unique changes of electron momentum in type-I DSMs [91]. It can be seen that the changes in electron momentum resemble the effect of a magnetic field, although no external magnetic field is present. This indicates that this phenomenon arises from the intrinsic properties, i.e., the topological natures. From the band characteristic and the Berry curvature of type-I DSMs, we can gain a deeper understanding in future studies of how their topological properties affect their physical phenomenon, such as OCs and plasmons.

Table 3.1: Na$_3$Bi band parameters are taken from Ref. [53]. Cd$_3$As$_2$ band parameters are taken from Ref. [82], the original parameters are $M_0' = -0.060$ eV, $M_1' = 96$ eVÅ^2, and $M_3 = 0.05$ eV, but in small momenta ($|k_z| \ll M_3/\sqrt{M_1'}$), the energy band structure of Cd$_3$As$_2$ yields the same as Na$_3$Bi, thus its band parameters in Eqs. (3.1) become [82]: $M_0 = M_0' + |M_3|$ and $M_1 = 0.5M_1'/|M_3|$.

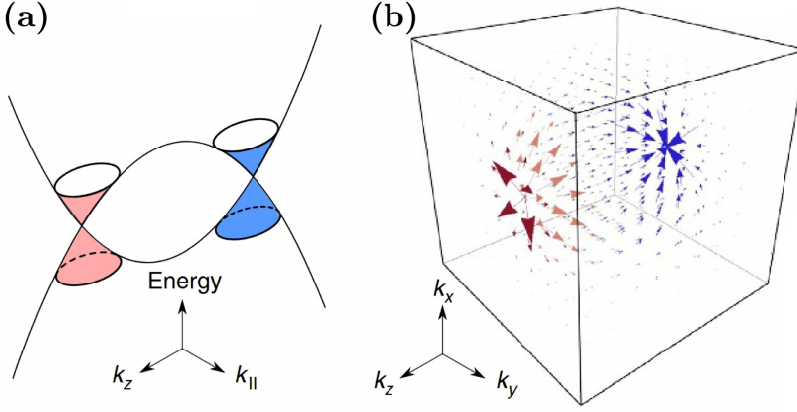| Band parameters of Na$_3$Bi and Cd$_3$As$_2$						
	C_0 (eV)	C_1 (eVÅ^2)	C_2 (eVÅ^2)	M_0 (eV)	M_1 (eVÅ^2)	M_2 (eVÅ^2)	A (eVÅ)
Na$_3$Bi	-0.06382	8.7536	-8.4008	-0.08686	-10.6424	-10.361	2.4598
Cd$_3$As$_2$	-0.219	-30	-16	-0.01	960	18	2.75

Figure 3.3: (a) Nontrivial band structure and (b) Berry curvature vector diagram of electron momentum for type-I 3D DSMs. The Dirac points correspond to magnetic monopoles in momentum space. The arrows represent the flux of Berry curvature flowing from one magnetic monopole (red) to another (blue), illustrating the nontrivial topological properties. The figure is adapted from Ref. [91].

Now, using the parameters in Tab. 3.1, we get the band structure of type-I 3D DSMs. Figs. 3.4(a) and 3.4(d), respectively, show the 3D band structures of Na_3Bi and Cd_3As_2. Figs. 3.4(b) and 3.4(c) show the $E_\mathbf{K}$-k relation at $k_z = k_c$ and the $E_\mathbf{K}$-k_z relation at $k = 0$ for Na_3Bi, while Figs. 3.4(e) and 3.4(f) present the $E_{\mathbf{K},l}$-k relation at $k_z = k_c$ and the $E_\mathbf{K}$-k_z relation at $k = 0$ for Cd_3As_2. The characteristics of the band structures of Na_3Bi and Cd_3As_2 in Fig. 3.4 are summarized below.

(i) Both Na_3Bi and Cd_3As_2 have a pair of symmetric Dirac points located at the top of the conduction band and the bottom of the valence band, with coordinates at $k = 0$ and $k_z = \pm k_c$, corresponding to an energy of $E_0 = C_0 + C_1 M_0 / M_1$ ($Na_3Bi \sim 7.62$ meV, $Cd_3As_2 \sim -218.68$ meV).

(ii) The band structure of type-I DSMs is isotropic in the k_x-k_y plane but anisotropic in the k-k_z plane. The electron energy exhibits a linear dispersion near the two Dirac points, but it transitions to a nonlinear and asymmetric dispersion away from the Dirac points.

(iii) As shown in Figs. 3.4(c) and 3.4(f), both systems exhibit an arch-like band inversion in the conduction and valence bands along the k_z direction (from $-k_c$ to k_c). Fig. 3.3 indicates that the Berry curvature in this region significantly affects the electron momentum. Unlike traditional 3D electronic materials, where the minimum conduction band is at $k = 0$ and $k_z = 0$, type-I DSMs feature a maximum conduction band inversion and a minimum valence band inversion at $k = 0$ and $k_z = 0$. The top of the conduction band inversion has an energy $E_1 = C_0 + |M_0|$ ($Na_3Bi \sim 23$ meV, $Cd_3As_2 \sim -209$ meV).

(iv) Due to the influence of the Berry curvature, the density of states $D(E)$ in the conduction band of Na_3Bi and Cd_3As_2 will exhibit unique variations with the electron energy E. Taking the conduction band inversion peak E_1 as a critical point, $D(E)$ will be significantly affected by the Berry curvature when $E < E_1$, leading to a different variation in the $D(E)$-E relation for $E < E_1$ compared to that for $E > E_1$. Furthermore, the effect of the Berry curvature in Na_3Bi is stronger than that in Cd_3As_2, resulting in a more pronounced variation in the $D(E)$-E relationship for Na_3Bi.
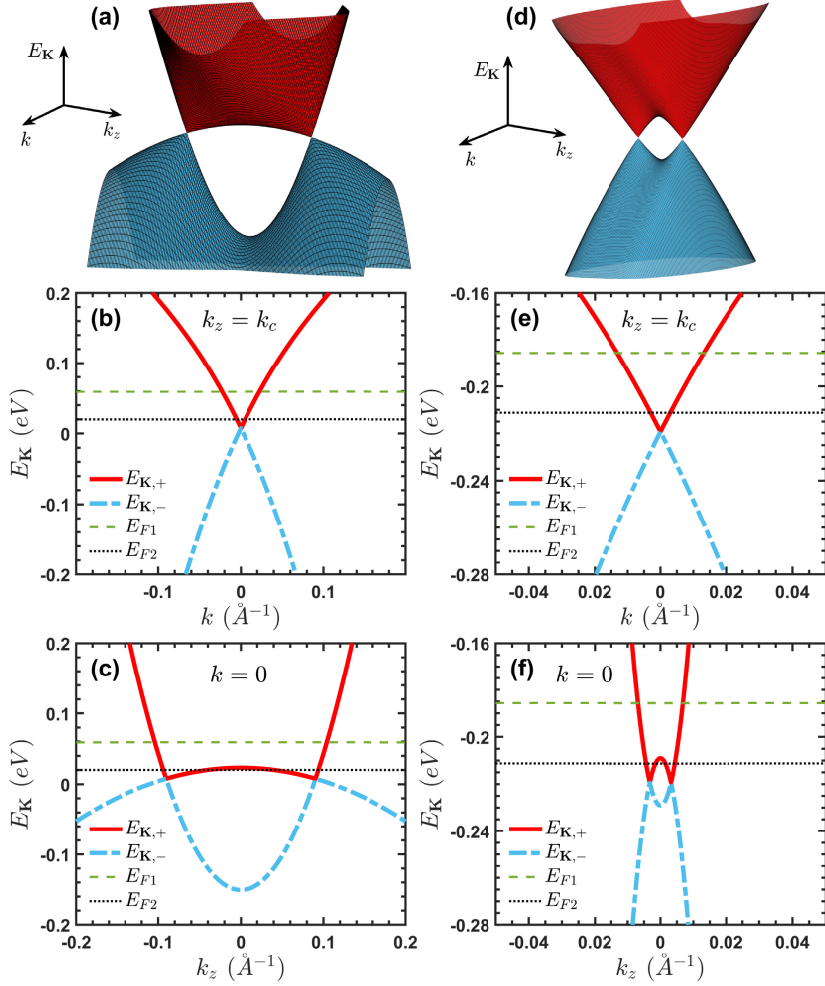
Figure 3.4: (a) Energy dispersion $E_{\mathbf{K}}$ of Na$_3$Bi as a function of k and k_z, as given by Eq. (3.2). (b) $E_{\mathbf{K}}$ as a function of k at $k_z = k_c$. The Dirac point is at $k = 0$ with energy $E_0 = 7.6$ meV. (c) $E_{\mathbf{K}}$ as a function of k_z at $k = 0$. There are two Dirac points at $k_z = \pm k_c$. The top of the band inversion in the conduction band is $E_1 \simeq 23$ meV, its bottom in the valence band at $E_2 \simeq -151$ meV, and they are both located at $k = 0$ and $k_z = 0$. (d), (e), (f): *idem.* as in (a), (b), and (c), respectively, for Cd$_3$As$_2$. The energy of the Dirac point is at $E_0 \simeq -218.68$ meV. The top of the band inversion in the conduction band is $E_1 \simeq -209$ meV and its bottom in the valence band at $E_2 \simeq -229$ meV. The red curve shows the conduction band and the blue-dash-dotted curve is the valance band. The green-dashed and black-dotted lines show the Fermi energy E_F for high and low electron density, respectively.

(v) Equation (3.6) defines the Fermi level of electrons E_F^e of type-I DSMs. For the n-doped Na$_3$Bi, the Fermi wave vector along the k_z axis, k_{Fz}, is much larger than the Fermi wave vector along the k direction, k_F, with k_{Fz} being approximately 10 to 20 times larger than k_F near the Dirac point, as indicated by the black-dashed lines in Figs. 3.4(b) and 3.4(c). However, in n-doped Cd$_3$As$_2$, k_{Fz} is only about two times larger than k_F, as shown by the black-dashed lines in Figs. 3.4(e) and 3.4(f). This indicates that the electronic excitations along the k and k_z directions

in Na_3Bi will be significantly different, while the differences in Cd_3As_2 are relatively small. Thus, the anisotropy in Na_3Bi will be much more pronounced than that in Cd_3As_2. This conclusion has also been reported in previous studies [53–58].

(vi) It is worth mentioning that there are differences in the band structures of Na_3Bi and Cd_3As_2, but the Fermi velocity of Na_3Bi, $v_F = 2A$ ($\simeq 7.473 \times 10^5$ m/s) [108], is very close to that of Cd_3As_2 ($\simeq 7.6 \times 10^5$ m/s). This is because the experimental effective mass of electrons in Cd_3As_2 ($\sim 0.02 - 0.042\ m_e$) [108] is much smaller than that of Na_3Bi ($\sim 0.11 - 0.24\ m_e$) [86]. Therefore, the mass term $M_0 - M_1 k_z^2$ in Eq. (3.1) results in very similar Fermi velocities for these two materials.

After a discussion of the band structure of type-I DSMs, we take Na_3Bi as an example to calculate the density of states (DOS) and Fermi levels using Eqs. (3.5)-(3.7), and further analyze the characteristics of the energy band. Fig. 3.5(a) shows the relationship between the density of states $D(E)$ and the energy E for Na_3Bi, and for comparison, it also shows the DOS for a three-dimensional electron gas (3DEG) and monolayer graphene. It is well known that the DOS for a 3DEG is given by $D(E)_{3D} = \sqrt{2m^{*3}E}/(\pi\hbar^2) \propto E^{1/2}$. The significant difference between $D(E)$ of Na_3Bi and 3DEG indicates that a type-I DSM possesses physical properties that are distinctly different from those of 3DEG. From Figs. 3.3 and 3.4, we find that in the region of $E < E_1$, $D(E)$ for Na_3Bi is nearly zero when E is very small and then increases rapidly with increasing E until $E = E_1$. In the region where $E > E_1$, $D(E) \propto E^2$ can be found for Na_3Bi. From Fig. 3.4(c), we can see that the electronic velocity $\partial E_{\mathbf{K}}/\partial k_z$ of the type-I DSMs has a van Hove singularity at $k = k_z = 0$, which corresponds to E_1. The unusual DOS for Na_3Bi arises from its nontrivial topological properties, such as the Berry curvature. For $E < E_1$, the electron momentum is strongly affected by the Berry curvature, leading to unique changes in its DOS. Since the band structure of Na_3Bi is essentially consistent with that of Cd_3As_2, the DOS shown in Fig. 3.5(a) will also exist in Cd_3As_2, but the anisotropy of Cd_3As_2 is smaller than that of Na_3Bi, so the variation in the DOS for Cd_3As_2 will also be less than that of Na_3Bi.

Figures 3.5(b) and 3.5(c) show the Fermi level of electrons and hole as functions of the carrier density of Na_3Bi at different temperatures. Combining Figs. 3.5 and 3.4, we first note that at
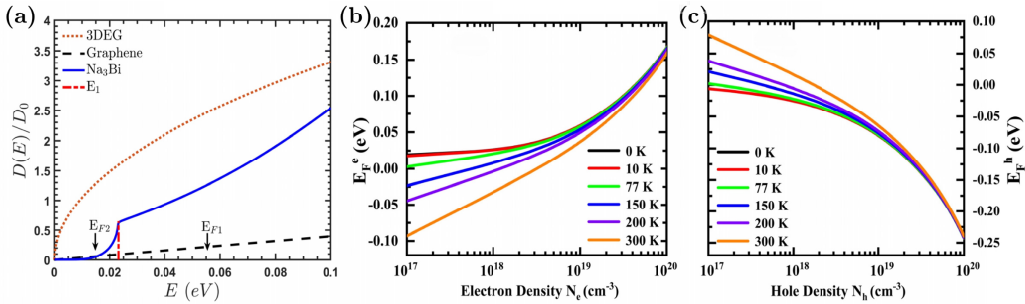
Figure 3.5: (a) The density of states $D(E)$ as a function of electron energy E for Na_3Bi is shown as a blue curve, with $D_0 = C_0^2/A^3$. The red dashed line marks the conduction band inversion vertex energy $E_1 \simeq 23.2$ meV. For comparison, the orange doted curve represents the density of states for a 3DEG, calculated using the effective mass of Na_3Bi ($m^* \simeq 0.11 m_e$) and $D_0 = m^{*3/2}\sqrt{2|C_0|}/(\pi\hbar^3)$; the black dashed curve indicates the density of states for monolayer graphene, given by $D_0 = C_0^2/(\hbar v_F)^3$. The two arrows correspond to E_{F1} (green dashed line) and E_{F2} (black dashed line) in Figs. 3.4(b) and 3.4(c), respectively.

$T \to 0$, both the Fermi level of electrons and holes in Na_3Bi are located at the Dirac point under zero carrier densities, that is, $E_F^e = E_F^h = E_0 \simeq 7.6$ meV when $N_e = N_h = 0$. Therefore, the Fermi level of Na_3Bi will start at E_0. In addition, E_F^e of Na_3Bi increases with increasing N_e but decreases with increasing T. In contrast, the behavior of E_F^h with respect to changes in N_h and T is opposite to that of E_F^e, a result similar to that of 3DEG. From the DOS of Na_3Bi with Fermi energy, we can find that at low temperatures, when N_e is less than $\sim 4 \times 10^{17}$ cm^{-3}, $E_F^e < E_1 - E_0$, which places E_F^e within the conduction band inversion. This indicates that the physical properties of Na_3Bi with lower electron densities will be strongly influenced by the Berry curvature, which was also reported in our previous transport study of Na_3Bi [87]. The similar band structure of Na_3Bi and Cd_3As_2 will endow Cd_3As_2 with similar properties as discussed above.

3.3.2 Anisotropic optical conductivities of type-I 3D DSMs

In this subsection, considering the band structure similarity between Na_3Bi and Cd_3As_2 as well as the more pronounced Berry curvature of Na_3Bi, we choose Na_3Bi as a representative to discuss the optical conductivities of type-I 3D DSMs and the related properties.

Type-I 3D DSMs produced by different growth techniques or with different sample qualities will have different carrier relaxation times [85–87], but the energy relaxation time under an external light field falls within approximately $1 - 10$ ps [136, 139, 202]. Therefore, we will study the effect of different energy relaxation times on the OCs of Na_3Bi. As mentioned in the previous subsection, when the electronic Fermi level of Na_3Bi is lower than the conduction band inversion, its electronic momentum and DOS will be significantly affected by the Berry curvature. Since temperature and carrier density will affect Fermi levels, we will also investigate the OCs of Na_3Bi at different temperatures and carrier densities.

Before performing numerical calculations, we first provide a schematic diagram of the carrier-photon (c-p) interactions based on the band structure of the n-doped bulk Na_3Bi, as shown in Fig. 3.6. From the figure, we can see that in the absence of an light field ($F_0 = 0$), all states below the electron Fermi level E_F^e in the conduction band are fully occupied. In the presence of a light field ($F_0 \neq 0$), electrons in the valence band are excited into the conduction band through photon absorption, while the photoexcited electrons fill the conduction band, increasing E_F^e, and holes are generated in the valence band (with the corresponding hole density N_h and hole Fermi level E_F^h). Similarly to other electronic systems, photon absorption in type-I DSMs can also be achieved through electron transitions from lower-occupied to higher-unoccupied states. Therefore, OCs due to intraband transitions occur not only in the conduction band (σ_{++}) but also in the valence band (σ_{--}). Intraband transitions are a direct result of the broadening of electronic states near the Fermi level and show themselves as energy relaxation processes in c-p interactions. Unlike traditional semiconductors with band gaps, because of the gapless nature of type-I DSMs, electrons in the valence band can more easily transition to the conduction band. Thus, type-I DSMs exhibit a strong interband OC due to interband transition channels (σ_{-+}). This strong interband OC is also present in other Dirac systems, such as graphene shown in Fig. 3.1 [215, 216, 219, 220].

In addition, due to the Moss-Burstein effect [222] or the Pauli blockade effect [223], which occurs when electrons transition from lower-occupied to higher-unoccupied states, the photon energy $\hbar\omega$ required for intraband transitions is relatively small, whereas interband transitions need a larger photon energy. In the cases of lower photon energy (in the long-wavelength region), σ_{++} and σ_{--} will decrease as the photon energy increases. When the photon energy continues to increase, the intraband transitions become smaller until it approaches zero, while the interband
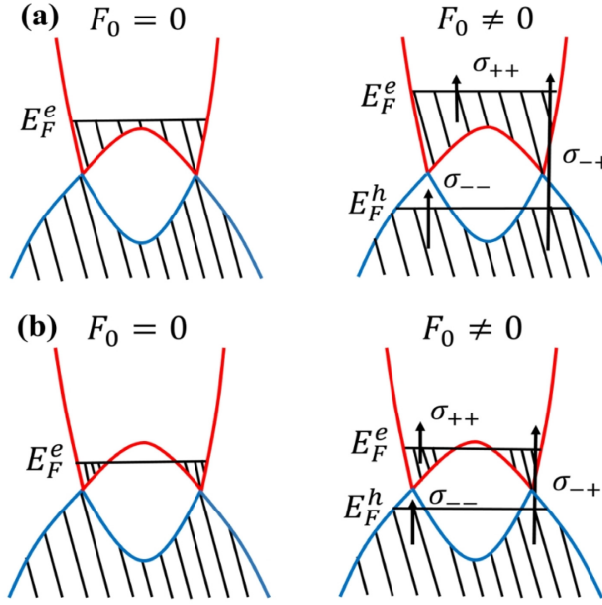
Figure 3.6: Schematic diagram of the carrier-photon scattering channels for an *n*-doped bulk Na$_3$Bi. $F_0 = 0$ and $F_0 \neq 0$ represent the cases without and with an external light field, respectively. E_F^e and E_F^h are the Fermi levels of electrons and holes, respectively. σ_{++} and σ_{--} represent the OCs due to electron transitions within the conduction and valence bands, while σ_{-+} represents the interband OC caused by electron transitions from the valence band to the conduction band by absorbing photon energy. (a), (b) Show cases where E_F^e is higher and lower than the conduction band inversion, respectively. In the case of (b), the Berry curvature significantly affects the momentum of electrons, thereby affects the occupied sates and low-energy excitations near the Dirac points. E_F^h is within the Berry curvature region in both cases.

transition increases rapidly, which is in line with the results shown in Fig. 3.2(c). At higher photon energies, the OC is mainly contributed from the interband transitions σ_{-+}. Therefore, our theoretical model can explain the phenomenon observed in type-I 3D DSMs, where there is an optical absorption window from mid-infrared to terahertz range, as shown in Fig. 3.2(b) [133, 134]. The reason is that the photon energy required for intraband and interband transitions differs in the long-wavelength or short-wavelength regions. In addition, Figs. 3.6(a) and 3.6(b) show the cases where E_F^e is located outside and within the band inversion, respectively. It can be seen that when E_F^e is located within the band inversion in Fig. 3.6(b), the occupied states in the conduction band is significantly reduced, leading to nontrivial changes in DOS of type-I DSMs as shown in Fig. 3.5(a). This is because the electron momentum is strongly affected by the Berry curvature where E_F^e is inside the band inversion region.

In Fig. 3.7, we show the in-plane OC $\sigma_{xx}(\omega)$ induced by light polarization along the *x* direction and the out-of-plane OC $\sigma_{zz}(\omega)$ induced by light polarization along the *z* direction of a bulk Na$_3$Bi, as well as the contributions of different electron transition channels to $\sigma_{xx}(\omega)$ and $\sigma_{zz}(\omega)$. From the figure, we notice the following features.

(i) In the short-wavelength region, $\sigma_{xx}(\omega)$ and $\sigma_{zz}(\omega)$ of Na$_3$Bi are mainly contributed by interband transitions, while in the long-wavelength region, intraband transitions dominate $\sigma_{xx}(\omega)$
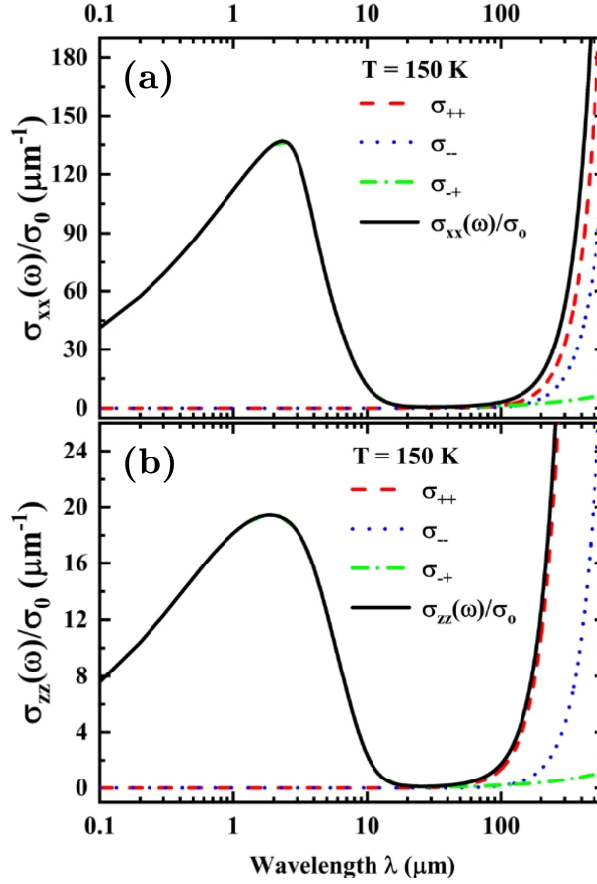
Figure 3.7: (a), (b) Contributions of different electronic transition channels to the in-plane OC $\sigma_{xx}(\omega)$ and the out-of-plane OC $\sigma_{zz}(\omega)$, respectively. The calculations are performed under the conditions of temperature $T = 150$ K, energy relaxation time $\tau = 6.71$ ps, electron density $N_e = 2 \times 10^{19}$ cm^{-3}, and hole density $N_h = 2 \times 10^{18}$ cm^{-3}. The quantum conductance is $\sigma_0 = e^2/\hbar \simeq 2.4341 \times 10^{-4}$ Ω^{-1}. σ_{++}, σ_{--}, and σ_{-+} are represented by red dashed curves, blue dotted curves, and green dotted-dashed curves, respectively.

and $\sigma_{zz}(\omega)$.

(ii) When $\lambda < 2$ μm, both $\sigma_{xx}(\omega)$ and $\sigma_{zz}(\omega)$ increase with increasing wavelength, leading to observable absorption peaks. This is in contrast to the universal conductance in graphene, $\sigma(\omega) = e^2/(4\hbar)$, as shown in Fig. 3.1 [215–220].

(iii) In the short-wavelength region, $\sigma_{xx}(\omega)$ is approximately five times larger than $\sigma_{zz}(\omega)$, indicating that type-I DSMs exhibit anisotropic OCs and a stronger in-plane OC. The absorption peak of $\sigma_{xx}(\omega)$ is also sharper than that of $\sigma_{zz}(\omega)$. From Figs. 3.4, 3.5, and 3.6, we find that this is because the $E_{\mathbf{K},l}$ of Na$_3$Bi has different dispersion relations along the k and k_z directions. The Berry curvature mainly affects the electron momentum in the k_z direction, resulting in fewer electron transition channels in the k_z direction, which in turn makes $\sigma_{xx}(\omega) > \sigma_{zz}(\omega)$.

(iv) Since optical absorption is proportional to OC, both $\sigma_{xx}(\omega)$ and $\sigma_{zz}(\omega)$ of Na$_3$Bi have optical absorption windows in the intermediate wavelength range (~ 2 μm $< \lambda < \sim 300$ μm in the x direction, and ~ 2 μm $< \lambda < \sim 200$ μm in the z direction). From Fig. 3.6, it can be seen that this is due to the Pauli principle, which causes different requirements of photon energy for intraband and interband transitions. Similar optical absorption windows can be observed in graphene [215–218], as shown in Fig. 3.1. Experimentally, the optical absorption window of $\sigma_{xx}(\omega)$ observed in type-I 3D DSM Cd$_3$As$_2$ is within the frequency range of approximately 200-10000 cm^{-1} (corresponding to a wavelength of about 1-50 μm) [133, 134], as shown in Fig. 3.2(b), which is basically consistent with our theoretical calculations. The minor differences in the position of the windows between Cd$_3$As$_2$ and Na$_3$Bi mainly come from their different band parameters.

(v) Figure 3.2(b) shows that, in the frequency range of about 1500-10000 cm^{-1} (or a wavelength of about 1-8 μm), $\sigma_{xx}(\omega)$ of Cd$_3$As2 increases linearly with increasing photon energy [133, 134], which aligns well with our theoretical calculations for $\sigma_{xx}(\omega)$ of Na$_3$Bi. In Na$_3$Bi, the short-wavelength boundary of the window is located in the range of about 2-10 μm and increases linearly with increasing photon energy. In Fig. 3.1, we can see that the position of the absorption window in graphene is at a lower photon energy range, which is significantly different from that of type-I 3D DSMs.

(vi) In the long-wavelength range ($\lambda > 100$ μm), both $\sigma_{xx}(\omega)$ and $\sigma_{zz}(\omega)$ are mainly contributed by intraband transitions and both increase rapidly with increasing wavelength. This is similar to the Drude model of free electrons, where OC increases rapidly with increasing wavelength [208].

In this study, we introduce the electron energy relaxation time τ as an input parameter in the calculations of the OCs of Na$_3$Bi to explore the effect of the broadening of the scattering state on the OCs. Under fixed conditions, the effects of τ on $\sigma_{xx}(\omega)$ and $\sigma_{zz}(\omega)$ are presented in Fig. 3.8. A longer τ corresponds to a smaller scattering state broadening, which in turn corresponds to a sample with a higher carrier mobility. From the figure, we can see that in the short-wavelength range, both $\sigma_{xx}(\omega)$ and $\sigma_{zz}(\omega)$ are not affected by τ. This is because the higher photon energy allows for interband transitions, while the broadening of scattering states near the Fermi surface is covered by interband scattering. Consequently, the interband OCs are not affected by τ. However, in the long-wavelength range, where the OCs are mainly contributed by intraband transitions, the influence of τ on the OCs becomes obviously. Even small changes in τ lead to noticeable variations in the intraband OCs, and increasing τ will cause a redshift in both $\sigma_{xx}(\omega)$ and $\sigma_{zz}(\omega)$ in the long-wavelength range. Therefore, in type-I 3D DSMs with longer energy relaxation times, or in other words, higher electron mobilities, wider optical absorption windows can be observed.

In Fig. 3.9, we show $\sigma_{xx}(\omega)$ and $\sigma_{zz}(\omega)$ of Na$_3$Bi as a function of the light wavelength λ at different temperatures and fixed conditions. As seen in the figure, when the photon energy is very high ($\lambda < 2$ μm), both $\sigma_{xx}(\omega)$ and $\sigma_{zz}(\omega)$ are not affected by temperatures. At higher photon energies (2 μm $< \lambda < 10$ μm), $\sigma_{xx}(\omega)$ and $\sigma_{zz}(\omega)$ show only a small temperature dependence. As shown in Fig. 3.6, when the photon energy $\hbar\omega$ is larger than $2E_F^e$, the interband transitions of electrons will occur. Figure 3.5 shows that E_F^e will change with temperature, however, when $2E_F^e \ll \hbar\omega$, the changes in the Fermi level caused by temperature fluctuations are negligible for interband transitions. Therefore, in the short wavelength range, $\sigma_{xx}(\omega)$ and $\sigma_{zz}(\omega)$ are independent of temperature, which is also observed in the experiments of Cd$_3$As$_2$ [133]. In the intermediate wavelength range, the optical absorption windows in $\sigma_{xx}(\omega)$ and $\sigma_{zz}(\omega)$ narrow with increasing temperature. From Figs. 3.4, 3.5, and 3.6, we can find that as the temperature increases,
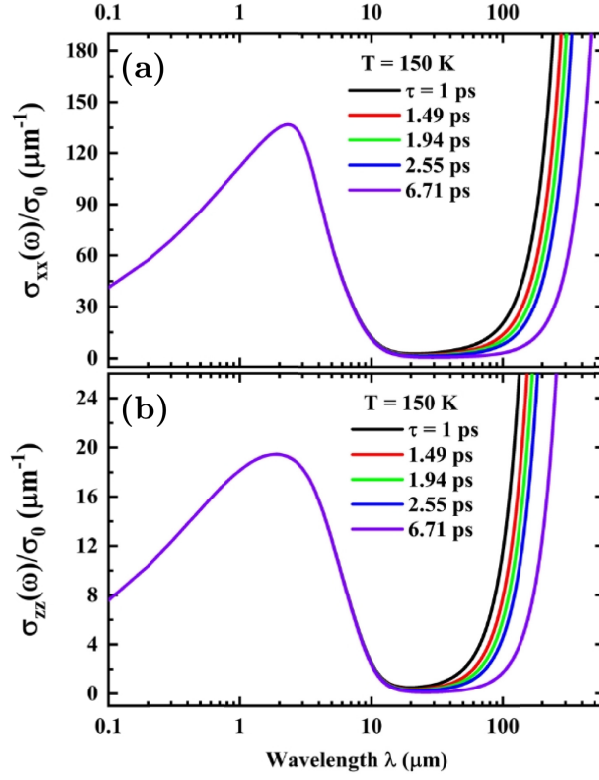
Figure 3.8: (a), (b) Show the effects of energy relaxation time on $\sigma_{xx}(\omega)$ and $\sigma_{zz}(\omega)$, respectively. The calculations are performed under the conditions of temperature $T = 150$ K, electron density $N_e = 2 \times 10^{19}$ cm^{-3}, and hole density $N_h = 2 \times 10^{18}$ cm^{-3}. The OCs under different energy relaxation times are represented by curves of different colors in the figure.

$E_F^e - E_F^h$ decreases due to the Pauli blocking effect [222, 223]. Thus, the photon energy required for interband transitions also decreases with increasing temperature, leading to small variations in $\sigma_{xx}(\omega)$ and $\sigma_{zz}(\omega)$ in the range of about $2 - 10$ μm. This explains the experimental results of Cd$_3$As$_2$ shown in Fig. 3.2 [133]. Furthermore, when E_F^e decreases while E_F^h increases, electrons require larger photon energies to overcome the thermal broadening of the electronic state distribution near the Fermi surface. Therefore, in the long wavelength range, intraband transitions will require higher photon energy at elevated temperatures, resulting in a blueshift of the OCs in the long wavelength range. This phenomenon has been reported in the reflection experiments of Na$_3$Bi [202].

Next, we further discuss the effect of different carrier densities on the OCs of Na$_3$Bi. Using fixed temperature, hole density, and energy relaxation time, the $\sigma_{xx}(\omega)$ and $\sigma_{zz}(\omega)$ as a function of the light wavelength λ at different electron densities are shown in Fig. 3.10. First, we can see that $\sigma_{xx}(\omega)$ and $\sigma_{zz}(\omega)$ in the short-wavelength region do not vary with electron densities. The reason is that when $\hbar\omega \gg E_F^e - E_F^h$, the changes in the Fermi level do not affect the interband transitions. This is similar to the optical conductance of monolayer graphene shown in Fig. 3.1 [215, 216]. In the intermediate wavelength region, the optical absorption window of both $\sigma_{xx}(\omega)$ and $\sigma_{zz}(\omega)$ undergoes a systematic blueshift with increasing electron density because increasing
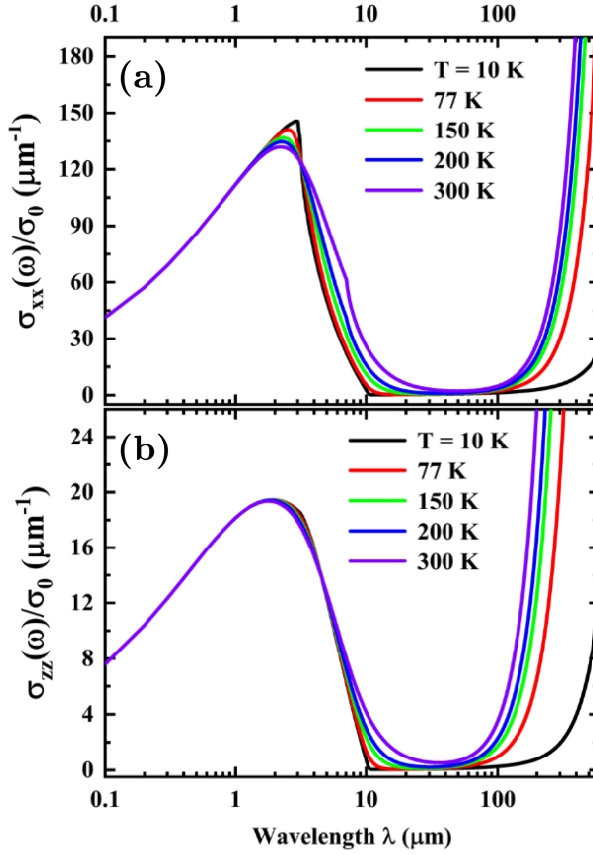
Figure 3.9: (a), (b) show the $\sigma_{xx}(\omega)$ and $\sigma_{zz}(\omega)$ as a function of the light wavelength λ at different temperatures, respectively. The fixed conditions are an electron density of $N_e = 2 \times 10^{19}$ cm^{-3}, a hole density of $N_h = 2 \times 10^{18}$ cm^{-3}, and an energy relaxation time of $\tau = 6.71$ ps. The OCs of Na$_3$Bi at different temperatures correspond to curves of different colors in the figure.

N_e increases E_F^e, requiring both intraband and interband electrons to absorb higher photon energies. Additionally, it is found that the blueshift of the absorption peak in the x direction becomes more pronounced with increasing electron density. We attribute this to the influence of the Berry curvature. As shown in Figs. 3.4 and 3.6, due to the presence of the Berry curvature, the DOS for electrons in the k_z direction is much smaller than in the k direction, leading to smaller changes in the electronic states in the k_z direction as the Fermi level changes. Therefore, the variations of $\sigma_{xx}(\omega)$ with varying electron densities are much stronger than in $\sigma_{zz}(\omega)$. In the long-wavelength region, when the photon energy is lower, an increasing N_e causes a blueshift in both $\sigma_{zz}(\omega)$ and $\sigma_{xx}(\omega)$, but the blueshift in $\sigma_{xx}(\omega)$ is weaker.

To further study the effect of the Berry curvature on the OCs of Na$_3$Bi, we calculate $\sigma_{xx}(\omega)$ and $\sigma_{zz}(\omega)$ for the lower N_e and N_h, shown as the orange curves in Fig. 3.10. At this point, N_e is sufficiently low and E_F^e is located in the band inversion region, where the electron momentum is strongly influenced by the Berry curvature. It can be seen that as N_e decreases, the absorption peak of $\sigma_{zz}(\omega)$ changes slightly, whereas $\sigma_{xx}(\omega)$ changes significantly. The presence of Berry curvature makes $\sigma_{zz}(\omega)$ of Na$_3$Bi less affected by E_F^e, giving rise to a unique OC in the z direction
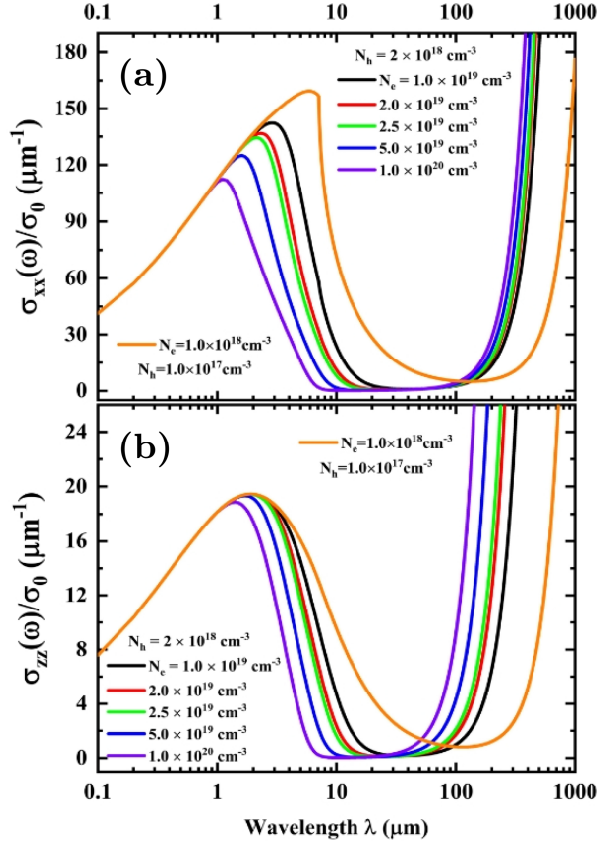
Figure 3.10: (a), (b) Show the $\sigma_{xx}(\omega)$ and $\sigma_{zz}(\omega)$ as a function of the light wavelength λ at different electron densities, respectively, where a fixed temperature $T = 150$ K, a hole density $N_h = 2 \times 10^{18}$ cm^{-3}, and an energy relaxation time $\tau = 6.71$ ps are applied. The OCs of Na$_3$Bi at different electron densities is represented by the differently colored curves in the figure. Additionally, the orange curve shows $\sigma_{xx}(\omega)$ and $\sigma_{zz}(\omega)$ for the case of low electron density $N_e = 1 \times 10^{18}$ cm^{-3} and low hole density $N_h = 1 \times 10^{17}$ cm^{-3}.

compared to other 3D electronic materials. We also find that the influence of the Berry curvature on the OCs is mainly concentrated in the interband transitions. Experimentally, methods for tuning the optical absorption window using gate-voltage in graphene have already been realized, as shown in Fig. 3.1 [216, 218], and in type-I DSMs, the gate-tunable Fermi level has also been reported in transport experiments [90, 115]. Based on our theoretical results, we propose that the OCs of type-I 3D DSMs can be tuned in all directions by changing the Fermi level, with the out-of-plane OC exhibiting unique phenomena. This provides a theoretical foundation for the application of type-I 3D DSMs in optoelectronic devices.

The results from Figs. 3.7-3.10 show that in the short-wavelength range, the $\sigma_{xx}(\omega)$ and $\sigma_{zz}(\omega)$ of type-I 3D DSMs, which are dominated by interband transitions, are not affected by temperature, electron density, and energy relaxation time. However, in contrast to the results for graphene shown in Fig. 3.1, $\sigma_{xx}(\omega)$ and $\sigma_{zz}(\omega)$ in the high photon energy range vary with wavelength λ and exhibit absorption peaks. The unique band structure of type-I 3D DSMs results in anisotropic

OCs throughout the wavelength range, with $\sigma_{xx}(\omega)$ generally larger than $\sigma_{zz}(\omega)$. The presence of Berry curvature leads to an overall smaller $\sigma_{zz}(\omega)$, indicating that stronger light absorption and optical response can be realized within the x-y plane of these materials. Finally, in type-I 3D DSMs, the electron density can be tuned by doping or applying an external gate-voltage; thus the tunable OCs of type-I 3D DSMs can be achieved.

3.4   Conclusions of this chapter

In this chapter, we first analyze the energy band characteristics of type-I 3D DSMs, with Na_3Bi as the main example. The electron density of states and Fermi levels in type-I 3D DSMs are evaluated. Then, using the energy balance equation method, we calculate the anisotropic optical conductivities (OCs) of an n-doped bulk Na_3Bi. After considering different energy relaxation times, temperatures, and electron densities, we also discussed the influence of Berry curvature and sample conditions on the OCs of Na_3Bi. The main conclusions of this chapter are as follows.

Type-I 3D DSMs possess an anisotropic energy dispersion and a pair of symmetric Dirac points. Along the k_z direction, the band has an inverted structure, which is related to the Berry curvature. Based on Na_3Bi, it is found that when the electron energy is below the vertex of the band inversion, the electron momentum is significantly influenced by the Berry curvature, leading to nontrivial density of states. Through the relationship between the Fermi level and electron density, it can be seen that at low electron densities, the Fermi level of Na_3Bi lies within the band inversion, causing electronic excitations to be strongly affected by the Berry curvature. Therefore, Na_3Bi at low electron densities will exhibit nontrivial excitations due to the Berry curvature.

The anisotropic OCs of an n-doped bulk Na_3Bi mainly arises from the band inversion and the Berry curvature in its band structure. At high photon energies ($\lambda < 2\ \mu$m), the $\sigma_{xx}(\omega)$ and $\sigma_{zz}(\omega)$ induced by different light polarization directions originate mainly from the interband transitions. In this wavelength range, both $\sigma_{xx}(\omega)$ and $\sigma_{zz}(\omega)$ vary with light wavelength λ but are not affected by sample conditions. In the intermediate wavelength range ($2\ \mu$m $< \lambda < 200\ \mu$m), both $\sigma_{xx}(\omega)$ and $\sigma_{zz}(\omega)$ exhibit absorption windows, arising from the different energy requirements for intraband and interband transitions. The Berry curvature mainly affects electronic states in the k_z direction, which results in $\sigma_{zz}(\omega)$ being smaller than $\sigma_{xx}(\omega)$, and changes in $\sigma_{zz}(\omega)$ with different sample conditions being smaller than those in $\sigma_{xx}(\omega)$. This is a unique feature of the OCs of type-I 3D DSMs, indicating that stronger optical absorption can be observed within the x-y plane of a bulk type-I 3D DSM. In the long-wavelength range ($\lambda > 100\ \mu$m), the photon energy is lower, and thus the OCs are mainly contributed by intraband transitions. At this point, both $\sigma_{xx}(\omega)$ and $\sigma_{zz}(\omega)$ increase rapidly with increasing λ, which is similar to the Durde optical conductivities. The width and position of the optical absorption windows of Na_3Bi are significantly influenced by the energy relaxation time, the temperature, and the electron density. Our theoretical study explains the experimental results, and in combination with experiments, we propose that the OCs of type-I 3D DSMs are tunable by changing the temperature and electron density.

These conclusions help to deepen our understanding of the topological band structure and OCs of type-I 3D DSMs. Our in-depth study of these materials also provides theoretical support for further exploration of their optoelectronic properties and applications in optoelectronic devices.

Plasmon modes of type-I 3D DSMs

The plasmon is the quantum of collective excitations of electrons, which can be regarded as the quasiparticle of plasma oscillations. By analyzing the plasmon dispersion relation between the frequency $\omega(q)$ and the momentum change q during electron-electron interactions, the properties of collective excitations in an electronic system can be studied. Theoretically, the plasmon dispersion and the corresponding energy loss spectrum of a material can be calculated using the RPA dielectric function; experimentally, as shown in Fig. 1.12(b), high-resolution energy loss spectroscopy can provide relevant information on the plasmon modes of the material [172].

After the discovery of Dirac electronic systems, research in the field of plasmonics related to these systems flourishes. Studies on graphene plasmons have revealed the plasmon dispersion in 2D Dirac systems. As shown in Fig. 4.1(b), the plasmon in a 2D Dirac system exhibits a dispersion relation of $\omega(q) \propto \sqrt{q}$ in the small q range. At large q, its collective excitations are damped by single-particle excitations [204]. Figures 4.1(c) and 4.1(d) respectively show the plasmon modes of a simple 3D Dirac cone (with the band structure $E_{\mathbf{K},l} = l\hbar v_F \mathbf{K}$, where l is the band index, $\mathbf{K}$ is the 3D wave vector, and v_F is the Fermi velocity) and a three-dimensional electron gas (3DEG) system [with the band structure $E_{\mathbf{K}} = (\hbar K)^2/(2m^*)$, where m^* is the effective mass of the electron] [204]. It can be seen that both the simple 3D Dirac cone and the 3DEG have an initial plasma frequency at $q \to 0$, with a dispersion relation of $\omega(q) \propto q^2$ as q increases. Moreover, their plasmon dispersions are isotropic [204, 208]. Most of the existing studies on plasmons of type-I 3D DSMs are based on a simple Dirac cone [203, 204], and some have only considered the linear term in Eq. (1.3) [202]. The theoretical results from these studies are similar to those shown in Fig. 4.1(c) and 4.1(d).

However, in the previous chapter, Fig. 3.4 specified the band characteristics of type-I 3D DSMs. Their electronic states possess topological structures, the electron momentum space exhibits the Berry curvature, and there is an inversion structure in the band. Transport experiments further demonstrate that electron excitations in type-I 3D DSMs cannot be explained by simple models [86, 87], such as the isotropic 3D Dirac cone or Hamiltonian considering only linear terms. Therefore, the theoretical results from previous studies on the plasmon properties of type-I 3D DSMs are incomplete. First, from the band structure, the plasmons in type-I 3D DSMs should have anisotropy. Second, the presence of Berry curvature affects the electron momentum, implying that Berry curvature should have a significant effect on plasmons as well. Finally, varying the electron density can position the Fermi level either inside or outside the band inversion, meaning that the plasmon modes should differ between high and low electron densities.

Consequently, this chapter will make a comprehensive study of the plasmon modes in type-I
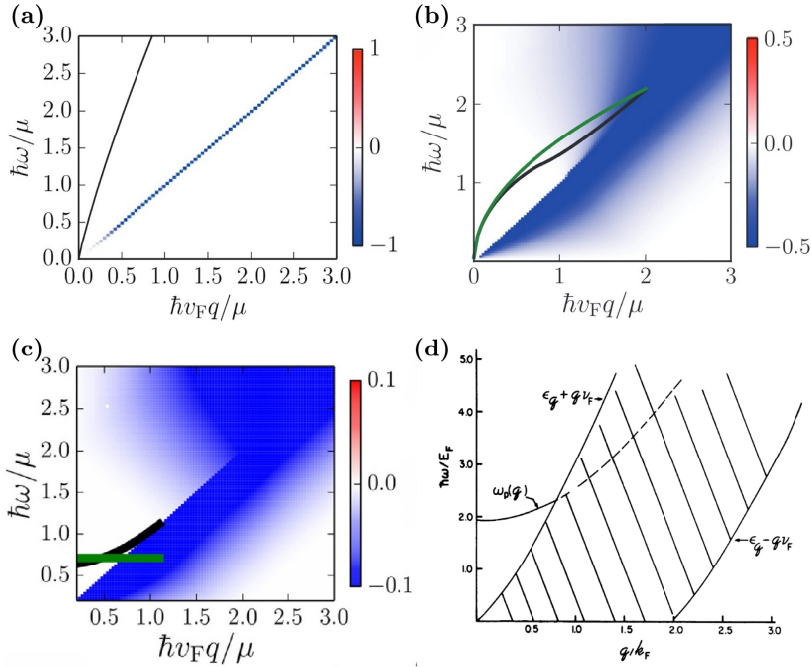
Figure 4.1: (a) Plasmon dispersion relation (black curve) and the electron-hole (*e-h*) excitation region (blue shaded area) of a one-dimensional Dirac system. For 1D systems, due to chirality conservation, the *e-h* excitation region is just a straight line. (b) Plasmon dispersion relation of a 2D Dirac system, graphene, where the green and black curves represent the long-wavelength limit and the full plasmon curve, respectively. The blue shaded area indicates the *e-h* excitation region. (c) Plasmon dispersion relation of an isotropic 3D Dirac cone. The green curve represents the long-wavelength limit of the plasmon dispersion, while the black curve is the numerically calculated full plasmon dispersion. The blue shaded area represents the *e-h* excitation region. (d) Plasmon mode in a 3DEG in metals is denoted by $\omega_p(q)$, with the shaded region representing the *e-h* excitations. In the figure, μ and E_F refer to the electronic chemical potential or Fermi energy, and $\mu/(\hbar v_F)$ and k_F refer to the Fermi wave vector. Adapted from Refs. [204, 208].

3D DSMs based on the effective Hamiltonian and using the RPA dielectric function. Considering scenarios where the electron Fermi level is either above or below the band inversion vertex, we will also explore the effect of Berry curvature on the plasmons of type-I 3D DSMs. Using the different band parameters of Na_3Bi and Cd_3As_2, we can investigate the differences between similar materials. From the band structure of type-I 3D DSMs, we will further discuss the similarities and differences in their plasmon modes compared to graphene [224–227], 3DEG [207], WSMs [228], and single Dirac cone models [203, 204].

4.1   RPA dielectric function for a type-I 3D DSM

The collective exciations in a solid normally occur within a range of smaller momentum and lower energy, where the electronic system maintains spin degeneracy. Thus, we can begin with the low-energy Hamiltonian, that is, Eq. (3.1) of the bulk type-I 3D DSMs. Assuming the Coulomb

potential arising from bare electron-electron (*e-e*) interactions is $V(\mathbf{R}) = e^2/(\kappa|\mathbf{R}|)$, using the RPA dielectric function, we can obtain the response to the electrostatic potential as

$$V_{ind}(\mathbf{Q},t) = V_Q \sum_{\mathbf{K}} \sum_{l,l'} \langle \mathbf{K}+\mathbf{Q},l'|\delta N|\mathbf{K},l\rangle \langle \mathbf{K}+\mathbf{Q},l'|e^{-i\mathbf{Q}\cdot\mathbf{R}}|\mathbf{K},l\rangle$$

$$= \lim_{\eta\to 0} V_Q V(\mathbf{Q},t) \sum_{\mathbf{K}} \sum_{l,l'} F_{l',l}(\mathbf{K},\mathbf{Q})\Pi_{l',l}(\omega;\mathbf{K},\mathbf{Q}), \qquad (4.1)$$

where

$$\Pi_{l',l}(\omega;\mathbf{K},\mathbf{Q}) = g_s \frac{f_{l'}(E_{\mathbf{K}+\mathbf{Q},l'}) - f_l(E_{\mathbf{K},l})}{E_{\mathbf{K}+\mathbf{Q},l'} - E_{\mathbf{K},l} - \hbar\omega + i\hbar\eta} \qquad (4.2)$$

is the density-density correlation function, $f_l(x) = [e^{(x-E_F^l)/k_B T} + 1]^{-1}$ is the Fermi-Dirac distribution function, where $l = +1$ and $l = -1$ denote the conduction and valence bands, respectively. In addition, E_F^l represents the Fermi level or chemical potential in the l band, $g_s = 2$ represents the spin degeneracy, κ is the dielectric constant of Na_3Bi or Cd_3As_2, $\mathbf{Q} = (\mathbf{q}, \varphi, q_z)$ is the change in the electron wave vector during *e-e* interactions, $V_Q = 4\pi e^2/(\kappa Q^2)$ is the Fourier transform of the 3D Coulomb potential, δN is the density fluctuation caused by the perturbation, and $V(\mathbf{Q},t)$ is the total self-consistent perturbative potential energy.

Using the definition of the dielectric function and Eq. (4.1), we can obtain

$$\hat{\varepsilon}(\omega,\mathbf{Q}) = 1 - \frac{V_{ind}(\mathbf{Q},t)}{V(\mathbf{Q},t)} = 1 - \lim_{\eta\to 0} V_Q \sum_{\mathbf{K}} \sum_{l,l'} F_{l',l}(\mathbf{K},\mathbf{Q})\Pi_{l',l}(\omega;\mathbf{K},\mathbf{Q}), \qquad (4.3)$$

where the many-body form factor $F_{l',l}(\mathbf{K},\mathbf{Q})$ reads as

$$F_{l',l}(\mathbf{K},\mathbf{Q}) = |\langle \mathbf{K}+\mathbf{Q},l'|e^{-i\mathbf{Q}\cdot\mathbf{R}}|\mathbf{K},l\rangle|^2 = |a_{\mathbf{K}+\mathbf{Q},l'}^* a_{\mathbf{K},l}(1 + b_{\mathbf{K}+\mathbf{Q},l'}^* b_{\mathbf{K},l})|^2$$

$$= \left| \frac{A^2 k|\mathbf{k}+\mathbf{q}|}{\sqrt{(\xi_{\mathbf{K}+\mathbf{Q},l'}^2 + A^2|\mathbf{k}+\mathbf{q}|^2)(\xi_{\mathbf{K},l}^2 + A^2 k^2)}} \left(1 + \frac{ll'\xi_{\mathbf{K},l}\xi_{\mathbf{K}+\mathbf{Q},l'}}{A^2[k^2 + (k_x - ik_y)(q_x + iq_y)]} \right) \right|^2, \qquad (4.4)$$

Here, $a_{\mathbf{K},l}$, $b_{\mathbf{K},l}$, and $\xi_{\mathbf{K},l}$ come from the wave functions given by Eqs. (3.3) and (3.4), with $|\mathbf{k}+\mathbf{q}|^2 = k^2 + q^2 + 2kq(\cos\theta\cos\varphi + \sin\theta\sin\varphi) = k^2 + q^2 + 2kq\cos(\theta - \varphi)$, where θ is the angle between $\mathbf{k}$ and the x axis, and φ is the angle between $\mathbf{q}$ and the x axis. Then, we can obtain the expression for the dielectric function of type-I 3D DSMs as

$$\hat{\varepsilon}(\omega,\mathbf{Q}) = 1 - \lim_{\eta\to 0} \frac{4\pi e^2 g_s}{\kappa Q^2} \sum_{\mathbf{K}} \sum_{l',l} F_{l',l}(\mathbf{K},\mathbf{Q}) \frac{f_{l'}(E_{\mathbf{K}+\mathbf{Q},l'}) - f_l(E_{\mathbf{K},l})}{E_{\mathbf{K}+\mathbf{Q},l'} - E_{\mathbf{K},l} - \hbar\omega - i\hbar\eta}. \qquad (4.5)$$

Through the Dirac identity, $\lim_{\eta\to 0}[1/(x\pm i\eta)] = P\{1/x\} \mp i\pi\delta(x)$, where $P\{1/x\}$ is the principal value and $\delta(x)$ is the Dirac-δ function, we can obtain the real and imaginary parts of the dielectric function of type-I 3D DSMs. Additionally, by replacing $\hbar\eta$ with a small energy Γ and assuming that Γ represents energy relaxations caused by scattering mechanisms such as impurities, we can avoid the issue of numerical nonconvergence in Eq. (4.5). Thus, we obtain the real part of Eq. (4.5) as

$$\varepsilon_{Re}(\omega,\mathbf{Q}) = 1 - \frac{4\pi e^2 g_s}{\kappa Q^2} \sum_{\mathbf{K}} \sum_{l',l} F_{l',l}(\mathbf{K},\mathbf{Q})[f_{l'}(E_{\mathbf{K}+\mathbf{Q},l'}) - f_l(E_{\mathbf{K},l})]$$

$$\times \frac{(E_{\mathbf{K}+\mathbf{Q},l'} - E_{\mathbf{K},l} - \hbar\omega)}{(E_{\mathbf{K}+\mathbf{Q},l'} - E_{\mathbf{K},l} - \hbar\omega)^2 + \Gamma^2}. \qquad (4.6)$$

Meanwhile, the imaginary part of Eq. (4.5) can be written as

$$
\begin{aligned}
\varepsilon_{Im}(\omega,\mathbf{Q}) = & \frac{4\pi^2 e^2 g_s}{\kappa Q^2} \sum_{\mathbf{K}} \sum_{l',l} F_{l',l}(\mathbf{K},\mathbf{Q})[f_{l'}(E_{\mathbf{K}+\mathbf{Q},l'}) - f_l(E_{\mathbf{K},l})] \\
& \times \delta(E_{\mathbf{K}+\mathbf{Q},l'} - E_{\mathbf{K},l} - \hbar\omega).
\end{aligned}
\tag{4.7}
$$

It is difficult to study the plasmon mode along any direction of the 3D wave vector $\mathbf{Q}$, $\mathbf{Q} = (\mathbf{q},\varphi,q_z)$ where φ is the angle between the $\mathbf{q}$ and x axis. Instead we separate it in two components: one perpendicular to the x-y plane of the type-I 3D DSMs, $\mathbf{Q}_\perp = (0,0,q_z)$, will only act on k_z direction and one that is parallel to this plane.

4.1.1   Q perpendicular to the x-y plane

For $\mathbf{Q}$ perpendicular to the x-y plane of a type-I 3D DSM, the real part of $\hat{\varepsilon}(\mathbf{K},\mathbf{Q})$ from Eq. (4.6) for $\mathbf{Q}_\perp = (0,0,q_z)$ becomes

$$
\begin{aligned}
\varepsilon_{Re}^{\perp}(\omega,q_z) = & 1 - \frac{8e^2}{\kappa \pi q_z^2} \sum_{l',l} \int_0^\infty dk_z \int_0^\infty dk k F_{l',l}(\mathbf{K},q_z)[f_{l'}(E_{\mathbf{K},q_z,l'}) - f_l(E_{\mathbf{K},l})] \\
& \times \frac{(E_{\mathbf{K},q_z,l'} - E_{\mathbf{K},l} - \hbar\omega)}{(E_{\mathbf{K},q_z,l'} - E_{\mathbf{K},l} - \hbar\omega)^2 + \Gamma^2},
\end{aligned}
\tag{4.8}
$$

with

$$
\begin{aligned}
E_{\mathbf{K},q_z,l'} &= C_0 + C_1(k_z + q_z)^2 + C_2 k^2 + l'\sqrt{M_{q_z}^2 + A^2 k^2}, \\
M_{q_z} &= [M_0 - M_1(k_z + q_z)^2 - M_2 k^2], \\
F_{l',l}(\mathbf{K},q_z) &= \left| \frac{A^2 k^2}{\sqrt{(\xi_{\mathbf{K},q_z,l'}^2 + A^2 k^2)(\xi_{\mathbf{K},l}^2 + A^2 k^2)}} \left(1 + \frac{l l' \xi_{\mathbf{K},l} \xi_{\mathbf{K},q_z,l'}}{/A^2 k^2}\right) \right|^2,
\end{aligned}
$$

where $\xi_{\mathbf{K},q_z,l'} = \sqrt{M_{q_z}^2 + A^2 k^2} - l' M_{q_z}$. Now, we assume that the broadening of the scattering states near the Fermi level is caused by impurity scattering, so we have $\Gamma = \hbar/\tau$, where τ is the relaxation time for electron-impurity scattering, and $\delta(x) \approx (\Gamma/\pi)(x^2 + \Gamma^2)^{-1}$ can be used for $\delta(x)$. Then the imaginary part of $\hat{\varepsilon}(\mathbf{K},\mathbf{Q})$ for $\mathbf{Q}_\perp = (0,0,q_z)$ becomes

$$
\begin{aligned}
\varepsilon_{Im}^{\perp}(\omega,q_z) = & \frac{8e^2 \hbar}{\kappa \pi \tau q_z^2} \sum_{l',l} \int_0^\infty dk_z \int_0^\infty dk k F_{l',l}(\mathbf{K},q_z)[f_{l'}(E_{\mathbf{K},q_z,l'}) - f_l(E_{\mathbf{K},l})] \\
& \times \left[\Gamma^2 + (E_{\mathbf{K},q_z,l'} - E_{\mathbf{K},l} - \hbar\omega)^2 \right]^{-1}.
\end{aligned}
\tag{4.9}
$$

4.1.2 Q parallel to the *x-y* plane

In this case we take the wave vector $\mathbf{Q}$ as $\mathbf{Q}_\parallel = (q, \varphi, 0)$ where φ is the angle between the $\mathbf{q}$ and x axis. From Eq. (4.5), we obtain the real part of $\hat{\varepsilon}(\mathbf{K}, \mathbf{Q})$ as

$$\varepsilon_{Re}^\parallel(\omega, \mathbf{q}, \varphi) = 1 - \frac{4e^2}{\kappa \pi^2 q^2} \sum_{l',l} \int_0^\infty dk_z \int_0^{2\pi - \varphi} d\phi \int_0^\infty dk k F_{l',l}(\mathbf{K}, \mathbf{q}, \varphi)$$

$$\times [f_{l'}(E_{\mathbf{K},\mathbf{q},\varphi}) - f_l(E_{\mathbf{K}})] \frac{E_{\mathbf{K},\mathbf{q},\varphi} - E_{\mathbf{K}} - \hbar\omega}{(E_{\mathbf{K},\mathbf{q},\varphi} - E_{\mathbf{K}} - \hbar\omega)^2 + \Gamma^2}, \tag{4.10}$$

where

$$E_{\mathbf{K},\mathbf{q},\varphi} = C_0 + C_1 k_z^2 + C_2 |\mathbf{k} + \mathbf{q}|^2 + l' \sqrt{M_q^2 + A^2 |\mathbf{k} + \mathbf{q}|^2},$$

$M_q = M_0 - M_1 k_z^2 - M_2 |\mathbf{k} + \mathbf{q}|^2$, and

$$F_{l',l}(\mathbf{K}, \mathbf{q}, \varphi) = \left| \frac{A^2 k |\mathbf{k} + \mathbf{q}|}{\sqrt{(\xi_{\mathbf{K},\mathbf{q},\varphi,l'}^2 + A^2 |\mathbf{k} + \mathbf{q}|^2)(\xi_{\mathbf{K},l}^2 + A^2 k^2)}} \left(1 + \frac{l' l \xi_{\mathbf{K},l} \xi_{\mathbf{K},\mathbf{q},\varphi,l'}}{A^2 k |\mathbf{k} + \mathbf{q}|} \right) \right|^2,$$

with $\xi_{\mathbf{K},\mathbf{q},\varphi,l'} = \sqrt{M_q^2 + A^2 |\mathbf{k} + \mathbf{q}|^2} - l' M_q$. By applying relaxation time approximation to Eq. (4.5), the imaginary part of $\hat{\varepsilon}(\mathbf{K}, \mathbf{Q})$ for $\mathbf{Q}_\parallel = (q, \varphi, 0)$ has the form

$$\varepsilon_{Im}^\parallel(\omega, \mathbf{q}, \varphi) = \frac{4e^2 \hbar}{\kappa \pi^2 \tau q^2} \sum_{l',l} \int_0^\infty dk_z \int_0^{2\pi - \varphi} d\phi \int_0^\infty dk k F_{l',l}(\mathbf{K}, \mathbf{q}, \varphi)$$

$$\times [f_{l'}(E_{\mathbf{K},\mathbf{q},\varphi}) - f_l(E_{\mathbf{K}})] \left[\Gamma^2 + (E_{\mathbf{K},\mathbf{q},\varphi,l'} - E_{\mathbf{K},l} - \hbar\omega)^2 \right]^{-1}. \tag{4.11}$$

Here, we made the change $\phi = \theta - \varphi$, so that $|\mathbf{k} + \mathbf{q}|^2 = k^2 + q^2 + 2kq \cos(\theta - \varphi)$. Then the integration over θ from 0 to 2π becomes one over ϕ from 0 to $(2\pi - \varphi)$, which describes how different wave vector $\mathbf{q}$ directions affect the dielectric function.

4.1.3 Plasmon dispersion relation and energy loss spectrum

In the expression for the dielectric function of type-I 3D DSMs, the band index $l = +1$ or -1 represents the conduction or valence band, respectively. Thus, the dielectric function will have four components as

$$\sum_{ll'} \hat{\varepsilon} = \varepsilon_{++} + \varepsilon_{-+} + \varepsilon_{+-} + \varepsilon_{--}. \tag{4.12}$$

Since we consider an *n*-doped type-I 3D DSM, where the valence band is fully occupied and the conduction band is partially occupied, we have $f_-(E_{\mathbf{K},-}) = 1$. Therefore, in the case of $l = l' = -1$, $\Pi_{l',l}(\omega; \mathbf{K}, \mathbf{Q}) = 0$. At the same time, the electron transitions from unoccupied states ($l = +1$) to occupied states ($l = -1$) have almost no effect on the plasmon mode, so we take $\varepsilon_{+-} \simeq 0$. Consequently, we only consider the case of electronic excitations within the conduction band (ε_{++}) and electron transitions from the valence band to the conduction band (ε_{-+}). The dispersion relation of collective excitations, that is, the relationship between ω and $\mathbf{Q}$, can be obtained by solving the condition where the real part of the RPA dielectric function is zero, so

we first solve for $Re[\hat{\varepsilon}(\omega,\mathbf{Q})] = |\varepsilon_{Re}(\omega,\mathbf{Q})| = 0$. The corresponding energy loss spectrum can be obtained by calculating the energy loss function, which is defined by the dielectric function as

$$E_{loss} = -Im\left[\frac{1}{\hat{\varepsilon}(\omega,\mathbf{Q})}\right] = \frac{-\varepsilon_{Im}(\omega,\mathbf{Q})}{\varepsilon_{Re}(\omega,\mathbf{Q})^2 - \varepsilon_{Im}(\omega,\mathbf{Q})^2}. \tag{4.13}$$

As shown in Fig. 3.4, a type-I 3D DSM exhibits an anisotropic energy dispersion; however, the energy dispersion is isotropic in the x-y plane. Therefore, we only consider the simple case where $\mathbf{q}$ is parallel to $\mathbf{k}$, that is, setting $\varphi = 0$ in Eqs. (4.10) and (4.11). Following the basic process [224], we first obtain the plasmon dispersion relation, and then we calculate the corresponding energy loss using Eq. (4.13).

4.2   Result and discussion

In numerical calculations, we utilize the band parameters from Tab. 3.1 to perform calculations for the plasmon modes of Na_3Bi and Cd_3As_2. Furthermore, the static dielectric constants κ for Na_3Bi (~ 5.99) and Cd_3As_2 (~ 12) are sourced from relevant research [203, 229]. Experimental studies in transport properties indicate that bulk samples of Na_3Bi and Cd_3As_2 both have fast lifetimes at low temperatures ($\sim 1-7$ ps) [86, 123]. Therefore, we adopt ~ 6.71 ps for Na_3Bi [86] and ~ 6.87 ps for Cd_3As_2 [123] for the numerical calculations.

In Fig. 3.5 of Chapter 3, we see that the DOSs for 3DEG, graphene, and type-I 3D DSMs are different, and therefore their plasmon dispersion relations should also be distinct. As shown in Fig. 4.1(d), in the long-wavelength limit ($\mathbf{Q} \to 0$), the plasmon dispersion of the 3DEG exhibits an optical mode, which is $\omega_Q = \omega_P + 3v_F^2 Q^2/(10\omega_P) \sim Q^2$, where $\omega_P = [N_e e^2/(m\kappa_0)]^{1/2}$ is the plasma frequency at $\mathbf{Q} = 0$, κ_0 is the vacuum permittivity, $v_F = \hbar k_F/m$ is the Fermi velocity of electrons, and m is the statistic electron mass. In actual metals, such as sodium, there is generally a high electron density of $N_e \sim 10^{23}$ cm^{-3}, so the plasma energy ($\hbar\omega_P \sim 5.9$ eV) is much higher than $k_B T \sim 25$ meV. This makes it difficult for plasmons in the 3DEG to be thermally excited, indicating that it is experimentally challenging to directly observe plasmon-related phenomena. As shown in Fig. 4.1(c), in the long-wavelength limit ($\mathbf{q} \to 0$) for a monolayer graphene, the plasmon dispersion is $\omega_q = (2e^2 E_F q/\kappa_0)^{1/2} \sim q^{1/2} \sim N_e^{1/4}$ [224–226], where $E_F = \hbar v_F k_F$ and $k_F = (\pi N_e)^{1/2}$. The plasmons in monolayer graphene exhibit an acoustic mode that strongly depends on q [224, 225]. Additionally, the plasmon dispersion of a conventional two-dimensional electron gas (2DEG) is similar to that of graphene, which is $\omega_q \sim q^{1/2} \sim N_e^{1/2}$ [226]. Thus, in monolayer graphene and 2DEG, as $q \to 0$, $\hbar\omega_P \to 0$, which differs significantly from the initial energy $\hbar\omega_P$ of the 3DEG when $Q \to 0$. Therefore, plasmons in 2D systems are more easily excited and can be more readily observed experimentally.

Figure 4.2 shows the plasmon dispersion and energy loss spectrum for different wave vector directions of high electron density Na_3Bi at fixed temperature. The corresponding Fermi level is much higher than the band inversion [cf. the green-dashed line in Figs. 3.4(b) and 3.4(c)], and the out-of-plane Fermi wave vector k_{Fz} is about five times larger than the in-plane Fermi wave vector k_F. We notice the following features.

(i) Figures 4.2(a) and 4.2(b) indicate that Na_3Bi has anisotropic plasmon dispersion relations along q and q_z. This result is in line with the anisotropic band structure of Na_3Bi along the k and k_z directions shown in Figs. 3.4(b) and 3.4(c). This result also suggests that the plasmon results
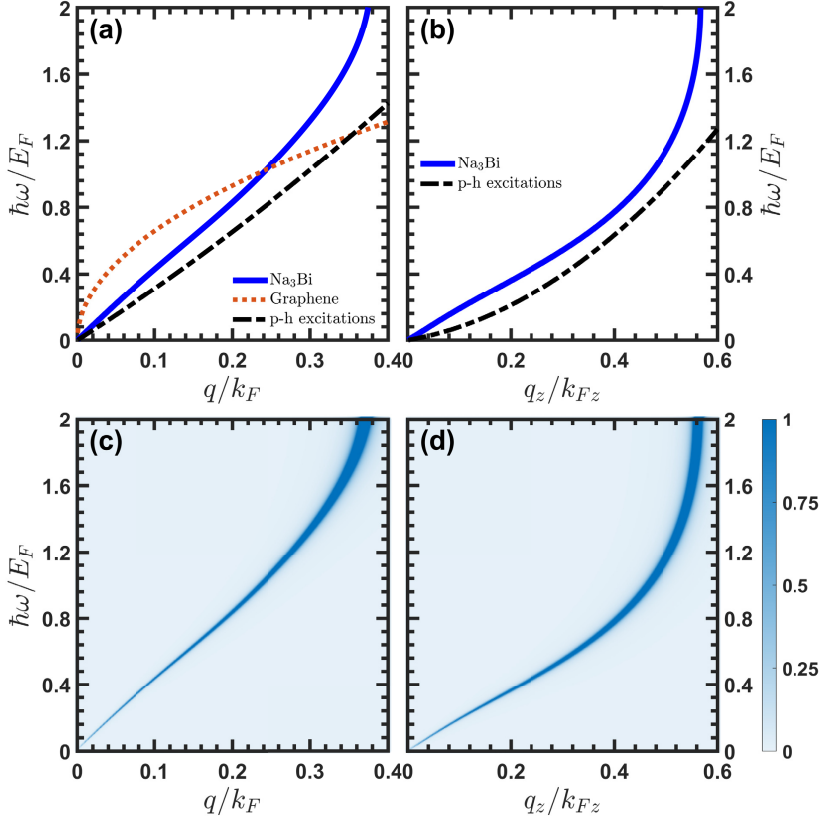
Figure 4.2: Dispersion relations and energy loss functions in Na_3Bi along different **Q** directions at temperature $T = 10$ K, electron density $N_e = 1 \times 10^{19}$ cm^{-3} [see green-dashed lines in Figs. 3.4(b) and 3.4(c), corresponding to $E_{F1} \simeq 59.076$ meV], and lifetime $\tau = 6.71$ ps. In (a) and (c) we have $Q_{\parallel} = (q, \varphi, 0)$ at $\varphi = 0$, the Fermi wave vector k_F along the k direction is about $\sim 2.25 \times 10^8$ m^{-1}. In (b) and (d) we have $Q_{\perp} = (0, 0, q_z)$, the Fermi wave vector k_{Fz} along the k_z direction is about $\sim 10.4 \times 10^8$ m^{-1}. The orange dotted curve in (a) is the graphene plasmon dispersion relation for $N_e = 1 \times 10^{12}$ cm^{-2}. The black dashed-dotted curves in (a) and (b) represent, for a 3DEG with $m^* \simeq 0.24 m_e$, the beginning of the particle-hole (p-h) excitations area in which $\omega \simeq \hbar^2(q^2 + 2qk_F)/2m^*$.

of the simple 3D Dirac cone shown in Fig. 4.1(c) are insufficient to describe the plasmon modes of type-I 3D DSMs.

(ii) In Fig. 4.2, it can be seen that at $q \to 0$ and $q_z \to 0$, the plasmon energy $\hbar\omega$ of Na_3Bi approaches zero in all directions, which is different from other 3D electronic systems, such as the results shown in Figs. 4.1(c) and 4.1(d). The 3DEG has an initial plasmon energy $\hbar\omega_P = [N_e e^2/(m\kappa_0)]^{1/2}$ when $q \to 0$ and $q_z \to 0$ [207]; the plasmon of the 3D Dirac cone is similar to the 3DEG [203]. Our results show differences from these 3D electronic systems, because we considered a complete Hamiltonian of type-I 3D DSMs.

(iii) From Figs. 4.2(a) and 4.2(b), we find that the plasmons of Na_3Bi exhibit a linear dispersion relation ($\omega \propto q$ and q_z) in a small range of Q; however, as Q increases, the dispersion relation

transitions to an optical-like dispersion similar to that of the 3DEG ($\omega \propto q^2$ and q_z^2). Additionally, the plasmon dispersion in the q direction remains linear over a larger momentum range. This unique plasmon behavior arises from the band structure of type-I 3D DSMs. In Fig. 3.4(b), the energy $E_{\mathbf{K},l}$ of Na$_3$Bi shows an approximately linear band structure along the k direction; in Fig. 3.4(c), the band structure along the k_z direction maintains linearity only near the Dirac point, while at higher momenta and energies, it resembles the parabolic band structure of the 3DEG. Therefore, we can find the unique plasmon dispersion relations of type-I 3D DSMs presented in Fig. 4.2.

(iv) In accordance with Figs. 4.2(a) and 4.2(b), the energy loss spectrum of Na$_3$Bi is presented in Figs. 4.2(c) and 4.2(d), respectively. It can be observed that the plasmon dispersion curves appear as energy loss peaks in the energy loss spectra for $\mathbf{Q}_\parallel$ and $\mathbf{Q}_\perp$. The energy loss spectra, which vary with the wave vectors q and q_z, have the same anisotropy as plasmon dispersions. Furthermore, the energy loss peaks gradually broaden with increasing q and q_z, but remain convergent even at higher energies $\hbar\omega = 2E_F$, which is different from graphene [224, 225]. The energy loss peaks obtained through theoretical calculations can be observed experimentally using high-resolution energy loss spectrum measurements, as shown in Fig. 1.12(b). Therefore, our theoretical research can provide guidance for experiments for plasmons in type-I 3D DSMs.

(v) Figure 4.1 shows that the plasmon dispersions of 3DEG [208], graphene [224, 225], and a single Dirac cone [203, 204] all enter the particle-hole (*p-h*) excitation continuum, indicating that these materials will have single-particle excitations in regions of higher energy and higher momentum, leading to the decay of collective excitations [207]. Taking the 3DEG result in Fig. 4.1(d) as an example, the plasmon energy for $Q > Q_c$ satisfies $\hbar\omega < \hbar^2(Q_c^2 + 2Q_cK_F)/(2m^*)$. In 3DEG, the momentum at the intersection of the plasmon energy and the boundary of the *p-h* excitation continuum is Q_c [207]. Considering that Na$_3$Bi is a 3D electronic system where the Fermi wave vector is difficult to define, we did not use the conventional definition of the *p-h* excitation continuum for Dirac systems [224, 225], but instead used the definition from 3DEG. As shown in Fig. 4.2, the plasmons in Na$_3$Bi appear only in a small momentum region, where the plasmon energy is overall higher than the *p-h* excitation continuum. It should be noted that the results based on the effective Hamiltonian are suitable only for excitations at smaller momenta and smaller energies. Therefore, we believe that in bulk Na$_3$Bi, for small q and q_z, the plasmons will not be affected by single-partical excitations and will not decay.

Figure 4.2 shows the anisotropic plasmon modes of bulk Na$_3$Bi at a high electron density. However, when the electron density is low, $N_e = 1 \times 10^{17}$ cm^{-3}, and the Fermi level is within the region of band inversion [see the green dashed lines in Figs. 3.4(b) and 3.4(c)], the collective excitations of the bulk Na$_3$Bi undergo significant changes, as shown in Fig. 4.3. Although the results in Figs. 4.2 and 4.3 appear to have a similar dispersion, the momentum range of the plasmons changes significantly. Specifically, the plasmon wave vector q_z in Fig. 4.3(b) is drastically reduced, shrinking by about 30 times compared to q_z in Fig. 4.2(b), while q is only reduced by a factor of 4, which is proportional to the reduction of the Fermi level from E_{F1} to E_{F2}. From the band structure characteristics of type-I 3D DSMs, as shown in Fig. 3.5(a), the presence of the Berry curvature strongly affects the electron momentum in Na$_3$Bi when E_F is below the band inversion vertex E_1, and the DOS decreases rapidly. As seen in Fig. 3.4(c), the Berry curvature mainly affects the DOS and electron excitations in the k_z direction. Therefore, reducing the electron density in an *n*-doped Na$_3$Bi will cause the collective excitations in the $\mathbf{Q}_\perp$ direction to reach a higher energy at smaller momenta. The influence of the Berry curvature on electron excitations is also reported in the previous transport studies of Na$_3$Bi [87].
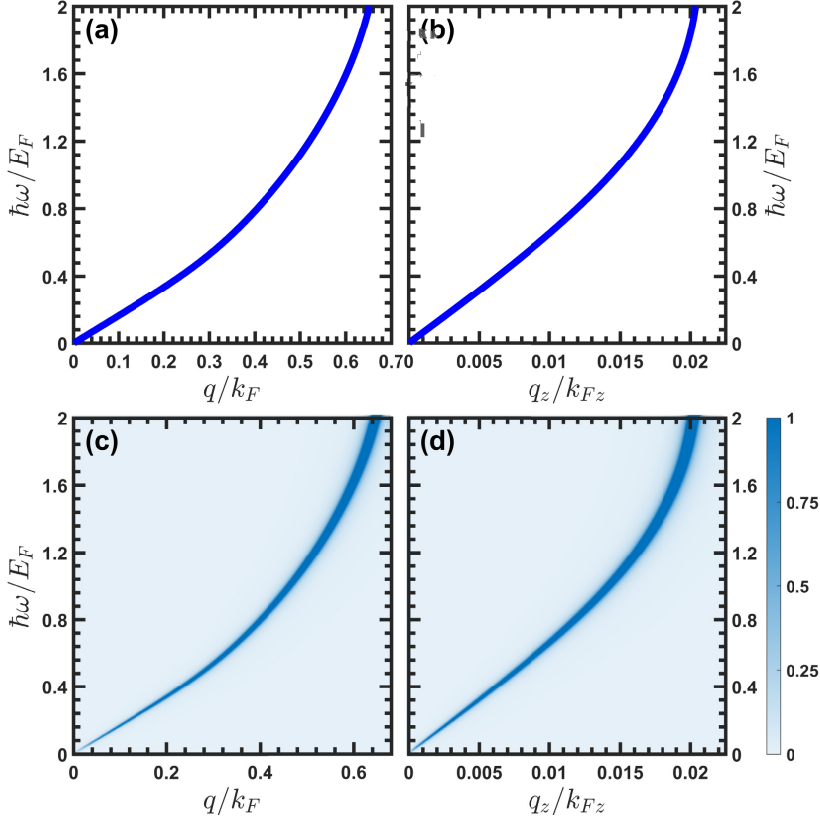
Figure 4.3: As in Fig. 4.2 with electron density of Na_3Bi being $N_e = 1 \times 10^{17}$ cm^{-3} [see black dotted lines in Fig. 3.4(b) and 3.4(c), corresponding to $E_{F2} \simeq 14.634$ meV]. For $Q_\parallel = (q, \varphi, 0)$ at $\varphi = 0$, the Fermi wave vector k_F along the k direction is about $\sim 0.298 \times 10^8$ m^{-1}. For $Q_\perp = (0, 0, q_z)$, the Fermi wave vector k_{Fz} along the k_z axis is about $\sim 9.24 \times 10^8$ m^{-1}.

The results in Figs. 4.2 and 4.3 are derived from bulk Na_3Bi, while the plasmon results based on Cd_3As_2 are shown in Figs. 4.4 and 4.5. From the figures, we can see that the plasmon dispersion relations and the energy loss spectra of bulk Cd_3As_2 exhibit similar characteristics to those of Na_3Bi. (i) The plasmon dispersion relations of a bulk Cd_3As_2 also shows $\hbar\omega \to 0$ as $q \to 0$ and $q_z \to 0$. (ii) Collective excitations in a bulk Cd_3As_2 are also anisotropic. Its plasmons exhibit an approximately linear dispersion relation within small ranges of q and q_z, but as q and q_z increase, the dispersion transitions to a parabolic-like relation. Additionally, the dispersion shows a broader linear range in the q direction. This is due to Cd_3As_2 having a type-I DSM band structure similar to that of Na_3Bi. (iii) The plasmon energy in bulk Cd_3As_2 also does not enter the *p-h* excitation continuum, avoiding decay. Figure 4.5 shows the plasmon modes of bulk Cd_3As_2 at low electron density, exhibiting changes similar to those seen in low-electron-density Na_3Bi in Fig. 4.3. The q_z corresponding to the plasmon energy is significantly reduced compared to the high-electron-density sample, which is due to the presence of the Berry curvature in Cd_3As_2 as well.

Figures 4.4 and 4.5 show that the plasmon modes of Cd_3As_2 are similar to those of Na_3Bi, but there are some differences. As introduced in Fig. 3.4 and the related discussion, the band
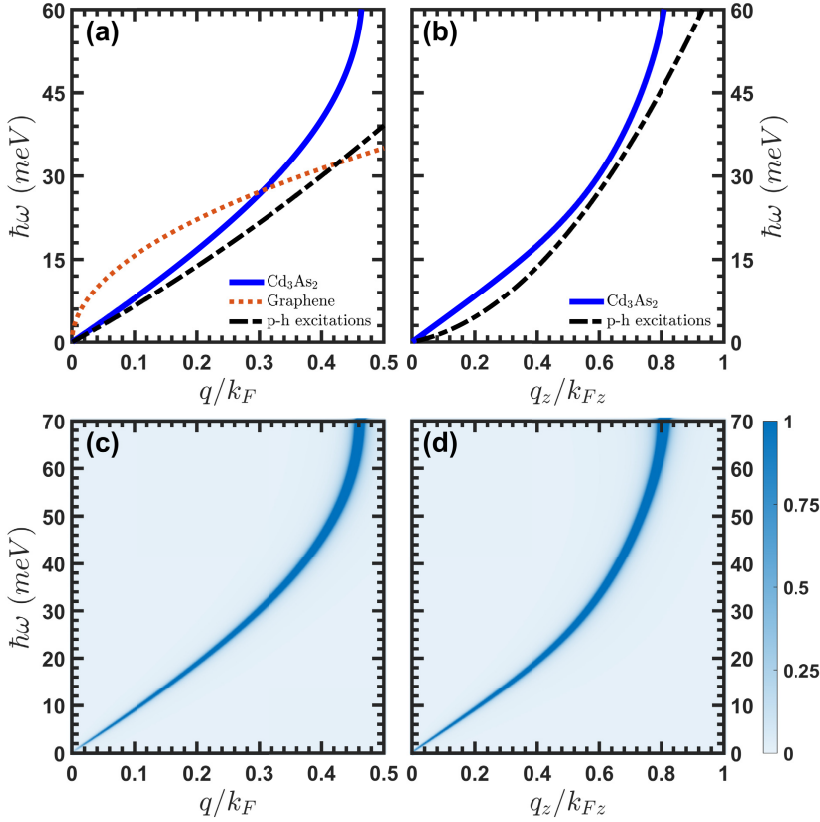
Figure 4.4: Plasmon dispersions and energy loss functions in Cd_3As_2 along different $\mathbf{Q}$ directions at fixed temperature $T = 10$ K, electron density $N_e = 1 \times 10^{19}$ cm^{-3} [see Fig. 3.4(e) and 3.4(f), corresponding to $E_{F1} \simeq -185.651$ meV], and lifetime $\tau = 6.87$ ps. For $Q_{\parallel} = (q, \varphi, 0)$ at $\varphi = 0$, the Fermi wave vector k_F along the k direction is about $\sim 1.33 \times 10^8$ m^{-1}. For $Q_{\perp} = (0, 0, q_z)$, the Fermi wave vector k_{Fz} along the k_z axis is about $\sim 0.68 \times 10^8$ m^{-1}. The orange dotted curve in (a) is graphene's dispersion relation for $N_e = 1 \times 10^{12}$ cm^{-2}. The black dashed-dotted curves in (a) and (b) represent, for a 3DEG with $m^* \simeq 0.24 m_e$, the beginning of the particle-hole (p-h) excitations area in which $\omega \simeq \hbar^2(q^2 + 2qk_F)/2m^*$.

inversion and the Berry curvature of Cd_3As_2 are smaller compared to Na_3Bi. When we reduce the electron density, the Fermi levels of both Na_3Bi and Cd_3As_2 decrease accordingly. However, as seen in Figs. 3.4(c) and 3.4(f), at lower Fermi levels, the band inversion in the k_z direction of Na_3Bi is much stronger than in Cd_3As_2. Therefore, the influence of Berry curvature on electron momentum in Na_3Bi is much bigger than in Cd_3As_2, resulting in stronger anisotropic collective excitations in Na_3Bi. Consequently, from the plasmon results of Na_3Bi in Figs. 4.2 and 4.3, we can observe that the reduction in electron density causes k_{Fz} to decrease to about 0.9 of its original value, but it remains approximately 20 times larger than k_F. At this point, the plasmon wave vector q decreases about 4 times, but q_z decreases about 30 times, showing the strong influence of the Berry curvature on the k_z-direction electron excitations of Na_3Bi. In contrast, the plasmon results of Cd_3As_2 in Figs. 4.4 and 4.5 show that at a high electron density, k_F of Cd_3As_2 is larger than k_{Fz}, but when the electron density is reduced, k_F becomes smaller than k_{Fz}. Therefore, we can see that the reduction in the plasmon wave vector of Cd_3As_2 is much less pronounced than in Na_3Bi,
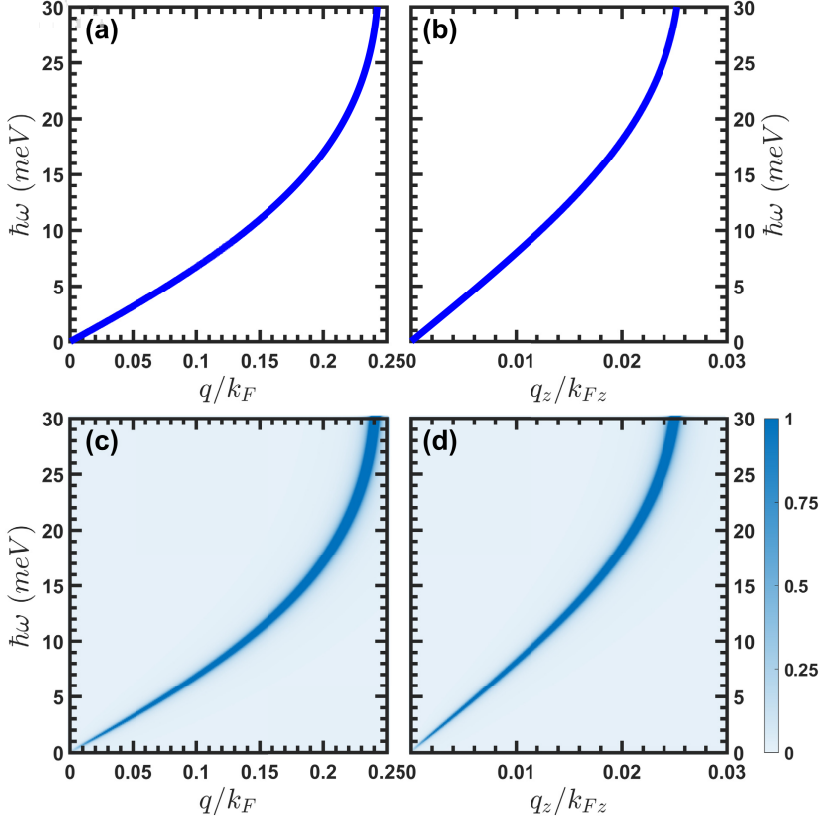
Figure 4.5: As in Fig. 4.4 with electron density of Cd_3As_2 being $N_e = 1 \times 10^{17}$ cm^{-3} [see Fig. 3.4(e) and 3.4(f), corresponding to $E_{F2} \simeq -211.237$ meV]. For $Q_\parallel = (\mathbf{q}, \varphi, 0)$ at $\varphi = 0$, the Fermi wave vector k_F along the k direction is about $\sim 0.301 \times 10^8$ m^{-1}). For $Q_\perp = (0, 0, q_z)$, the Fermi wave vector k_{Fz} along the k_z axis is about $\sim 0.438 \times 10^8$ m^{-1}.

indicating that Cd_3As_2 has a smaller Berry curvature effect and a less anisotropic plasmon mode.

Finally, Fig. 4.6 shows the plasmon modes of type-I 3D DSMs when both q and q_z are not zero. We calculated the dispersion relation of $\hbar\omega$ and q_z for different fixed values of q, and we also calculated the dispersion relation of $\hbar\omega$ and q for different fixed values of q_z. Figs. 4.6(a) and 4.6(b) present the results for Na_3Bi, while Figs. 4.6(c) and 4.6(d) show the corresponding results for Cd_3As_2. In these figures, we observe that for $q_z \neq 0$ or $q \neq 0$, the plasmon dispersion relation in type-I 3D DSMs exhibits a parabolic-like dispersion similar to that of 3DEG, but the anisotropy of the collective excitations is still clearly visible. Additionally, in Fig. 4.6(c), when $q_z \neq 0$, we observe a peculiar behavior where $\hbar\omega$ first decreases and then increases as q increases at small q. In Fig. 4.6(d), a similar situation arises where, at very small q, a single $\hbar\omega$ corresponds to two different values of q_z. We believe this is due to the significant influence of the Berry curvature on the electron momentum near the Dirac point in type-I 3D DSMs. As shown in Fig. 3.3, Berry curvature exerts a strong influence on electron momentum near the Dirac point, leading to a nontrivial topological structure in electron momentum. During the process of the collective excitations, this phenomenon affects the plasmon dispersion near small Q, which explains the nontrivial plasmon modes observed in Fig. 4.6(c).
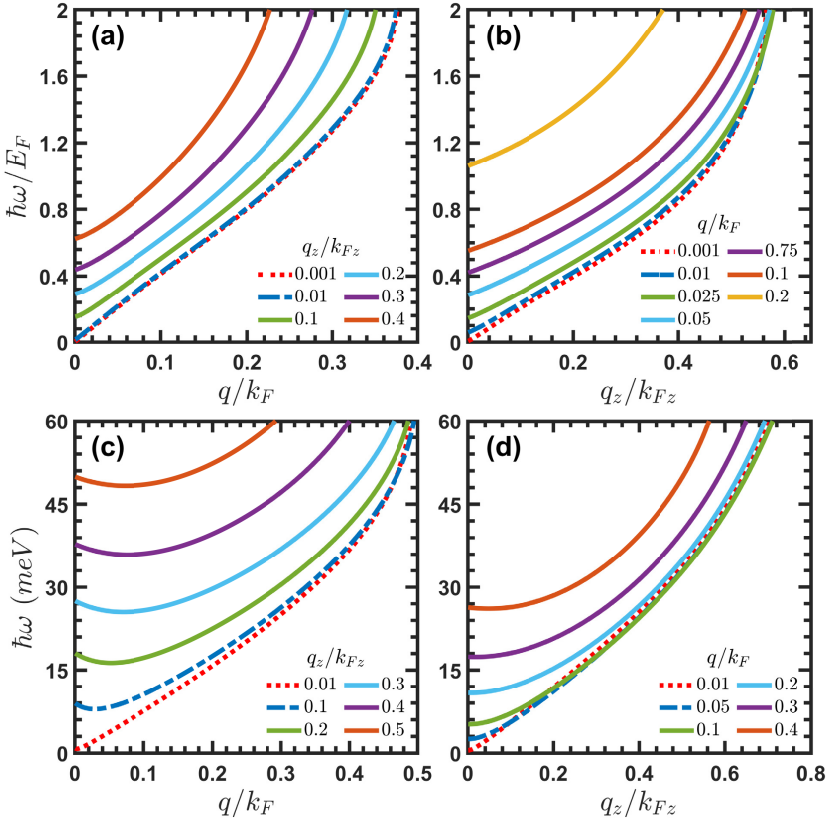
Figure 4.6: (a) Plasmon dispersion for Na_3Bi as a function of q at fixed temperature $T = 10$ K, electron density $N_e = 1 \times 10^{19}$ cm^{-3}, lifetime $\tau = 6.71$ ps, and fixed q_z. (b) Plasmon dispersion for Na_3Bi with q and q_z interchanged is shown. (c), (d): *idem.* as in (a) and (b), respectively, for Cd_3As_2 for the same temperature and electron density, and $\tau = 6.87$ ps. All curves for selected q_z or q isovalues are marked as shown in the insets.

After synthesizing all the results from Figs. 4.2 to 4.6, we can see that the collective excitations in bulk samples of type-I 3D DSMs possess unique properties that differ from those of other materials. Both graphene and type-I 3D DSMs exhibit similar properties of gapless Dirac fermions, such as high carrier mobility and excellent optoelectronic properties. However, as a 3D material, it is easier to obtain high-quality samples of type-I 3D DSMs. Besides, in type-I 3D DSMs, plasmons can be readily thermal-excited and observed. In contrast, in metallic 3D materials, plasmons are difficult to thermally excite and observe because their plasmon energy $\hbar\omega_P$ is much higher than $k_B T$. The tunability of the Fermi level in type-I 3D DSMs has been reported [90, 115, 123]. Therefore, we propose that controlling the distance between the Fermi level and the band inversion can tune the collective excitations of type-I 3D DSMs, particularly in the k_z direction. This distinguishes them from traditional 3D electronic materials, multilayer graphene [227], WSMs [228], and isotropic DSMs [203, 204]. Furthermore, in type-I 3D DSMs, it is also possible to find anisotropic surface plasmons influenced by Berry curvature. Considering the effects of magnetic fields, optical fields, or phonons, type-I 3D DSMs are also expected to exhibit anisotropic plasmon polaritons.

4.3 Conclusions of this chapter

In this chapter, we based on the effective $\mathbf{k} \cdot \mathbf{p}$ Hamiltonian of type-I 3D DSMs, using the RPA dielectric function to calculate the plasmon dispersion relations and energy loss spectra of Na_3Bi and Cd_3As_2 under different directions and electron densities.

Our research finds the following features. (i) Both Na_3Bi and Cd_3As_2 exhibit anisotropic plasmon dispersion relations due to the similar band structure of type-I 3D DSMs, but the anisotropy in Cd_3As_2 is smaller than that in Na_3Bi, which arises from the smaller band inversion and Berry curvature of Cd_3As_2. (ii) The plasmon energy approaches zero as their plasmon wave vector nears zero, and a same phenomenon appears in the energy loss spectra, indicating that the collective excitations in type-I 3D DSMs can be more easily excited, which distinguishes them from metals and other 3D electronic systems. (iii) Corresponding to the band structure of type-I 3D DSMs, their plasmons exhibit a linear dispersion relation at a small wave vector, which transitions to a parabolic dispersion relation as the wave vector increases. (iv) By studying the plasmon modes of Na_3Bi and Cd_3As_2 at different electron densities, we find that the Berry curvature in type-I 3D DSMs has a significant effect on their collective excitations, especially along the k_z direction, where the plasmon wave vector experiences a substantial reduction when the Fermi level lowers into the band inversion region. (v) By controlling the electron density to adjust the the Fermi level, the plasmon modes in type-I 3D DSMs can be tuned, particularly in the k_z direction.

From our results in this chapter, we further propose that anisotropic surface plasmons and plasmon polaritons should also exist in type-I 3D DSMs, and these properties should be influenced by the Berry curvature as well. Furthermore, our research helps for a deeper understanding of the topological properties of type-I 3D DSMs, as well as for understanding the mechanisms of electronic excitations near their Dirac points.

Chapter 5

Anisotropic optical conductivity of type-II 3D DSMs

In Chapter 3, we show the experimental results of the optoelectroni properties of monolayer graphene and the type-I 3D DSM Cd_3As_2 in Figs. 3.1 and 3.2, respectively. Our research in Chapter 3 explains the optical conductivity (OC) of Cd_3As_2 and explored the physical mechanisms of OC based on the band structure of type-I 3D DSMs. In recent years, another type of Dirac semimetal, the type-II 3D DSMs, has been theoretically predicted and experimentally verified. This new type of Dirac semimetal also exhibits characteristics of Dirac fermions, such as massless, gapless, and linear energy dispersion at the Dirac point. Therefore, it can be expected that the OC of type-II 3D DSMs should have similarities with that of type-I, such as the optical absorption window presented in Figs. 3.1 and 3.2. However, as shown in Fig. 1.10, the 3D Dirac cone of type-II 3D DSMs is strongly tilted along the k_z direction, resulting in a Fermi surface at the Dirac point that outlines a 2D wave vector contour of both conduction and valence bands. This is in sharp contrast to the point-like Fermi surface at the Dirac point of type-I 3D DSMs [see Fig. 1.5(f)]. Consequently, the OC of type-II and type-I 3D DSMs should exhibit essential differences because of the distinct band structures, prompting us to investigate the OC of type-II 3D DSMs.

As introduced in Sec. 1.2.4, most research on the optoelectronic properties of type-II 3D DSMs is based on their thin-film samples. In such cases, their semimetallic state will have a phase transition to a semiconductor state [170]. Additionally, a limited amount of work has studied the ideal tilted 3D Dirac cone, but these mainly consider the effect of the tilt index of the 3D Dirac cone on optoelectronic properties at without a specific material [205, 206]. Thus, the properties of OC for bulk samples of type-II 3D DSMs remain unclear. Among the reported type-II 3D DSMs, $PtTe_2$ stands out from other DSMs due to easier preparation and strong stability in air [70, 153, 154], quickly becoming an important material for studying the physical properties of type-II DSMs. In research on $PtTe_2$, many unique properties have been discovered, such as anisotropic and high carrier mobility [156, 157], ultrahigh electrical conductivity [160–162], and a phase transition from DSM to semiconductor state with reducing thickness [170]. In terms of optoelectronic properties, experiments have reported wide-spectrum photodetectors and sensors based on $PtTe_2$, as well as other related optoelectronic devices [180–183, 190, 191]. The unique and excellent terahertz optoelectronic properties of $PtTe_2$ have also been discovered [178, 179]. In addition, the tunability of the Fermi level of bulk $PtTe_2$ has been experimentally reported [230]. These studies demonstrate the potential of type-II 3D DSMs in optoelectronic applications. Furthermore, in-depth exploration of these properties can not only advance the fundamental condensed matter

physics but also promote further technological developments.

Therefore, in this chapter, we consider the interaction between an n-doped bulk PtTe$_2$ and the linearly polarized light incident from different directions. Based on the effective Hamiltonian of bulk PtTe$_2$, we use the energy balance equation to calculate its OC. In addition, considering the experimental conditions, we further investigate the effects of temperature, energy relaxation time, and electron density on the OC of the bulk PtTe$_2$.

5.1 One-electron aspects

PtTe$_2$ crystallizes in the trigonal CdI$_2$-type crystal structure, space group $P\bar{3}m1$ (No. 164). The bulk PtTe$_2$ is a periodic stack of basic monolayers with weak interactions between those layers. In each monolayer, the Pt atoms are sandwiched by top and bottom Te atoms, whereas two Te atoms are related by crystal symmetries [see Figs. 1.10(a) and 1.10(b)]. The band structure, calculated using density functional theory (DFT) [69] and verified using ARPES [70], indicates that two symmetric Dirac points appear on the $A - \Gamma - A'$ axis at $\pm D$. In addition, the ARPES results show that the energy dispersion of bulk PtTe$_2$ remains linear up to about 0.8 eV counting from Dirac points [70], thus the linearized Hamiltonian of 3D DSMs is effective in studying its near- to far-infrared optical properties [69, 172].

5.1.1 Effective Hamiltonian of the type-II 3D DSMs

In the vicinity of the two Dirac points, the effective low-energy Hamiltonian for a type-II 3D DSM, which describes an anisotropic and tilted 3D Dirac cone, is given by [69]

$$H_{\mathbf{K},\chi} = \hbar(\chi v_t k_z I + v_x k_x \sigma_x - v_y k_y \sigma_y - \chi v_z k_z \sigma_z)$$
$$= \hbar \begin{bmatrix} \chi k_z(v_t - v_z) & v_x k_x + i v_y k_y \\ v_x k_x - i v_y k_y & \chi k_z(v_t + v_z) \end{bmatrix}. \tag{5.1}$$

Here, $\chi = \pm 1$ represents two Dirac cones located at $\mp D$ along the $A - \Gamma - A'$ axis with tilt in the opposite direction, I is the 2×2 identity matrix, and σ_i's are the Pauli matrices. The corresponding eigenvalues were analytically obtained and read as

$$E_{\mathbf{K},l}^{\chi} = \chi \hbar v_t k_z + l\hbar \sqrt{v_x^2 k_x^2 + v_y^2 k_y^2 + v_z^2 k_z^2}, \tag{5.2}$$

where the band index $l = +1(-1)$ denotes the conduction (valence) band. Low-energy fittings based on Eq. (5.2) to the structure of the DFT band find that in-plane velocities are isotropic, $v_x = v_y$, whereas out-of-plane velocities give $v_t > v_z$, thus the 3D Dirac cones are strongly tilted in k_z direction [69, 70]. In a cylindrical coordinate system, we have $\mathbf{K} = (k_x, k_y, k_z) = (\mathbf{k}, \theta, k_z)$ with θ being the angle between the $\mathbf{k}$ and the x-axis. Due to the isotropic velocities in the x-y plane, we can rewrite Eq. (5.2) as

$$E_{\mathbf{K},l}^{\chi} = \chi \hbar v_t k_z + l\hbar \sqrt{v_x^2 k^2 + v_z^2 k_z^2} = \chi \hbar v_t k_z + l\hbar \varepsilon_{\mathbf{K}}, \tag{5.3}$$

with

$$\varepsilon_{k_x} = v_x k_x, \ \varepsilon_{k_y} = v_y k_y, \ \varepsilon_{k_z} = v_z k_z,$$

and

$$\varepsilon_{\mathbf{K}} = \sqrt{\varepsilon_{k_x}^2 + \varepsilon_{k_y}^2 + \varepsilon_{k_z}^2} = \sqrt{v_x^2 k^2 + \varepsilon_{k_z}^2}.$$

Meanwhile, the eigenfunction of the electrons can also be analytically obtained as

$$\psi_{\mathbf{K},l}^{\chi}(\mathbf{R}) = |\mathbf{K}, \chi, l\rangle = \frac{a_{\mathbf{K},l}^{\chi}}{\sqrt{2}} \begin{pmatrix} 1 \\ b_{\mathbf{K},l}^{\chi} \end{pmatrix} e^{-i\mathbf{K}\cdot\mathbf{R}}, \tag{5.4}$$

where

$$a_{\mathbf{K},l}^{\chi} = \left[\frac{\varepsilon_{k_x}^2 + \varepsilon_{k_y}^2}{\varepsilon_{\mathbf{K}}^2 + \chi l \varepsilon_{k_z} \varepsilon_{\mathbf{K}}} \right]^{1/2} = \frac{v_x k}{(\varepsilon_{\mathbf{K}}^2 + \chi l \varepsilon_{k_z} \varepsilon_{\mathbf{K}})^{1/2}},$$

$$b_{\mathbf{K},l}^{\chi} = \frac{\chi \varepsilon_{k_z} + l \varepsilon_{\mathbf{K}}}{\varepsilon_{k_x} + i\varepsilon_{k_y}} = \frac{\chi \varepsilon_{k_z} + l \varepsilon_{\mathbf{K}}}{v_x k e^{i\theta}}.$$

5.1.2 Fermi level of electrons and holes

With the time-reversal symmetry in type-II 3D DSMs, we have $H_{\mathbf{K},+} = H_{-\mathbf{K},-}^*$ and can introduce a valley degeneracy factor $g_v = 2$. In addition, for a low energy case the system retains spin degeneracy [69, 70]. Therefore, in the following calculations we use the degeneracy factor $g = g_s g_v = 4$.

In an n-doped Type-II 3D DSM, the relationship between the Fermi level E_F^e of electrons and the electron density N_e at a finite temperature can be obtained by applying the carrier number conservation, which reads as

$$N_e = \frac{2}{\pi^2} \int_{-\infty}^{\infty} dk_z \int_0^{\infty} dk k [e^{(E_{\mathbf{K},+} - E_F^e)/k_B T} + 1]^{-1}, \tag{5.5}$$

with $f(x) = [e^{(x - E_F)/k_B T} + 1]^{-1}$ being the Fermi-Dirac distribution function.

It should be noted that for an n-doped Dirac system, if N is the electron concentration in the absence of the light field, the electron density in the presence of the light field should be $N_e = N + \Delta N_e$, with ΔN_e being the photo-excited electron density. Due to carrier number conservation, we have $\Delta N_e = N_h$, with N_h being the hole density in the valence band. Thus, the Fermi level of holes E_F^h in the valence band can be found through

$$N_h = \frac{2}{\pi^2} \int_{-\infty}^{\infty} dk_z \int_0^{\infty} dk k \{1 - [e^{(E_{\mathbf{K},-} - E_F^h)/k_B T} + 1]^{-1}\}. \tag{5.6}$$

5.2 Anisotropic optical conductivity of a type-II 3D DSM

In the present study, we consider electrons in an n-doped Type-II 3D DSM that interact with a linearly polarized light field as a continuous wave. Because of the asymmetric electronic energy spectrum, as given by Eq. (5.3), the polarization direction in the x-y plane and the z direction must be considered separately.

5.2.1 Carrier-photon scattering rates

Assuming that the light field is sufficiently weak, we can take the carrier-photon (c-p) inter-actions as an elastic scattering process. Therefore, we can treat c-p interactions as perturbations by taking $\mathbf{K} \to \mathbf{K} - e\mathbf{A}(t)/\hbar$ in Eq. (5.1) with $\mathbf{A}(t)$ being the vector potential of the light field. Considering only one tilted Dirac cone by taking $\chi = +1$ with valley degeneracy, the perturbation Hamiltonian with the linearly polarized light field in the x-y plane (here we chose the x direction) and along the z direction through $H[\mathbf{K} - e\mathbf{A}(t)/\hbar] \simeq H_\mathbf{K} + H_{c-p}(t)$ can be obtained, respectively, as

$$H_{c-p}^x(t) = -ev_x A(t) \begin{pmatrix} 0 & 1 \\ 1 & 0 \end{pmatrix}, \tag{5.7}$$

and

$$H_{c-p}^z(t) = eA(t) \begin{pmatrix} (v_z - v_t) & 0 \\ 0 & -(v_z + v_t) \end{pmatrix}, \tag{5.8}$$

where $A(t) = (F_0/\omega)\sin(\omega t) = (F_0/2i\omega)(e^{i\omega t} - e^{-i\omega t})$, with F_0 being the electric field strength and ω the frequency of the light field.

Using Fermi's golden rule as we introduced in Eq. (2.24), the first-order steady-state electronic transition rate of the c-p interaction reads as

$$\begin{aligned} W_{\zeta\zeta'}^{j,c-p} &= \frac{2\pi}{\hbar} |\langle \zeta'|H_{c-p}^j|\zeta\rangle|^2 \delta(E_{\zeta'} - E_\zeta - \hbar\omega) \\ &= \frac{2\pi}{\hbar}\left(\frac{ev_x^2 F_0}{2\omega}\right)^2 |G_{\zeta\zeta'}^j|^2 \delta_{\mathbf{K},\mathbf{K}'}\delta(E_{\zeta'} - E_\zeta - \hbar\omega), \end{aligned} \tag{5.9}$$

where we used the notation $|\zeta\rangle \equiv |\mathbf{K}, l\rangle$ for clarity. $\delta_{\mathbf{K},\mathbf{K}'}$ and $\delta(E_{\zeta'} - E_\zeta - \hbar\omega)$ are due to momentum and energy conservation laws during a electron-photon scattering process with absorption of a photon $\hbar\omega$. $j = x$ or z represents the light field polarizing parallel or perpendicular to the x-y plane, with

$$|G_{\zeta\zeta'}^x|^2 = \frac{2k^2[\varepsilon_{k_z}^2 + \varepsilon_\mathbf{K}^2 + \varepsilon_{k_z}\varepsilon_\mathbf{K}(l'+l)]}{\varepsilon_\mathbf{K}^4 + ll'\varepsilon_{k_z}^2\varepsilon_\mathbf{K}^2 + \varepsilon_{k_z}\varepsilon_\mathbf{K}^3(l+l')} + \frac{2k^2[\varepsilon_{k_z}^2 + ll'\varepsilon_\mathbf{K}^2 + \varepsilon_{k_z}\varepsilon_\mathbf{K}(l+l')]\cos(2\theta)}{\varepsilon_\mathbf{K}^4 + ll'\varepsilon_{k_z}^2\varepsilon_\mathbf{K}^2 + \varepsilon_{k_z}\varepsilon_\mathbf{K}^3(l+l')},$$

and

$$|G_{\zeta\zeta'}^z|^2 = \frac{\left[(v_z - v_t)k^2 - (v_z + v_t)(\varepsilon_{k_z} + l'\varepsilon_\mathbf{K})(\varepsilon_{k_z} + l\varepsilon_\mathbf{K})/v_x^2\right]^2}{\varepsilon_\mathbf{K}^4 + ll'\varepsilon_{k_z}^2\varepsilon_\mathbf{K}^2 + \varepsilon_{k_z}\varepsilon_\mathbf{K}^3(1+l')}.$$

5.2.2 Optical conductivity of a type-II 3D DSM

In this study, we assume that the momentum distribution function of carriers in a type-II 3D DSM can be described by a statistical energy distribution function, that is, $f_\zeta = f_l(\mathbf{K}) \approx f_l(E_{\mathbf{K},l})$ with $f_+(E_{\mathbf{K},+}) = [e^{(E_{\mathbf{K},+} - E_F^e)/K_B T} + 1]^{-1}$ and $f_-(E_{\mathbf{K},-}) = [e^{(E_{\mathbf{K},-} - E_F^h)/K_B T} + 1]^{-1}$ being, respectively, the Fermi-Dirac function for electrons and holes. We change only the polarized directions of the light field and retain its strength, so we take $F_0 = F_x = F_z$ while we calculate the OCs of

PtTe$_2$ by using Eqs. (5.9) and (2.33). Applying the c-p scattering rates $W_{\zeta\zeta'}^{j;c-p}$ obtained from Eq. (5.9) to Eq. (2.33) with $\mathbf{K} = \mathbf{K}'$ from the momentum conservation and $E_{\zeta'} - E_{\zeta} = \hbar\omega$ from the energy conservation, the in-plane OCs, $\sigma_{xx}^{ll'}(\omega)$, for light polarized parallel to the x-y plane read as

$$\sigma_{xx}^{ll'}(\omega) = \frac{4e^2 v_x^4}{\pi^2 \omega} \sum_{l,l'} \int_{-\infty}^{\infty} dk_z \int_0^{2\pi} d\theta \int_0^{\infty} dk k |G_{\zeta\zeta'}^x|^2 \delta_{\mathbf{K},\mathbf{K}'}$$
$$\times f_l(E_{\mathbf{K},l})[1 - f_{l'}(E_{\mathbf{K},l'})]\delta(E_{\mathbf{K},l'} - E_{\mathbf{K},l} - \hbar\omega). \tag{5.10}$$

Here, by applying Eq. (5.9), $|G_{\zeta\zeta'}^x|^2$ can be written in the form $|G_{\zeta\zeta'}^x|^2 = g_{ll'}^x(\mathbf{K}) + g_1 \cos(2\theta)$, and $\int_0^{2\pi} \cos(2\theta) d\theta = 0$ analytically proves that $\sigma_{xx}^{ll'}(\omega)$ of a type-II 3D DSM is independent of the polarization directions; consequently, we have $\sigma_{xx}^{ll'}(\omega) = \sigma_{yy}^{ll'}(\omega)$. By using the relaxation-time approximation of the Dirac-δ function, i.e., $\delta(E) \approx (\Gamma/\pi)(E^2 + \Gamma^2)^{-1}$ is the Lorentzian function with $\Gamma = \hbar/\tau$, we now get the intraband OCs as

$$\sigma_{xx}^{ll}(\omega) = \frac{8\sigma_0 v_x^4}{\pi^2 \omega^2} \frac{\omega\tau}{1 + (\omega\tau)^2} \int_{-\infty}^{\infty} dk_z \int_0^{\infty} dk k g_{ll}^x(\mathbf{K}) f_l(E_{\mathbf{K},l})[1 - f_l(E_{\mathbf{K},l})], \tag{5.11}$$

with

$$g_{ll}^x(\mathbf{K}) = \frac{2k^2[\varepsilon_{k_z}^2 + \varepsilon_{\mathbf{K}}^2 + 2l\varepsilon_{k_z}\varepsilon_{\mathbf{K}}]}{\varepsilon_{\mathbf{K}}^4 + \varepsilon_{k_z}^2 \varepsilon_{\mathbf{K}}^2 + 2l\varepsilon_{k_z}\varepsilon_{\mathbf{K}}^3}.$$

Here, $\sigma_0 = e^2/\hbar$ is the quantum conductance, τ is the energy relaxation time due to the broadening scattering of the c-p interaction. For interband transitions, we only consider the photon absorption so that we have $\sigma_{xx}^{+-}(\omega) \simeq 0$, and the interband OC for electrons scattered by photons from the valence band to the conduction band reads as

$$\sigma_{xx}^{-+}(\omega) = \frac{16\sigma_0 v_x^4 \tau}{\pi^2 \omega} \int_{-\infty}^{\infty} dk_z \int_0^{\infty} dk \frac{k^3(\varepsilon_{k_z}^2 + \varepsilon_{\mathbf{K}}^2)}{\varepsilon_{\mathbf{K}}^4 - \varepsilon_{k_z}^2 \varepsilon_{\mathbf{K}}^2} \frac{f_-(E_{\mathbf{K},-})[1 - f_+(E_{\mathbf{K},+})]}{1 + (\omega - 2\sqrt{v_x^2 k^2 + v_z^2 k_z^2})^2 \tau^2}. \tag{5.12}$$

For light polarized in the z direction, the same approach as $\sigma_{xx}^{ll'}(\omega)$ can be applied, and the out-of-plane OC, $\sigma_{zz}^{ll'}(\omega)$, has the formula

$$\sigma_{zz}^{ll'}(\omega) = \frac{8e^2 v_x^4}{\pi\omega} \sum_{l,l'} \int_{-\infty}^{\infty} dk_z \int_0^{\infty} dk k |G_{\zeta\zeta'}^z|^2 \delta_{\mathbf{K},\mathbf{K}'}$$
$$\times f_l(E_{\mathbf{K},l})[1 - f_{l'}(E_{\mathbf{K},l'})]\delta(E_{\mathbf{K},l'} - E_{\mathbf{K},l} - \hbar\omega). \tag{5.13}$$

Here, intraband OCs ($l = l' = \pm 1$) read as

$$\sigma_{zz}^{ll}(\omega) = \frac{8\sigma_0 v_x^4}{\pi^2 \omega^2} \frac{\omega\tau}{1 + (\omega\tau)^2} \int_{-\infty}^{\infty} dk_z \int_0^{\infty} dk k |G_{ll}^z(\mathbf{K})|^2 f_l(E_{\mathbf{K},l})[1 - f_l(E_{\mathbf{K},l})], \tag{5.14}$$

where

$$|G_{ll}^z(\mathbf{K})|^2 = \frac{[(v_z - v_t)k^2 - (v_z + v_t)(\varepsilon_{k_z} + l\varepsilon_{\mathbf{K}})^2/v_x^2]^2}{\varepsilon_{\mathbf{K}}^4 + \varepsilon_{k_z}^2 \varepsilon_{\mathbf{K}}^2 + 2l\varepsilon_{k_z}\varepsilon_{\mathbf{K}}^3}.$$

For interband OCs, $\sigma_{zz}^{+-}(\omega) \simeq 0$ because we only consider photon absorption, and $\sigma_{zz}^{-+}(\omega)$ can be written as

$$\sigma_{zz}^{-+}(\omega) = \frac{16\sigma_0 v_x^4 \tau}{\pi^2 \omega} \int_{-\infty}^{\infty} dk_z \int_0^{\infty} dk k |G_{-+}^z(\mathbf{K})|^2 \frac{f_-(E_{\mathbf{K},-})[1 - f_+(E_{\mathbf{K},+})]}{1 + (\omega - 2\sqrt{v_x^2 k^2 + v_z^2 k_z^2})^2 \tau^2}, \qquad (5.15)$$

with

$$|G_{-+}^z(\mathbf{K})|^2 = \frac{[(v_z - v_t)k^2 - (v_z + v_t)(\varepsilon_{k_z}^2 - \varepsilon_{\mathbf{K}}^2)/v_x^2]^2}{\varepsilon_{\mathbf{K}}^4 - \varepsilon_{k_z}^2 \varepsilon_{\mathbf{K}}^2}.$$

5.3   Result and discussion

It is worth emphasizing that band structures of bulk 3D DSMs are different from those of single-layer or multilayer 3D DSMs. While in bulk 3D DSM samples, which are unconfined along the z axis, k_z is a continuous variable, in a confined system, k_z is quantized for sufficiently small thickness due to the formed quantum-well structure [53, 54, 122]. Such finite-size effect removes the band inversion and opens a band gap for sufficiently thin samples. Hence, the topological phase transition can be achieved in 3D DSMs through reducing the dimension (by reducing the thickness to a few layers), where the semimetal-insulator phase transition in type-I 3D DSMs [53, 54, 129] and the semimetal-semiconductor phase transition in type-II 3D DSMs [171] can be observed. In our case, the bulk PtTe$_2$ with a stable Dirac semimetal state is extended, and the corresponding effective Hamiltonian can be described by Eq. (5.1).

In numerical calculations, the low-energy fittings to the DFT band structure show that the corresponding velocities around the Dirac point of a bulk PtTe$_2$ are $v_x = v_y = 0.65 \times 10^6$ m/s, $v_z = 0.35 \times 10^6$ m/s, and $v_t = 0.51 \times 10^6$ m/s [172]. Supercritically tilted ($v_t > v_x$) type-II Dirac cones have open hyperbolic isoenergy contours. Therefore, the Fermi wave vector k_{Fz} along k_z, which has two components $k_{Fz}^{\pm} = E_F^e/[\hbar(v_t \pm v_z)]$ due to the geometric structure of the energy spectrum, should be applied to the numerical integrals [205, 206]. At a finite temperature, the Fermi-Dirac function indicates that electrons are distributed mainly within the range from $-2k_{Fz}^-$ to $2k_{Fz}^-$, which gives reasonable limits to use in our calculations. In addition, optical pump-terahertz probe (OPTP) spectroscopy and ultrafast time-resolved degenerate optical pump-optical probe (OPOP) measurements show that high quality PtTe$_2$ samples have fast lifetimes ($\tau < 1$ ps) [178, 179], which motivates the consideration of different energy relaxation times in our study.

Figure 5.1 summarizes the basic properties of PtTe$_2$, i.e., its crystal structure in Figs. 5.1(a) and 5.1(b), the calculated 3D tilted Dirac cone in Figs. 5.1(c) and 5.1(d), and the low-energy dispersion of its electrons or holes in Figs. 5.1(e) and 5.1(f). As shown in Figs. 5.1(a) and 5.1(b), the atomic structure of PtTe$_2$ consists of three covalently bonded Te-Pt-Te atomic planes, where six Te atoms surround the central Pt atom with crystal constants of $a = b = 4.09$ Å, and $c = 5.34$ Å [70]. The spacing between the layers is 0.59 nm, exhibiting weak van der Waals (vdW) interactions. Based on DFT calculations, the effective 4×4 Hamiltonian with time-reversal, inversion, and D_{3d}^3 symmetries is obtained, resulting in an energy dispersion with two gapless 3D Dirac cones at $\mathbf{K^c} = (0, 0, \pm k_z^c)$ [69]. One of the tilted 3D Dirac cones around $\mathbf{K^c} = (0, 0, k_z^c)$ is shown in Figs. 5.1(c) and 5.1(d). By expanding the Hamiltonian near the $\mathbf{K^c}$ point and keeping only the linear order terms, we arrive at Eq. (5.1). The corresponding energy spectrum is shown in Figs. 5.1(e) and 5.1(f), and the Dirac point is settled at zero energy. Equation (5.2) can be written in the form $E_{\mathbf{K},\pm} = T_{\mathbf{K}} \pm U_{\mathbf{K}}$, where $U_{\mathbf{K}}$ is a potential energy component and $T_{\mathbf{K}}$ is a linear
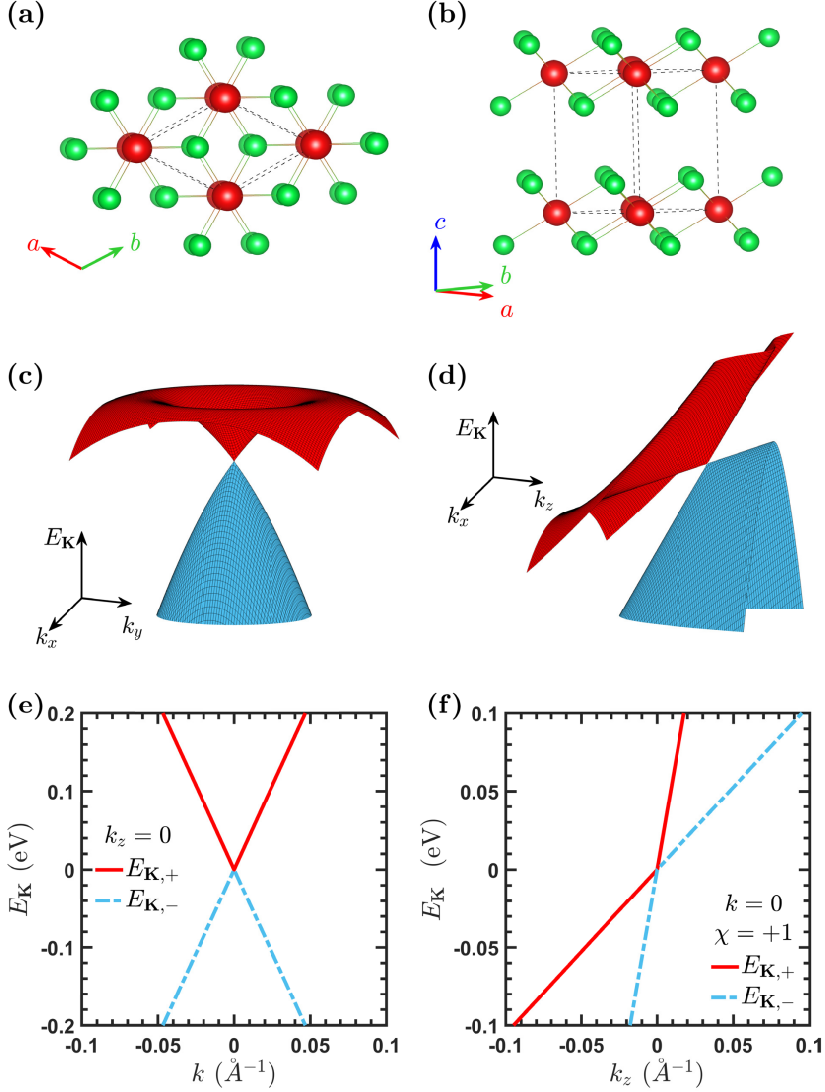
Figure 5.1: Crystal structure and energy dispersion of a type-II 3D DSM PtTe$_2$. Top (a) and side (b) views of the PtTe$_2$ crystal structure with $P\bar{3}m1$ symmetry. Green balls are Te atoms, and red balls are Pt atoms. The dashed lines delimit the unit cell. 3D band structure of PtTe$_2$ on the k_x-k_y plane and k_x-k_z plane is shown in (c) and (d), respectively, where the k_x-k_y plane corresponds to the a-b plane in (a) and k_z corresponds to the c axis in (b). PtTe$_2$ has two Dirac points located at $\mathbf{K^c} = (0, 0, \pm k_z^c)$. (c), (d) Only show one Dirac point around $\mathbf{K^c} = (0, 0, k_z^c)$. The red (blue) surface represents the conduction (valence) band [69]. By expanding the Hamiltonian near $\mathbf{K^c}$ and keeping only the linear terms, the type-II 3D Dirac cones with spin degeneracy can be obtained as Eq. (5.1), which are (e) isotropic in the k_x-k_y plane, and (f) pronouncedly tilted along the k_z direction.

kinetic term that tilts the Dirac cone. Due to $T_{\mathbf{K}} > U_{\mathbf{K}}$ along k_z in PtTe$_2$, the Lorentz invariance is violated and strongly tilted Dirac cones emerge at the topologically protected touching points between the electron and hole pockets [70]. Such an energy spectrum will lead to unique optical

Figure 5.2: The chemical potential for electrons E_F^e in an n-doped PtTe$_2$ as a function of electron density N_e at different temperatures (as indicated). The inset shows the magnified details of E_F^e in the marked area, for N_e from 10^{17} to 2×10^{17} cm^{-3}. E_F^e values practically coincide for $T < 10$ K.
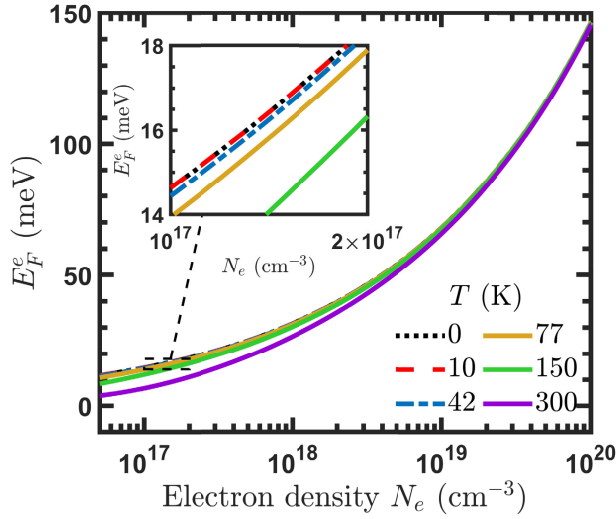
properties that are different from those of other Dirac systems.

In Fig. 5.2, we show the chemical potential (or Fermi level at zero temperature) of electrons E_F^e as a function of electron density N_e at different temperatures. The carrier number conservation law mandates that if the hole density N_h has the same concentration as N_e, the Fermi level of the holes E_F^h in the valence band is simply equal to $-E_F^e$. If N_e and N_h are zero, $E_F^e \simeq 0$ and $E_F^h \simeq 0$ at the Dirac point can be found using the integral bounds $(-2k_{F_z}^-, 2k_{F_z}^-)$ for k_z in Eqs. (5.5) and (5.6), which proves the numerical results. Similarly to a conventional semiconductor, the Fermi level for electrons in a Type-II 3D DSM increases with increasing electron density but decreases with increasing temperature, as shown in Fig. 5.2. Bulk PtTe$_2$ has high electron density [159] and Fermi-level tunability has been achieved in the doped Ir$_x$Pt$_{1-x}$Te$_2$ [230]. Therefore, in this work, the optical conductivity affected by different carrier densities and temperatures is also evaluated.

Figure 5.3 shows the contributions from different electronic transition channels to optical conductivities (OCs), for the light field linearly polarized along the x and z directions. The conditions for numerical calculations are specified in the caption of Fig. 5.3. To better visualize the details of the OCs, the wavelength λ is plotted in logarithmic scale in Figs. 5.3(b) and 5.3(d). We notice the following important features. (i) In both $\sigma_{xx}(\omega)$ and $\sigma_{zz}(\omega)$, intraband transitions give rise to long-wavelength optical absorption, whereas inter-band transitions mainly contribute to the optical absorption in the short-wavelength range ($\lambda < 2$ μm or $\omega > 150$ THz). (ii) $\sigma_{xx}(\omega)$ of a type-II 3D DSM is strongly dependent on photon energy in the long-wavelength range ($\lambda > 2$ μm or $\omega < 150$ THz), but varies very little when the photon energy is kept increasing beyond this range. This is similar to graphene [215, 216] that hosts the non-tilted and isotropic Dirac cone in the x-y plane [see Fig. 3.1]. (iii) As shown in Fig. 5.1(d), $\sigma_{zz}(\omega)$, which changes throughout the wavelength range, is different from $\sigma_{xx}(\omega)$ and exhibits the anisotropic optical properties of a type-II 3D DSM. More specifically, in the short-wavelength range $\sigma_{zz}(\omega)$ increases with increasing photon energy and in the long-wavelength range $\sigma_{zz}(\omega)$ requires less photon energy than $\sigma_{xx}(\omega)$. (iv) Optical absorption windows can be found in the $\approx$ 3-200 μm wavelength range
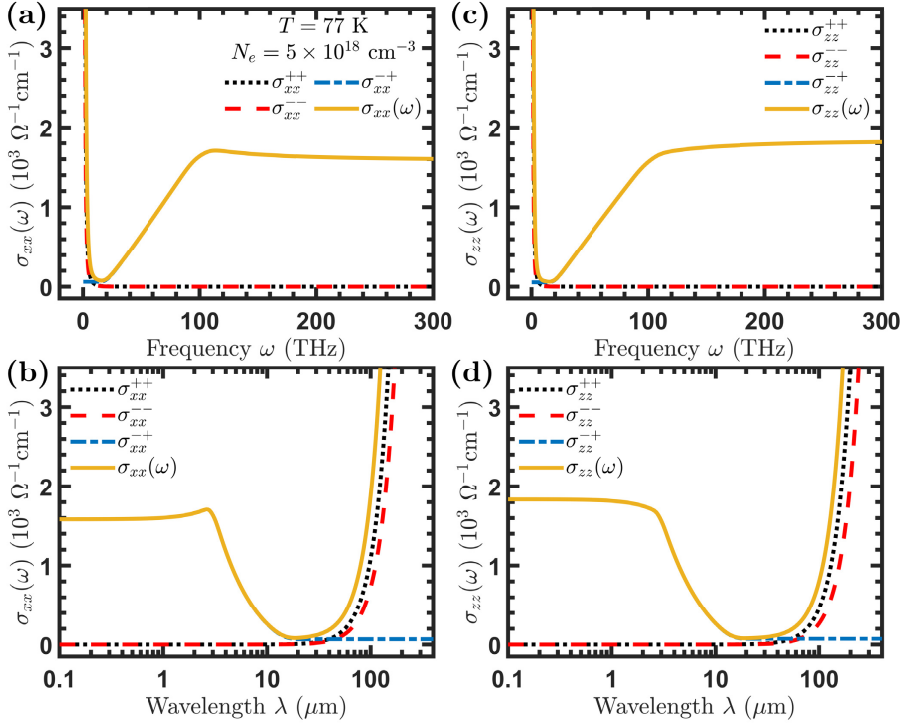
Figure 5.3: Contributions from different electronic transition channels to optical conductivities for the light field linearly polarized along the x and z directions at fixed temperature $T = 77$ K, electron density $N_e = 5 \times 10^{18}$ cm^{-3}, hole density $N_h = 5 \times 10^{17}$ cm^{-3}, and energy relaxation time $\tau = 0.5$ ps. (a), (b) Show the in-plane optical conductivity $\sigma_{xx}(\omega)$ as a function of frequency ω and light wavelength λ, respectively. (c), (d) Out-of-plane optical conductivity $\sigma_{zz}(\omega)$ as a function of ω and λ, respectively. Both $\sigma_{xx}(\omega)$ and $\sigma_{zz}(\omega)$ include intraband transitions (black dotted curve for σ_{++} and red dashed curve for σ_{--}) and the interband transition from the valence band to the conduction band (blue dashed-dotted curve for σ_{-+}). Ω is the unit of resistance Ohm.

for both $\sigma_{xx}(\omega)$ and $\sigma_{zz}(\omega)$. Such infrared absorption windows can be observed in other 2D and 3D Dirac systems and stem from the gapless Dirac cones in the energy band [133, 215, 216], as shown in Figs. 3.1 and 3.2.

The interesting features of the anisotropic optical absorptions shown in Fig. 5.3 can be understood with the help of Fig. 5.4, which shows the mechanism of carrier-photon scattering based on the electronic energy spectrum of the bulk PtTe$_2$. When the light radiation field is absent in an n-doped type-II 3D DSM, there is a single Fermi level of electrons E_F^e in the conduction band and all states below E_F^e are occupied, that is, there is no hole density ($N_h = 0$). When a light field is applied to the system [see Figs. 5.4(a) and 5.4(b)], the electrons in the valence band can gain energy from the external light field and be excited into the conduction band through photon absorption. Thus, both the electron density N_e and the Fermi level of electrons E_F^e in the conduction band increase, while the holes are left in the valence band with the Fermi level of the holes E_F^h corresponding to the hole density N_h. In such a case, the intraband electronic transitions accompanied by the absorption of photons can occur not only in the conduction band (σ_{xx}^{++} and σ_{zz}^{++}) but also in the valence band (σ_{xx}^{--} and σ_{zz}^{--}), which are a direct consequence of the broadening
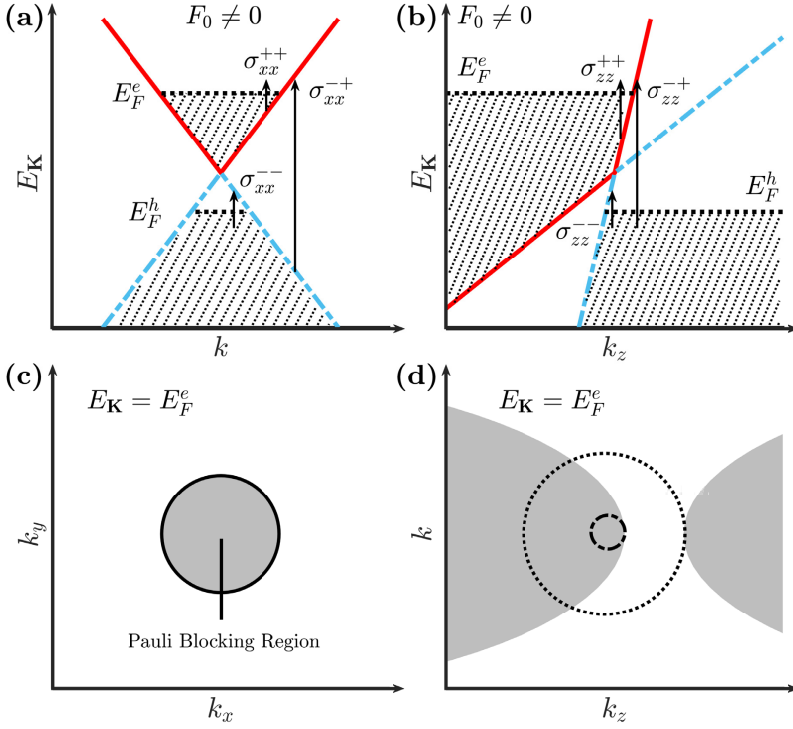
Figure 5.4: Schematic diagram of the electronic transitions accompanied by the photon absorption in an n-doped type-II 3D DSM. The optical absorption process for the light polarized (a) in the x-y plane and (b) along the z direction. $F_0 \neq 0$ refers to the case in the presence of the linearly polarized light field. E_F^e and E_F^h are, respectively, the Fermi level for electrons and holes, and the shaded areas refer to the occupied states. In-plane optical conductivities $\sigma_{xx}^{ll'}(\omega)$ and out-of-plane optical conductivities $\sigma_{zz}^{ll'}(\omega)$ are induced both by intraband ($ll' = ++$ and $--$) and interband ($ll' = -+$) transition channels. In line with (a) and (b), the isoenergy contours of $E_{\mathbf{K}} = E_F^e$ in the k_x-k_y plane and in the k-k_z plane are shown in (c) and (d), respectively. The solid-shaded areas represent the Pauli blocking regions, and the rest areas represent the allowed transitions. The wave vector contour $\Lambda_x = \hbar\omega/(2\hbar v_x)$ for k_x is marked by the solid curve in (c). Two critical wave vector cutoffs, $\Lambda_z^{\pm} = \hbar\omega/[2\hbar(v_t \pm v_z)]$ for k_z, are marked in (d): Λ_z^- as a dotted curve and Λ_z^+ as a dashed-dotted curve.

of the scattering states around the Fermi levels. Furthermore, as shown in Fig. 5.3, intraband transitions, which occur under low photon energy, are similar to the free carrier absorption, i.e., Eqs. (5.11) and (5.14) have a formula similar to the Drude OC of free electrons [208]. The Dirac cone in type-II 3D DSMs is tilted along k_z, so that in the long-wavelength range $\sigma_{zz}(\omega)$ requires less photon energy than $\sigma_{xx}(\omega)$ due to more intraband transition channels appearing along k_z [cf. solid shaded areas in Figs. 5.4(c) and 5.4(d)].

The interband OCs, σ_{xx}^{-+} and σ_{zz}^{-+} of PtTe$_2$ show more clearly the anisotropic features for a type-II 3D DSM and can also be explained by Fig. 5.4. In the presence of the light field, the interband OC at a photon energy $\hbar\omega$ is governed by $f(E_{\mathbf{K},-})[1 - f(E_{\mathbf{K},+})]\delta_{\mathbf{K},\mathbf{K}'}\delta(E_{\mathbf{K},+} - E_{\mathbf{K},-} - \hbar\omega)$ in Eqs. (5.12) and (5.15), where $f(E_{\mathbf{K},-})[1 - f(E_{\mathbf{K},+})]$ is imposed by the Pauli principle, $\delta_{\mathbf{K},\mathbf{K}'}$ denotes momentum conservation, and $\delta(E_{\mathbf{K},+} - E_{\mathbf{K},-} - \hbar\omega)$ denotes energy conservation.

Introducing the Fermi level E_F^e into energy conservation, while momentum conservation provides momentum alignment as shown in Figs. 5.4(a) and 5.4(b), $E_{\mathbf{K},+} - E_{\mathbf{K},-} = 2E_F^e = \hbar\omega$ gives the wave vector contour $\Lambda_x = \hbar\omega/(2\hbar v_x)$ in the k_x-k_y plane, while two wave vector cutoffs $\Lambda_z^{\pm} = \hbar\omega/[2\hbar(v_t \pm v_z)]$ can be found for k_z, as shown in Figs. 5.4(c) and 5.4(d). For light linearly polarized along the x direction, there are two cases: (i) in the low photon energy range [$\hbar\omega \leq 2E_F^e$, solid shaded area inside the solid curve in Fig. 5.4(c)], due to Fermi-Dirac distribution at a finite temperature the interband transitions are almost Pauli-blocked, which leads to a very small σ_{xx}^{-+} in this range, but intraband transitions can still occur as we mentioned before; (ii) in the high photon energy range [$\hbar\omega > 2E_F^e$, outside the solid contour in Fig. 5.4(c)], σ_{xx}^{-+} increases rapidly and then varies very little with increasing photon energy because only viable states are allowed to contribute to σ_{xx}^{-+}. This case is analogous to other isotropic and non-tilted Dirac systems at finite temperatures, such as graphene [see Fig. 3.1] [215, 216]. Since the energy dispersions of PtTe$_2$ and graphene in the x-y plane are both isotropic, their in-plane OCs are contributed by intraband and interband transitions, while the interband transition channels are limited by the closed 2D Fermi surface because only viable states are allowed to contribute to interband transitions. Consequently, their in-plane OCs have similar absorption windows and are nearly ω independent at a high photon energy regime in the case of finite temperature [152, 215, 216], as shown in Figs. 3.1 and 5.3.

In contrast to σ_{xx}^{-+}, σ_{zz}^{-+} induced by the polarization of light along k_z has unique properties that stem from the hyperbolic isoenergy contours opened by the tilted Dirac cone, as shown in Figs. 5.4(b) and 5.4(d). Two wave vector cutoffs $\Lambda_z^{\pm}$ indicate that σ_{zz}^{-+} has three photon energy regimes: (i) in the low photon energy regime [$\hbar\omega \leq 2E_F^e/(\gamma+1)$ with $\gamma = v_t/v_z$ being the tilt index, inside the dashed-dotted curve in Fig. 5.4(d)], interband transitions are almost Pauli-blocked, so that σ_{zz}^{-+} nearly vanishes and intraband transitions mainly contribute to the OC in this case; (ii) in the intermediate photon energy regime [$2E_F^e/(\gamma+1) < \hbar\omega \leq 2E_F^e/(\gamma-1)$, outside the dashed-dotted curve and inside the dotted curve in Fig. 5.4(d)], some states are Pauli-blocked by the left branch of the hyperbola, where σ_{zz}^{-+} increases rapidly with increasing photon energy; (iii) in the high photon energy regime [$\hbar\omega > 2E_F^e/(\gamma-1)$, outside the dotted curve in Fig. 5.4(d)], the contour of contributing states is intersected by the right branch of the hyperbolic Pauli blocking region near the tilt axis. Due to momentum alignment, the right branch of Pauli blocking significantly reduces the absorption of high-frequency photons, hence, σ_{zz}^{-+} still increases, but increases slowly with increasing photon energy [see Figs. 5.3(c) and 5.3(d)]. In a word, since optical absorption describes transitions from occupied states to empty states, the intraband transitions require fewer photon energies whereas a relatively larger photon energy is needed for the interband transitions for a type-II 3D DSM. Consequently, an optical absorption window can be achieved through different energy requirements for intertransition and intratransition channels, and the anisotropic optical conductivities are induced by the tilted 3D Dirac cone in a type-II 3D DSM.

In this study, we take the electronic energy relaxation time τ as an input parameter that accounts for the effect of the broadening of the scattering states. The dependence of $\sigma_{xx}(\omega)$ and $\sigma_{zz}(\omega)$ on τ is shown, respectively, in Figs. 5.5(a) and 5.5(d) for fixed temperature, electron density and hole density. A longer energy relaxation time corresponds to a smaller broadening of the scattering state, and thus to a sample with higher carrier mobility. Neither $\sigma_{xx}(\omega)$ nor $\sigma_{zz}(\omega)$ changes with varying τ in the high photon energy regime but they both strongly depend on τ at a lower photon energy. This is because the broadening of the scattering states mainly affects the intraband transitions, as shown in Fig. 5.4. In addition, both $\sigma_{xx}(\omega)$ and $\sigma_{zz}(\omega)$ in the low photon energy regime exhibit redshift with increasing τ, so that wider and deeper optical absorption windows of $\sigma_{xx}(\omega)$ and $\sigma_{zz}(\omega)$ can be observed for the bulk PtTe$_2$ samples with higher electronic mobilities.

Figure 5.5: (a), (b) In-plane OC, $\sigma_{xx}(\omega)$, and out-of-plane OC, $\sigma_{zz}(\omega)$, as a function of light wavelength λ at different energy relaxation times, respectively. The conditions maintained shown in the legends of (a) for $\sigma_{xx}(\omega)$ are also applied to (b) for $\sigma_{zz}(\omega)$, with an invariable hole density $N_h = 5 \times 10^{18}$ cm^{-3}.

Figures 5.6(a) and 5.6(b) show $\sigma_{xx}(\omega)$ and $\sigma_{zz}(\omega)$ as a function of the light wavelength λ at different temperatures T, respectively. The fixed energy relaxation time, electron density and hole density are specified in the figure. Combining the results with Figs. 5.2 and 5.4, we notice: (i) E_F^e decreases and E_F^h increases with increasing temperature at the fixed electron and hole densities; (ii) in the high photon energy regime ($\lambda < 2$ μm), $E_F^e - E_F^h \ll \hbar\omega$ leads to temperature independent $\sigma_{xx}(\omega)$ and $\sigma_{zz}(\omega)$; (iii) in the intermediate wavelength range (2 μm $< \lambda < 20$ μm), $\sigma_{xx}(\omega)$ is slightly affected by the temperature, which is similar to the experimental results observed in a bulk sample of type-I 3D DSM Cd$_3$As$_2$ (see Fig. 3.2) due to the similar energy dispersion for the k_x-k_y plane [133], whereas $\sigma_{zz}(\omega)$ is nearly temperature independent since the Dirac cone tilts along the k_z direction; (iv) intraband electronic transitions need the photon
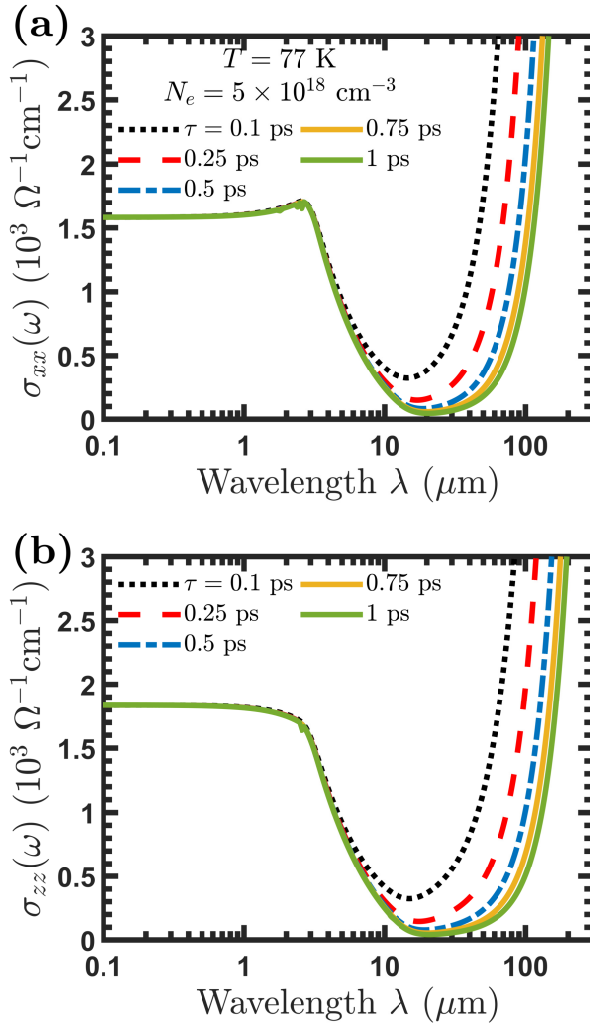
Figure 5.6: (a), (b) Show the in-plane OC, $\sigma_{xx}(\omega)$, and the out-of-plane OC, $\sigma_{zz}(\omega)$, as a function of light wavelength λ at different temperatures, respectively. The fixed conditions shown in the legends of (a) for $\sigma_{xx}(\omega)$ are also applied to (b) for $\sigma_{zz}(\omega)$, with an invariable hole density $N_h = 5 \times 10^{18}$ cm^{-3}.

energy to overcome the effect of thermal broadening of the electron distribution function, thus both $\sigma_{xx}(\omega)$ and $\sigma_{zz}(\omega)$ are sensitive to temperature in the low photon energy regime ($\lambda > 20$ μm). As a result, wider and deeper optical absorption windows can be achieved in both $\sigma_{xx}(\omega)$ and $\sigma_{zz}(\omega)$ by decreasing the temperature.

In Figs. 5.7(a) and 5.7(b), $\sigma_{xx}(\omega)$ and $\sigma_{zz}(\omega)$ versus light wavelength λ are evaluated at different electron densities, for fixed temperature, energy relaxation time and hole density. With increasing electron density N_e, the Fermi level of electrons E_F^e becomes higher, as shown in Fig. 5.2, which implies that the empty states in the conduction band have higher energies due to the linear shape of the energy spectrum. Since optical transitions occur mainly through exciting electrons from occupied states to empty states, a higher E_F^e corresponds to a higher transition energy.
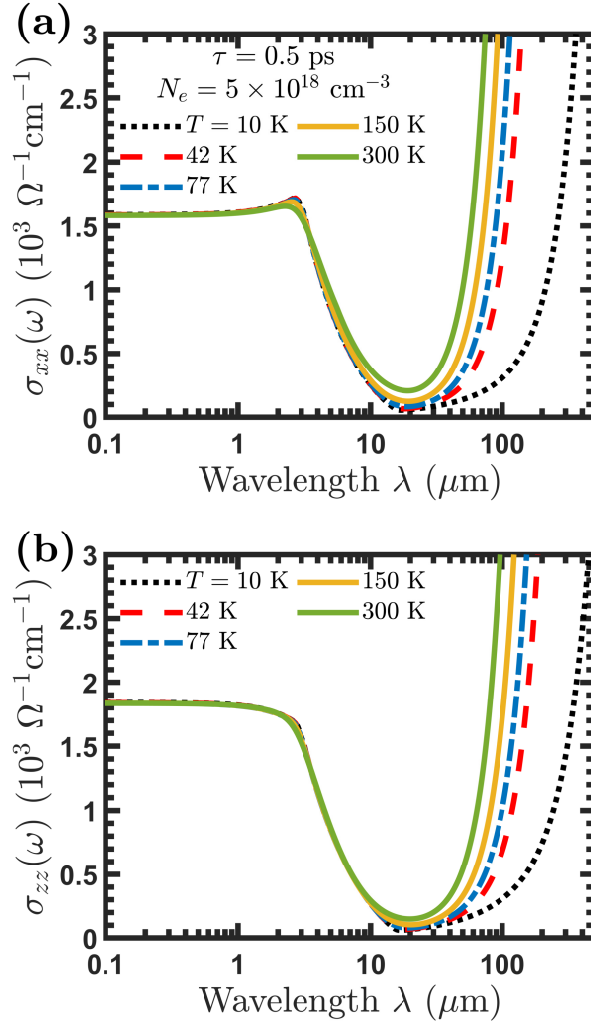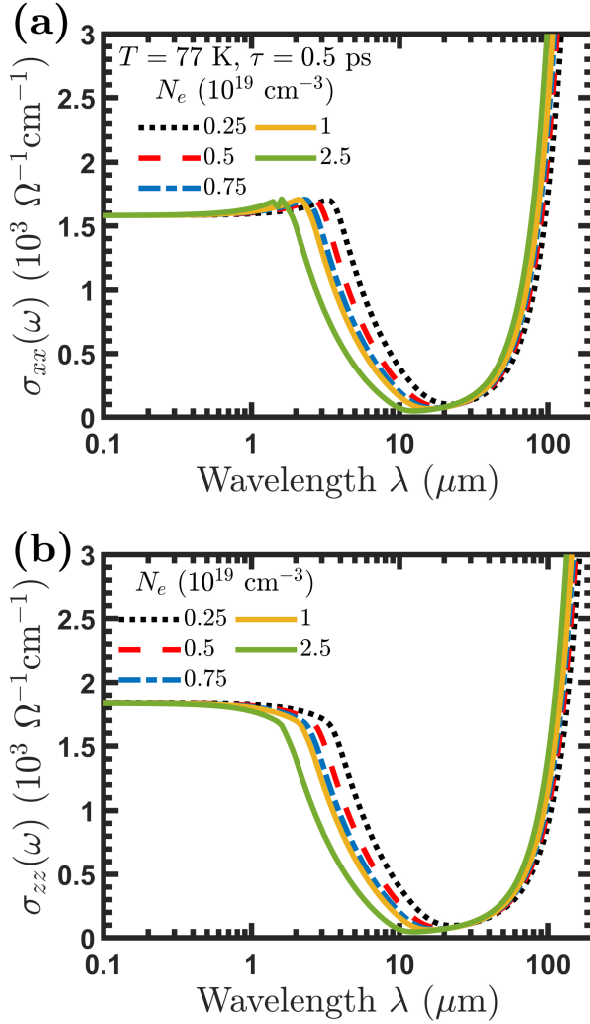
Figure 5.7: (a), (b) Show the in-plane OC, $\sigma_{xx}(\omega)$, and the out-of-plane OC, $\sigma_{zz}(\omega)$, as a function of light wavelength λ at different electron densities, respectively. The fixed conditions shown in the legends of (a) for $\sigma_{xx}(\omega)$ are also applied to (b) for $\sigma_{zz}(\omega)$, with an invariable hole density $N_h = 5 \times 10^{18}$ cm^{-3}.

As a result, systematic blueshift for both $\sigma_{xx}(\omega)$ and $\sigma_{zz}(\omega)$ can be observed throughout the light wavelength range in a higher electron density PtTe$_2$ sample. Furthermore, when E_F^e becomes higher, interband transitions also require a higher photon energy, that is, $\hbar\omega > 2E_F^e$, but intraband transitions only require a few photon energies to overcome the broadening of scattering states, as shown in Fig. 5.4. Consequently, increasing E_F^e in PtTe$_2$ corresponds to a more conspicuous blueshift of $\sigma_{xx}(\omega)$ and $\sigma_{zz}(\omega)$ in the high photon energy regime, and thus results in wider optical absorption windows. Furthermore, our results for $\sigma_{xx}(\omega)$ shown in Fig. 5.5(c) are very similar to the gate-tunable optical absorption window in the 2D Dirac system graphene [see Fig. 3.1(d)] [216], and it is because the energy dispersion of PtTe$_2$ in the x-y plane is similar to that of graphene. The Fermi level tunability in the doped Ir$_x$Pt$_{1-x}$Te$_2$ has been reported [230], therefore,

based on our analysis we propose that anisotropic and tunable optical absorption windows could be achieved in the bulk PtTe$_2$ sample as well, which can help to further explore and optimize the optoelectronic applications of type-II 3D DSMs.

By synthesizing the results of this chapter with the findings from Chapter 3, we can find that the OCs of type-II and type-I 3D DSMs exhibit both similarities and differences. Both possess anisotropic OCs, but the anisotropy of type-II is more pronounced in the higher photon energy range. Both type-I and type-II DSMs have optical absorption windows, but the response of this window to temperature, energy relaxation time, and electron density is different. The primary reason is that electron excitations in type-I DSMs is mainly influenced by the Berry curvature and band inversion structure, whereas in type-II DSMs, electron excitations near the Dirac point is predominantly affected by the tilted band structure. From the similarities in their OCs, we can see that both type-I and type-II DSMs share the properties of Dirac fermions; however, the differences denote fundamental distinctions in the electron excitation mechanisms near the Dirac point. Our results, therefore, reveal the unique OC of type-II 3D DSMs, offering a theoretical expansion of the study of Dirac semimetals and providing a supplement for materials with tilted Dirac cones. Additionally, the tunability of the OCs that we have proposed will provide guidance for the experiment and application of type-II DSMs in the optical and optoelectronic areas.

5.4 Conclusion of this chapter

Based on the effective Hamiltonian of the *n*-doped type-II 3D DSM PtTe$_2$, we employ the energy balance equation to calculate its anisotropic optical conductivity in different linearly polarized directions of a light field. In addition, we further study the effects of energy relaxation time, temperature, and electron density on its optical conductivity.

As a typical type-II 3D DSM, PtTe$_2$ has the strongly tilted 3D Dirac cone along the k_z direction and the isotropic energy spectrum in the k_x-k_y plane. When bulk PtTe$_2$ interacts with the linearly polarized light field, its in-plane optical conductivity $\sigma_{xx}(\omega)$ is distinctly different from the out-of-plane optical conductivity $\sigma_{zz}(\omega)$ due to its anisotropic energy dispersion. The intraband transitions dominate $\sigma_{xx}(\omega)$ and $\sigma_{zz}(\omega)$ at a low photon energy, whereas the interband transitions give rise to $\sigma_{xx}(\omega)$ and $\sigma_{zz}(\omega)$ in the high photon energy range accompanied by distinguishable anisotropic optical absorptions, which indicates that the tilted 3D Dirac cones of PtTe$_2$ mainly affect interband transitions. Interestingly, with the different energy requirements for intertransition and intratransition channels, for both $\sigma_{xx}(\omega)$ and $\sigma_{zz}(\omega)$ the tilted 3D Dirac cones of a type-II 3D DSM will lead to the anisotropic optical absorption windows. We found that the dependence of $\sigma_{xx}(\omega)$ on energy relaxation times, temperature, and electron densities is similar to that of other Dirac systems with isotropic energy in the *x-y* plane, but $\sigma_{zz}(\omega)$ has a distinctly different behavior that stems from the unique energy spectrum of a type-II 3D DSM. In addition, for bulk PtTe$_2$ we also propose that the position and width of the optical absorption windows are tunable by tuning its Fermi level.

This theoretical foundation will facilitate further understanding of the anisotropic optical properties of type-II 3D DSMs and enable further exploration of the possible applications of bulk PtTe$_2$ and similar materials in optoelectronic devices.

Chapter 6

Transport and quantum lifetimes of type-II 3D DSMs

The transport lifetime of a solid material is the average time during which electrons move without changing their momentum direction, while the quantum lifetime is the average time during which electrons maintain a given quantum state [208, 209]. Experimentally, the transport lifetime can be obtained by measuring the Hall mobility, whereas the quantum lifetime is indirectly obtained through quantum oscillations that come from the quantized Landau levels when a magnetic field is applied [158]. Quantum oscillations studied in solid materials usually are based on the Shubnikov-de Haas (SdH) effect or the de Haas-van Alphen (dHvA) effect. The SdH effect refers to the phenomenon in which the electrical conductivity of a material exhibits periodic oscillations with the inverse of the magnetic field at a low temperature. The dHvA effect, on the other hand, refers to the periodic oscillations of the magnetization of a material with the inverse of the magnetic field under similar conditions.

Taking the dHvA effect as an example, we introduce the experimental methods used to obtain the quantum lifetime, effective mass, and mobility of a type-II 3D DSM. As shown in Fig. 6.1, under different temperatures (T) and different magnetic directions (with $B \parallel c$ representing the out-of-plane case and $B \parallel ab$ representing the in-plane case), the magnetization of a high-quality PtTe$_2$ bulk sample is measured as the magnetic field changes. The oscillatory components of the magnetization (ΔM) as a function of the inverse magnetic field ($1/B$) are obtained for different orientations. By applying a Fast Fourier Transform (FFT), the oscillation frequency F accompanied by the oscillation amplitude of ΔM versus $1/B$ can be determined for both the in-plane and out-of-plane cases [157]. Using the Onsager relation, $F = (\Phi_0/2\pi^2)A_F$, where $\Phi_0 = h/2e$ is the magnetic flux quantum, the Fermi surface area A_F corresponding to different frequencies F can be obtained [156, 157]. Considering the Berry phase, the dHvA effect in a 3D Dirac electronic system can be described by the Lifshitz-Kosevich (LK) formula [156, 157]:

$$\Delta M \propto -B^{0.5} R_T R_D R_S \sin\left[2\pi\left(\frac{F}{B} - \gamma - \delta\right)\right].$$

Here, $R_T = (\alpha T m^*/B)/[\sinh(\alpha T m^*/B)]$, $R_D = \exp(-\alpha T_D m^*/B)$, $R_s = \cos(\pi g m^*/2m_e)$, where m^* and m_e are the effective mass and rest mass of the electron, respectively, T_D is the Dingle temperature, and $\alpha = 2\pi^2 k_B/e\hbar$ is a constant. R_T and R_D derive from the broadening in Landau levels induced by temperature effect in Fermi-Dirac distribution and electron scattering, respectively. R_T describes the temperature dependence of the oscillation amplitude, while R_D captures the field-dependent damping of the oscillation amplitude. In addition, the periodic oscillation of ΔM is
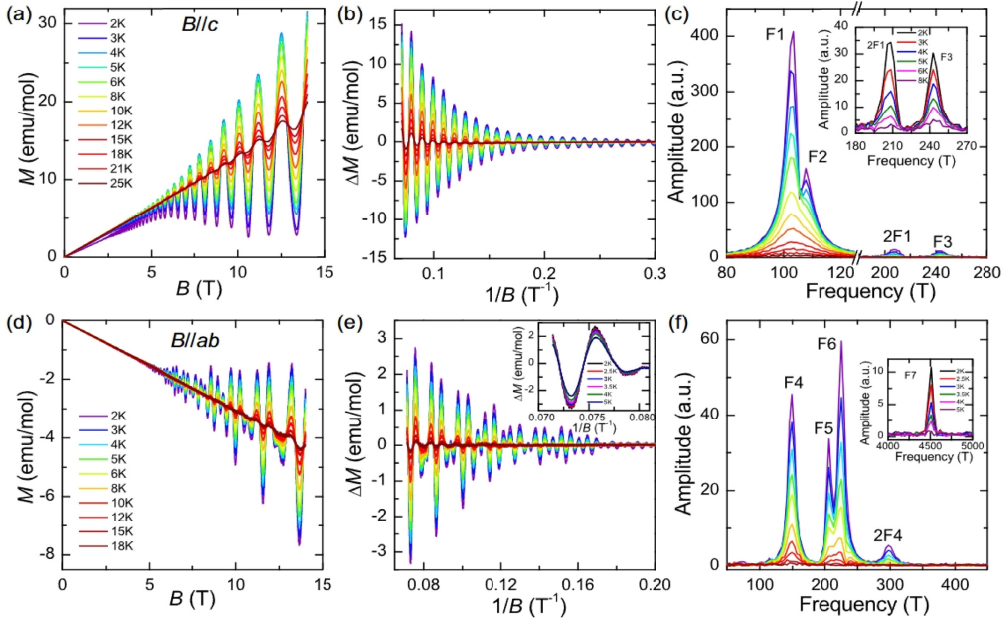
Figure 6.1: The de Haas-van Alphen (dHvA) oscillation experimental results of high-quality bulk $PtTe_2$ samples. (a), (d) Show the variation of out-of-plane and in-plane isothermal magnetization of bulk $PtTe_2$ with respect to the magnetic field at different temperatures, respectively. Corresponding to (a) and (d), (b) and (e) show the oscillatory components of the in-plane and out-of-plane magnetization as a function of the inverse magnetic field ($1/B$) in bulk $PtTe_2$, respectively. (c), (f) Fast Fourier transform (FFT) spectra of the quantum oscillations from (b) and (e), where the x axis represents the oscillation frequency obtained from the FFT. The results are adapted from Ref. [157].

depicted by the term of the sine function with a phase factor $-\gamma - \delta$, where $\gamma = 1/2 - \phi_B/2\pi$ and ϕ_B is the Berry phase [156, 157]. The dimensionality of the Fermi surface determines the phase shift δ, and for a 3D Dirac electronic system, $\delta = \pm 1/8$ [106, 107], as mentioned in Sec. 1.2.2.

Then, in Figs. 6.2(a) and 6.2(c), by fitting the temperature dependence of the FFT amplitude using the thermal damping factor R_T, the effective mass corresponding to different FFT frequencies can be obtained. As shown in Figs. 6.2(b) and 6.2(d), fitting the oscillation data with the multiband LK formula accurately yields the oscillations of ΔM when $B \parallel c$ and $B \parallel ab$, from which the corresponding transport properties can be derived. The quantum lifetime $\tau = \hbar/(2\pi k_B T_D)$ can be obtained from the Dingle temperature T_D. Furthermore, using the definition of mobility $\mu = e\tau/m^*$ and combining the effective mass with the quantum lifetime, the quantum mobility can be evaluated. The experimental data for the bulk $PtTe_2$ derived from Figs. 6.1 and 6.2 are summarized in the Tab. 6.1. In addition to the dHvA experiment, the SdH experiment can also measure the transport properties of type-II 3D DSMs [159]. From Figs. 6.1, 6.2, Tab. 6.1, and related SdH experimental results, unique features of type-II 3D DSMs can be observed: $PtTe_2$ and $PdTe_2$ have high carrier mobilities, reaching the order of about 10^4 $cm^2V^{-1}s^{-1}$ [156]; both $PtTe_2$ and $PdTe_2$ are type-II 3D DSMs, and anisotropic transport properties have been observed in their bulk samples [156, 157]. The band structure of type-II DSMs features anisotropic and tilted Dirac cones [70], which is speculated to be the reason for the anisotropic transport prop-
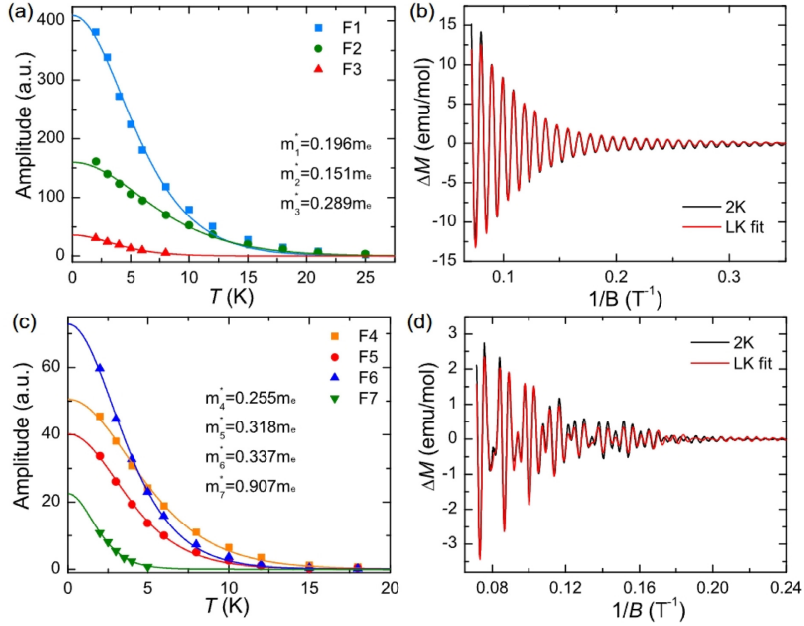
Figure 6.2: (a), (c) Temperature dependence of out-of-plane ($B \parallel c$) and in-plane ($B \parallel ab$) FFT amplitude; the solid curves represent the LK fit for effective mass. The results of the fitting are shown in (a) and (c). (b), (d) The multiband LK fitting (red curves) of the out-of-plane and in-plane oscillation patterns (black curves) at $T = 2$ K. The results are adapted from Ref. [157].

erties [157], as shown in Tab. 6.1, there are significant differences between the in-plane and out-of-plane quantum lifetimes, effective masses, and quantum mobilities.

However, to date, research on the lifetime and mobility of type-II 3D DSMs still remains for the case of the aforementioned experimental measurements, and a systematic theoretical explanation of the experiments is still lacking. Therefore, we aim to conduct a theoretical study of properties

Table 6.1: The derived parameters from dHvA oscillations for high-quality bulk PtTe$_2$. F is the oscillation frequency from the FFT spectra, T_D is the Dingle temperature, m^* (in terms of m_e) is the effective mass, τ_q is the quantum lifetime, and μ_q is the quantum mobility. μ_1 to μ_6 mark the different oscillation frequencies. The parameters of this table are adapted from Ref. [157].

	F (T)	T_D (K)	m^*/m_e	τ (Ps)	μ_q (cm^2/Vs)
		$T = 2$ K, $B \parallel c$			
μ_1	102.7	4.3	0.196	0.28	9642
μ_2	107.8	9.5	0.151	0.13	6007
μ_3	232.2	4.2	0.289	0.29	3754
		$T = 2$ K, $B \parallel ab$			
μ_4	142.1	6.8	0.255	0.18	1238
μ_5	196.8	2.8	0.318	0.44	2443
μ_6	215.1	4.2	0.337	0.29	1523

such as the momentum lifetime for type-II 3D DSMs, starting from their effective Hamiltonian. As mentioned in the previous chapter, PtTe$_2$ has a typical type-II 3D DSM state [70], and its bulk samples are very stable in air and easy to prepare [70, 153, 154]. As a result, many studies have been reported on the transport properties of PtTe$_2$, which prompted us to choose PtTe$_2$ as the basis for our theoretical research. In theory, the momentum balance equation, derived from the Boltzmann equation, is an efficient tool for calculating the transport properties of electronic systems. Its advantage lies in that by only using the impurity density as an input parameter in the derivation, one can obtain a clear and specific expression for the momentum lifetime, as shown in Eq. (2.40). Based on the Boltzmann equation, not only can the quantum lifetime corresponding to small-angle scattering be calculated, but large-angle scattering can also be considered to obtain the transport lifetime, which is an important advantage of the Boltzmann equation [208]. The derivation process of the momentum balance equation can be traced step by step, making the physical process of scattering very clear [209].

In a few words, the main objective of this chapter is to calculate the momentum lifetime of bulk PtTe$_2$ using the traceable momentum balance equation based on its effective Hamiltonian, and to combine the calculation results with existing experiments to provide a detailed explanation of the transport properties of type-II 3D DSMs. We have discussed the one electron aspects of type-II 3D DSMs based on PtTe$_2$ in the previous chapter, such as band structure and chemical potential. Therefore, this chapter will not repeat that introduction but instead directly proceed with the derivation and calculation of the transport properties of the *n*-doped bulk PtTe$_2$.

6.1   Eletron-electron screening length of type-II 3D DSMs

In electronic systems at low temperatures, carrier-impurity (*c-i*) scattering is the principle channel for carrier relaxation processes. Considering the interaction between charged impurities and electrons through the Coulomb potential in an *n*-doped high-quality bulk PtTe$_2$, we first need to find the screening length of electron-electron (*e-e*) interactions in its sample at low temperatures.

The induced potential from the *e-e* scattering in Sec. 2.1 can be written as

$$V_{ind}(\mathbf{Q},t) = V_Q \sum_{\mathbf{K}} \sum_{l,l'} \langle \mathbf{K}+\mathbf{Q},l'|\delta N|\mathbf{K}l\rangle \langle \mathbf{K}+\mathbf{Q},l'|e^{-i\mathbf{Q}\cdot\mathbf{R}}|\mathbf{K}l\rangle$$

$$= \lim_{\eta \to 0} V_Q V(\mathbf{Q},t) \sum_{\mathbf{K}} \sum_{l,l'} F_{l,l'}(\mathbf{K},\mathbf{Q})\Pi_{l,l'}(\omega;\mathbf{K},\mathbf{Q}), \qquad (6.1)$$

where $\mathbf{Q} = (q_x,q_y,q_z)$ is the change of electron wave vector during the *e-e* scattering events, $V_Q = (4\pi e^2)/(\kappa Q^2)$ is the Fourier transform of the 3D Coulomb potential $V(\mathbf{R}) = e^2/(\kappa|\mathbf{R}|)$, with κ being the static dielectric constant of the system. δN represents the density fluctuations induced by the perturbation, and $V(\mathbf{Q},t)$ is the total self-consistent perturbation potential. Additionally, $F_{l,l'}(\mathbf{K},\mathbf{Q}) = |\langle\mathbf{K}+\mathbf{Q},l'|e^{-i\mathbf{Q}\cdot\mathbf{R}}|\mathbf{K},l\rangle|^2$ is the form factor of the many-body interaction, and

$$\Pi_{l,l'}(\omega;\mathbf{K},\mathbf{Q}) = g\frac{f(E_{\mathbf{K}+\mathbf{Q},l'}) - f(E_{\mathbf{K},l})}{E_{\mathbf{K}+\mathbf{Q},l'} - E_{\mathbf{K},l} - \hbar\omega + i\hbar\eta} \qquad (6.2)$$

is the corresponding density-density correlation function, $g = g_s g_v = 4$ represents spin and valley degeneracy, and $f(E_{\mathbf{K},l})$ is the Fermi-Dirac distribution function for the electron in the initial state $|\mathbf{K},l\rangle$. Using the definition $\hat{\varepsilon}(\mathbf{q},t) = 1 - V_{ind}(\mathbf{q},t)/V(\mathbf{q},t)$ [207], we can obtain the expression for

the RPA dielectric function as

$$\hat{\varepsilon}(\omega, \mathbf{Q}) = 1 - \lim_{\eta \to 0} V_Q \sum_{\mathbf{K}} \sum_{l,l'} F_{l,l'}(\mathbf{K}, \mathbf{Q}) \Pi_{l',l}(\omega; \mathbf{K}, \mathbf{Q}). \tag{6.3}$$

Through the Dirac identity $\lim_{\eta \to 0}[1/(x \pm i\eta)] = P\{1/x\} \mp i\pi\delta(x)$ with $P\{1/x\}$ being the principle value and $\delta(x)$ being the Dirac-δ function, the real part of the RPA dielectric function can be obtained as

$$\varepsilon_{Re}(\omega, \mathbf{Q}) = 1 - \frac{4\pi e^2}{\kappa Q^2} \sum_{\mathbf{K}} \sum_{l,l'} F_{l,l'}(\mathbf{K}, \mathbf{Q}) \Pi_{l',l}^{Re}(\omega; \mathbf{K}, \mathbf{Q}), \tag{6.4}$$

where the real part of the density-density correlation function reads as

$$\Pi_{l,l'}^{Re}(\omega; \mathbf{K}, \mathbf{Q}) = g \frac{f(E_{\mathbf{K}+\mathbf{Q},l'}) - f(E_{\mathbf{K},l})}{E_{\mathbf{K}+\mathbf{Q},l'} - E_{\mathbf{K},l} - \hbar\omega}. \tag{6.5}$$

For the n-doped PtTe$_2$ studied in our research, impurity scattering is insufficient to cause interband transitions for electrons and the valence band is fully occupied, which means that there will be no intraband electron transitions in the valence band. Therefore, in Eqs. (6.4) and (6.5), we only consider the case of intraband electron scattering with $l = l' = +1$ in the conduction band. The transport properties of a material are normally measured at very low temperature, so we consider the low-temperature limit ($T \to 0$). Additionally, the static dielectric function and the long-wavelength limit give $\omega = 0$ and $Q \to 0$. Hence, from $Q \to 0$, we can first obtain $F_{++}(\mathbf{K}, \mathbf{Q}) \simeq 1$, and with $\omega = 0$, the summation over the density-density correlation function can be written as

$$\Lambda = -\lim_{Q \to 0} g \sum_{\mathbf{K}} \Pi_{++}^{Re}(0; \mathbf{K}, \mathbf{Q}) = -g \sum_{\mathbf{K}} \frac{\partial f(E_{\mathbf{K},+})}{\partial E_{\mathbf{K},+}}, \tag{6.6}$$

where $f(E_{\mathbf{K},+})$ is the electronic Fermi-Dirac function. At the $T \to 0$ limit, $\partial f(E_{\mathbf{K},+})/E_{\mathbf{K},+} = -\delta(E_F - E_{\mathbf{K},+})$ allows us to further iterate Eq. (6.6) into

$$\Lambda = \frac{2}{\pi^2} \int_0^\infty dk \int_{-\infty}^\infty dk_z k \delta(E_F - E_{\mathbf{K},+}) \tag{6.7}$$

with E_F being the Fermi level of electrons. Then, through the properties of Dirac-δ function, which read as

$$\delta[f(x)] = \sum_i \frac{\delta(x - x_i)}{|f'(x_i)|}, \tag{6.8}$$

and

$$\int_{-\infty}^\infty g(x)\delta(x - x_i)dx = g(x_i), \tag{6.9}$$

where x_i is the ith root of $f(x) = 0$, $f'(x_i) = \partial f(x)/\partial x|_{x=x_i}$, we can analytically solve the integral over k_z in Eq. (6.7) and obtain

$$\Lambda = \frac{2}{\pi^2} \sum_i \int_0^\infty dk \frac{k}{|Z_{\mathbf{K}}|}, \tag{6.10}$$

where

$$Z_{\mathbf{K}} = \frac{\partial(E_F - E_{\mathbf{K},+})}{\partial k_z} = -\frac{\partial E_{\mathbf{K},+}}{\partial k_z} = -\left(\hbar v_t + \frac{\hbar v_z^2 k_z}{\sqrt{v_x^2 k^2 + v_z^2 k_z^2}}\right),$$

and $k_z \equiv k_z^i$ with

$$k_z^i = \frac{-v_t E_F + i\sqrt{\hbar^2(v_t^2 - v_z^2)v_x^2 k^2 + v_z^2 E_F^2}}{\hbar(v_t^2 - v_z^2)}.$$

Here, the band parameters $v_t > v_z$ of PtTe$_2$ indicate that two roots of k_z can be found in $E_F - E_{\mathbf{K},+} = 0$, which are k_z^i with $i = \pm 1$.

The real part of the static dielectric function reads $\varepsilon_{Re}(0, \mathbf{Q}) = 1 + K_s^2(\mathbf{Q})/Q^2$, where the inverse screening length, K_s, can be obtained through $K_s^2(\mathbf{Q}) = -(4\pi e^2/\kappa)g\sum_{\mathbf{K}} \Pi_{++}(0; \mathbf{K}, \mathbf{Q})$. At a long-wavelength limit ($\mathbf{Q} \to 0$) and a low-temperature limit ($T \to 0$), one can obtain

$$K_s^2(\mathbf{Q}) \to K_s^2 = \frac{4\pi e^2}{\kappa}\Lambda. \tag{6.11}$$

Now, we have the expression of the *e-e* screening length of a type-II 3D DSM, which depends on the Fermi level of electrons.

6.2 Carrier-impurity scattering rate of type-II 3D DSMs

Consider a high-quality *n*-doped bulk PtTe$_2$, where the concentration of charged impurities is very low and the impurities are sufficiently dilute and uniformly distributed, so interference between successive scatterings can be ignored. Hence, carrier-impurity (*c-i*) scattering can be regarded as a process where carriers are influenced by the weak Coulomb potential of the 3D charged impurities. Thus, the *c-i* interaction Hamiltonian can be written as

$$H_{c-i} = \frac{e^2}{\kappa|\mathbf{R} - \mathbf{R}_i|}, \tag{6.12}$$

where $\mathbf{R} = (x, y, z)$ is the carrier coordinates, the charged impurity is located at $\mathbf{R}_i = (x_i, y_i, z_i)$, κ is the static dielectric constant of the material. We assume that the electronic state of the system $|\zeta\rangle \equiv |\mathbf{K}, l\rangle$ and the background impurity state $|I\rangle$ can be described separately, i.e., $|\zeta; I\rangle = |\zeta\rangle|I\rangle$. Then, using the relevant methods from Sec. 2.2.2, we can first obtain the many-body interaction form factor for the *c-i* scattering process, including the *e-e* screening, in a type-II 3D DSM as

$$\langle I; \zeta'|H_{c-i}|\zeta; I\rangle = \frac{\sqrt{N_i}e^2}{2\kappa}[a_{\zeta'}^* a_\zeta(1 + b_{\zeta'}^* b_\zeta)]\int e^{-i\mathbf{K}'\cdot\mathbf{R}}e^{i\mathbf{K}\cdot\mathbf{R}}\frac{1}{|\mathbf{R} - \mathbf{R}_i|}d\mathbf{R}$$

$$= V_Q F_{\zeta\zeta'}\sqrt{N_i}e^{-i\mathbf{Q}\cdot\mathbf{R}_i}\delta_{\mathbf{K}',\mathbf{K}+\mathbf{Q}}, \tag{6.13}$$

where $a_\zeta = a_{\mathbf{K},l}$ and $b_\zeta = b_{\mathbf{K},l}$ come from the eigenfunctions of the carriers in the type-II 3D DSM, $\mathbf{Q} = (q_x, q_y, q_z)$ represents the carrier's momentum change during the *c-i* scattering event, $V_Q = 4\pi e^2/[\kappa(K_s^2 + Q^2)]$ is the Fourier transform of the Coulomb potential, including the *e-e* screening, where K_s is the inverse screening length, obtained from Eq. (6.11), $\sqrt{N_i} = \langle I|I\rangle$ with N_i being the impurity density, $\delta_{\mathbf{K}',\mathbf{K}+\mathbf{Q}}$ denotes momentum conservation in the scattering

event. Using Eq. (2.26), we can then obtain the first-order steady-state transition rate for carriers scattered from the initial state $|\zeta\rangle$ to the final state $|\zeta'\rangle$ under interaction with impurities as

$$
\begin{aligned}
W_{\zeta\zeta'} &= \frac{2\pi}{\hbar}|\langle I;\zeta'|H_{c-i}|\zeta;I\rangle|^2\delta(E_{\zeta'}-E_\zeta) \\
&= \frac{2\pi}{\hbar}N_i|V_Q|^2|F_{\zeta\zeta'}|^2\delta_{\mathbf{K'},\mathbf{K}+\mathbf{Q}}\delta(E_{\zeta'}-E_\zeta).
\end{aligned}
\tag{6.14}
$$

Here, from $\delta_{\mathbf{K'},\mathbf{K}+\mathbf{Q}}$ we have

$$
Q^2 = (k_z' - k_z)^2 + k^2 + k'^2 - 2kk'\cos\varphi,
$$

where φ is the angle between $\mathbf{k}$ and $\mathbf{k'}$ in the x-y plane. Through the geometric relation $|\mathbf{k}+\mathbf{q}|\cos\varphi = k + q\cos\phi$, where ϕ is the angle between $\mathbf{k}$ and $\mathbf{q}$, one can iterate the form factor $|F_{\zeta\zeta'}|^2$ in Eq. (6.14) into

$$
\begin{aligned}
|F_{\zeta\zeta'}|^2 &= |a_{\zeta'}^*a_\zeta(1+b_{\zeta'}^*b_\zeta)|^2 = \left|\frac{v_x^2 kk'[1 + \frac{(\varepsilon_{k_z'}+l'\varepsilon_{K'})(\varepsilon_{k_z}+l\varepsilon_K)}{v_x^2 ke^{i\theta}(ke^{-i\theta}+qe^{-i(\theta+\phi)})}]}{(\varepsilon_{\mathbf{K'}}^2 + l'\varepsilon_{k_z'}\varepsilon_{K'})^{1/2}(\varepsilon_{\mathbf{K}}^2 + l\varepsilon_{k_z}\varepsilon_{\mathbf{K}})^{1/2}}\right|^2 \\
&= \frac{v_x^4 k^2 k'^2 + (\varepsilon_{k_z'}+l'\varepsilon_{K'})^2(\varepsilon_{k_z}+l\varepsilon_K)^2}{(\varepsilon_{\mathbf{K'}}^2+l'\varepsilon_{k_z'}\varepsilon_{K'})(\varepsilon_{\mathbf{K}}^2+l\varepsilon_{k_z}\varepsilon_{\mathbf{K}})} + \frac{2v_x^2 kk'(\varepsilon_{k_z'}+l'\varepsilon_{K'})(\varepsilon_{k_z}+l\varepsilon_K)}{(\varepsilon_{\mathbf{K'}}^2+l'\varepsilon_{k_z'}\varepsilon_{K'})(\varepsilon_{\mathbf{K}}^2+l\varepsilon_{k_z}\varepsilon_{\mathbf{K}})}\cos\varphi.
\end{aligned}
\tag{6.15}
$$

6.3 Transport and quantum lifetimes of type-II 3D DSMs

In Sec. 2.2.5, we have already provided a detailed derivation of the momentum balance equation from the Boltzmann equation, and also presented the specific expression for the momentum lifetimes in a 3D electronic system, which is given by Eq. (2.40):

$$
\frac{1}{\tau_j^l} = \frac{g^2}{N_0}\sum_{\zeta,\zeta'}(k_j'-k_j)W_{\zeta\zeta'}^{c-i}\frac{\partial E_\zeta}{\partial k_j}\frac{\partial f_l(E_\zeta)}{\partial E_\zeta}.
$$

Here, $j = x$, y, or z represents different scattering directions; $E_\zeta = E_{\mathbf{K},l}$ is the energy dispersion of the carriers, with $l = +1$ representing the conduction band and $l = -1$ representing the valence band; $N_0 = N_e + N_h$ is the total carrier density in the system, where N_e is the electron density and N_h is the hole density; $f_l(E_\zeta)$ is the Fermi-Dirac distribution function for electrons or holes.

In our study, the valence band of the n-doped PtTe$_2$ is fully occupied, so $f_-(E_{\mathbf{K},-}) \simeq 1$ makes $N_h \simeq 0$. The c-i interaction is sufficiently weak and the conservation of momentum and energy implies that interband transitions (i.e., $l \neq l'$) are forbidden. Therefore, the momentum lifetimes in the system are mainly contributed by intraband electronic transitions in the conduction band, so we take $l = l' = +1$. When the temperature is sufficiently low ($T \to 0$), the Fermi-Dirac distribution function $f(x)$ and the relation $\partial f(x)/\partial x = -\delta(x - E_F)$ allow us to iterate energy conservation $\delta(E_{\zeta'} - E_\zeta)$ in Eq. (6.14) into $\delta(E_{\mathbf{K},+} - E_F)\delta(E_{\mathbf{K'},+} - E_F)$. Hence, the expression for the momentum lifetimes in a type-II 3D DSM can be written as

$$
\begin{aligned}
\frac{1}{\tau_j} = &-\frac{32\pi N_i}{\hbar N_e}\sum_{\mathbf{K},\mathbf{K'}}(k_j'-k_j)|V_Q|^2|F_{\mathbf{K},\mathbf{K'}}|^2\frac{\partial E_{\mathbf{K},+}}{\partial k_j} \\
&\times \delta_{\mathbf{K'},\mathbf{K}+\mathbf{Q}}\delta(E_{\mathbf{K},+}-E_F)\delta(E_{\mathbf{K'},+}-E_F).
\end{aligned}
\tag{6.16}
$$

Here, $|F_{\mathbf{K},\mathbf{K}'}|^2$ can be obtained from Eq. (6.15) by taking $l = l' = +1$. The summation rule in the above expression can be written as $V \int d\mathbf{K} \int d\mathbf{K}'$ with $V = 1/(2\pi)^6$. Since the band structure of the type-II 3D DSM is independent of the angle θ between $\mathbf{k}$ and the x axis, we have $\int_0^{2\pi} d\theta = 2\pi$ in the above expression, and one can be further written as

$$\frac{1}{\tau_j} = -\frac{4N_i}{\pi^4 \hbar N_e} \int_0^\infty dk \int_0^\infty dk' \int_0^{2\pi} d\varphi \int_{-\infty}^\infty dk_z \int_{-\infty}^\infty dk_z'$$

$$\times kk'(k_j' - k_j)|V_Q|^2 |F_{\mathbf{K},\mathbf{K}'}|^2 \frac{\partial E_{\mathbf{K},+}}{\partial k_j} \delta_{\mathbf{K}',\mathbf{K}+\mathbf{Q}} \delta(E_{\mathbf{K},+} - E_F)\delta(E_{\mathbf{K}',+} - E_F). \qquad (6.17)$$

Here, we have used the cylindrical coordinates of the wave vector $\mathbf{K} = (k, \theta, k_z)$ and $\mathbf{K}' = (k', \theta + \varphi, k_z')$. From the Dirac-$\delta$ functions, there are $E_{\mathbf{K},+} - E_F = 0$ and $E_{\mathbf{K}',+} - E_F = 0$, and we can obtain the analytical solutions for k_z and k_z', respectively, as

$$k_{zn} = \frac{-v_t E_F + n\sqrt{\hbar^2(v_t^2 - v_z^2)v_x^2 k^2 + v_z^2 E_F^2}}{\hbar(v_t^2 - v_z^2)},$$

and

$$k_{zm}' = \frac{-v_t E_F + m\sqrt{\hbar^2(v_t^2 - v_z^2)v_x^2 k'^2 + v_z^2 E_F^2}}{\hbar(v_t^2 - v_z^2)}.$$

Here, we substitute the parameters for PtTe$_2$: $\{v_x, v_y, v_z, v_t\} = \{0.65, 0.65, 0.35, 0.51\} \times 10^6$ m/s [172]. Since $v_t > v_z$, it implies that both k_z and k_z' will have two solutions, and we use $n = \pm 1$ and $m = \pm 1$ to represent the two solutions for k_z and k_z', respectively. Using the properties of the Dirac-δ function in Eqs. (6.8) and (6.9), we can analytically solve the integrals over k_z and k_z' in Eq. (6.17), resulting in

$$\frac{1}{\tau_j} = \frac{4N_i}{\pi^4 \hbar N_e} \sum_{n,m} \int_0^\infty dk \int_0^\infty dk' \int_0^{2\pi} d\varphi kk'(k_j' - k_j)$$

$$\times \frac{|V_Q|^2 |F_{\mathbf{K},\mathbf{K}'}|^2}{|Z_{\mathbf{K}} Z_{\mathbf{K}'}|} \frac{\partial E_{\mathbf{K},+}}{\partial k_j} \delta_{\mathbf{K}',\mathbf{K}+\mathbf{Q}} \delta_{k_z,k_{zn}} \delta_{k_z',k_{zm}'}, \qquad (6.18)$$

with

$$Z_{\mathbf{K}} = \frac{\partial(E_{\mathbf{K},+} - E_F)}{\partial k_z} = \frac{\partial E_{\mathbf{K},+}}{\partial k_z} = \hbar v_t + \frac{\hbar v_z^2 k_z}{\sqrt{v_x^2 k^2 + v_z^2 k_z^2}}.$$

Thus, we have obtained the specific expression for calculating the momentum lifetimes of the carrier-impurity scattering in a type-II 3D DSM.

For the n-doped PtTe$_2$ bulk sample, the c-i scattering in the x-y plane has $\tau_x = \tau_y$ due to its isotropic band structure in the x-y plane, as shown in Fig. 5.1. Therefore, we focus on studying the scattering in the x direction. From Eq. (6.18), we can obtain the in-plane transport lifetime of the system as

$$\frac{1}{\tau_x^t} = \frac{4N_i}{\pi^4 \hbar N_e} \sum_{n,m} \int_0^\infty dk \int_0^\infty dk' \int_0^{2\pi} d\varphi \left(1 - \frac{k'}{k}\cos\varphi\right)$$

$$\times \frac{k^2 k' |V_Q|^2 |F_{\mathbf{K},\mathbf{K}'}|^2 X_{\mathbf{K}}}{|Z_{\mathbf{K}} Z_{\mathbf{K}'}|} \delta_{\mathbf{K}',\mathbf{K}+\mathbf{Q}} \delta_{k_z,k_{zn}} \delta_{k_z',k_{zm}'}, \qquad (6.19)$$

where $\delta_{k_z, k_{zn}}$ and $\delta_{k'_z, k'_{zm}}$ denote $k_z \equiv k_{zn}$ and $k'_z \equiv k'_{zm}$, and

$$X_{\mathbf{K}} = \frac{\partial E_{\mathbf{K},+}}{\partial k_x} = \frac{\hbar v_x^2 k}{\sqrt{v_x^2 k^2 + v_z^2 k_z^2}}.$$

In the above expression, for small-angle scattering, $\cos \varphi \approx 1$ does not contribute to the carrier momentum lifetime. Therefore, the importance of the factor $(1 - k' \cos \varphi / k)$ lies in its significant contribution to a large-angle scattering of carriers, which in turn has a notable effect on the carrier mobility and conductivity. This is an important advantage of the Boltzmann equation and the momentum balance equation [208, 209]. Considering the case of small-angle scattering for carriers, we can derive the in-plane quantum lifetime of the system as

$$\frac{1}{\tau_x^q} = \frac{4N_i}{\pi^4 \hbar N_e} \sum_{n,m} \int_0^\infty dk \int_0^\infty dk' \int_0^{2\pi} d\varphi (k' - k)$$
$$\times \frac{kk'|V_Q|^2 |F_{\mathbf{K},\mathbf{K}'}|^2 X_{\mathbf{K}}}{|Z_{\mathbf{K}} Z_{\mathbf{K}'}|} \delta_{\mathbf{K}',\mathbf{K}+\mathbf{Q}} \delta_{k_z, k_{zn}} \delta_{k'_z, k'_{zm}}. \quad (6.20)$$

Meanwhile, the out-of-plane quantum lifetime of a type-II 3D DSM along the z direction can be obtained as

$$\frac{1}{\tau_z^q} = \frac{4N_i}{\pi^4 \hbar N_e} \sum_{n,m} \int_0^\infty dk \int_0^\infty dk' \int_0^{2\pi} d\varphi (k'_z - k_z)$$
$$\times \frac{kk'|V_Q|^2 |F_{\mathbf{K},\mathbf{K}'}|^2 Z_{\mathbf{K}}}{|Z_{\mathbf{K}} Z_{\mathbf{K}'}|} \delta_{\mathbf{K}',\mathbf{K}+\mathbf{Q}} \delta_{k_z, k_{zn}} \delta_{k'_z, k'_{zm}}. \quad (6.21)$$

6.4 Result and discussion

The properties of the lattice structure and the energy band structure of bulk PtTe$_2$ are shown in Fig. 5.1, and we have analyzed in Sec. 5.3. Here, we directly provide the relevant parameters for PtTe$_2$ required for numerical calculations as $\{v_x, v_y, v_z, v_t\} = \{0.65, 0.65, 0.35, 0.51\} \times 10^6$ m/s [172]. The experimental results indicate that the static dielectric constants of type-II 3D DSMs, such as PdSe$_2$ [231] and PtSe$_2$ [176], range from about 12 to 13. Although there are no experimental results for the static dielectric constant of PtTe$_2$, we take $\kappa \approx 12$ in this study based on the similar lattice structure and electronic bands of these materials.

In Fig. 6.3, we show the variation of the Fermi level E_F and the inverse screening length K_s with the electron density N_e for bulk PtTe$_2$. Figure 6.4 shows the tilted Dirac cone near a Dirac point in n-doped PtTe$_2$, along with a schematic of E_F and the occupied states. From Figs. 6.3 and 6.4, we summarize the following features.

(i) The strong tilt of the Dirac cone along the k_z direction results in a non-closed band structure for PtTe$_2$ in the k_z direction, which means that the infinite integral over k_z in numerical calculations will yield unphysical results. Based on the Fermi-Dirac distribution of electrons, the integration range for k_z should be $\{-2k_{Fz}^-, 2k_{Fz}^-\}$. As shown in Fig. 6.4(d), at a finite temperature, the distribution of electrons will lie outside the black dashed curve but will not exceed the range of $\{-2k_{Fz}^-, 2k_{Fz}^-\}$. Using this and taking $T \simeq 0$ and $N_e \simeq 0$, we can obtain $E_F \simeq 0$, which proves our numerical calculations.
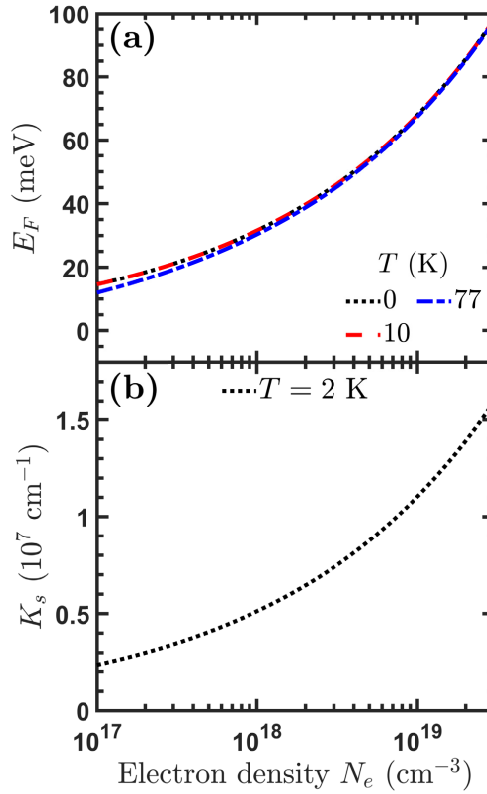
Figure 6.3: (a) In n-doped bulk PtTe$_2$, the electronic chemical potential E_F as a function of electron density N_e in different temperatures, as indicated. We can see that the results are nearly identical for temperatures $T < 10$ K. (b) The inverse of the electron-electron interaction screening length K_s as a function of N_e at $T = 2$ K.

(ii) The results in Fig. 6.3(a) indicate that the E_F of n-doped PtTe$_2$ increases with increasing N_e, but decreases with increasing temperature T. From Figs. 6.4(a) and 6.4(b), we can see that the increasing N_e leads to an increasing E_F, which in turn also increases the electronic density of states. This suggests that increasing N_e will provide electrons with more channels for intraband transitions. At low temperatures, $T < 10$ K, the results show that the variation of E_F with respect to N_e is nearly consistent, indicating that the electronic excitations should also be nearly identical for low temperatures $T < 10$ K.

(iii) Figure 6.3(b) shows the inverse screening length K_s of n-doped PtTe$_2$ as a function of N_e, calculated using Eq. (6.11) at $T = 2$ K and the long-wavelength limit $Q \to 0$. From Figs. 6.3 and 6.4, we can see that a larger N_e corresponds to a higher E_F and a higher density of states, which also corresponds to stronger electron-electron interactions. Therefore, increasing N_e results in a stronger screening effect in the system, as shown in Fig. 6.3(b). This result is similar to the theoretical results for type-I 3D DSM Na$_3$Bi [87].

(iv) In the transport studies of Dirac systems such as graphene, the effective mass of electrons m^* can be estimated by $m^* = \hbar k_F / (2 v_F)$, which is related to the Fermi wave vector k_F [214]. However, for PtTe$_2$, its 3D Fermi wave vector is anisotropic, and an analytical expression for the
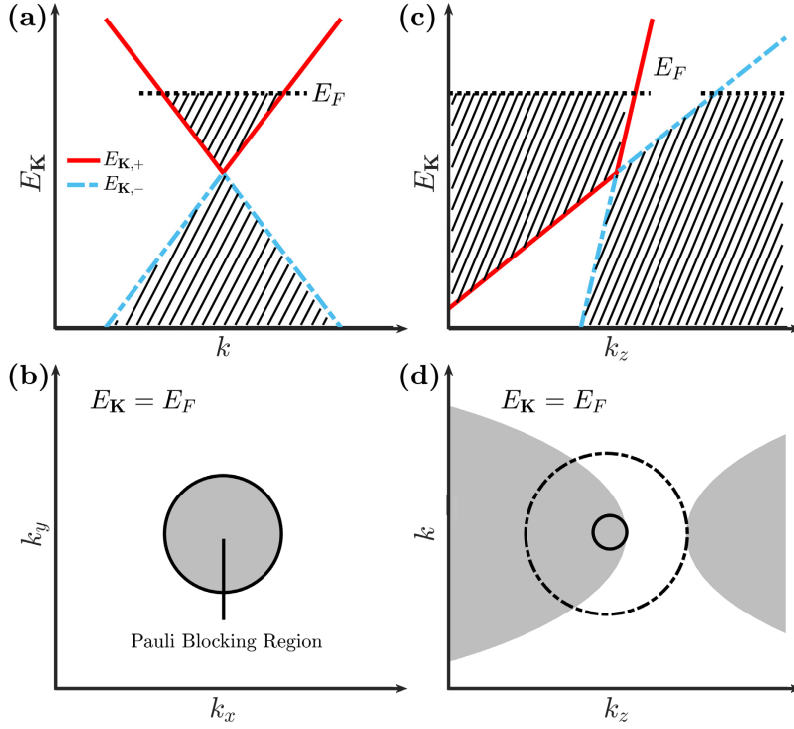
Figure 6.4: Schematic diagram of the band structure and Fermi level of n-doped bulk PtTe$_2$. (a) The energy dispersion of PtTe$_2$ as a function of $k = \sqrt{k_x^2 + k_y^2}$ at $k_z = 0$. The Fermi level of the electrons, E_F, is located within the conduction band, with the shaded area below E_F indicating the occupied states. (b) The 2D projection of the band structure on the k_x-k_y plane when $E_{\mathbf{K}} = E_F$. The energy dispersion is isotropic in the k_x-k_y plane. The black solid curve corresponds to the Fermi wave vector $k_F = E_F/(\hbar v_x)$ of the electrons in the k_x-k_y plane when $k_z = 0$. The solid shaded areas represent the Pauli Blocking region. (c) The heavily tilted energy dispersion in the k_z direction for PtTe$_2$ at $k = 0$. (d) The 2D projection of the band structure on the k-k_z plane when $E_{\mathbf{K}} = E_F$. The tilted Dirac cone results in an anisotropic energy dispersion in the k-k_z plane, with a non-closed hyperbolic contour of wave vector. The geometric structure of the band indicates that the Fermi wave vector k_{Fz} of electrons in the k_z direction has two components $k_{Fz}^{\pm} = E_F/[\hbar(v_t \pm v_z)]$, where k_{Fz}^{+} corresponds to the black solid curve and k_{Fz}^{-} corresponds to the black dashed curve.

Fermi wave vector cannot be found. From Figs. 6.4(b) and 6.4(d), we can see that if $k \neq 0$ and $k_z \neq 0$, we cannot obtain an analytical expression for k_F and k_{Fz} solely from $E_{(k_F,k_{Fz}),+} - E_F^e = 0$. Therefore, in the following discussion, we will focus primarily on the quantitative analysis of the momentum lifetimes for PtTe$_2$, while the discussion of mobility will utilize the effective mass of electrons measured experimentally for qualitative analysis.

(v) As shown in Fig. 6.2 and Tab. 6.1, the experimental data derived from the dHvA oscillations indicate that the average effective mass of electrons in the out-of-plane direction for bulk PtTe$_2$ is much larger than that in the in-plane direction [157]. From the schematic in Fig. 6.4, we can see that the electron motion in the k_z direction has a larger Fermi wave vector range k_{Fz}^{-} due to the tilted Dirac cone, with $(v_t - v_z) < v_x$, resulting in k_{Fz}^{-} being significantly larger than k_F. This can
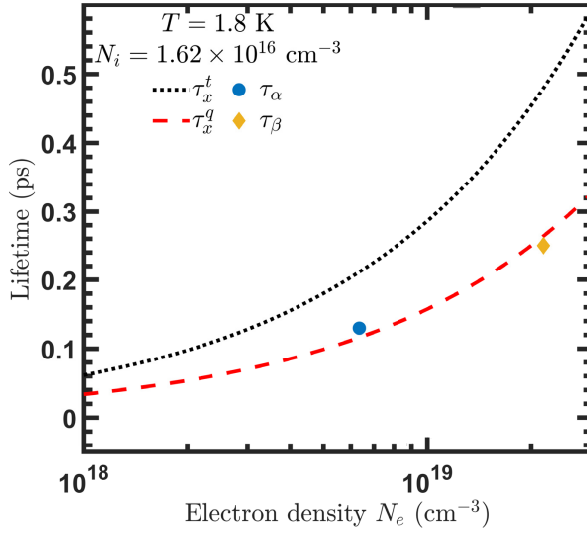
Figure 6.5: For the n-doped bulk PtTe$_2$ at a fixed temperature $T = 1.8$ K and impurity density $N_i = 1.62 \times 10^{16}$ cm^{-3}, the transport lifetime τ_x^t and the quantum lifetime τ_x^q as functions of the electron density N_e are indicated by black dotted curve and red dashed curve, respectively. τ_α and τ_β represent the experimental data from Tab. 6.2.

Table 6.2: Experimental data derived from the Shubnikov-de Haas (SdH) oscillations of a high-quality PtTe$_2$ bulk sample. The bulk PtTe$_2$ cuts from a single crystal and has dimensions of $2.9 \times 1.3 \times 0.04$ mm^3. Under a strong magnetic field, the SdH oscillations of this sample have two typical frequencies, labeled α and β. In the table, F represents the oscillation frequency, T_D is the Dingle temperature, m_e is the rest mass and m^* is the effective mass of the electron, τ_q is the quantum lifetime, μ_q is the quantum mobility, and N_e is the electron density. The parameters in the table are sourced from Ref. [159].

			$T = 1.8$ K, $B \parallel c$			
	F (T)	T_D (K)	m^*/m_e	τ_q (ps)	μ_q (cm^2/Vs)	N_e (cm^{-3})
α	108	9.1	0.11	0.134	2138	6.35×10^{18}
β	246	5	0.21	0.243	2038	2.17×10^{19}

explain the observed phenomenon that the out-of-plane effective mass is larger than the in-plane effective mass in experiments.

   For high-quality bulk PtTe$_2$, the quantum lifetimes and mobilities in the x-y plane with electron densities can be measured from the Shubnikov-de Haas (SdH) oscillation experiments, as listed in Tab. 6.2 [159]. Meanwhile, Fig. 6.5 shows our theoretical calculations for the transport lifetime τ_x^t and quantum lifetime τ_x^q of the n-doped bulk PtTe$_2$ in the x-y plane as functions of the electron density N_e, with a fixed impurity density N_i and temperature T. Additionally, the experimental data from Tab. 6.2 is marked with different symbols in Fig. 6.5. From Fig. 6.5 and Tab. 6.2, we notice the following important features.

   (i) Under the fixed conditions of T and N_i, both τ_x^t and τ_x^q increase with increasing N_e. The difference between Eqs. (6.19) and (6.20) is the factor $(1 - k' \cos \varphi / k)$, which indicates that

small-angle scattering reduces the scattering channels for electrons, leading to a shorter quantum lifetime. Therefore, τ_x^q is significantly less than τ_x^t in PtTe$_2$, which is similar to the theoretical and experimental results for the type-I 3D DSM Na$_3$Bi [86, 87]. Moreover, the variation of τ_x^q with respect to N_e is slightly lower than that of τ_x^t, which is also similar to Na$_3$Bi [87] but significantly different from 2D electronic materials [232]. This is because, in 3D DSMs, the effective electron scattering channels in the *x-y* plane is influenced by scattering in the *z* direction, resulting in a smaller variation difference between τ_x^q and τ_x^t.

(ii) Our theory takes N_i as the only fitting parameter in the transport study, providing a method to estimate the background impurities of type-II 3D DSMs. As shown in Fig. 6.5, when the background impurity density is fitted at $N_i = 1.62 \times 10^{16}$ cm^{-3} with the experimental temperature $T = 1.8$ K, our calculated τ_x^q matches excellently with the experimental data τ_α and τ_β listed in Tab. 6.2. This demonstrates the precision of our theoretical study and indicates that our research can be used to study the background impurity of bulk PtTe$_2$ and the similar materials. Moreover, the fitted N_i is much smaller than 1% of N_e, which is in line with the high-quality samples used in experiments [159].

(iii) In experimental studies of type-II DSMs, many works have explored their properties such as Fermi surface structure, effective mass, quantum lifetime, quantum mobility, and Berry phase using the SdH and dHvA effects [155–159]. However, to date, there has been no research on their transport lifetime and mobility. In this work, we theoretically derived the expression for the in-plane transport lifetime τ_x^t of type-II 3D DSMs by considering large-angle scattering; see Eq. (6.19). As shown in Fig. 6.5, after determining the temperature and impurity density, we can obtain how the transport lifetime of type-II 3D DSMs changes with the electron density. Thus, our theoretical calculations can predict the transport lifetime of type-II 3D DSMs, as well as their transport mobility.

(iv) As mentioned in the previous discussion and in Fig. 6.4, the effective mass is related to the Fermi wave vector, which in turn depends on the Fermi energy and electron density. From the experimental data in Tab. 6.2, we can see that the in-plane effective mass of electrons varies with the electron density. However, theoretically, we cannot accurately obtain the analytical expression for the Fermi wave vector of type-II 3D DSMs, so we are unable to estimate the corresponding quantum mobility. Therefore, in the following discussion, we will only conduct a qualitative analysis of the mobility.

Figure 6.6 shows the momentum lifetimes and carrier mobilities of *n*-doped bulk PtTe$_2$ along different directions at fixed T and N_i. The experimental results marked in the figure are derived from the dHvA effect shown in Figs. 6.1, 6.2, and Tab. 6.1 [157]. Here, we only provide a qualitative analysis of the relevant phenomena, since we cannot analytically obtain the effective mass. Our analysis is as follows.

(i) For a bluk PtTe$_2$, its lattice structure and energy band allow its transport lifetime to be obtained only in the *x-y* plane, as shown in Fig. 5.1. This situation is similar to the type-I DSM Na$_3$Bi [86, 87].

(ii) Figure 6.6(a) shows the variation of τ_x^t, τ_x^q, and the out-of-plane quantum lifetime τ_z^q with N_e at fixed T and N_i. From Eqs. (6.20) and (6.21), we can see that the difference between τ_x^q and τ_z^q relates mainly to the terms associated with the electronic velocity $\partial E_{\mathbf{K},+}/\partial k_j$. Under small-angle scattering, the effect produced by the electronic velocity is minimal, leading to very small differences between τ_x^q and τ_z^q. However, τ_x^q remains slightly higher than τ_z^q in the entire range of N_e. This indicates that even under small-angle scattering, the tilted Dirac cone still induces
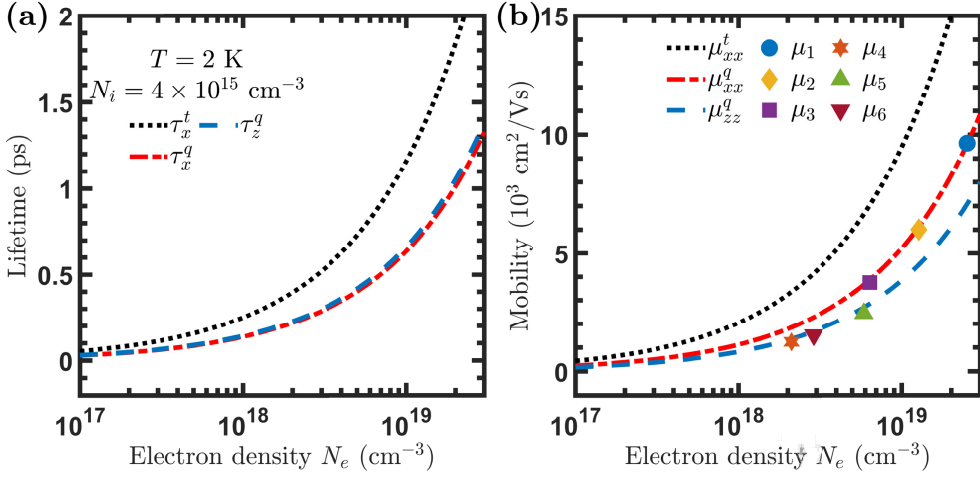
Figure 6.6: For the n-doped bulk PtTe$_2$ at a fixed temperature $T = 2$ K and impurity density $N_i = 4 \times 10^{15}$ cm^{-3}. (a) The in-plane transport lifetime τ_x^t and quantum lifetime τ_x^q are indicated by the black dotted curve and the red dashed-dotted curve, respectively, while the out-of-plane quantum lifetime is indicated by the blue dashed curve. (b) Corresponding to (a), the transport and quantum mobilities are calculated using the definition $\mu = e\tau/m^*$, where the average in-plane effective mass $m_x^* = (0.196 + 0.151 + 0.289)m_e/3$ and out-of-plane effective mass $m_z^* = (0.255 + 0.318 + 0.337) * m_e/3$ are taken from the experimental data in Tab. 6.1. μ_1 to μ_6 mark the results from the dHvA experiment in Tab. 6.1.

$\partial E_{\mathbf{K},+}/\partial k_j$ to exhibit anisotropy in the k_x and k_z directions, resulting in anisotropic quantum lifetimes of a type-II 3D DSM. The experimental data in Tab. 6.1 shows that the average quantum lifetime in the z direction is slightly higher than that in the x direction [157], which is consistent with our theoretical calculations.

(iii) Figure 6.6(b) shows the variation of the in-plane transport mobility μ_{xx}^t, the in-plane quantum mobility μ_{xx}^q, and the out-of-plane quantum mobility μ_{zz}^q with electron density N_e at fixed T and N_i, using the average effective mass of electrons derived from Tab. 6.1. The experimental data in Tab. 6.1 indicate that the mobilities of μ_4 to μ_6 for PtTe$_2$ are significantly lower than those of μ_1 to μ_3. The authors of the experiment point out that this arises from the out-of-plane effective mass being larger than that in the plane [157]. Our analysis of Fig. 6.4 provides further explanation. This is because the Fermi wave vector in the k_z direction is much larger than in the k direction. Therefore, we can see that even though τ_z^q is only slightly higher than τ_x^q, μ_{zz}^q will be pronounced lower than μ_{xx}^q. This conclusion reasonably explains the anisotropic mobilities observed in type-II 3D DSMs.

(4) From Figs. 6.5(a) and 6.6(a) with Eqs. (6.19) to (6.21), we find that the momentum lifetimes of PtTe$_2$ follow $\tau \propto N_i^{-1}$. In n-doped intrinsic 3D semiconductors, the momentum lifetimes due to the scattering of ionized impurities obey $\tau \propto N_i^{-1}T^{3/2}$ [208]. Therefore, similar to a conventional semiconductor, type-II 3D DSMs can also have longer momentum lifetimes and higher mobilities in samples with lower charged impurity densities.

6.5 Conclusion of this chapter

In this chapter, we used the RPA dielectric function and the momentum balance equation to calculate the in-plane transport lifetime τ_x^t, the in-plane quantum lifetime τ_x^q, and the out-of-plane quantum lifetime τ_z^q of the n-doped bulk PtTe$_2$. Additionally, we further derived the corresponding anisotropic carrier mobilities. After comparing the experimental results with our theoretical calculations, we arrived at the following conclusions.

(i) The inverse screening length K_s of a type-II 3D DSM increases with increasing electron density N_e. (ii) At fixed temperature T and charged impurity density N_i, τ_x^t and τ_x^q increase with increasing N_e in an n-doped type-II 3D DSM. (iii) Our theoretical study uses N_i as the only fitting parameter to obtain τ_x^q, while the results agree well with the experiment, which proves the accuracy of our theory. (iv) The calculated τ_x^t is much larger than τ_x^q, which shows that large-angle scattering significantly contributes to τ_x^t. Furthermore, our calculation of τ_x^t provides a theoretical prediction for the transport lifetime of type-II 3D DSMs and a guide for their further transport experiments. (v) At fixed T and N_i, τ_z^q increases with increasing N_e. (vi) For small-angle scattering, τ_z^q is slightly higher than τ_x^q at the same N_e, whereas μ_{zz}^q is much smaller than μ_{xx}^q. From the experimental results and our theoretical analysis, we find that this is due to the tilt of the Dirac cone along the k_z direction, which causes the in-plane effective mass to be smaller than the out-of-plane effective mass, thereby resulting in the anisotropic carrier mobilities. (vii) Similar to traditional semiconductor materials, the momentum lifetime and carrier mobility of type-II 3D DSMs are inversely proportional to the impurity density, indicating that their higher quality samples should exhibit longer momentum lifetimes and higher mobilities.

In this study, we theoretically explained the transport experiments of type-II 3D DSMs. Using the impurity density as the only fitting parameter in the calculations, we have obtained results that are in line with experimental data, indicating that our theoretical approach can be applied to estimate the background impurity of the type-II 3D DSMs. Moreover, our research contributes to a deeper understanding of the electron scattering mechanisms near the Dirac point in type-II 3D DSMs and provides a theoretical foundation for future transport experiments.

Chapter 7

Conclusion and outlook

7.1   Conclusion of the thesis

The research goals of the thesis are listed in Sec. 1.3, which intend to present detailed studies on the optoelectronic and transport properties of three-dimensional (3D) Dirac semimetals (DSMs). Starting from effective Hamiltonians of type-I and type-II 3D DSMs, this thesis investigates the optical conductivities (OCs), plasmon properties, and transport properties of type-I and type-II 3D DSMs using the RPA dielectric function, momentum balance equation, and energy balance equation approaches. Based on the research goals, the conclusions of the thesis are summarized as follows.

In chapter 3, we analyze the energy band characteristics and calculate the OC of type-I 3D DSMs based on Na_3Bi. We find that the nontrivial changes in the density of states (DOS) of Na_3Bi at lower electron densities are mainly induced by the Berry curvature and band inversion along the k_z direction, which will further affect the low-energy excitations. Following this, the anisotropic OC of bulk Na_3Bi, where the out-of-plane OC $\sigma_{zz}(\omega)$ is smaller than the in-plane OC $\sigma_{xx}(\omega)$, can be observed. Intraband and interband transitions contribute to the long-wavelength OC and the short-wavelength OC, respectively, leading to observable optical absorption windows in both $\sigma_{xx}(\omega)$ and $\sigma_{zz}(\omega)$, which explains the experimental results. The variation of $\sigma_{xx}(\omega)$ with electron density is more pronounced, while $\sigma_{zz}(\omega)$ shows less variation, indicating that the Berry curvature primarily affects $\sigma_{zz}(\omega)$ in this type of topological materials. In addition, the changes with energy relaxation time, temperature, and electron density demonstrate the tunability of the OC of type-I 3D DSMs. This chapter is the first to propose the effects of band inversion and Berry curvature on OC among the studies of type-I 3D DSMs and to provide both quantitative and qualitative explanations of the corresponding experimental results, which contributes to the research on the optoelectronic properties of 3D DSMs.

In chapter 4 the plasmon modes of the type-I 3D DSMs Na_3Bi and Cd_3As_2 are evaluated considering the nontrivial band structure and Berry curvature. When the plasmon wave vector (q and q_z) approaches zero, the plasmon energy ($\hbar\omega$) of type-I DSMs also approaches zero. However, as the q and q_z increase, the plasmon dispersion initially exhibits linear behavior and then transitions to parabolic dispersion, which aligns with nontrivial band structures of Na_3Bi and Cd_3As_2 but differs from the plasmon modes of three-dimensional electron gases (3DEG) and graphene. Lowering the electron density so that the Fermi level lies within the band inversion reveals a dramatic reduction in the q_z for both Na_3Bi and Cd_3As_2. This reduction arises from the influence of the

Berry curvature on the electron momentum and DOS in the k_z direction. The reduction in the q_z is noticeably smaller in Cd_3As_2 than in Na_3Bi, indicating that Na_3Bi exhibits stronger band inversion and Berry curvature. This study of type-I 3D DSMs, which uses a complete effective Hamiltonian to study the plasmon modes, discovers and explains the effects of their topological properties on their plasmon modes, deepening the understanding of the collective excitations in 3D DSMs.

In chapter 5 the calculated OCs of n-doped bulk PtTe2 under different light polarization directions shows that the anisotropy between the in-plane OC $\sigma_{xx}(\omega)$ and the out-of-plane OC $\sigma_{zz}(\omega)$ of a type-II 3D DSM arises from the strong tilt of the 3D Dirac cone along the k_z direction. This indicates that the physical mechanisms behind the anisotropic OCs of type-I and type-II 3D DSMs are essentially different. The interband and intraband transitions dominate $PtTe_2$'s OCs at higher and lower photon energies, respectively, resulting in observable optical absorption windows for both $\sigma_{xx}(\omega)$ and $\sigma_{zz}(\omega)$, similar to type-I DSMs and graphene, highlighting the Dirac fermion characteristics of $PtTe_2$. In the short-wavelength region, the anisotropy between $\sigma_{xx}(\omega)$ and $\sigma_{zz}(\omega)$ is particularly pronounced, indicating that the tilted Dirac cone primarily affects the interband transitions. The OCs of $PtTe_2$ are also significantly influenced by temperature, energy relaxation time, and electron density, showing the tunable optoelectronic properties of type-II 3D DSMs. This theoretical research studies the OCs of the type-II 3D DSM $PtTe_2$, which identifies and explains the essential differences in OCs between type-II 3D DSMs and other Dirac materials and provides theoretical guidance for further experiments.

In chapter 6 the in-plane transport lifetime τ_x^t, the in-plane quantum lifetime τ_x^q, and the out-of-plane quantum lifetime τ_z^q of the n-doped type-II 3D DSM $PtTe_2$ as functions of electron density N_e are calculated at fixed impurity density N_i and temperature T. The calculated τ_x^q versus N_e, where N_i is the only fitting parameter, is excellently consistent with the Shubnikov-de Haas (SdH) experiment. At the same N_e, τ_x^t is much larger than τ_x^q, indicating that the angle of carrier-impurity scattering mainly contributes to τ_x^t. The calculated τ_z^q is slightly higher than τ_x^q, which is also in line with experiments. The effective mass measured in the z direction is much larger than that in the x direction, which arises from the Dirac cones that tilt along the k_z direction, leading to a much larger Fermi wave vector in the z direction. Consequently, the in-plane quantum mobility μ_{xx}^q can be much larger than the out-of-plane quantum mobility μ_{zz}^q. This work provides an expression for the momentum lifetimes of type-II 3D DSMs and offers a theoretical model for fitting their background impurity densities. Furthermore, the transport lifetime of type-II 3D DSMs can be predicted by our theoretical study as well, which calls for further experimental studies.

In summary, in this thesis we theoretically studied the optoelectronic and transport properties of 3D DSMs by investigating their optical conductivities, plasmon modes, and momentum lifetimes. The physical mechanisms of these properties are analyzed, the corresponding experimental phenomena are explained, and many novel properties are theoretically predicted as well, which not only advances the fundamental condensed matter physics, but also promotes further technological developments.

7.2   A research outlook

As introduced and studied in the thesis, optoelectronic and transport research of three-dimensional Dirac semimetals continues to progress at a tremendous pace. However, there are still many unanswered questions regarding the use of 3D DSMs as platforms for optical, optoelectronic,

plasmonic, and transport applications or for new and unexpected physics. Therefore, there is great potential to extend the work presented in this thesis.

In the study of the opitcal conductivity and plasmon mode in this thesis, electron-phonon interactions were not considered. However, some experiments indicate that for both type-I and type-II three-dimensional Dirac semimetals, phonons will affect their optoelectronic and plasmonic properties, leading to phenomena such as nonlinear absorption peaks in the optical conductivity. Hence, in future research, it is worth considering further electron-photon-phonon interactions to present more accurate theoretical research for Dirac semimetals.

The Hamiltonians used in this thesis are based on bulk samples of Dirac semimetals, where we only consider the case of unconfined electron momentum by sample thickness. In studies of materials, the thickness of samples plays an important role that influences the Dirac properties, topological properties, etc. In some cases, thickness variations should be introduced as a parameter in the studies, such as the thickness-dependent optical response, quantum Hall effect, and topological phase transition. Therefore, the effect of thickness on the optoelectronic and transport properties of Dirac semimetals needs to be explored further.

Both Weyl and Dirac semimetals belong to topological semimetals. They have many similarities, but there are also essential differences. For example, in momentum space, Dirac semimetals have fourfold degeneracy at the Dirac point, while Weyl semimetals only have twofold degeneracy. Research on Weyl semimetals also finds rich and interesting physical properties, as well as many unanswered questions. Thus, exploring the optoelectronic and transport properties of Weyl semimetals can also contribute to the broader research field of topological materials and topological properties in general.

The thesis is based on the effective $\mathbf{k} \cdot \mathbf{p}$ Hamiltonian theory, which has advantages such as fast computation, traceable derivation, and highly accurate results under low-energy and small-momentum conditions. However, as momentum and energy increase, the effective model is no longer sufficient to describe the electronic excitations, and at this point, the tight-binding model and first-principles calculations become more effective. First-principles, tight-binding theory, and the effective Hamiltonian model are powerful tools for studying the physical properties of materials, each with its own advantages and disadvantages. Upon the effective Hamiltonian model employed in this thesis, using first-principles and tight-binding theory will allow for more extensive and comprehensive theoretical research, towards better understanding and control of the microscopic mechanisms behind the phenomena revealed in this thesis.

List of publications

1. **Q. N. Li**, P. Vasilopoulos, F. M. Peeters, W. Xu, Y. M. Xiao, and M. V. Milošević, "Collective excitations in three-dimensional Dirac systems", Phys. Rev. B **109**, 115123 (2024).

2. **Q. N. Li**, Y. M. Xiao, W. Xu, F. M. Peeters, and M. V. Milošević, "Anisotropic optical conductivity of the n-doped type-II three-dimensional Dirac semimetal $PtTe_2$", Phys. Rev. B **110**, 165203 (2024).

3. **Q. N. Li**, W. Xu, Y. M. Xiao, L. Ding, B. Van Duppen, and F. M. Peeters, "Optical absorption window in Na_3Bi based three-dimensional Dirac electronic system", J. Appl. Phys. **128**, 155707 (2020).

4. H. Y. Zhang, Y. M. Xiao, **Q. N. Li**, L. Ding, B. Van Duppen, W. Xu, and F. M. Peeters, "Anisotropic and tunable optical conductivity of a two-dimensional semi-Dirac system in the presence of elliptically polarized radiation", Phys. Rev. B **105**, 115423 (2022).

5. Lei Hou, Yunkun Yang, Aolong Li, Qiujin Wang, **Qinan Li**, Min Wu, Pengcheng Ji, Yujun Zhang, Yiming Xiao, Wen Xu, Faxian Xiu, and Lan Ding, "Temperature-dependent terahertz properties of carriers and phonons in the topological Dirac semimetal Cd_3As_2", Phys. Rev. B **108**, 115416 (2023).

Acknowledgements

As time goes by, it has been eleven years since I started studying at Yunnan University in 2013, and now my doctoral journey is coming to an end. On the occasion of completing this dissertation, I would like to express my heartfelt gratitude to all those who have cared and helped me along my doctoral journey.

This dissertation was completed under the careful supervision of my supervisor, Prof. Wen Xu. The timely and effective communication and discussions with Prof. Xu provided the most favorable guarantee for the dissertation. Throughout my three years of master's study and over four years of doctoral life, Professor Xu's rigorous and positive academic attitude have profoundly influenced me. It is his guidance that has led me to physics. As I graduate, I express my sincere thanks to Prof. Wen Xu!

The successful completion of my doctoral dissertation is also inseparable from the support and assistance of the joint PhD program. I would like to thank Professors François M. Peeters and Milorad V. Milošević from the University of Antwerp, for providing me with the valuable opportunity to study abroad, and I also thank the Chinese government for funding my overseas study. Professors François and Milorad are internationally renowned condensed matter physicists. My experience in their research group deepened my understanding of advanced research methods, improved my knowledge of the field, and broadened my horizons. I am grateful to Professors F. M. Peeters and M. V. Milošević for their patient guidance during my doctoral studies.

I would like to extend special thanks to Professors Lan Ding and Yiming Xiao from Yunnan University, who provided me with detailed tutelage when I became a master student and helped me adjust to my new academic life. During the process of my doctoral study, Professors Lan Ding and Yiming Xiao also gave me a lot of support.

I am grateful to Prof. Panagiotis Vasilopoulos from Concordia University for his attentive tuition during my time studying abroad. I deeply admire Prof. Vasilopoulos's profound academic achievements and humble academic style, and learning from him has benefited me immensely.

I also would like to thank the professors at Yunnan University and University of Antwerp for the informative lectures they provided, which laid a solid foundation for me. Thanks to my fellow students in the research group and the classmates, their companionship has made my doctoral life rich and colorful.

I am grateful to Yunnan University and University of Antwerp for nurturing me.

Finally, I would like to express my heartfelt gratitude to my family for their support, help, understanding, and patience during my studies. Every achievement I have taken has been inseparable from their selfless care and love.

Bibliography

[1]   P. A. M. Dirac, "The quantum theory of the electron", Proc. R. Soc. A **117**, 610 (1928).

[2]   H. Weyl, "GRAVITATION AND THE ELECTRON", Proc. Natl. Acad. Sci. U.S.A. **15**, 323 (1929).

[3]   S. R. Elliott and M. Franz, "Colloquium: Majorana fermions in nuclear, particle, and solid-state physics", Rev. Mod. Phys. **87**, 137 (2015).

[4]   K. S. Novoselov, A. K. Geim, S. V. Morozov, D. Jiang, Y. Zhang, S. V. Dubonos, I. V. Grigorieva, and A. A. Firsov, "Electric Field Effect in Atomically Thin Carbon Films", Science **306**, 666 (2004).

[5]   K. Novoselov, A. Geim, S. Morozov, D. Jiang, M. Katsnelson, I. Grigorieva, S. Dubonos, and A. Firsov, "Two-dimensional gas of massless Dirac fermions in graphene", Nature **438**, 197 (2005).

[6]   A. Bostwick, T. Ohta, T. Seyller, K. Horn, and E. Rotenberg, "Quasiparticle dynamics in graphene", Nat. Phys. **3**, 36 (2007).

[7]   F. Schedin, A. K. Geim, S. V. Morozov, E. W. Hill, P. Blake, M. I. Katsnelson, and K. S. Novoselov, "Detection of individual gas molecules adsorbed on graphene", Nat. Mater. **6**, 652 (2007).

[8]   Y.-W. Tan, Y. Zhang, K. Bolotin, Y. Zhao, S. Adam, E. H. Hwang, S. Das Sarma, H. L. Stormer, and P. Kim, "Measurement of Scattering Rate and Minimum Conductivity in Graphene", Phys. Rev. Lett. **99**, 246803 (2007).

[9]   S. V. Morozov, K. S. Novoselov, M. I. Katsnelson, F. Schedin, D. C. Elias, J. A. Jaszczak, and A. K. Geim, "Giant Intrinsic Carrier Mobilities in Graphene and Its Bilayer", Phys. Rev. Lett. **100**, 016602 (2008).

[10] Y. Zhang, Y. Tan, H. Stormer, and P. Kim, "Experimental observation of the quantum Hall effect and Berry's phase in graphene", Nature **438**, 201 (2005).

[11] C. Herring, "Accidental Degeneracy in the Energy Bands of Crystals", Phys. Rev. **52**, 365 (1937).

[12] S. L. Adler, "Axial-Vector Vertex in Spinor Electrodynamics", Phys. Rev. **177**, 2426 (1969).

[13] J. S. Bell and R. Jackiw, "A PCAC puzzle: $\pi 0 \rightarrow \gamma\gamma$ in the σ-model", Nuovo Cimento **60**, 47 (1969).

[14] H. Nielsen and M. Ninomiya, "The Adler-Bell-Jackiw anomaly and Weyl fermions in a crystal", Phys. Lett. B **130**, 389 (1983).

[15] X. Wan, A. M. Turner, A. Vishwanath, and S. Y. Savrasov, "Topological semimetal and Fermi-arc surface states in the electronic structure of pyrochlore iridates", Phys. Rev. B **83**, 205101 (2011).

[16] R. Karplus and J. M. Luttinger, "Hall Effect in Ferromagnetics", Phys. Rev. **95**, 1154 (1954).

[17] D. J. Thouless, M. Kohmoto, M. P. Nightingale, and M. den Nijs, "Quantized Hall Conductance in a Two-Dimensional Periodic Potential", Phys. Rev. Lett. **49**, 405 (1982).

[18] M. V. Berry, "Aspects of Degeneracy", in *Chaotic Behavior in Quantum Systems: Theory and Applications*, edited by G. Casati (Springer US, Boston, MA, 1985), pp. 123–140.

[19] J. M. Kosterlitz and D. J. Thouless, "Ordering, metastability and phase transitions in two-dimensional systems", J. Phys. C: Solid State Phys. **6**, 1181 (1973).

[20] J. M. Kosterlitz and D. J. Thouless, "Long range order and metastability in two dimensional solids and superfluids. (Application of dislocation theory)", J. Phys. C: Solid State Phys. **5**, L124 (1972).

[21] X. Dai, "Topological phases and transitions in condensed matter systems", PHYSICS **45**, 757 (2016).

[22] X.-L. Qi and S.-C. Zhang, "Topological insulators and superconductors", Rev. Mod. Phys. **83**, 1057 (2011).

[23] H. Zhang, C.-X. Liu, X.-L. Qi, X. Dai, Z. Fang, and S.-C. Zhang, "Topological insulators in Bi_2Se_3, Bi_2Te_3 and Sb_2Te_3 with a single Dirac cone on the surface", Nat. Phys. **5**, 438 (2009).

[24] F. D. M. Haldane, "Model for a Quantum Hall Effect without Landau Levels: Condensed-Matter Realization of the "Parity Anomaly"", Phys. Rev. Lett. **61**, 2015 (1988).

[25] C. L. Kane and E. J. Mele, "Quantum Spin Hall Effect in Graphene", Phys. Rev. Lett. **95**, 226801 (2005).

[26] C. L. Kane and E. J. Mele, "Z_2 Topological Order and the Quantum Spin Hall Effect", Phys. Rev. Lett. **95**, 146802 (2005).

[27] B. A. Bernevig, T. L. Hughes, and S.-C. Zhang, "Quantum Spin Hall Effect and Topological Phase Transition in HgTe Quantum Wells", Science **314**, 1757 (2006).

[28] L. Fu and C. L. Kane, "Topological insulators with inversion symmetry", Phys. Rev. B **76**, 045302 (2007).

[29] L. Fu, C. L. Kane, and E. J. Mele, "Topological Insulators in Three Dimensions", Phys. Rev. Lett. **98**, 106803 (2007).

[30] J. E. Moore and L. Balents, "Topological invariants of time-reversal-invariant band structures", Phys. Rev. B **75**, 121306 (2007).

[31] D. Hsieh, D. Qian, L. Wray, Y. Xia, Y. S. Hor, R. J. Cava, and M. Z. Hasan, "A topological Dirac insulator in a quantum spin Hall phase", Nature **452**, 970 (2008).

[32] Y. L. Chen, J. G. Analytis, J.-H. Chu, Z. K. Liu, S.-K. Mo, X. L. Qi, H. J. Zhang, D. H. Lu, X. Dai, Z. Fang, S. C. Zhang, I. R. Fisher, Z. Hussain, and Z.-X. Shen, "Experimental Realization of a Three-Dimensional Topological Insulator, Bi_2Te_3", Science **325**, 178 (2009).

[33] Y. Xia, D. Qian, D. Hsieh, L. Wray, A. Pal, H. Lin, A. Bansil, D. Grauer, Y. S. Hor, R. J. Cava, and et al., "Observation of a large-gap topological-insulator class with a single Dirac cone on the surface", Nat. Phys. **5**, 398 (2009).

[34] M. Z. Hasan and C. L. Kane, "Colloquium: Topological insulators", Rev. Mod. Phys. **82**, 3045 (2010).

[35] L.-Q. Zhou, Y.-F. Xu, H.-M. Weng, and Z. Fang., "Magnetic Weyl semimetal materials", PHYSICS **49**, 807 (2020).

[36] N. P. Armitage, E. J. Mele, and A. Vishwanath, "Weyl and Dirac semimetals in three-dimensional solids", Rev. Mod. Phys. **90**, 015001 (2018).

[37] H. Weng, C. Fang, Z. Fang, B. A. Bernevig, and X. Dai, "Weyl Semimetal Phase in Non-centrosymmetric Transition-Metal Monophosphides", Phys. Rev. X **5**, 011029 (2015).

[38] B. Q. Lv, N. Xu, H. M. Weng, J. Z. Ma, P. Richard, X. C. Huang, L. X. Zhao, G. F. Chen, C. E. Matt, F. Bisti, and et al., "Observation of Weyl nodes in TaAs", Nat. Phys. **11**, 724 (2015).

[39] B. Q. Lv, H. M. Weng, B. B. Fu, X. P. Wang, H. Miao, J. Ma, P. Richard, X. C. Huang, L. X. Zhao, G. F. Chen, Z. Fang, X. Dai, T. Qian, and H. Ding, "Experimental Discovery of Weyl Semimetal TaAs", Phys. Rev. X **5**, 031013 (2015).

[40] G. Xu, H. Weng, Z. Wang, X. Dai, and Z. Fang, "Chern Semimetal and the Quantized Anomalous Hall Effect in $HgCr_2Se_4$", Phys. Rev. Lett. **107**, 186806 (2011).

[41] A. A. Burkov and L. Balents, "Weyl Semimetal in a Topological Insulator Multilayer", Phys. Rev. Lett. **107**, 127205 (2011).

[42] A. A. Burkov, M. D. Hook, and L. Balents, "Topological nodal semimetals", Phys. Rev. B **84**, 235126 (2011).

[43] Q. Wang, Y. Xu, R. Lou, Z. Liu, M. Li, Y. Huang, D. Shen, H. Weng, S. Wang, and H. Lei, "Large intrinsic anomalous Hall effect in half-metallic ferromagnet $Co_3Sn_2S_2$ with magnetic Weyl fermions", Nat. Commun. **9**, 3681 (2018).

[44] E. Liu, Y. Sun, N. Kumar, L. Muechler, A. Sun, L. Jiao, S.-Y. Yang, D. Liu, A. Liang, Q. Xu, and et al., "Giant anomalous Hall effect in a ferromagnetic kagome-lattice semimetal", Nat. Phys. **14**, 1125 (2018).

[45] H. Weng, "Magnetic Weyl semimetal finally confirmed", Sci. China Phys. Mech. Astron. **62**, 12 (2019).

[46] D. Xiao, M.-C. Chang, and Q. Niu, "Berry phase effects on electronic properties", Rev. Mod. Phys. **82**, 1959 (2010).

[47] M. V. Berry, "Quantal phase factors accompanying adiabatic changes", Proc. R. Soc. A **392**, 45 (1984).

[48] Z. Fang, N. Nagaosa, K. S. Takahashi, A. Asamitsu, R. Mathieu, T. Ogasawara, H. Yamada, M. Kawasaki, Y. Tokura, and K. Terakura, "The Anomalous Hall Effect and Magnetic Monopoles in Momentum Space", Science **302**, 92 (2003).

[49] G. B. Halász and L. Balents, "Time-reversal invariant realization of the Weyl semimetal phase", Phys. Rev. B **85**, 035103 (2012).

[50] C. J. Tabert and J. P. Carbotte, "Optical conductivity of Weyl semimetals and signatures of the gapped semimetal phase transition", Phys. Rev. B **93**, 085442 (2016).

[51] M. Koshino and I. F. Hizbullah, "Magnetic susceptibility in three-dimensional nodal semimetals", Phys. Rev. B **93**, 045201 (2016).

[52] S. M. Young, S. Zaheer, J. C. Y. Teo, C. L. Kane, E. J. Mele, and A. M. Rappe, "Dirac Semimetal in Three Dimensions", Phys. Rev. Lett. **108**, 140405 (2012).

[53] Z. Wang, Y. Sun, X.-Q. Chen, C. Franchini, G. Xu, H. Weng, X. Dai, and Z. Fang, "Dirac semimetal and topological phase transitions in A_3Bi (A = Na, K, Rb)", Phys. Rev. B **85**, 195320 (2012).

[54] Z. Wang, H. Weng, Q. Wu, X. Dai, and Z. Fang, "Three-dimensional Dirac semimetal and quantum transport in Cd_3As_2", Phys. Rev. B **88**, 125427 (2013).

[55] Z. K. Liu, B. Zhou, Y. Zhang, Z. J. Wang, H. M. Weng, D. Prabhakaran, S.-K. Mo, Z. X. Shen, Z. Fang, X. Dai, Z. Hussain, and Y. L. Chen, "Discovery of a Three-Dimensional Topological Dirac Semimetal, Na_3Bi", Science **343**, 864 (2014).

[56] S.-Y. Xu, C. Liu, S. K. Kushwaha, R. Sankar, J. W. Krizan, I. Belopolski, M. Neupane, G. Bian, N. Alidoust, T.-R. Chang, H.-T. Jeng, C.-Y. Huang, W.-F. Tsai, H. Lin, P. P. Shibayev, F.-C. Chou, R. J. Cava, and M. Z. Hasan, "Observation of Fermi arc surface states in a topological metal", Science **347**, 294 (2015).

[57] M. Neupane, S.-Y. Xu, R. Sankar, N. Alidoust, G. Bian, C. Liu, I. Belopolski, T.-R. Chang, H.-T. Jeng, H. Lin, and et al., "Observation of a three-dimensional topological Dirac semimetal phase in high-mobility Cd_3As_2", Nat. Commun. **5**, 3786 (2014).

[58] Z. K. Liu, J. Jiang, B. Zhou, Z. J. Wang, Y. Zhang, H. M. Weng, D. Prabhakaran, S.-K. Mo, H. Peng, P. Dudin, and et al., "A stable three-dimensional topological Dirac semimetal Cd_3As_2", Nat. Mater. **13**, 677 (2014).

[59] S. Borisenko, Q. Gibson, D. Evtushinsky, V. Zabolotnyy, B. Büchner, and R. J. Cava, "Experimental Realization of a Three-Dimensional Dirac Semimetal", Phys. Rev. Lett. **113**, 027603 (2014).

[60] L. P. He, X. C. Hong, J. K. Dong, J. Pan, Z. Zhang, J. Zhang, and S. Y. Li, "Quantum Transport Evidence for the Three-Dimensional Dirac Semimetal Phase in Cd_3As_2", Phys. Rev. Lett. **113**, 246402 (2014).

[61] H. Yi, Z. Wang, C. Chen, Y. Shi, Y. Feng, A. Liang, Z. Xie, S. He, J. He, Y. Peng, and et al., "Evidence of Topological Surface State in Three-Dimensional Dirac Semimetal Cd_3As_2", Sci. Rep. **4**, 6106 (2014).

[62] S. K. Kushwaha, J. W. Krizan, B. E. Feldman, A. Gyenis, M. T. Randeria, J. Xiong, S.-Y. Xu, N. Alidoust, I. Belopolski, T. Liang, M. Zahid Hasan, N. P. Ong, A. Yazdani, and R. J. Cava, "Bulk crystal growth and electronic characterization of the 3D Dirac semimetal Na_3Bi", APL Mater. **3**, 041504 (2015).

[63] S.-Y. Xu, C. Liu, I. Belopolski, S. K. Kushwaha, R. Sankar, J. W. Krizan, T.-R. Chang, C. M. Polley, J. Adell, T. Balasubramanian, K. Miyamoto, N. Alidoust, G. Bian, M. Neupane, H.-T. Jeng, C.-Y. Huang, W.-F. Tsai, T. Okuda, A. Bansil, F. C. Chou, R. J. Cava, H. Lin, and M. Z. Hasan, "Lifshitz transition and Van Hove singularity in a three-dimensional topological Dirac semimetal", Phys. Rev. B **92**, 075115 (2015).

[64] Y. Du, B. Wan, D. Wang, L. Sheng, C.-G. Duan, and X. Wan, "Dirac and Weyl Semimetal in XYBi (X = Ba, Eu; Y = Cu, Ag and Au)", Sci. Rep. **5**, 14423 (2015).

[65] Q. D. Gibson, L. M. Schoop, L. Muechler, L. S. Xie, M. Hirschberger, N. P. Ong, R. Car, and R. J. Cava, "Three-dimensional Dirac semimetals: Design principles and predictions of new materials", Phys. Rev. B **91**, 205128 (2015).

[66] I. Y. Sklyadneva, I. P. Rusinov, R. Heid, K.-P. Bohnen, P. M. Echenique, and E. V. Chulkov, "Pressure-induced topological phases of KNa_2Bi", Sci. Rep. **6**, 24137 (2016).

[67] H. Weng, X. Dai, and Z. Fang, "Topological semimetals predicted from first-principles calculations", J. Phys.: Condens. Matter **28**, 303001 (2016).

[68] A. A. Soluyanov, D. Gresch, Z. Wang, Q. Wu, M. Troyer, X. Dai, and B. A. Bernevig, "Type-II Weyl semimetals", Nature **527**, 495 (2015).

[69] H. Huang, S. Zhou, and W. Duan, "Type-II Dirac fermions in the **PtSe$_2$** class of transition metal dichalcogenides", Phys. Rev. B **94**, 121117 (2016).

[70] M. Yan, H. Huang, K. Zhang, E. Wang, W. Yao, K. Deng, G. Wan, H. Zhang, M. Arita, H. Yang, and et al., "Lorentz-violating type-II Dirac fermions in transition metal dichalcogenide PtTe$_2$", Nat. Commun. **8**, 257 (2017).

[71] K. Zhang, M. Yan, H. Zhang, H. Huang, M. Arita, Z. Sun, W. Duan, Y. Wu, and S. Zhou, "Experimental evidence for type-II Dirac semimetal in PtSe$_2$", Phys. Rev. B **96**, 125102 (2017).

[72] F. Fei, X. Bo, R. Wang, B. Wu, J. Jiang, D. Fu, M. Gao, H. Zheng, Y. Chen, X. Wang, H. Bu, F. Song, X. Wan, B. Wang, and G. Wang, "Nontrivial Berry phase and type-II Dirac transport in the layered material PdTe$_2$", Phys. Rev. B **96**, 041201 (2017).

[73] H.-J. Noh, J. Jeong, E.-J. Cho, K. Kim, B. I. Min, and B.-G. Park, "Experimental Realization of Type-II Dirac Fermions in a PdTe$_2$ Superconductor", Phys. Rev. Lett. **119**, 016401 (2017).

[74] P.-J. Guo, H.-C. Yang, K. Liu, and Z.-Y. Lu, "Type-II Dirac semimetals in the YPd$_2$Sn class", Phys. Rev. B **95**, 155112 (2017).

[75] T.-R. Chang, S.-Y. Xu, D. S. Sanchez, W.-F. Tsai, S.-M. Huang, G. Chang, C.-H. Hsu, G. Bian, I. Belopolski, Z.-M. Yu, S. A. Yang, T. Neupert, H.-T. Jeng, H. Lin, and M. Z. Hasan, "Type-II Symmetry-Protected Topological Dirac Semimetals", Phys. Rev. Lett. **119**, 026404 (2017).

[76] G. G. Pyrialakos, N. S. Nye, N. V. Kantartzis, and D. N. Christodoulides, "Emergence of Type-II Dirac Points in Graphynelike Photonic Lattices", Phys. Rev. Lett. **119**, 113901 (2017).

[77] M. Bahramy, O. Clark, B.-J. Yang, J. Feng, L. Bawden, J. Riley, I. Marković, F. Mazzola, V. Sunko, D. Biswas, et al., "Ubiquitous formation of bulk Dirac cones and topological surface states from a single orbital manifold in transition-metal dichalcogenides", Nat. Mater. **17**, 21 (2018).

[78] Z. Hu, J. Deng, H. Li, M. O. Ogunbunmi, X. Tong, Q. Wang, D. Graf, W. R. Pudełko, Y. Liu, H. Lei, et al., "Robust three-dimensional type-II Dirac semimetal state in SrAgBi", npj Quantum Mater. **8**, 20 (2023).

[79] E. Haidemenakis, J. Mavroides, M. Dresselhaus, and D. Kolesar, "Observation of interband transitions in Cd$_3$As$_2$", Solid State Commun. **4**, 65 (1966).

[80] L. Żdanowicz and T. Kwiecień, "4.6 Some optical properties of thin Cd$_3$As$_2$ films", Vacuum **27**, 409 (1977).

[81] D. Houde, S. Jandl, M. Banville, and M. Aubin, "The infrared spectrum of Cd$_3$As$_2$", Solid State Commun. **57**, 247 (1986).

[82] S. Jeon, B. B. Zhou, A. Gyenis, B. E. Feldman, I. Kimchi, A. C. Potter, Q. D. Gibson, R. J. Cava, A. Vishwanath, and A. Yazdani, "Landau quantization and quasiparticle interference in the three-dimensional Dirac semimetal Cd$_3$As$_2$", Nat. Mater. **13**, 851 (2014).

[83] B.-J. Yang and N. Nagaosa, "Classification of stable three-dimensional Dirac semimetals with nontrivial topology", Nat. Commun. **5**, 4898 (2014).

[84] M. N. Ali, Q. Gibson, S. Jeon, B. B. Zhou, A. Yazdani, and R. J. Cava, "The Crystal and Electronic Structures of Cd$_3$As$_2$, the Three-Dimensional Electronic Analogue of Graphene", Inorganic Chemistry **53**, 4062 (2014).

[85] T. Liang, Q. Gibson, M. N. Ali, M. Liu, R. J. Cava, and N. P. Ong, "Ultrahigh mobility and giant magnetoresistance in the Dirac semimetal Cd_3As_2", Nat. Mater. **14**, 280 (2015).

[86] J. Xiong, S. Kushwaha, J. Krizan, T. Liang, R. J. Cava, and N. P. Ong, "Anomalous conductivity tensor in the Dirac semimetal Na_3Bi", Europhys. Lett. **114**, 27002 (2016).

[87] H. F. Yuan, W. Xu, X. N. Zhao, D. Song, G. R. Zhang, Y. M. Xiao, L. Ding, and F. M. Peeters, "Quantum and transport mobilities of a Na_3Bi-based three-dimensional Dirac system", Phys. Rev. B **99**, 235303 (2019).

[88] Z. Jia, C. Li, X. Li, J. Shi, Z. Liao, D. Yu, and X. Wu, "Thermoelectric signature of the chiral anomaly in Cd_3As_2", Nat. Commun. **7**, 13013 (2016).

[89] C. Zhang, E. Zhang, W. Wang, Y. Liu, Z.-G. Chen, S. Lu, S. Liang, J. Cao, X. Yuan, L. Tang, Q. Li, C. Zhou, T. Gu, Y. Wu, J. Zou, and F. Xiu, "Room-temperature chiral charge pumping in Dirac semimetals", Nat. Commun. **8**, 13741 (2017).

[90] C.-Z. Li, L.-X. Wang, H. Liu, J. Wang, Z.-M. Liao, and D.-P. Yu, "Giant negative magnetoresistance induced by the chiral anomaly in individual Cd_3As_2 nanowires", Nat. Commun. **6**, 10137 (2015).

[91] H. Li, H. He, H.-Z. Lu, H. Zhang, H. Liu, R. Ma, Z. Fan, S.-Q. Shen, and J. Wang, "Negative magnetoresistance in Dirac semimetal Cd_3As_2", Nat. Commun. **7**, 10301 (2016).

[92] S. Zhang, Q. Wu, L. Schoop, M. N. Ali, Y. Shi, N. Ni, Q. Gibson, S. Jiang, V. Sidorov, W. Yi, J. Guo, Y. Zhou, D. Wu, P. Gao, D. Gu, C. Zhang, S. Jiang, K. Yang, A. Li, Y. Li, X. Li, J. Liu, X. Dai, Z. Fang, R. J. Cava, L. Sun, and Z. Zhao, "Breakdown of three-dimensional Dirac semimetal state in pressurized Cd_3As_2", Phys. Rev. B **91**, 165133 (2015).

[93] L. He, Y. Jia, S. Zhang, X. Hong, C. Jin, and S. Li, "Pressure-induced superconductivity in the three-dimensional topological Dirac semimetal Cd_3As_2", npj Quant. Mater. **1**, 16014 (2016).

[94] A. Y. Kitaev, "Unpaired Majorana fermions in quantum wires", Phys. Usp. **44**, 131 (2001).

[95] J. Alicea, "New directions in the pursuit of Majorana fermions in solid state systems", Rep. Prog. Phys. **75**, 076501 (2012).

[96] C. Beenakker, "Search for Majorana Fermions in Superconductors", Annu. Rev. Condens. Matter Phys. **4**, 113 (2013).

[97] L. Fu and C. L. Kane, "Superconducting Proximity Effect and Majorana Fermions at the Surface of a Topological Insulator", Phys. Rev. Lett. **100**, 096407 (2008).

[98] L. Aggarwal, A. Gaurav, G. S. Thakur, Z. Haque, A. K. Ganguli, and G. Sheet, "Unconventional superconductivity at mesoscopic point contacts on the 3D Dirac semimetal Cd_3As_2", Nat. Mater. **15**, 32 (2016).

[99] H. Wang, H. Wang, H. Liu, H. Lu, W. Yang, S. Jia, X.-J. Liu, X. C. Xie, J. Wei, and J. Wang, "Observation of superconductivity induced by a point contact on 3D Dirac semimetal Cd_3As_2", Nat. Mater. **15**, 38 (2016).

[100] A. Chen, D. I. Pikulin, and M. Franz, "Josephson current signatures of Majorana flat bands on the surface of time-reversal-invariant Weyl and Dirac semimetals", Phys. Rev. B **95**, 174505 (2017).

[101] C.-Z. Li, C. Li, L.-X. Wang, S. Wang, Z.-M. Liao, A. Brinkman, and D.-P. Yu, "Bulk and surface states carried supercurrent in ballistic Nb-Dirac semimetal Cd_3As_2 nanowire-Nb junctions", Phys. Rev. B **97**, 115446 (2018).

[102] W. Yu, W. Pan, D. L. Medlin, M. A. Rodriguez, S. R. Lee, Z.-q. Bao, and F. Zhang, "π and 4π Josephson Effects Mediated by a Dirac Semimetal", Phys. Rev. Lett. **120**, 177704 (2018).

[103] A.-Q. Wang, C.-Z. Li, C. Li, Z.-M. Liao, A. Brinkman, and D.-P. Yu, "4π-Periodic Supercurrent from Surface States in Cd_3As_2 Nanowire-Based Josephson Junctions", Phys. Rev. Lett. **121**, 237701 (2018).

[104] C. Huang, B. T. Zhou, H. Zhang, B. Yang, R. Liu, H. Wang, Y. Wan, K. Huang, Z. Liao, E. Zhang, S. Liu, Q. Deng, Y. Chen, X. Han, J. Zou, X. Lin, Z. Han, Y. Wang, K. T. Law, and F. Xiu, "Proximity-induced surface superconductivity in Dirac semimetal Cd_3As_2", Nat. Commun. **10**, 2217 (2019).

[105] E. Uykur, R. Sankar, D. Schmitz, and C. A. Kuntscher, "Optical spectroscopy study on pressure-induced phase transitions in the three-dimensional Dirac semimetal Cd_3As_2", Phys. Rev. B **97**, 195134 (2018).

[106] C. M. Wang, H.-Z. Lu, and S.-Q. Shen, "Anomalous Phase Shift of Quantum Oscillations in 3D Topological Semimetals", Phys. Rev. Lett. **117**, 077201 (2016).

[107] G. P. Mikitik and Y. V. Sharlai, "Manifestation of Berry's Phase in Metal Physics", Phys. Rev. Lett. **82**, 2147 (1999).

[108] A. Narayanan, M. D. Watson, S. F. Blake, N. Bruyant, L. Drigo, Y. L. Chen, D. Prabhakaran, B. Yan, C. Felser, T. Kong, P. C. Canfield, and A. I. Coldea, "Linear Magnetoresistance Caused by Mobility Fluctuations in n-Doped Cd_3As_2", Phys. Rev. Lett. **114**, 117201 (2015).

[109] J. Cao, S. Liang, C. Zhang, Y. Liu, J. Huang, Z. Jin, Z.-G. Chen, Z. Wang, Q. Wang, J. Zhao, S. Li, X. Dai, J. Zou, Z. Xia, L. Li, and F. Xiu, "Landau level splitting in Cd_3As_2 under high magnetic fields", Nat. Commun. **6**, 7779 (2015).

[110] Y. Zhao, H. Liu, C. Zhang, H. Wang, J. Wang, Z. Lin, Y. Xing, H. Lu, J. Liu, Y. Wang, S. M. Brombosz, Z. Xiao, S. Jia, X. C. Xie, and J. Wang, "Anisotropic Fermi Surface and Quantum Limit Transport in High Mobility Three-Dimensional Dirac Semimetal Cd_3As_2", Phys. Rev. X **5**, 031037 (2015).

[111] A. Pariari, P. Dutta, and P. Mandal, "Probing the Fermi surface of three-dimensional Dirac semimetal Cd_3As_2 through the de Haas–van Alphen technique", Phys. Rev. B **91**, 155139 (2015).

[112] Z. J. Xiang, D. Zhao, Z. Jin, C. Shang, L. K. Ma, G. J. Ye, B. Lei, T. Wu, Z. C. Xia, and X. H. Chen, "Angular-Dependent Phase Factor of Shubnikov–de Haas Oscillations in the Dirac Semimetal Cd_3As_2", Phys. Rev. Lett. **115**, 226401 (2015).

[113] J. Feng, Y. Pang, D. Wu, Z. Wang, H. Weng, J. Li, X. Dai, Z. Fang, Y. Shi, and L. Lu, "Large linear magnetoresistance in Dirac semimetal Cd_3As_2 with Fermi surfaces close to the Dirac points", Phys. Rev. B **92**, 081306 (2015).

[114] W. Desrat, S. S. Krishtopenko, B. A. Piot, M. Orlita, C. Consejo, S. Ruffenach, W. Knap, A. Nateprov, E. Arushanov, and F. Teppe, "Band splitting in Cd_3As_2 measured by magnetotransport", Phys. Rev. B **97**, 245203 (2018).

[115] Y. Liu, C. Zhang, X. Yuan, T. Lei, C. Wang, D. Di Sante, A. Narayan, L. He, S. Picozzi, S. Sanvito, R. Che, and F. Xiu, "Gate-tunable quantum oscillations in ambipolar Cd_3As_2 thin films", NPG Asia Mater. **7**, e221 (2015).

[116] A. C. Potter, I. Kimchi, and A. Vishwanath, "Quantum oscillations from surface Fermi arcs in Weyl and Dirac semimetals", Nat. Commun. **5**, 5161 (2014).

[117] L.-X. Wang, C.-Z. Li, D.-P. Yu, and Z.-M. Liao, "Aharonov-Bohm oscillations in Dirac semimetal Cd_3As_2 nanowires", Nat. Commun. **7**, 10769 (2016).

[118] B.-C. Lin, S. Wang, L.-X. Wang, C.-Z. Li, J.-G. Li, D. Yu, and Z.-M. Liao, "Gate-tuned Aharonov-Bohm interference of surface states in a quasiballistic Dirac semimetal nanowire", Phys. Rev. B **95**, 235436 (2017).

[119] U. Fano, "Effects of Configuration Interaction on Intensities and Phase Shifts", Phys. Rev. **124**, 1866 (1961).

[120] S. Wang, B.-C. Lin, W.-Z. Zheng, D. Yu, and Z.-M. Liao, "Fano Interference between Bulk and Surface States of a Dirac Semimetal Cd_3As_2 Nanowire", Phys. Rev. Lett. **120**, 257701 (2018).

[121] P. J. W. Moll, N. L. Nair, T. Helm, A. C. Potter, I. Kimchi, A. Vishwanath, and J. G. Analytis, "Transport evidence for Fermi-arc-mediated chirality transfer in the Dirac semimetal Cd_3As_2", Nature **535**, 266 (2016).

[122] B. Zhou, H.-Z. Lu, R.-L. Chu, S.-Q. Shen, and Q. Niu, "Finite Size Effects on Helical Edge States in a Quantum Spin-Hall System", Phys. Rev. Lett. **101**, 246807 (2008).

[123] A.-Q. Wang, X.-G. Ye, D.-P. Yu, and Z.-M. Liao, "Topological Semimetal Nanostructures: From Properties to Topotronics", ACS Nano **14**, 3755 (2020).

[124] M. Uchida, Y. Nakazawa, S. Nishihaya, K. Akiba, M. Kriener, Y. Kozuka, A. Miyake, Y. Taguchi, M. Tokunaga, N. Nagaosa, Y. Tokura, and M. Kawasaki, "Quantum Hall states observed in thin films of Dirac semimetal Cd_3As_2", Nat. Commun. **8**, 2274 (2017).

[125] S. Nishihaya, M. Uchida, Y. Nakazawa, M. Kriener, Y. Kozuka, Y. Taguchi, and M. Kawasaki, "Gate-tuned quantum Hall states in Dirac semimetal $(Cd_{1-x}Zn_x)_3As_2$", Sci. Adv. **4**, eaar5668 (2018).

[126] C. M. Wang, H.-P. Sun, H.-Z. Lu, and X. C. Xie, "3D Quantum Hall Effect of Fermi Arcs in Topological Semimetals", Phys. Rev. Lett. **119**, 136806 (2017).

[127] C. Zhang, Y. Zhang, X. Yuan, S. Lu, J. Zhang, A. Narayan, Y. Liu, H. Zhang, Z. Ni, R. Liu, E. S. Choi, A. Suslov, S. Sanvito, L. Pi, H.-Z. Lu, A. C. Potter, and F. Xiu, "Quantum Hall effect based on Weyl orbits in Cd_3As_2", Nature **565**, 331 (2019).

[128] B.-C. Lin, S. Wang, S. Wiedmann, J.-M. Lu, W.-Z. Zheng, D. Yu, and Z.-M. Liao, "Observation of an Odd-Integer Quantum Hall Effect from Topological Surface States in Cd_3As_2", Phys. Rev. Lett. **122**, 036602 (2019).

[129] A. C. Lygo, B. Guo, A. Rashidi, V. Huang, P. Cuadros-Romero, and S. Stemmer, "Two-Dimensional Topological Insulator State in Cadmium Arsenide Thin Films", Phys. Rev. Lett. **130**, 046201 (2023).

[130] W. J. Turner, A. S. Fischler, and W. E. Reese, "Physical Properties of Several II-V Semiconductors", Phys. Rev. **121**, 759 (1961).

[131] M. Clavaguera, "Piezoresistance in cadmium arsenide", J. Phys. Chem. Solids **36**, 1205 (1975).

[132] J.-P. Jay-Gerin, M. J. Aubin, and L.-G. Caron, "Thermoelectric power and transverse Nernst-Ettingshausen coefficient of Cd_3As_2 at 300 K", Phys. Rev. B **18**, 4542 (1978).

[133] D. Neubauer, J. P. Carbotte, A. A. Nateprov, A. Löhle, M. Dressel, and A. V. Pronin, "Interband optical conductivity of the [001]-oriented Dirac semimetal Cd_3As_2", Phys. Rev. B **93**, 121202 (2016).

[134] A. Akrap, M. Hakl, S. Tchoumakov, I. Crassee, J. Kuba, M. O. Goerbig, C. C. Homes, O. Caha, J. Novák, F. Teppe, W. Desrat, S. Koohpayeh, L. Wu, N. P. Armitage, A. Nateprov, E. Arushanov, Q. D. Gibson, R. J. Cava, D. van der Marel, B. A. Piot, C. Faugeras, G. Martinez, M. Potemski, and M. Orlita, "Magneto-Optical Signature of Massless Kane Electrons in Cd_3As_2", Phys. Rev. Lett. **117**, 136401 (2016).

[135] L.-k. Shi and J. C. W. Song, "Large optical conductivity of Dirac semimetal Fermi arc surface states", Phys. Rev. B **96**, 081410 (2017).

[136] Q. Wang, C.-Z. Li, S. Ge, J.-G. Li, W. Lu, J. Lai, X. Liu, J. Ma, D.-P. Yu, Z.-M. Liao, and D. Sun, "Ultrafast Broadband Photodetectors Based on Three-Dimensional Dirac Semimetal Cd_3As_2", Nano Lett. **17**, PMID: 28099030, 834 (2017).

[137] F. H. L. Koppens, T. Mueller, P. Avouris, A. C. Ferrari, M. S. Vitiello, and M. Polini, "Photodetectors based on graphene, other two-dimensional materials and hybrid systems", Nat. Nanotech. **9**, 780 (2014).

[138] F. Xia, T. Mueller, Y.-m. Lin, A. Valdes-Garcia, and P. Avouris, "Ultrafast graphene photodetector", Nat. Nanotech. **4**, 839 (2009).

[139] W. Lu, S. Ge, X. Liu, H. Lu, C. Li, J. Lai, C. Zhao, Z. Liao, S. Jia, and D. Sun, "Ultrafast relaxation dynamics of photoexcited Dirac fermions in the three-dimensional Dirac semimetal Cd_3As_2", Phys. Rev. B **95**, 024303 (2017).

[140] M. Yang, J. Wang, J. Han, J. Ling, C. Ji, X. Kong, X. Liu, Z. Huang, J. Gou, Z. Liu, F. Xiu, and Y. Jiang, "Enhanced Performance of Wideband Room Temperature Photodetector Based on Cd_3As_2 Thin Film/Pentacene Heterojunction", ACS Photonics **5**, 3438 (2018).

[141] Y. Meng, C. Zhu, Y. Li, X. Yuan, F. Xiu, Y. Shi, Y. Xu, and F. Wang, "Three-dimensional Dirac semimetal thin-film absorber for broadband pulse generation in the near-infrared", Opt. Lett. **43**, 1503 (2018).

[142] W. Lu, J. Ling, F. Xiu, and D. Sun, "Terahertz probe of photoexcited carrier dynamics in the Dirac semimetal Cd_3As_2", Phys. Rev. B **98**, 104310 (2018).

[143] K. J. A. Ooi, Y. S. Ang, Q. Zhai, D. T. H. Tan, L. K. Ang, and C. K. Ong, "Nonlinear plasmonics of three-dimensional Dirac semimetals", APL Photonics **4**, 034402 (2018).

[144] W. Zhang, Y. Yang, P. Suo, W. Zhao, J. Guo, Q. Lu, X. Lin, Z. Jin, L. Wang, G. Chen, F. Xiu, W. Liu, C. Zhang, and G. Ma, "Ultrafast photocarrier dynamics in a 3D Dirac semimetal Cd_3As_2 film studied with terahertz spectroscopy", Appl. Phys. Lett. **114**, 221102 (2019).

[145] Y. Sun, Y. Meng, H. Jiang, S. Qin, Y. Yang, F. Xiu, Y. Shi, S. Zhu, and F. Wang, "Dirac semimetal saturable absorber with actively tunable modulation depth", Opt. Lett. **44**, 582 (2019).

[146] H. T. Chorsi, S. Yue, P. P. Iyer, M. Goyal, T. Schumann, S. Stemmer, B. Liao, and J. A. Schuller, "Widely Tunable Optical and Thermal Properties of Dirac Semimetal Cd_3As_2", Adv. Opt. Mater. **8**, 1901192 (2020).

[147] Z. Huang, Y. Jiang, Q. Han, M. Yang, J. Han, F. Wang, M. Luo, Q. Li, H. Zhu, X. Liu, J. Gou, and J. Wang, "High responsivity and fast UV–vis–short-wavelength IR photodetector based on Cd_3As_2/MoS_2 heterojunction", Nanotechnology **31**, 064001 (2019).

[148] S. Kovalev, R. M. A. Dantas, S. Germanskiy, J.-C. Deinert, B. Green, I. Ilyakov, N. Awari, M. Chen, M. Bawatna, J. Ling, F. Xiu, P. H. M. van Loosdrecht, P. Surowka, T. Oka, and Z. Wang, "Non-perturbative terahertz high-harmonic generation in the three-dimensional Dirac semimetal Cd_3As_2", Nat. Commun. **11**, 2451 (2020).

[149] Z. Dai, M. Manjappa, Y. Yang, T. C. W. Tan, B. Qiang, S. Han, L. J. Wong, F. Xiu, W. Liu, and R. Singh, "High Mobility 3D Dirac Semimetal (Cd_3As_2) for Ultrafast Photoactive Terahertz Photonics", Adv. Funct. Mater. **31**, 2011011 (2021).

[150] X. Zhang, R. Pan, Y. Yang, Q. Han, X. Liu, C. Zhang, H. Zhou, J. Han, J. Gou, and J. Wang, "High-Performance Photodetector based on a 3D Dirac Semimetal Cd_3As_2/Tungsten Disulfide (WS_2) van der Waals Heterojunction", Adv. Photonics Res. **2**, 2000194 (2021).

[151] W. Lu, Z. Fan, Y. Yang, J. Ma, J. Lai, X. Song, X. Zhuo, Z. Xu, J. Liu, X. Hu, S. Zhou, F. Xiu, J. Cheng, and D. Sun, "Ultrafast photothermoelectric effect in Dirac semimetallic Cd_3As_2 revealed by terahertz emission", Nat. Commun. **13**, 1623 (2022).

[152] L. Hou, Y. Yang, A. Li, Q. Wang, Q. Li, M. Wu, P. Ji, Y. Zhang, Y. Xiao, W. Xu, F. Xiu, and L. Ding, "Temperature-dependent terahertz properties of carriers and phonons in the topological Dirac semimetal Cd_3As_2", Phys. Rev. B **108**, 115416 (2023).

[153] K. Zhang, M. Yan, H. Zhang, H. Huang, M. Arita, Z. Sun, W. Duan, Y. Wu, and S. Zhou, "Experimental evidence for type-II Dirac semimetal in $PtSe_2$", Phys. Rev. B **96**, 125102 (2017).

[154] L. Fu, D. Hu, R. G. Mendes, M. H. Rümmeli, Q. Dai, B. Wu, L. Fu, and Y. Liu, "Highly Organized Epitaxy of Dirac Semimetallic $PtTe_2$ Crystals with Extrahigh Conductivity and Visible Surface Plasmons at Edges", ACS Nano **12**, 9405 (2018).

[155] F. Fei, X. Bo, R. Wang, B. Wu, J. Jiang, D. Fu, M. Gao, H. Zheng, Y. Chen, X. Wang, H. Bu, F. Song, X. Wan, B. Wang, and G. Wang, "Nontrivial Berry phase and type-II Dirac transport in the layered material $PdTe_2$", Phys. Rev. B **96**, 041201 (2017).

[156] W. Zheng, R. Schönemann, N. Aryal, Q. Zhou, D. Rhodes, Y.-C. Chiu, K.-W. Chen, E. Kampert, T. Förster, T. J. Martin, G. T. McCandless, J. Y. Chan, E. Manousakis, and L. Balicas, "Detailed study of the Fermi surfaces of the type-II Dirac semimetallic candidates XTe$_2$ (X=Pd, Pt)", Phys. Rev. B **97**, 235154 (2018).

[157] D. Fu, X. Bo, F. Fei, B. Wu, M. Gao, X. Wang, M. Naveed, S. A. Shah, H. Bu, B. Wang, L. Cao, W. Zou, X. Wan, and F. Song, "Quantum oscillations in type-II Dirac semimetal $PtTe_2$", Phys. Rev. B **97**, 245109 (2018).

[158] Amit, R. K. Singh, N. Wadehra, S. Chakraverty, and Y. Singh, "Type-II Dirac semimetal candidates ATe$_2$ (A = Pt, Pd): A de Haas-van Alphen study", Phys. Rev. Mater. **2**, 114202 (2018).

[159] O. Pavlosiuk and D. Kaczorowski, "Galvanomagnetic properties of the putative type-II Dirac semimetal $PtTe_2$", Sci. Rep. **8**, 11297 (2018).

[160] S. Hao, J. Zeng, T. Xu, X. Cong, C. Wang, C. Wu, Y. Wang, X. Liu, T. Cao, G. Su, L. Jia, Z. Wu, Q. Lin, L. Zhang, S. Yan, M. Guo, Z. Wang, P. Tan, L. Sun, Z. Ni, S.-J. Liang, X. Cui, and F. Miao, "Low-Temperature Eutectic Synthesis of $PtTe_2$ with Weak Antilocalization and Controlled Layer Thinning", Adv. Funct. Mater. **28**, 1803746 (2018).

[161] H. Xu, J. Wei, H. Zhou, J. Feng, T. Xu, H. Du, C. He, Y. Huang, J. Zhang, Y. Liu, H.-C. Wu, C. Guo, X. Wang, Y. Guang, H. Wei, Y. Peng, W. Jiang, G. Yu, and X. Han, "High Spin Hall Conductivity in Large-Area Type-II Dirac Semimetal $PtTe_2$", Adv. Mater. **32**, 2000513 (2020).

[162] L. Fu, D. Hu, R. G. Mendes, M. H. Rümmeli, Q. Dai, B. Wu, L. Fu, and Y. Liu, "Highly Organized Epitaxy of Dirac Semimetallic $PtTe_2$ Crystals with Extrahigh Conductivity and Visible Surface Plasmons at Edges", ACS Nano **12**, 9405 (2018).

[163] J. Meng, H. Xue, M. Liu, W. Jiang, Z. Zhang, J. Ling, L. He, R. Dou, C. Xiong, and J. Nie, "Planar Hall effect induced by anisotropic orbital magnetoresistance in type-II Dirac semimetal PdTe2", J. Phys.: Condens. Matter **32**, 015702 (2019).

[164] A. A. Burkov, "Giant planar Hall effect in topological metals", Phys. Rev. B **96**, 041110 (2017).

[165] S. Nandy, G. Sharma, A. Taraphder, and S. Tewari, "Chiral Anomaly as the Origin of the Planar Hall Effect in Weyl Semimetals", Phys. Rev. Lett. **119**, 176804 (2017).

[166] J.-Y. Ba, F.-Y. Chen, H.-J. Duan, M.-X. Deng, and R.-Q. Wang, "Planar Hall effect in topological materials", Acta Phys. Sin. **72**, 207201 (2023).

[167] H. Li, H.-W. Wang, H. He, J. Wang, and S.-Q. Shen, "Giant anisotropic magnetoresistance and planar Hall effect in the Dirac semimetal Cd_3As_2", Phys. Rev. B **97**, 201110 (2018).

[168] J.-j. Guo, Z.-y. Luo, J.-j. Liao, Y.-z. Nie, Q.-l. Xia, R. Xiong, and G.-h. Guo, "Anisotropic magnetoresistance and planar Hall effect in type-II Dirac semimetal $PtTe_2$", J. Appl. Phys. **130**, 233901 (2021).

[169] R. Singha, S. Roy, A. Pariari, B. Satpati, and P. Mandal, "Planar Hall effect in the type-II Dirac semimetal VAl_3", Phys. Rev. B **98**, 081103 (2018).

[170] R. A. B. Villaos, C. P. Crisostomo, Z.-Q. Huang, S.-M. Huang, A. A. B. Padama, M. A. Albao, H. Lin, and F.-C. Chuang, "Thickness dependent electronic properties of Pt dichalcogenides", npj 2D Mater. Appl. **3**, 2 (2019).

[171] M.-K. Lin, R. A. B. Villaos, J. A. Hlevyack, P. Chen, R.-Y. Liu, C.-H. Hsu, J. Avila, S.-K. Mo, F.-C. Chuang, and T.-C. Chiang, "Dimensionality-Mediated Semimetal-Semiconductor Transition in Ultrathin $PtTe_2$ Films", Phys. Rev. Lett. **124**, 036402 (2020).

[172] A. Politano, G. Chiarello, B. Ghosh, K. Sadhukhan, C.-N. Kuo, C. S. Lue, V. Pellegrini, and A. Agarwal, "3D Dirac Plasmons in the Type-II Dirac Semimetal $PtTe_2$", Phys. Rev. Lett. **121**, 086804 (2018).

[173] D. P. Gulo, H. Yeh, W.-H. Chang, and H.-L. Liu, "Temperature-dependent optical and vibrational properties of $PtSe_2$ thin films", Sci. Rep. **10**, 19003 (2020).

[174] F. Ghasemi, R. Taghavimendi, and A. Bakhshayeshi, "Electronic and optical properties of monolayer and bulk of $PtSe_2$", Opt. Quant. Electron. **52**, 492 (2020).

[175] J. He, W. Jiang, X. Zhu, R. Zhang, J. Wang, M. Zhu, S. Wang, Y. Zheng, and L. Chen, "Optical properties of thickness-controlled $PtSe_2$ thin films studied via spectroscopic ellipsometry", Phys. Chem. Chem. Phys. **22**, 26383 (2020).

[176] G. A. Ermolaev, K. V. Voronin, M. K. Tatmyshevskiy, A. B. Mazitov, A. S. Slavich, D. I. Yakubovsky, A. P. Tselin, M. S. Mironov, R. I. Romanov, A. M. Markeev, I. A. Kruglov, S. M. Novikov, A. A. Vyshnevyy, A. V. Arsenin, and V. S. Volkov, "Broadband Optical Properties of Atomically Thin PtS_2 and $PtSe_2$", Nanomaterials **11**, 3269 (2021).

[177] M. Wei, J. Lian, Y. Zhang, C. Wang, Y. Wang, and Z. Xu, "Layer-dependent optical and dielectric properties of centimeter-scale $PdSe_2$ films grown by chemical vapor deposition", npj 2D Mater. Appl. **6**, 1 (2022).

[178] P. Suo, H. Zhang, S. Yan, W. Zhang, J. Fu, X. Lin, S. Hao, Z. Jin, Y. Zhang, C. Zhang, F. Miao, S.-J. Liang, and G. Ma, "Observation of Negative Terahertz Photoconductivity in Large Area Type-II Dirac Semimetal $PtTe_2$", Phys. Rev. Lett. **126**, 227402 (2021).

[179] P. Suo, S. Yan, R. Pu, W. Zhang, D. Li, J. Chen, J. Fu, X. Lin, F. Miao, S.-J. Liang, W. Liu, and G. Ma, "Ultrafast photocarrier and coherent phonon dynamics in type-II Dirac semimetal $PtTe_2$ thin films probed by optical spectroscopy", Photon. Res. **10**, 653 (2022).

[180] J. Lai, J. Ma, Y. Liu, K. Zhang, X. Zhuo, J. Chen, S. Zhou, and D. Sun, "Photocurrent response of type-II Dirac semimetal PtTe$_2$", 2D Mater. **7**, 034003 (2020).

[181] Y. Yang, K. Zhang, L. Zhang, G. Hong, C. Chen, H. Jing, J. Lu, P. Wang, X. Chen, L. Wang, and H. Xu, "Controllable growth of type-II Dirac semimetal PtTe$_2$ atomic layer on Au substrate for sensitive room temperature terahertz photodetection", InfoMat **3**, 705 (2021).

[182] H. Xu, C. Guo, J. Zhang, W. Guo, C.-N. Kuo, C. S. Lue, W. Hu, L. Wang, G. Chen, A. Politano, X. Chen, and W. Lu, "PtTe$_2$-Based Type-II Dirac Semimetal and Its van der Waals Heterostructure for Sensitive Room Temperature Terahertz Photodetection", Small **15**, 1903362 (2019).

[183] T. Wei, X. Wang, Q. Yang, Z. He, P. Yu, Z. Xie, H. Chen, S. Li, and S. Wu, "Mid-Infrared Photodetection of Type-II Dirac Semimetal 1T-PtTe$_2$ Grown by Molecular Beam Epitaxy", ACS Appl. Mater. Interfaces **13**, 22757 (2021).

[184] X.-W. Tong, Y.-N. Lin, R. Huang, Z.-X. Zhang, C. Fu, D. Wu, L.-B. Luo, Z.-J. Li, F.-X. Liang, and W. Zhang, "Direct Tellurization of Pt to Synthesize 2D PtTe$_2$ for High-Performance Broadband Photodetectors and NIR Image Sensors", ACS Appl. Mater. Interfaces **12**, 53921 (2020).

[185] X. Hu, K. P. Wong, L. Zeng, X. Guo, T. Liu, L. Zhang, Q. Chen, X. Zhang, Y. Zhu, K. H. Fung, and S. P. Lau, "Infrared Nanoimaging of Surface Plasmons in Type-II Dirac Semimetal PtTe$_2$ Nanoribbons", ACS Nano **14**, 6276 (2020).

[186] P. K. Cheng, S. Ahmed, J. Qiao, L. W. Wong, C. F. Yuen, A. M. Saleque, M. N. A. S. Ivan, S. U. Hani, M. I. Hossain, J. Zhao, Q. Wen, and Y. H. Tsang, "Nonlinear optical properties of two-dimensional palladium ditelluride (PdTe$_2$) and its application as aerosol jet printed saturable absorbers for broadband ultrafast photonics", Appl. Mater. Today **26**, 101296 (2022).

[187] K. Zhang, H. Xing, and L. Wang, "PtTe$_2$-based terahertz photodetector integrated with an interdigital antenna", Infrared Phys. Tech. **123**, 104168 (2022).

[188] S. Macis, A. D'Arco, L. Mosesso, M. C. Paolozzi, S. Tofani, L. Tomarchio, P. P. Tummala, S. Ghomi, V. Stopponi, E. Bonaventura, C. Massetti, D. Codegoni, A. Serafini, P. Targa, M. Zacchigna, A. Lamperti, C. Martella, A. Molle, and S. Lupi, "Terahertz and Infrared Plasmon Polaritons in PtTe$_2$ Type-II Dirac Topological Semimetal", Advanced Materials **n/a**, 2400554 (2024).

[189] L. Zhang, Z. Chen, K. Zhang, L. Wang, H. Xu, L. Han, W. Guo, Y. Yang, C.-N. Kuo, C. S. Lue, D. Mondal, J. Fuji, I. Vobornik, B. Ghosh, A. Agarwal, H. Xing, X. Chen, A. Politano, and W. Lu, "High-frequency rectifiers based on type-II Dirac fermions", Nat. Commun. **12**, 1584 (2021).

[190] P. Yadav, C. Xinhou, S. Bhatt, S. Das, H. Yang, and R. Mishra, "Highly Efficient Spintronic Terahertz Emitter Utilizing a Large Spin Hall Conductivity of Type-II Dirac Semimetal PtTe$_2$", Nano Lett. **24**, 2376 (2024).

[191] Z. Chen, H. Qiu, X. Cheng, J. Cui, Z. Jin, D. Tian, X. Zhang, K. Xu, R. Liu, W. Niu, L. Zhou, T. Qiu, Y. Chen, C. Zhang, X. Xi, F. Song, R. Yu, X. Zhai, B. Jin, R. Zhang, and X. Wang, "Defect-induced helicity dependent terahertz emission in Dirac semimetal PtTe$_2$ thin films", Nat. Commun. **15**, 2605 (2024).

[192] R. W. Wood, "On a Remarkable Case of Uneven Distribution of Light in a Diffraction Grating Spectrum", Proc. Phys. Soc. London **18**, 269 (1902).

[193] U. Fano, "The Theory of Anomalous Diffraction Gratings and of Quasi-Stationary Waves on Metallic Surfaces (Sommerfeld's Waves)", J. Opt. Soc. Am. **31**, 213 (1941).

[194] R. H. Ritchie, "Plasma Losses by Fast Electrons in Thin Films", Phys. Rev. **106**, 874 (1957).

[195] C. J. Powell and J. B. Swan, "Origin of the Characteristic Electron Energy Losses in Aluminum", Phys. Rev. **115**, 869 (1959).

[196] E. A. Stern and R. A. Ferrell, "Surface Plasma Oscillations of a Degenerate Electron Gas", Phys. Rev. **120**, 130 (1960).

[197] A. Otto, "Excitation of nonradiative surface plasma waves in silver by the method of frustrated total reflection", Z. Physik **216**, 398 (1968).

[198] E. Kretschmann, "Die Bestimmung optischer Konstanten von Metallen durch Anregung von Oberflächenplasmaschwingungen", Z. Physik **241**, 313 (1971).

[199] S. A. Maier, *Plasmonics: Fundamentals and Applications* (Springer New York, NY, 2007).

[200] Z. Wang, "A REVIEW ON RESEARCH PROGRESS IN SURFACE PLASMONS", Progress In Physics **29**, 287 (2009).

[201] P. A. D. Gonçalves and N. M. R. Peres, *An Introduction to Graphene Plasmonics* (World Scientific, 2016).

[202] G. S. Jenkins, C. Lane, B. Barbiellini, A. B. Sushkov, R. L. Carey, F. Liu, J. W. Krizan, S. K. Kushwaha, Q. Gibson, T.-R. Chang, H.-T. Jeng, H. Lin, R. J. Cava, A. Bansil, and H. D. Drew, "Three-dimensional Dirac cone carrier dynamics in Na_3Bi and Cd_3As_2", Phys. Rev. B **94**, 085121 (2016).

[203] O. V. Kotov and Y. E. Lozovik, "Dielectric response and novel electromagnetic modes in three-dimensional Dirac semimetal films", Phys. Rev. B **93**, 235417 (2016).

[204] A. Thakur, R. Sachdeva, and A. Agarwal, "Dynamical polarizability, screening and plasmons in one, two and three dimensional massive Dirac systems", J. Phys.: Condens. Matter **29**, 105701 (2017).

[205] J.-T. Hou, C.-X. Yan, C.-Y. Tan, Z.-Q. Li, P. Wang, H. Guo, and H.-R. Chang, "Effects of spatial dimensionality and band tilting on the longitudinal optical conductivities in Dirac bands", Phys. Rev. B **108**, 035407 (2023).

[206] J. P. Carbotte, "Dirac cone tilt on interband optical background of type-I and type-II Weyl semimetals", Phys. Rev. B **94**, 165111 (2016).

[207] M. Dressel and G. Grüner, *Electrodynamics of Solids: Optical Properties of Electrons in Matter* (Cambridge University Press, 2002).

[208] G. D. Mahan, *Many-Particle Physics* (Springer New York, NY, 2000).

[209] K. Seeger, *Semiconductor Physics* (Springer Berlin, Heidelberg, 2004).

[210] H. Ehrenreich and M. H. Cohen, "Self-Consistent Field Approach to the Many-Electron Problem", Phys. Rev. **115**, 786 (1959).

[211] J. Hubbard and R. E. Peierls, "The description of collective motions in terms of many-body perturbation theory", Proc. R. Soc. Lond. A **240**, 539 (1957).

[212] F. W. Han, W. Xu, L. L. Li, C. Zhang, H. M. Dong, and F. M. Peeters, "Electronic and transport properties of *n*-type monolayer black phosphorus at low temperatures", Phys. Rev. B **95**, 115436 (2017).

[213]   H. Y. Zhang, Y. M. Xiao, Q. N. Li, L. Ding, B. Van Duppen, W. Xu, and F. M. Peeters, "Anisotropic and tunable optical conductivity of a two-dimensional semi-Dirac system in the presence of elliptically polarized radiation", Phys. Rev. B **105**, 115423 (2022).

[214]   L. F. Man, W. Xu, Y. M. Xiao, H. Wen, L. Ding, B. Van Duppen, and F. M. Peeters, "Terahertz magneto-optical properties of graphene hydrodynamic electron liquid", Phys. Rev. B **104**, 125420 (2021).

[215]   A. B. Kuzmenko, E. van Heumen, F. Carbone, and D. van der Marel, "Universal Optical Conductance of Graphite", Phys. Rev. Lett. **100**, 117401 (2008).

[216]   Z. Q. Li, E. A. Henriksen, Z. Jiang, Z. Hao, M. C. Martin, P. Kim, H. L. Stormer, and D. N. Basov, "Dirac charge dynamics in graphene by infrared spectroscopy", Nat. Phys. **4**, 532 (2008).

[217]   R. R. Nair, P. Blake, A. N. Grigorenko, K. S. Novoselov, T. J. Booth, T. Stauber, N. M. R. Peres, and A. K. Geim, "Fine structure constant defines visual transparency of graphene", Science **320**, 1308 (2008).

[218]   F. Wang, Y. Zhang, C. Tian, C. Girit, A. Zettl, M. Crommie, and Y. R. Shen, "Gate-variable optical transitions in graphene", Science **320**, 206 (2008).

[219]   H. M. Dong, W. Xu, Z. Zeng, T. C. Lu, and F. M. Peeters, "Quantum and transport conductivities in monolayer graphene", Phys. Rev. B **77**, 235402 (2008).

[220]   W. Xu, H. M. Dong, L. L. Li, J. Q. Yao, P. Vasilopoulos, and F. M. Peeters, "Optoelectronic properties of graphene in the presence of optical phonon scattering", Phys. Rev. B **82**, 125304 (2010).

[221]   J.-Y. Yang, B.-B. Wang, and E.-K. Liu, "Berry curvature induced unconventional electronic transport behaviors in magnetic topological semimetals", Acta Phys. Sin. **72**, 177103 (2023).

[222]   E. Burstein, "Anomalous Optical Absorption Limit in InSb", Phys. Rev. **93**, 632 (1954).

[223]   H. J. Krenner, E. C. Clark, T. Nakaoka, M. Bichler, C. Scheurer, G. Abstreiter, and J. J. Finley, "Optically Probing Spin and Charge Interactions in a Tunable Artificial Molecule", Phys. Rev. Lett. **97**, 076403 (2006).

[224]   B. Wunsch, T. Stauber, F. Sols, and F. Guinea, "Dynamical polarization of graphene at finite doping", New J. Phys. **8**, 318 (2006).

[225]   X.-F. Wang and T. Chakraborty, "Collective excitations of Dirac electrons in a graphene layer with spin-orbit interactions", Phys. Rev. B **75**, 033408 (2007).

[226]   H. Dong, L. Li, W. Wang, S. Zhang, C. Zhao, and W. Xu, "Terahertz plasmon and infrared coupled plasmon–phonon modes in graphene", Physica E: Low-dimensional Systems and Nanostructures **44**, 1889 (2012).

[227]   J.-J. Zhu, S. M. Badalyan, and F. M. Peeters, "Plasmonic excitations in Coulomb-coupled N-layer graphene structures", Phys. Rev. B **87**, 085401 (2013).

[228]   J. Zhou, H.-R. Chang, and D. Xiao, "Plasmon mode as a detection of the chiral anomaly in Weyl semimetals", Phys. Rev. B **91**, 035114 (2015).

[229]   M. Dadsetani and A. Ebrahimian, "Optical Distinctions Between Weyl Semimetal TaAs and Dirac Semimetal Na_3Bi: An *Ab Initio* Investigation", J. Electron. Mater. **45**, 5867 (2016).

[230]   J. Jiang, S. Lee, F. Fei, F. Song, E. Vescovo, K. Kaznatcheev, F. J. Walker, and C. H. Ahn, "A comprehensive ARPES study on the type-II Dirac semimetal candidate $Ir_{1_x}Pt_xTe_2$", APL Mater. **8**, 061106 (2020).

[231] G. Ermolaev, K. Voronin, D. G. Baranov, V. Kravets, G. Tselikov, Y. Stebunov, D. Yakubovsky, S. Novikov, A. Vyshnevyy, A. Mazitov, I. Kruglov, S. Zhukov, R. Romanov, A. M. Markeev, A. Arsenin, K. S. Novoselov, A. N. Grigorenko, and V. Volkov, "Topological phase singularities in atomically thin high-refractive-index materials", Nat. Commun. **13**, 2049 (2022).

[232] J. P. Harrang, R. J. Higgins, R. K. Goodall, P. R. Jay, M. Laviron, and P. Delescluse, "Quantum and classical mobility determination of the dominant scattering mechanism in the two-dimensional electron gas of an AlGaAs/GaAs heterojunction", Phys. Rev. B **32**, 8126 (1985).